Mathematical Modeling for Instruments Sizing and Analyzing Aerosols

Operation of Multiple Monodisperse Outlets Differential Mobility Analyzer, Volatility and Hygroscopicity Measurements Analysis

Dissertation by

Maria N. Giamarelou

Department of Environment
University of the Aegean

Mytilini, Greece
2014
(Defended, 16 June 2014)

Η παρούσα έρευνα έχει συγχρηματοδοτηθεί από την Ευρωπαϊκή Ένωση (Ευρωπαϊκό Κοινωνικό Ταμείο - ΕΚΤ) και από εθνικούς πόρους μέσω του Επιχειρησιακού Προγράμματος «Εκπαίδευση και Δια Βίου Μάθηση» του Εθνικού Στρατηγικού Πλαισίου Αναφοράς (ΕΣΠΑ) – Ερευνητικό Χρηματοδοτούμενο Έργο: Ηράκλειτος ΙΙ . Επένδυση στην κοινωνία της γνώσης μέσω του Ευρωπαϊκού Κοινωνικού Ταμείου.

This research has been co-financed by the European Union (European Social Fund – ESF) and Greek national funds through the Operational Program "Education and Lifelong Learning" of the National Strategic Reference Framework (NSRF) - Research Funding Program: Heracleitus II. Investing in knowledge society through the European Social Fund.

European Union
European Social Fund

OPERATIONAL PROGRAMME
EDUCATION AND LIFELONG LEARNING
investing in knowledge society
MINISTRY OF EDUCATION & RELIGIOUS AFFAIRS
MANAGING AUTHORITY
Co- financed by Greece and the European Union

NSRF
2007-2013
programme for development
EUROPEAN SOCIAL FUND

«χαλεπὰ τὰ καλά»
Πλάτων, Πολιτεία

"Nothing is beautiful without effort"
Plato, The Republic

To my newborn nephew

Acknowledgements

A long trip has finally come to an end. It would have never started in the first place had it not been for Prof. Dias Haralambopoulos who initially encouraged me to start my research. He has always been there for me to provide help, support and inspiration, when needed. His quotes have accompanied me during the years of my research.

First, I would like to thank George Biskos for being a wonderful advisor. He gave me the opportunity to work in an exciting field, he has been very understanding and has always been there to answer questions, to provide guidance and support. I appreciate the balance he kept between demanding and expecting. I truly thank him for helping me in making a dream come true. I would also like to thank Dr. Mark Stolzenburg for his assistance over the years, for all the interesting and challenging conversation on Skype during late hours, and for reminding me how small the world is, how infinite science is, and what a Mathematician can accomplish.

I would also like to thank Dr. Konstantinos Eleftheriadis and Dr. Stephan Nyeki who have trusted me with the analysis of the precious VTDMA data from Ny-Alesund and for the long and interesting discussions, it was a pleasure working with both of you. Many thanks are due to Dr. Evangelos Papapanagiotou for his help during the TDMAfit program creation and for sharing his valuable knowledge on programming and geospatial analysis. Likewise, I would like to thank Prof. Da-Ren Chen for providing the experimental data and for his help during the validation of my theory, as well as Prof. Juan Fernandez de la Mora for answering my questions. I would also like to thank Dr. Martin Gysel for giving me access to TDMAinv and for finding time to answer questions. I would like to thank Prof. Christos Matsoukas who always took time to answer questions and help. Also, I want to thank Dr. Dwane Paulsen and Dr. Mackenzie Smith for their help.

Of course, I should not neglect to thank Dr. Michael Attoui for his answers and for sharing his ideas. I would like also to thank the whole Aerosol group; Lena, Kostis, Spyros, Dimitris, and Panos for varied discussions about science and other "topics", and for their support all these years.

Last but not least, I am grateful to my parents Niko and Evangelia for their support and understanding and to my brother and sister-in-law for their support and for adding a new member in the family.

Abstract

Quantifying the contribution of natural and anthropogenic particles on regional and global climate and on human health requires information both of their size and of their chemical composition. The most prevalently invoked technique for measuring size and other intrinsic properties of ultrafine aerosol particles (e.g., volatility and hygroscopicity) is by electrical mobility. With the advent of aerosol instrumentation, Differential Mobility Analyzers (DMAs) are the most commonly used instruments to classify or select particles within a narrow distribution of mobility diameter. When combining DMAs in series (i.e., Tandem-DMA system) the distribution selected by the first DMA after conditioning will be interrogated by the second DMA to determine, for example, hygroscopicity, volatility or composition. The motivation of this thesis is to improve our understanding of the theory which describes the operation of a multiple monodisperse outlet differential mobility analyzer (MMO-DMA), and to probe the volatility and hygroscopicity properties of aerosol particles generated in the laboratory and observed in the field.

Analytical expressions are developed for estimating the transfer function and the resolution of DMAs with multiple monodisperse outlets. The theoretical framework provided can be employed to optimize the design of DMAs with more than one monodisperse-particle outlets, and to analyze the measurements when such DMAs are used in aerosol mobility spectrometers. The theoretical model is compared with the experimental performance of a MMO-DMA with 3 monodisperse outlets (3-MO-DMA).

Hygroscopic Tandem-DMA (H-TDMA) systems have been used during the last decades, both in laboratory and in field campaigns in various environments globally. These investigations have yielded valuable information regarding the hygroscopic behavior of aerosol particles. The hygroscopic growth factor value is used to indicate internally or externally mixed particles, and provide insights into the sources and processes regulating the aerosol. Thus, the knowledge of accurate estimations of the growth factor is crucial. TDMA data inversion codes are used to retrieve growth factor values. TDMAfit and TDMAinv data inversion algorithms are widely used for the analysis of the hygroscopicity TDMA measurements. The validation of a modified version of the TDMAfit and the TDMAinv inversion codes is performed using laboratory and field measurements.

Hygroscopic properties of new formed aerosol particles having diameter less of ca. 50 nm vary significantly from those of their larger-particles counterparts. As aerosol particles experience continuous modification by atmospheric aging processes, the hygroscopic behavior of ambient aerosol particles vary strongly depending on the origin of the air masses and the location. To understand the hygroscopic behavior of ambient aerosol particles presumes to fully understand the properties of the pure particles. New measurements of the deliquescence and efflorescence relative humidity (DRH, ERH) and hygroscopic growth of potassium-halide particles (namely, KBr, KCl, KI) having diameters from 8 to 60 nm are analyzed.

Finally, the mechanisms leading to new particle formation in high Arctic have been investigated. Characterization of atmospheric aerosols observed in the summertime high Arctic was made based on: 1) particle size distributions, and 2) the volatility of monodisperse particles.

Περίληψη

Η ποσοτικοποίηση της επίδρασης των φυσικών και ανθρωπογενών σωματιδίων στο κλίμα, σε τοπικό και παγκόσμιο επίπεδο, καθώς και στην ανθρώπινη υγεία απαιτεί την ύπαρξη πληροφοριών τόσο για το μέγεθός τους όσο και για τη χημική τους σύσταση. Η πιο ευρέως χρησιμοποιούμενη μέθοδος για τη μέτρηση του μεγέθους και άλλων εγγενών ιδιοτήτων των υπέρλεπτων αιωρούμενων σωματιδίων (π.χ. πτητικότητα και υγροσκοπικότητα) είναι η ηλεκτρική κινητικότητα. Με την εμφάνιση οργάνων για τη μέτρηση αιωρούμενων σωματιδίων, οι αναλυτές διαφορικής κινητικότητας (Differential Mobility Analyzers, DMAs) είναι τα πιο ευρέως χρησιμοποιούμενα όργανα για την ταξινόμηση ή την επιλογή σωματιδίων σε ένα στενό εύρος κατανομής της κινητικής διαμέτρου. Όταν συνδυάζονται DMAs σε σειρά (δηλαδή σύστημα Tandem-DMA, TDMA), η κατανομή που επιλέγεται από το πρώτο DMA μετά από κατάλληλη επεξεργασία θα μελετηθεί στο δεύτερο DMA, για να καθοριστεί, για παράδειγμα, η υγροσκοπικότητα, η πτητικότητα ή η σύσταση. Το κίνητρο για αυτή τη διατριβή ήταν η περαιτέρω κατανόηση της θεωρίας που περιγράφει τη λειτουργία ενός αναλυτή διαφορικής κινητικότητας πολλαπλών μονο-μεγεθών εξόδων (MMO-DMA) και η εξέταση των ιδιοτήτων πτητικότητας και υγροσκοπικότητας αιωρούμενων σωματιδίων, τόσο δημιουργημένων σε εργαστήριο όσο και παρατηρημένων στο πεδίο.

Αναλυτικές εκφράσεις έχουν αναπτυχθεί για τον υπολογισμό της συνάρτησης μεταφοράς και τη διακριτική ικανότητα των DMAs με πολλαπλές εξόδους μονο-μεγεθών σωματιδίων. Το θεωρητικό πλαίσιο που παρουσιάζεται μπορεί να εφαρμοστεί για τη βελτιστοποίηση του σχεδιασμού DMA με περισσότερες της μίας εξόδων μονο-μεγεθών σωματιδίων αλλά και στην ανάλυση μετρήσεων, όταν τέτοιοι αναλυτές χρησιμοποιούνται σε φασματογράφους κινητικότητας αιωρούμενων σωματιδίων. Το

θεωρητικό μοντέλο συγκρίνεται με πειραματικές μετρήσεις για ένα MMO-DMA με 3 εξόδους (3-MO-DMA).

Συστήματα υγροσκοπικότητας TDMA (H-TDMA) έχουν χρησιμοποιηθεί τις τελευταίες δεκαετίες, τόσο σε εργαστηριακές μετρήσεις όσο και σε μετρήσεις πεδίου σε διαφορετικά περιβάλλοντα παγκοσμίως. Αυτές οι παρατηρήσεις έχουν προσφέρει πολύτιμες πληροφορίες σχετικά με την υγροσκοπική συμπεριφορά των αιωρούμενων σωματιδίων. Η τιμή του λόγου υγροσκοπικής αύξησης χρησιμοποιείται για να προσδιορίσει εσωτερικά ή εξωτερικά αναμεμειγμένα σωματίδια και να παρέχει ενδείξεις για τις πηγές και τις διαδικασίες που καθορίζουν το αεροζόλ. Επομένως, ο ακριβής υπολογισμός του λόγου αύξησης είναι μεγίστης σημασίας. Αλγόριθμοι αντιστροφής δεδομένων TDMA χρησιμοποιούνται για τον υπολογισμό των λόγων αύξησης. Οι αλγόριθμοι αντιστροφής δεδομένων TDMAfit και TDMAinv χρησιμοποιούνται ευρέως για την ανάλυση TDMA μετρήσεων υγροσκοπικότητας. Η αξιολόγηση μιας τροποποιημένης έκδοσης του αλγόριθμου TDMAfit σε σύγκριση με το TDMAinv γίνεται με τη χρήση εργαστηριακών μετρήσεων και μετρήσεων πεδίου.

Οι ιδιότητες υγροσκοπικότητας νεο-σχηματισμένων αιωρούμενων σωματιδίων με διάμετρο μικρότερη από 50 nm περίπου, διαφέρουν σημαντικά από αυτές των μεγαλύτερων σωματιδίων. Καθώς τα σωματίδια υπόκεινται συνεχώς σε τροποποιήσεις από διαδικασίες ατμοσφαιρικής ωρίμανσης, η υγροσκοπική συμπεριφορά των ατμοσφαιρικών σωματιδίων ποικίλει σημαντικά ανάλογα με την προέλευση των αέριων μαζών και την τοποθεσία τους. Η κατανόηση της υγροσκοπικής συμπεριφοράς των ατμοσφαιρικών αιωρούμενων σωματιδίων προϋποθέτει την πλήρη κατανόηση των ιδιοτήτων των καθαρών σωματιδίων. Νέες μετρήσεις των σχετικών υγρασιών υγροποίησης και στερεοποίησης (Deliquescence και Efflorescence Relative Humidity,

DRH, ERH) και της υγροσκοπικής ανάπτυξης σωματιδίων αλογόνων του καλίου (ονομαστικά KBr, KCl, KI) με μέγεθος από 8 έως 60 nm παρουσιάζονται.

Τέλος, εξετάζονται οι μηχανισμοί που οδηγούν στο σχηματισμό νέων σωματιδίων στην περιοχή πάνω από τον Αρκτικό Κύκλο. Ο χαρακτηρισμός των ατμοσφαιρικών αιωρούμενων σωματιδίων που παρατηρούνται κατά τη θερινή περίοδο στην περιοχή αυτή γίνεται με βάση: 1) τις κατανομές μεγέθους των σωματιδίων και 2) την πτητικότητα μονο-μεγεθών σωματιδίων.

Contents

List of Figures

List of Tables

Nomenclature

$\mathrm{a_w}$	water activity
b	radial distance between the two coaxial electrodes
C_c	Cunningham slip correction factor
CS	the condensational sink (s^{-1})
d	particle mobility diameter
d_p	particle mobility diameter
$d_p(RH)$	particle mobility diameter at the dry state
$d_{p,dry}$	particle mobility diameter at increased relative humidity
d_{ve}	particle volume equivalent diameter
D	diffusion coefficient
$\widetilde{D}_i$	dimensionless diffusion coefficient
e	charge of the electron
$\boldsymbol{E}$	electric field vector
E_r	radial component of the electric field
E_z	axial component of the electric field
$\boldsymbol{e}_r$	unit vector in the radial direction
$\boldsymbol{e}_z$	unit vector in the axial direction
$\mathrm{erf}(x)$	error function
f	geometric parameter
f_{in}	probability of a particle entering the DMA on a specific streamline
f_{trans_i}	probability of a particle exiting the DMA at the *i*th monodisperse-particle outlet
f_γ	dimensionless velocity profile
$f(x)$	the unknown size distribution function (Chapter 4)
F_γ	flow fraction
g	growth factor

$g(RH)$	growth factor as a function of relative humidity
G_i	geometric and flow parameter for the i^{th} monodisperse-particle outlet
$I(V)$	the response of the sensor as a function of the rod voltage
$I_\gamma(\gamma)$	geometric integral parameter
k	Boltzmann's constant
k	a temperature-dependent reaction rate constant (cm^3.molec^{-1}.s^{-1}) (Appendix C)
K_i	the kernel function of the i^{th} instrument channel
L_i	distance between the middle of the aerosol flow inlet and the middle of the i^{th} sample outlet
m	molality
M	the air density
M_w	the molar mass of water
n	number of monodisperse-particle outlets
$n\left(d_p, n_p\right)\mathrm{d}d_p$	number of particles per unit volume entering the classifier carrying n_p number of charges and diameter in the range d_p and $d_p + \mathrm{d}d_p$
$\hat{n}\left(Z_p\right)\mathrm{d}Z_p$	number of particles per unit volume entering the classifier with electrical mobility in the range Z_p and $Z_p + \mathrm{d}Z_p$.
$P\left(Z_{p1}\right)$	the penetration efficiency of the aerosol conditioner
Pe	*Péclet* number
q	particle charge
Q_a	aerosol flow rate
Q_{m_i}	excess flow rate after the i^{th} monodisperse-particle outlet
Q_{s_i}	sample flow rate of the i^{th} monodisperse-particle outlet

Q_{sh}	sheath air flow rate
Q_{sh_i}	sheath air flow before the i^{th} monodisperse-particle outlet
Q_t	total flow rate
Q_{t_i}	total flow rate corresponding to the i^{th} segment
$\boldsymbol{r}$	position vector
r	radial position
$\tilde{r}$	dimensionless radial position
R_1	inner radius
R_2	outer radius
$\mathcal{R}$	resolution
R	the universal gas constant
R	the global radiation (W.m^{-2}) (Appendix C)
$R(d_p, n_p)$	response of receiving particle counter per unit concentration of particles having charge n_p and diameter d_p
$\mathcal{R}_{nd}$	resolution when considering non-diffusing particles (conventional DMA)
$\mathcal{R}_{nd_i}$	resolution of the i^{th} outlet of the MMO-DMA when considering non-diffusing particles
$\mathcal{R}_k$	limiting resolution
$\mathcal{R}_{diff_i}$	resolution of the i^{th} outlet of the MMO-DMA using the approximate diffusional transfer function
$\mathcal{R}_{approx_i}$	approximate resolution of the i^{th} outlet of the MMO-DMA
s	distance along the particle streamline Γ_{in}
S_d^2	variance of transfer function

T	temperature
t	time
$\tilde{t}_i$	dimensionless time of the particles traveling to the i^{th} sample outlet of the MMO-DMA
$U^*_{E_i}$	electrophoretic migration velocity of $Z^*_{p_i}$ at R_2
U_j	average flow velocity of the j^{th} MMO-DMA segment
u	flow velocity
u_r	radial velocity component of the flow
u_z	axial velocity component of the flow
υ	particle speed
$\boldsymbol{\upsilon}$	particle velocity vector
$\tilde{\upsilon}_j$	dimensionless particle velocity in the j^{th} MMO-DMA segment
υ_r	radial particle velocity component
υ_z	axial particle velocity component
υ_E	electrophoretic migration velocity
V	applied voltage
V_{diff_i}	diffusion-onset voltage
w_t	water content
x	perpendicular distance from particle streamline Γ_{in} (Chapter 2)
x	a size parameter (Chapter 4)
y_i	the discrete measurements points
z	axial position
Z_p	particle electrical mobility
$Z^*_{p_i}$	centroid particle electrical mobility corresponding to the i^{th} outlet

$\tilde{Z}_p$	dimensionless electrical mobility
$\tilde{Z}_{p_i}$	dimensionless electrical mobility

Greek Letters

β_i	dimensionless flow ratio
γ	geometric parameter
Γ	particle stream function
δ_i	dimensionless flow ratio
δ_D	Dirac delta function
$\boldsymbol{\nabla}$	gradient operator
ε_i	the instrument error in i^{th} channel
$\mathcal{E}(x)$	integral of the error function
ζ_i	dimensionless mobility
λ	mean free path of the carrier gas
$\rho_{aq}(w_t)$	the density of the aqueous-solution droplets
ρ_s	the density of the dry particle
ρ_w	the density of the water
σ_{aq}	the surface tension of the aqueous droplet
σ_i	dimensionless total diffusional broadening parameter of particles exiting through the i^{th} outlet
$\sigma_{i,j}$	dimensionless diffusional broadening parameter within the j^{th} MMO-DMA segment of particles exiting through the i^{th} outlet
σ_i^*	dimensionless diffusional broadening parameter of particles with centroid electrical mobility corresponding to the i^{th} outlet
σ_{Γ_i}	total diffusional broadening of particles exiting through the i^{th} outlet

$\sigma_{\Gamma_{i,j}}$	diffusional broadening parameter within the *j*th MMO-DMA segment of particles exiting through the *i*th outlet
σ_{Γ}	diffusional broadening parameter around particle streamline Γ
σ_x	standard deviation in the direction perpendicular to the particle streamline
τ_i	characteristic transit time through the MMO-DMA for $Z_{p_i}^*$ particle
Ψ	flow stream function
Φ	electric flux function
χ	the shape correction factor of the dry particles
ω	dimensionless radial position
Ω	transfer function
Ω_{nd_i}	transfer function of the *i*th monodisperse-particle outlet for non-diffusing particles
Ω_{d_i}	transfer function of the *i*th monodisperse-sparticle outlet for diffusing particles

Chapter 1

1. Introduction

1.1 Introduction

Aerosols are suspensions of fine solid or liquid particles in a gas, with size ranging from a few nanometers to tens of micrometers in diameter. Atmospheric aerosols are produced by particles emitted either from natural sources, e.g., windborne dust, sea spray, and volcanic eruptions, or from anthropogenic sources such as fuels combustion or biomass burning. They typically contain inorganic salts, crustal elements, carbonaceous materials, and water (Seinfeld and Pandis, 2006). Apart from being directly emitted (primary aerosols), airborne particles can also be formed by gas-to-particle conversion processes in the atmosphere (secondary aerosols).

Atmospheric aerosols, especially those produced by human activities, can have adverse effects upon human health and climate. A number of epidemiological and laboratory studies, suggest that increased particle concentration of atmospheric aerosols is associated with pulmonary and cardiovascular diseases (Dockery et al., 1993; Donaldson et al., 1998).

Atmospheric aerosol particles can have an important effect on the planetary radiative balance as they can scatter and absorb the incident sunlight, thereby contributing to the radiative budget of the Earth and affect climate in a direct and indirect way (Charlson et al., 1992; Schwartz, 1996). The direct effect, refers to the direct interaction of the aerosol particles with radiation (through scattering and absorption, e.g., Haywood et al., 2001; Loeb and Kato, 2002), while the indirect effect is related to the ability of the particles to form cloud droplets. Changes in the number concentrations and properties of atmospheric aerosol particles, due to human activities, result in increased number concentrations of cloud condensation nuclei (CCN), which in turn alters the microphysical properties of the clouds, enhances the radiative forcing (i.e., the imbalance between solar radiation and infrared radiation) (Twomey, 1974; Twomey, 1977b; Pruppacher and Klett, 1997; Kuang and Yung, 2000; IPCC, 2007).

Both scattering and absorption of incoming solar radiation depend on the particle size, with the intensity of the scattered light being proportional to the sixth power of the particle diameter (Hinds, 1999). Since the size of the atmospheric particles in the accumulation mode is of the same order as the wavelength of the radiation, solar radiation is efficiently scattered, while smaller particles are not efficient scatterers. The absorption depends not only on the variation of droplet size but also on the cloud liquid water path. Thus, for “deep” or semi-infinite clouds, absorption increases monotonically with increasing effective radius, but the reverse dependence is established for thin clouds (Ackerman and Stephans, 1987). Water constitutes a substantial fraction of the atmospheric aerosol particles, thus the response of particles to changes in relative humidity (RH) is important in determining ambient particle size. At a given RH, the water content and activation of CCN into cloud droplets is determined by particle size and chemical composition, as described by the Köhler theory (Köhler, 1936) (McFiggans et al., 2006; Fierz-Schmidhauser et al., 2010).

Both atmospheric conditions and atmospheric aerosol particles can vary greatly both spatially and temporally. As the detailed chemical composition of the atmospheric aerosol is rarely known, indirect measurements of their composition can be achieved through measurements of their hygroscopicity and/or volatility. The most common approach for probing the hygroscopicity or the volatility of aerosol particles, is by using the hygroscopicity- or volatility tandem differential mobility analyzer (e.g., H-TDMA; Liu et al., 1978; Swietlicki et al., 2008; V-TDMA; Frey et al., 2008). At first, in these systems, an aerosol is size classified with the first DMA, then is humidified or heated and the resulting size distribution is measured by the second DMA. The hygroscopic data are reported in terms of the growth factor ratio, i.e., the ratio of the mean diameter of the humidified particles to that of the dry particles, while the volatility data can be expressed either as shrinking factor, or as fraction of remaining particles.

These systems require the use of DMAs. Since the first electric mobility analyzer (Hewitt, 1957) various designs have been developed and used. The classification range of a DMA is determined by its geometry and operating conditions (Stolzenburg, 1988) and underlie limitations (e.g., turbulence flow, breakdown voltage, etc.). The size range of commercially available DMAs is 10 nm to 1 μm (TSI, Model 3081). Challenge, however, is to design and operate a DMA that will enable a wider classification size range in less time. This can be achieved with DMAs with more than one monodisperse-particle outlet. These designs can offer a number of advantages compared to conventional single monodisperse-particle outlet designs, e.g., shorter time scans, wider size range, more efficient TDMA measurements, if used as a first DMA of the system. Chen et al. (2007) have designed and tested a DMA with three monodisperse-particle outlets (3-MO-DMA).

The understanding of the theoretical transfer function that describes the operation of a multiple monodisperse outlet DMA (MMO-DMA) establishes a link between aerosol particle size distribution and hygroscopicity TDMA measurements. This is a monumental task. The challenges, however, are not limited to the theory governing the transport of particles in the DMA column and their probability in being classified and detected, i.e., the transfer function. They also extend to the analysis and the inversion of the measurements. For the scanning mobility particle analyzer (SMPS), i.e., a DMA coupled with a condensation particle counter (CPC), the response signal is the convolution of the transfer function, the counter response and the aerosol size distribution, as a function of the applied voltage. In order to estimate the growth factor distribution by TDMA measurements, the recorded data should be properly inverted. To invert such measurements, we need a good theoretical understanding of the performance of DMAs as well as the appropriate mathematical tools for defining and solving the inversion problem.

1.2 Organization of Thesis

The motivation of this thesis is to improve our understanding of the theory that describes the operation of a MMO-DMA, and to better understand the volatility and hygroscopicity properties of aerosol particles measured by volatility- or hygroscopicity-TDMA systems. Chapter 2 provides the derivation of the transfer function and resolution of MMO-DMAs. In Chapter 3, the validation of the theoretical framework is performed via its comparison with experimental data as derived by the 3-MO-DMA described in Chen et al. (2007). Chapter 4 develops a modified TDMA data inversion code, and compares its performance with that of another widely used TMDA data inversion code. Chapter 5 provides new measurements of the DRH, ERH, and hygroscopic growth of potassium-halide particles (namely, KBr, KCl, KI) with diameters ranging from 8 to 60 nm. Chapter 6 focuses on the species involved in new particle formation and growth in the high Arctic and characterize their composition, based on measurements of their size distribution and of their volatility properties performed using a V-TDMA system. Finally, Chapter 7 presents a summary of the most important conclusions of the results described in this thesis.

1. Εισαγωγή

1.1 Εισαγωγή

Τα αεροζόλ (αερολύματα) είναι διαλύματα υπέρλεπτων στερεών ή υγρών σωματιδίων σε αέριο, με μεγέθη που κυμαίνονται από μερικά νανόμετρα μέχρι μερικές δεκάδες μικρόμετρα σε διάμετρο. Τα ατμοσφαιρικά αεροζόλ προέρχονται από σωματίδια που εκπέμπονται είτε από φυσικές πηγές, π.χ. σκόνη, θαλάσσια αύρα και ηφαιστειακές εκρήξεις, ή από ανθρωπογενής πηγές, όπως η καύση καυσίμων ή βιομάζας. Τυπικά, περιέχουν ανόργανα άλατα, κρυσταλλικά στοιχεία, οργανικά υλικά και νερό (Seinfeld and Pandis, 2006). Εκτός από την άμεση εκπομπή τους (πρωτογενή αεροζόλ), τα αιωρούμενα σωματίδια μπορούν επίσης να σχηματιστούν από διαδικασίες μετατροπής αερίου σε σωματίδιο στην ατμόσφαιρα (δευτερογενή αεροζόλ).

Τα ατμοσφαιρικά αεροζόλ, ειδικά αυτά που παράγονται από ανθρώπινες δραστηριότητες, μπορούν να έχουν ποικίλες επιδράσεις στην ανθρώπινη υγεία και στο κλίμα. Πλήθος επιδημιολογικών και εργαστηριακών μελετών υποδεικνύουν ότι η αύξηση της συγκέντρωσης των ατμοσφαιρικών αιωρούμενων σωματιδίων συνδέεται με πνευμονολογικές και καρδιαγγειακές ασθένειες (Dockery et al., 1993; Donaldson et al., 1998).

Τα ατμοσφαιρικά σωματίδια έχουν, επιπλέον, σημαντική επίδραση στο πλανητικό ισοζύγιο ακτινοβολίας, καθώς σκεδάζουν και απορροφούν την προσπίπτουσα ηλιακή ακτινοβολία και ως εκ τούτου συμβάλλουν στο ισοζύγιο ακτινοβολίας της Γης και επηρεάζουν το κλίμα με έμμεσο και άμεσο τρόπο (Charlson et al., 1992; Schwartz, 1996). Η άμεση επίδραση αναφέρεται στην άμεση αλληλεπίδραση των αιωρούμενων σωματιδίων με την ακτινοβολία (μέσω της σκέδασης και της απορρόφησης, π.χ., Haywood et al., 2001; Loeb and Kato, 2002), ενώ η έμμεση επίδραση σχετίζεται με την ικανότητα των σωματιδίων να σχηματίζουν σταγονίδια νεφών. Αλλαγές στην αριθμητική συγκέντρωση και στις ιδιότητες των ατμοσφαιρικών αιωρούμενων σωματιδίων, οφειλόμενες σε ανθρώπινες δραστηριότητες, επιφέρουν αύξηση στην αριθμητική συγκέντρωση των πυρήνων συμπύκνωσης νεφών (Cloud condensation nuclei, CCN), η οποία διαδοχικά αλλάζει τις μικροφυσικές ιδιότητες των νεφών, ενισχύοντας τη διαφορά στο ενεργειακό ισοζύγιο (radiative forcing, δηλαδή στην έλλειψη ισορροπίας μεταξύ της ηλιακής και της υπέρυθρης ακτινοβολίας) (Twomey, 1974; Twomey, 1977b; Pruppacher and Klett, 1997; Kuang and Yung, 2000; IPCC, 2007).

Τόσο η σκέδαση όσο και η απορρόφηση της εισερχόμενης ηλιακής ακτινοβολίας εξαρτάται από το μέγεθος των σωματιδίων, με την έντασή του σκεδαζόμενου φωτός να είναι ανάλογη της έκτης δύναμης της διαμέτρου του σωματιδίου (Hind, 1999). Καθώς το μέγεθος των ατμοσφαιρικών σωματιδίων της κλάσης συσσωμάτωσης (accumulation mode) είναι της ίδιας τάξης μεγέθους με το μήκος κύματος της ακτινοβολίας, η ηλιακή ακτινοβολία διαχέεται αποτελεσματικά, ενώ τα μικρότερα σωματίδια δεν είναι αποτελεσματικοί σκεδαστές. Η απορρόφηση εξαρτάται όχι μόνο από τη διαφοροποίηση του μεγέθους του σταγονιδίου, αλλά και από τη ποσότητα νερού το νέφος. Έτσι, για σύννεφα μεγάλης κατακόρυφης ανάπτυξης ("βαθιά") , η απορρόφηση αυξάνεται μονότονα με την αύξηση της ενεργούς ακτίνας, ενώ η αντίστροφη αναλογία ισχύει για τα λεπτά σύννεφα (Ackerman and Stephens, 1987). Το νερό αποτελεί ένα σημαντικό μέρος των ατμοσφαιρικών σωματιδίων, έτσι ώστε η απόκριση των σωματιδίων σε αλλαγές της σχετικής υγρασίας (RH) είναι σημαντική για τον καθορισμό του μεγέθους των σωματιδίων στον ατμοσφαιρικό αέρα. Σε δεδομένη σχετική υγρασία, το υδατικό περιεχόμενο και η ενεργοποίηση των πυρήνων συμπύκνωσης μέσα στα υδροσταγονίδια του νέφους καθορίζεται από το μέγεθος του σωματιδίου και τη χημική σύσταση, όπως περιγράφεται από την θεωρία Köhler (Köhler, 1936) (McFiggans et al., 2006; Fierz-Schmidhauser et al., 2010).

Οι ατμοσφαιρικές συνθήκες καθώς και τα ατμοσφαιρικά αιωρούμενα σωματίδια μπορούν να ποικίλουν σημαντικά, τόσο χωρικά όσο και χρονικά. Καθώς η λεπτομερής χημική σύσταση των ατμοσφαιρικών σωματιδίων είναι σπανίως γνωστή, έμμεσες μετρήσεις της σύστασής τους μπορούν να επιτευχθούν μέσω μετρήσεων της υγροσκοπικότητας και/ή της πτητικότητάς τους. Η συνηθέστερη μέθοδος διερεύνησης της υγροσκοπικότητας ή της πτητικότητας των αιωρούμενων σωματιδίων, είναι με τη χρήση του υγροσκοπικού ή πτητικού αναλυτή διαφορικής κινητικότητας σε σειρά (π.χ., H-TDMA; Liu et al., 1978; Swietlicki et al., 2008; V-TDMA; Frey et al., 2008). Αρχικά, σε αυτό το σύστημα, ένα αεροζόλ ταξινομείται με βάση το μέγεθος στο πρώτο DMA και έπειτα υγραίνεται ή θερμαίνεται και η προκύπτουσα κατανομή μεγέθους μετριέται από το δεύτερο DMA. Τα δεδομένα υγροσκοπικότητας παρουσιάζονται ως ρυθμός αύξησης, μεσω του λόγου της μέσης διαμέτρου των υγραμένων σωματιδίων προς τη μέση διάμετρο των ξηρών σωματιδίων, ενώ τα δεδομένα πτητικότητας παρουσιάζονται είτε ως ρυθμός συρρίκνωσης είτε ως ποσοστό των εναπομεινάντων σωματιδίων.

Αυτά τα συστήματα χρησιμοποιούν DMAs. Από την εμφάνιση του πρώτου αναλυτή ηλεκτρικής κινητικότητας (Hewitt, 1957) διάφορα σχέδια έχουν αναπτυχθεί και χρησιμοποιηθεί. Το εύρος ταξινόμησης ενός DMA καθορίζεται τόσο από τη γεωμετρία του όσο και από τις συνθήκες λειτουργίας (Stolzenburg, 1988) και τους υποκείμενους περιορισμούς (π.χ. τυρβώδη ροή, τάση διάσπασης κ.ά.). Το εύρος ταξινόμησης των εμπορικά διαθέσιμων DMA είναι 10 nm μέχρι 1 μm (TSI, Model

3081). Η πρόκληση, ωστόσο, είναι η σχεδίαση και η λειτουργία ενός DMA το οποίο θα μπορεί να ταξινομήσει τα σωματίδια σε μεγαλύτερο εύρος μεγεθών και σε λιγότερο χρόνο. Αυτό μπορεί να επιτευχθεί με DMAs με περισσότερες της μιας εξόδου μονο-μεγεθών σωματιδίων. Αυτός ο σχεδιασμός οργάνων μπορεί να προσφέρει ένα πλήθος προτερημάτων συγκριτικά με τα συμβατικά σχέδια με μια έξοδο μονο-μεγεθών σωματιδίων, για παράδειγμα συντομότερο χρόνο σκαναρίσματος, μεγαλύτερο εύρος ταξινομούμενων μεγεθών, πιο αποδοτικές TDMA μετρήσεις, αν χρησιμοποιηθεί ως πρώτο DMA σε ένα τέτοιο σύστημα. Οι Chen et al. (2007) σχεδίασαν και δοκίμασαν ένα DMA με τρεις εξόδους μονο-μεγεθών σωματιδίων (3-MO-DMA).

Η κατανόηση της θεωρητικής συνάρτησης μεταφοράς (transfer function), η οποία περιγράφει τη λειτουργία ενός DMA πολλαπλών μονο-μεγεθών εξόδων (MMO-DMA), δημιουργεί μια σύνδεση μεταξύ των κατανομών μεγέθους των αιωρούμενων σωματιδίων και των TDMA μετρήσεων υγροσκοπικότητας. Αυτός είναι ένα σημαντικός στόχος. Οι προκλήσεις, ωστόσο, δεν περιορίζονται στη θεωρία που διέπει τη μεταφορά των σωματιδίων μέσα στην κολώνα του DMA και στην πιθανότητα να ταξινομηθούν και να ανιχνευθούν, δηλαδή στη συνάρτηση μεταφοράς. Επεκτείνονται, ακόμα, στην ανάλυση και στην αντιστροφή των μετρήσεων. Για τον αναλυτή ηλεκτρικής κινητικότητας σωματιδίων (SMPS), δηλαδή ένα DMA μαζί με ένα μετρητή σωματιδίων συμπύκνωσης (CPC), το σήμα απόκρισης είναι η συνέλιξη της συνάρτησης μεταφοράς, της απόκρισης του μετρητή και της κατανομής μεγέθους των σωματιδίων, ως συνάρτηση της εφαρμοζόμενης τάσης. Για να εκτιμηθεί η κατανομή του λόγου αύξησης των σωματιδίων από μετρήσεις TDMA, οι μετρήσεις θα πρέπει να έχουν αντιστραφεί κατάλληλα. Για την αντιστροφή τέτοιων μετρήσεων, χρειάζεται η καλή θεωρητική κατανόηση της επίδοσης των DMA καθώς και η ύπαρξη των κατάλληλων μαθηματικών εργαλείων για τη διατύπωση και επίλυση του προβλήματος αντιστροφής.

1.2 Οργάνωση της Διατριβής

Το κίνητρο για αυτή τη διατριβή ήταν η εκτενέστερη κατανόηση της θεωρίας που περιγράφει τη λειτουργία ενός MMO-DMA και η καλύτερη κατανόηση των ιδιοτήτων πτητικότητας και υγροσκοπικότητας των αιωρούμενων σωματιδίων, όπως αυτές μετριούνται με συστήματα πτητικότητας ή υγροσκοπικότητας TDMA. Το Κεφάλαιο 2 παρουσιάζει την παραγωγή της συνάρτησης μεταφοράς και της διακριτικής ικανότητας (ανάλυσης) των MMO-DMAs. Στο Κεφάλαιο 3, ο έλεγχος εγκυρότητας του θεωρητικού πλαισίου πραγματοποιείται μέσω της σύγκρισης με πειραματικά δεδομένα από το 3-MO-DMA των Chen et al. (2007). Στο Κεφάλαιο 4, αναπτύσσεται ένας τροποποιημένος κώδικας αντιστροφής TDMA δεδομένων και συγκρίνεται η απόδοσή του με αυτή ενός άλλου ευρέως χρησιμοποιούμενου κώδικα αντιστροφής TDMA δεδομένων. Το Κεφάλαιο 5 παρουσιάζει μετρήσεις των σχετικών υγρασιών υγροποίησης και στερεοποίησης (DRH και ERH) και την υγροσκοπική συμπεριφορά σωματιδίων των αλογόνων καλίου (ονομαστικά, KBr, KCl, KI) με διαμέτρους μεταξύ των 8 και 60 nm. Το Κεφάλαιο 6 επικεντρώνεται στα είδη που συμμετέχουν στο σχηματισμό νέων σωματιδίων πάνω από τον Αρκτικό Κύκλο και στον προσδιορισμό της σύστασής τους βάσει των μετρήσεων κατανομής μεγέθους καθώς και των πτητικών τους ιδιοτήτων, όπως αυτές προσδιορίστηκαν από ένα V-TDMA σύστημα μετρήσεων. Τέλος, το Κεφάλαιο 7 συνοψίζει τα σημαντικότερα συμπεράσματα των αποτελεσμάτων που παρουσιάστηκαν σε αυτή τη διατριβή.

Chapter 2

2. The Multiple Monodisperse Outlet Differential Mobility Analyzer: Derivation of its Transfer Function and Resolution

Note: This chapter appeared as reference: M. Giamarelou, M. Stolzenburg, G. Biskos, 2012. The Multiple Monodisperse Outlet Differential Mobility Analyzer: Derivation of Its Transfer Function and Resolution, *Aerosol Science and Technology*, 46: 951-965.

2.1 Abstract

Conventional Differential Mobility Analyzers (DMAs) for classification of aerosol particles have one polydisperse-particle inlet and one monodisperse-particle outlet. As a result, when they are used as particle classifiers in aerosol-mobility spectrometers it is needed to scan through different operating conditions, thereby requiring a significant amount of time (i.e., of the order of a minute) for a single mobility distribution measurement. DMAs with multiple outlets can significantly reduce this scanning time because particles of different mobility can be classified and detected simultaneously. In addition, depending on the relative location of the first and the last outlet from the inlet, one can increase the dynamic mobility range of the selected particles in a single particle mobility distribution measurement. This chapter provides the derivation of analytical expressions for estimating the transfer function and the resolution of DMAs with multiple monodisperse outlets. Starting with the simple consideration of non-diffusing particles, I extend the analysis for diffusing particles and provide expressions of different complexity and accuracy. The theoretical framework provided in this chapter can be employed to optimize the design of DMAs with more than one monodisperse-particle outlet, and to analyze the measurements when such DMAs are used in aerosol mobility spectrometers, as well as in inverting TDMA data when MMO-DMAs are employed.

2.2 Introduction

Differential mobility analyzers (DMAs) are widely used in aerosol research as a tool for sizing and for producing monodisperse airborne particles having diameters in the submicron and nanometer range (cf. Flagan, 1998; McMurry, 2000; Biskos et al., 2008). In view of improving several aspects of their performance (e.g., particle size range, resolution, etc.), several DMA designs have been proposed over the last decades (e.g., Liu and Pui, 1974; Knutson and Whitby, 1975; Pourprix and Daval, 1990; Pourprix, 1994; Zhang et al., 1995; Zhang and Flagan, 1996; Fissan et al., 1996; Brunelli et al., 2009; Santos et al., 2009). The most popular DMA design employs two coaxial cylindrical electrodes between which an annular flow carries the sample particles in a particle-free sheath flow (Liu and Pui, 1974; Knutson and Whitby, 1975). Applying a potential difference between the two cylindrical electrodes, the charged particles migrate from one electrode to the other so that only particles having mobilities within a very narrow range can exit through the monodisperse-particle outlet.

Conventional DMAs employ one monodisperse-particle outlet. As a result, particles having mobilities only within a specific narrow range can be classified for each combination of operating conditions (i.e., flows and applied voltage between the two electrodes). This, however, poses the limitation that when DMAs are used as particle classifiers in aerosol-mobility spectrometers, it is required to scan through different operating conditions, thereby requiring a significant amount of time (from 30 seconds up to a few minutes depending on the required accuracy of the measurement) for a single mobility distribution measurement (Wang and Flagan, 1990; Endo et al., 1997). In addition, because the flow field is usually kept constant and only the electric field is altered in order to classify particles of different mobility, the dynamic size range of conventional DMAs can typically span over one order of magnitude (McMurry, 2000). DMAs with multiple outlets on the other hand can significantly reduce the scanning time when used as classifiers in mobility spectrometers because particles of different mobility can be selected and detected simultaneously. Depending on the relative distances of the first and the last outlets from the inlet, one can also increase the dynamic mobility range of the selected particles in a single measurement.

To measure particles having diameters from one and up to a few hundred nanometers, Seol et al. (2002) designed an adjustable-length DMA. Working in the same direction, Takeuchi et al. (2005) proposed a dual-type DMA that employs two cylindrical, coaxial classifiers. The sample flow in the dual-type DMA is split in two parts before passing through either one of two classifiers that select particles having mobilities of different ranges. In an attempt to make a DMA that could scan faster through the instrument's channels, Chen et al. (2007) built and tested a classifier having three monodisperse-particle outlets. The performance of this DMA has only been determined experimentally and numerically (Li, 2006), and to the best of our knowledge there is still lack of a theoretical model for predicting its behavior.

The performance of DMAs can be fully described by their transfer function (Knutson and Whitby, 1975; Hoppel, 1978; Haaf, 1980; Stolzenburg, 1988; Kousaka et al., 1985;1986; Rosell-Llombart et al., 1996). Knutson and Whitby (1975) provided a derivation of the transfer function for an ideal DMA and showed that this has a triangular shape if the polydisperse-particle sample inlet flow and monodisperse-particle exit flow rates are equal (i.e., balanced flows), or a trapezoidal shape if the flows are not perfectly balanced. Motion of particles in the nanometer size range within the DMA is also affected by the Brownian motion of the particles, resulting in a Gaussian-shape transfer function (Tammet, 1970; Kousaka et al., 1985; Kousaka et al., 1986; Stolzenburg, 1988; Rosell-Llompart et al., 1996; Stratmann et al., 1997; Hagwood et al., 1999; de la Mora, 2002).

This chapter focuses on the derivation of the transfer function of the Multiple Monodisperse Outlet DMA (MMO-DMA), and the formula for determining the resolution of each outlet. Using the approach followed by Knutson and Whitby (1975) and Stolzenburg (1988) for the conventional DMA, I first derive the transfer function of the MMO-DMA for non-diffusing particles, and then extend it to include particle diffusivity. Considering that the transfer function of the MMO-DMA can be approximated by a Gaussian distribution, the diffusion-limited resolution of each outlet it is also derived using the approach proposed by Flagan (1999).

2.3 Derivation of the MMO-DMA Transfer Function

In this section is employed the theoretical approach proposed by Stolzenburg (1988) to derive the transfer function of cylindrical DMAs with multiple monodisperse-particle outlets. Considering that the flow field is axisymmetric and steady (cf. Figure 2.1a), and that the air flow is laminar and incompressible, the flow stream function is define as:

$$\Psi(r,z) \equiv \int^{r,z} [r u_r dz - r u_z dr] \ . \tag{2.1}$$

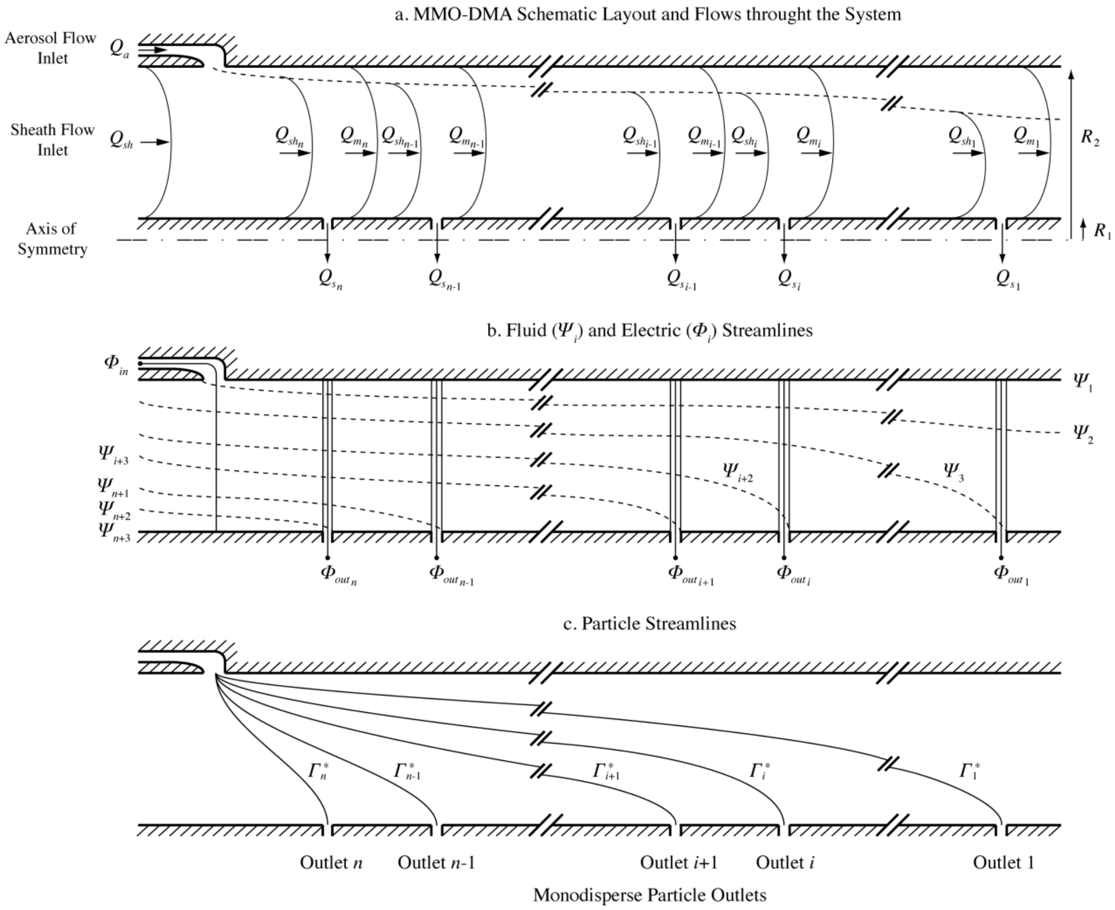

Figure 2.1: Schematic diagram of the MMO-DMA showing (a) the flows associated with each monodisperse-particle outlet, (b) the fluid and electric field streamlines, and (c) the particle streamlines. Key: $\boldsymbol{Q_a}$ is the polydisperse aerosol inlet flow rate; $\boldsymbol{Q_{sh}}$ is the sheath air flow rate; $\boldsymbol{Q_{s_i}}$ is the sample flow rate of the i^{th} monodisperse-particle outlet; $\boldsymbol{Q_{m_i}}$ is the excess flow rate after the i^{th} monodisperse-particle outlet; $\boldsymbol{Q_{sh_i}}$ is the sheath-air flow rate before the i^{th} monodisperse-particle outlet; $\boldsymbol{R_1}$ and $\boldsymbol{R_2}$ are the outer and the inner radii of the MMO-DMA, respectively.

Assuming also that the space charge and image charges are negligible it can be further defined the axisymmetric and steady electric flux function as:

$$\Phi(r,z) \equiv \int^{r,z}[rE_r dz - rE_z dr] \ . \tag{2.2}$$

In Equations 2.1 and 2.2, u is the flow velocity and E the electric field strength, whereas r and z denote the radial and axial components, respectively.

As shown in Figure 2.1b, streamlines Ψ_1 and Ψ_2 bound the aerosol inlet flow, whereas Ψ_{i+2} and Ψ_{i+3} bound the monodisperse-particle sample flow of the i^{th} exit. If the positive z direction is taken to be in the same direction as the flow, then by definition $\Psi_1 < \Psi_2 < \Psi_{i+2} < \Psi_{i+3}$. Based on these characteristic stream functions, one can determine the following volumetric flow rates:

$$Q_a = 2\pi(\Psi_2 - \Psi_1)\ , \tag{2.3}$$

$$Q_{s_i} = 2\pi(\Psi_{i+3} - \Psi_{i+2})\ , \tag{2.4}$$

$$Q_{sh_i} = 2\pi(\Psi_{i+3} - \Psi_2)\ , \tag{2.5}$$

$$Q_{m_i} = 2\pi(\Psi_{i+2} - \Psi_1)\ . \tag{2.6}$$

Here Q_a is the incoming polydisperse-particle sample flow rate, Q_{s_i} is the sample flow rate of the *i*th outlet, whereas Q_{sh_i} and Q_{m_i} are the sheath and the excess air flow rates just before and just after the *i*th outlet, respectively. The total flow through the DMA is:

$$Q_t = Q_a + Q_{sh}\ , \tag{2.7}$$

where Q_{sh} is the initial sheath-air flow (cf. Figure 2.1a). The following relations for the flow rates also hold:

$$Q_{sh_i} = \begin{cases} Q_{sh} & \text{for} \quad i = n \\ Q_{m_{i+1}} - Q_a & \text{for} \quad 1 \le i \le n-1 \end{cases}, \quad \text{and} \tag{2.8}$$

$$Q_{m_i} = \begin{cases} Q_{sh} + Q_a - Q_{s_i} & \text{for} \quad i = n \\ Q_{m_{i+1}} - Q_{s_i} & \text{for} \quad 1 \le i \le n-1 \end{cases}, \tag{2.9}$$

where n is the number of the monodisperse-particle sample outlets of the MMO-DMA.

The electric field is zero and Φ is uniform deep inside the aerosol inlet and the exit channels, having values Φ_{in} and Φ_{out_i}, respectively. The electric flux corresponding to the *i*th monodisperse-particle exit is the difference between these two values and also a function of the electric field (cf. Equation 2.2). The axial and the radial components of the electric field along the classification column are respectively given by:

$$E_z = 0 \text{ , and} \tag{2.10}$$

$$E_r = \frac{-V}{r \cdot ln(\frac{R_1}{R_2})} \; . \tag{2.11}$$

Here R_1 and R_2 are the radii of the central rod and the outer electrode, respectively, and V is the signed potential difference between the inner and outer electrodes. The integration limits in Equation 2.2 are the positions r and z of the particles at the midpoint locations of the entrance and the i^{th} exit slit, which are spaced at a distance L_i apart. Thus,

$$\Delta\Phi_i \equiv \Phi_{out_i} - \Phi_{in} = \frac{-L_i V}{ln(\frac{R_1}{R_2})} \; . \tag{2.12}$$

The objective now is to estimate the probability of any particle entering the DMA to exit through the i^{th} monodisperse-particle exit. Considering that the values of the stream function at the entrance and the exit are Ψ_{in} and Ψ_{out_i}, respectively, it can be written $\Psi_1 \leq \Psi_{in} \leq \Psi_2$, and $\Psi_{i+2} \leq \Psi_{out_i} \leq \Psi_{i+3}$.

Defining $f_{in}(\Psi_{in})d\Psi_{in}$ to be the probability of a particle entering the classifier on a streamline between Ψ_{in} and $\Psi_{in} + d\Psi_{in}$, and $f_{trans_i}(\Psi_{out_i}, \Psi_{in})d\Psi_{out_i}$ the probability of a particle that enters the classifier on streamline Ψ_{in} to exit on a streamline between Ψ_{out_i} and $\Psi_{out_i} + d\Psi_{out_i}$, the transfer function of the i^{th} exit of the MMO-DMA can be expressed as:

$$\Omega_i = \int_{\Psi_1}^{\Psi_2} \left[\int_{\Psi_{i+2}}^{\Psi_{i+3}} f_{trans_i}(\Psi_{out_i}, \Psi_{in}) d\Psi_{out_i} \right] f_{in}(\Psi_{in}) d\Psi_{in} \; . \tag{2.13}$$

Assuming that there is no variation in aerosol concentration across the inlet channel, the particles can enter the classifier in any streamline between Ψ_1 and Ψ_2 with equal probability so that it can be written as:

$$f_{in} = \frac{1}{\Psi_2 - \Psi_1} \; . \tag{2.14}$$

To determine f_{trans_i} one needs to know the velocity $\boldsymbol{v}$ of the particles at any point within the DMA. If we assume that particle inertia is negligible, this is given by:

$$\boldsymbol{v} = \boldsymbol{u} + Z_p \boldsymbol{E}, \tag{2.15}$$

where bold letters indicate vectors. In Equation 2.15, $Z_p = \frac{qD}{kT}$ is the electrical mobility of the particle with charge q and diffusion coefficient *D* at a temperature T (k is the Boltzmann constant). The function f_{trans_i} can be determined by the stream function Ψ and the electric flux function Φ, which can be combined to form the particle stream function Γ (Stolzenburg, 1988), defined as:

$$\Gamma(r,z) \equiv \Psi + Z_p \Phi = \int^{r,z} [r v_r dz - r v_z dr] \, . \tag{2.16}$$

Here v_r and v_z are the radial and the axial particle velocity components, respectively. In fact, f_{trans_i} depends on the difference between the entering and the exiting particle streamline Γ. For a particle that enters on particle stream function $\Gamma_{in}(r,z) = \Psi_{in} + Z_p \Phi_{in}$, successfully traverses the classifier and exits on particle stream function $\Gamma_{out_i}(r,z) = \Psi_{out_i} + Z_p \Phi_{out_i}$, this difference can be estimated by:

$$\Delta\Gamma_i \equiv \Gamma_{out_i} - \Gamma_{in} = \Delta\Psi_i + Z_p \Delta\Phi_i \, , \tag{2.17}$$

where $\Delta\Psi_i \equiv \Psi_{out_i} - \Psi_{in}$ and $\Delta\Phi_i \equiv \Phi_{out_i} - \Phi_{in}$. For the conventional DMA with one monodisperse-particle outlet, Knutson and Whitby (1975) and Stolzenburg (1988) showed that $\Delta\Psi = -Z_p \Delta\Phi$, or $\Delta\Gamma = 0$, along the deterministic trajectory of a non-diffusing particle. Extending this for the MMO-DMA it is obtained that $\Delta\Psi_i = -Z_p \Delta\Phi_i$, or $\Delta\Gamma_i = 0$.

When particle diffusivity is taken into account (Section 2.3.2), $\Delta\Gamma_i \neq 0$ and therefore the estimation of particle deviations from their deterministic streamlines is required.

To do that one needs to calculate the associated particle streamline standard deviation, σ_Γ, which in turn depends on the gradient of Γ given by:

$$\boldsymbol{\nabla}\Gamma = -rv_z\boldsymbol{e}_r + rv_r\boldsymbol{e}_z\ . \tag{2.18}$$

Here $\boldsymbol{e}_r$ and $\boldsymbol{e}_z$ are the unit vectors in the radial and the axial direction (Stolzenburg, 1988). An expression for f_{trans_i} with or without considering particle diffusivity can be derived, and by plugging it in Equation 2.13 one can obtain the exact transfer functions for the respective cases. Considering that the flow is laminar and without disturbances along the column (especially upstream and downstream each monodisperse-particle outlet), Sections 2.3.1 and 2.3.2 that follow provide the derivation of f_{trans_i} and from that the transfer function of the MMO-DMA for non-diffusing and diffusing particles, respectively. If the effect of potential disturbances resulted by the formation of recirculation zones around each outlet need to be considered, one has to employ a numerical model which, is beyond the scope of the present work.

2.3.1 The MMO-DMA Transfer Function for Non-diffusing Particles

If it is assumed that the diffusivity of the particles is negligible, their motion is completely determined by Equation 2.15. In this case, Γ remains constant along the path of the particles, and thus $\Delta\Gamma = 0$ (Riley et al., 2009). Consequently, $\Delta\Gamma_i = 0$, and therefore from Equation 2.17 it is obtained:

$$\Psi_{out_i} = \Psi_{in} - Z_p\Delta\Phi_i\ . \tag{2.19}$$

In this case the probability function f_{trans_i} can be expressed as:

$$f_{trans_i}\left(\Psi_{out_i}, \Psi_{in}\right) = \delta_D\left(\Psi_{out_i} - \Psi_{in} + Z_p\Delta\Phi_i\right)\ , \tag{2.20}$$

where δ_D is the Dirac delta function. Substituting Equation 2.20, along with f_{in} given by Equation 2.14, in Equation 2.13 and integrating (cf. Appendix A-Part A), yields the transfer function of the *i*th exit of the MMO-DMA for non-diffusing particles:

$$\begin{aligned}\Omega_{nd_i} = \frac{1}{2(\Psi_2-\Psi_1)}\Big\{&\left|\Psi_{i+3}-\Psi_1+Z_p\Delta\Phi_i\right| - \left|\Psi_{i+3}-\Psi_2+Z_p\Delta\Phi_i\right| \\ &-\left|\Psi_{i+2}-\Psi_1+Z_p\Delta\Phi_i\right| + \left|\Psi_{i+2}-\Psi_2+Z_p\Delta\Phi_i\right|\Big\}\end{aligned} . \qquad (2.21)$$

Key flow streamlines are those associated with the centroid points at the aerosol inlet and the monodisperse-particle outlets of the MMO-DMA, respectively, defined as:

$$\Psi_a \equiv \frac{1}{2}(\Psi_2+\Psi_1)\text{ , and} \qquad (2.22)$$

$$\Psi_{s_i} \equiv \frac{1}{2}(\Psi_{i+3}+\Psi_{i+2}) . \qquad (2.23)$$

From Equations 2.22 and 2.23 one can also define:

$$\Delta\Psi_i^* \equiv \Psi_{s_i}-\Psi_a = \frac{1}{2}(\Psi_{i+3}+\Psi_{i+2}) - \frac{1}{2}(\Psi_2+\Psi_1) = \frac{Q_{sh_i}+Q_{m_i}}{4\pi} , \qquad (2.24)$$

which is the change in flow stream function experienced by a particle traversing the classifier along particle streamline Γ_i^* from Ψ_a to Ψ_{s_i}. Combining Equation 2.24 with Equations 2.12 and 2.17 one can predict the midpoint electrical mobility $Z_{p_i}^*$, i.e., the electrical mobility of the particles traversing from the midpoint of the inlet to the midpoint of the *i*th exit when particle diffusivity is considered negligible (i.e., $\Delta\Gamma_i = 0$), by:

$$Z_{p_i}^* \equiv \frac{-\Delta\Psi_i^*}{\Delta\Phi_i} = \frac{\left(Q_{sh_i}+Q_{m_i}\right)ln(\frac{R_1}{R_2})}{4\pi L_i V} . \qquad (2.25)$$

The midpoint electrical mobility for each monodisperse-particle outlet can be used to define the dimensionless particle electrical mobility:

$$\tilde{Z}_{p_i} \equiv \frac{Z_p}{Z_{p_i}^*} . \qquad (2.26)$$

Further, the following dimensionless flow parameters that correspond to the i^{th} exit are defined:

$$\beta_i \equiv \frac{Q_{s_i}+Q_a}{Q_{sh_i}+Q_{m_i}}\text{, and} \tag{2.27}$$

$$\delta_i \equiv \frac{Q_{s_i}-Q_a}{Q_{s_i}+Q_a}\,. \tag{2.28}$$

Using Equations 2.3-2.6 and the definitions given by Equations 2.24-2.28, the transfer function for non-diffusing particles (Equation 2.21) can be written in dimensionless form as (cf. Appendix A-Part A):

$$\begin{aligned}\Omega_{nd_i} = \frac{1}{2\beta_i(1-\delta_i)}\Big\{&\left|\tilde{Z}_{p_i}-(1+\beta_i)\right| - \left|\tilde{Z}_{p_i}-(1+\beta_i\delta_i)\right| \\ &-\left|\tilde{Z}_{p_i}-(1-\beta_i\delta_i)\right| + \left|\tilde{Z}_{p_i}-(1-\beta_i)\right|\Big\}\,.\end{aligned} \tag{2.29}$$

Equation 2.29 is similar to that derived by Stolzenburg (1988) for the single monodisperse-particle outlet DMA, with the difference that all the non-dimensional variables correspond to the i^{th} exit as described by Equations 2.26-2.28.

2.3.2 The MMO-DMA Transfer Function for Diffusing Particles

Small particles traversing the DMA column on a given particle streamline, defined by Equation 2.16, deviate from their paths as a result of Brownian motion. The relative importance of particle migration and diffusion can be expressed in terms of the migration *Peclét* number defined by (Flagan, 1999):

$$Pe_{\text{mig}} = \frac{b\upsilon_E}{D}\,. \tag{2.30}$$

Here υ_E is the electrophoretic migration velocity of the particles, and $b = R_2 - R_1$ is the radial distance between the two coaxial electrodes. The electrophoretic velocity of the particles is proportional to their electrical mobility and the electric field strength which varies only in the radial direction (cf. Equation 2.11). The particle diffusion coefficient D is also proportional to the electrical mobility such that, for singly-charged particles, the *Peclét* number has no explicit dependence on particle size but is proportional to the classification voltage V.

Because diffusion across even a small fraction of the aerosol inlet flow can substantially distort the transfer function, it is sufficient to consider small deviations from the starting particle stream function Γ (Zhang and Flagan, 1996). Stolzenburg (1988) modeled the diffusive departure of the particles from their streamline in the cylindrical DMA using a local orthogonal curvilinear coordinate system based on stream-wise and cross-stream coordinates. To do so, he defined s as the distance traversed by the particle along the particle streamline Γ, and x the perpendicular distance of the particle from Γ. Because typical particle migration *Peclét* numbers are small for sub-10 nm particles, it is sufficient to consider only cross-stream diffusion (x-direction) and to neglect diffusion in the stream-wise direction. It is also assumed that the cross-stream shear does not affect cross-stream diffusion as stream-wise flow does not affect the distance of the diffusing particle from the non-diffusing particle streamline, and that the particle losses to the walls of the classifier column are negligible. The root-mean-square displacement of the particles from the mean trajectory increases with the time the particles spend in the DMA according to (Hinds, 1999):

$$\langle x_{rms} \rangle = \sqrt{2Dt}\ . \tag{2.31}$$

The distribution of the particles' deviation about their mean trajectory can be approximated with a Gaussian distribution having standard deviation $\sigma_x = \langle x_{rms} \rangle$.

When diffusion is significant, motion of the particles cannot be completely determined by Equation 2.15 that gives the mean velocity of the particle moving on well-defined stream functions Γ as described by Equation 2.16. In other words, Γ is no longer constant along a particle path when particle Brownian motion is significant. To derive the transfer function of the DMA in this case one needs to determine the probability distribution for $\Delta\Gamma = \Gamma_{out} - \Gamma_{in}$ when the particle reaches the vicinity of the monodisperse-particle outlet slit.

The deterministic velocity of the particles within the DMA can be expressed as:

$$\boldsymbol{v} \equiv \frac{d\boldsymbol{r}}{dt} = v_s\left(\frac{\partial \boldsymbol{r}}{\partial s}\right) + v_x\left(\frac{\partial \boldsymbol{r}}{\partial x}\right), \tag{2.32}$$

where $\boldsymbol{r}$ and $\boldsymbol{v}$ are vectors representing the particle position (relative to the origin) and velocity, respectively, and $v_s \equiv \frac{ds}{dt}$ and $v_x \equiv \frac{dx}{dt}$ represent the particle velocity components. In a conventional DMA, the developing probability distribution for the perpendicular distance x of a particle from its deterministic streamline is Gaussian having a peak value at $x = 0$ and a standard deviation σ_x. This deviation changes with time according to Equation 2.31, and thus it can be written as:

$$(d\sigma_x^2)_{diffusion} = 2Ddt\ . \tag{2.33}$$

Following Stolzenburg's analysis, for small deviations, Γ can be approximated by a first-order Taylor series:

$$\Gamma(x) \approx \Gamma|_{x=0} + \left.\frac{\partial \Gamma}{\partial x}\right|_{x=0} x\ . \tag{2.34}$$

The difficulty in estimating $\Gamma(x)$ is in determining the slope of the equation above, which can be expressed as $\frac{\partial \Gamma}{\partial x} = \frac{\partial \boldsymbol{r}}{\partial x} \cdot \boldsymbol{\nabla}\Gamma$. At $x = 0$, however, $\Gamma = \Gamma_{in}$ whereas $\frac{\partial \boldsymbol{r}}{\partial x}$ and $\boldsymbol{\nabla}\Gamma$ are perpendicular to the particle streamline. Using Equation 2.18 one can therefore estimate the rate of change in Γ with respect to x, and thus obtain (Riley et al., 2009):

$$\frac{\partial \Gamma}{\partial x} = \frac{\partial \boldsymbol{r}}{\partial x} \cdot \boldsymbol{\nabla}\Gamma = \left|\frac{\partial \boldsymbol{r}}{\partial x}\right| |\boldsymbol{\nabla}\Gamma| = \sqrt{(rv_z)^2 + (rv_r)^2} = rv\ . \tag{2.35}$$

Equation 2.34 can now be written as:

$$\mathit{\Gamma}(x) \approx \mathit{\Gamma}_{in} + rvx \ , \qquad (2.36)$$

where r and υ are evaluated at $x = 0$. The probability distribution in x can then be transformed to a Gaussian distribution in $\mathit{\Gamma}$ centered at $\mathit{\Gamma} = \mathit{\Gamma}_{in}$ and having a standard deviation

$$\sigma_{\mathit{\Gamma}} = \left[\frac{\partial \mathit{\Gamma}}{\partial x}\right] \sigma_x = r\upsilon\sigma_x \ . \qquad (2.37)$$

In the absence of diffusion, the particles move along fixed particle streamlines (i.e., $\mathit{\Gamma}$ remains constant), so that the distribution of $\mathit{\Gamma}$ as a whole and $\sigma_{\mathit{\Gamma}}$ in particular remain constant. In calculating the change in $\sigma_{\mathit{\Gamma}}$ from Equation 2.37, one needs to consider only the differentials resulting from diffusion, and therefore, using Equation 2.33, can obtain:

$$\sigma_{\mathit{\Gamma}}^2 = r^2\upsilon^2\sigma_x^2 \Rightarrow d\sigma_{\mathit{\Gamma}}^2 = (r\upsilon)^2 2Ddt \ . \qquad (2.38)$$

For the case of the MMO-DMA, the variance $\sigma_{\mathit{\Gamma}_i}^2$ of the distance of the particles about the trajectory that leads to the *i*th monodisperse-particle outlet increases as the particles traverse each segment of the DMA. The segments of the MMO-DMA are the sections between successive outlets so that the *j*th MMO-DMA segment is defined as the section between the *j*+1 and *j*th sample outlet (cf. Figure 2.2a). In the case of the *n*th sample outlet, i.e., the one closest to the aerosol inlet, the corresponding MMO-DMA segment is that between the aerosol inlet and the *n*th sample outlet. As the total flow rate through the MMO-DMA column decreases by Q_{s_j} after the particles pass each outlet, the contribution to diffusional broadening must be calculated separately for each segment. Thus, the diffusional broadening along the whole path of the particles traveling along the *i*th particle streamline can be expressed as:

$$\sigma_{\mathit{\Gamma}_i}^2 = \textstyle\sum_{j=n}^{i} \sigma_{\mathit{\Gamma}_{i,j}}^2 \ . \qquad (2.39)$$

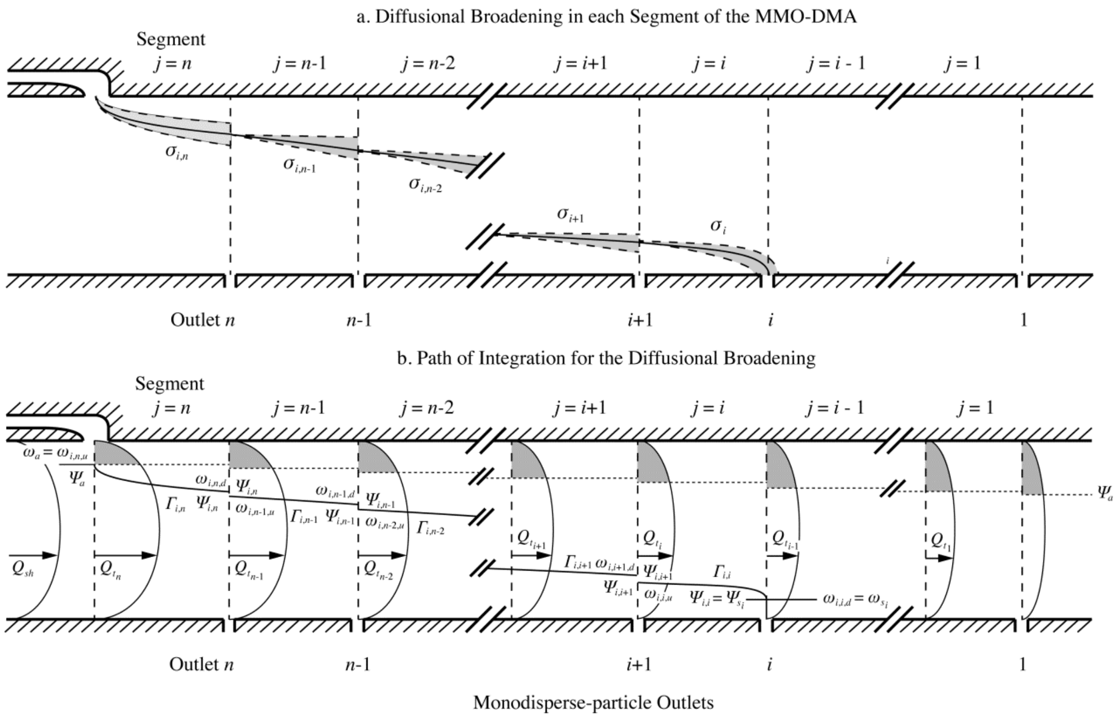

Figure 2.2: Schematic diagram of the MMO-DMA showing (a) the individual segments of the column, and the associated diffusional broadening parameters $\boldsymbol{\sigma_{i,j}}$ for the particles exiting through the i^{th} outlet (note that the total broadening is the sum of the spreading parameters in each segment given by Equation 2.39), and (b) the integration path along the particle streamline with the associated steps over each monodisperse particle outlet. Key: $\boldsymbol{\omega_{i,j,u}}$ and $\boldsymbol{\omega_{i,j,d}}$ are the dimensionless radial positions of a particle classified through the i^{th} outlet when it enters and exits, respectively, the j^{th} segment; $\boldsymbol{Q_{t_j}}$ is the total flow rate at the j^{th} segment.

Here, $\sigma^2_{\Gamma_{i,j}}$ denotes the contribution to the diffusional broadening of the particles classified through the i^{th} monodisperse-particle outlet when traversing the j^{th} segment of the MMO-DMA on the particle streamline leading to the i^{th} monodisperse-particle outlet. This can be estimated by integrating Equation 2.38 along the part of the particle streamline in that segment (cf. Figure 2.2a):

$$\sigma^2_{\Gamma_{i,j}} = 2D\int_{\Gamma_{i,j}} r^2 {\upsilon_j}^2 dt\ . \qquad (2.40)$$

The probability of a particle that has entered the classifier on particle streamline Γ_{in}, to arrive at the i^{th} exit, on a particle streamline between Γ_{out_i} and $\Gamma_{out_i} + d\Gamma_{out_i}$ is:

$$\frac{1}{\sqrt{2\pi}\sigma_{\Gamma_i}} exp\left[-\frac{1}{2}\left(\frac{\Gamma_{out_i}-\Gamma_{in}}{\sigma_{\Gamma_i}}\right)^2\right] d\Gamma_{out_i}\ . \qquad (2.41)$$

Using this probability for $f_{trans_i}(\Psi_{out_i}, \Psi_{in})$ and $d\Gamma_{out_i} = d\Psi_{out_i}$ it is derived the transfer probability distribution function of a diffusing particle for the *i*th exit as:

$$f_{trans_i}(\Psi_{out_i}, \Psi_{in}) = \frac{1}{\sqrt{2\pi}\sigma_{\Gamma_i}} exp\left[-\frac{1}{2}\left(\frac{\Psi_{out_i} - \Psi_{in} + Z_p \Delta\Phi_i}{\sigma_{\Gamma_i}}\right)^2\right]. \tag{2.42}$$

In order to estimate f_{trans_i} by Equation 2.42, and from that to obtain the transfer function of the *i*th monodisperse-particle exit using Equation 2.13, one needs to estimate $\sigma_{\Gamma_{i,j}}$ and from that σ_{Γ_i}.

2.3.2.1 The Dimensionless Diffusional Broadening Parameter

For the calculation of $\sigma_{\Gamma_{i,j}}$ using Equation 2.40, all paths of integration Γ_{in} can be approximated by the centroid particle streamline ${\Gamma_{i,j}}^*$ for each segment corresponding to $\Psi_{in} = \Psi_a$ and $Z_p = Z_{p_i}^*$. This approximation allows to write:

$$\sigma_{\Gamma_{i,j}}^2 \approx 2D \int_{\Gamma_{i,j}^*} \upsilon_{i,j}^2 r^2 dt \tag{2.43}$$

where $\upsilon_{i,j} = \upsilon_j(Z_p = \mathrm{Z}_{p_i}^*)$.

The dimensionless diffusional spread parameter that characterizes the broadening of the transfer function in the *j*th segment for the *i*th monodisperse-particle outlet of the MMO-DMA is defined as:

$$\sigma_{i,j} \equiv \frac{\sigma_{\Gamma_{i,j}}}{\Delta\Psi_i^*} = \left(\frac{4\pi}{Q_{sh_i} + Q_{m_i}}\right)\sigma_{\Gamma_{i,j}} = \frac{2\pi(1+\beta_i)}{Q_{t_i}}\sigma_{\Gamma_{i,j}} , \tag{2.44}$$

where

$$Q_{t_j} \equiv Q_{sh_j} + Q_a = Q_{m_j} + Q_{s_j} \tag{2.45}$$

is the total flow within the *j*th segment as depicted in Figure 2.2a. Correspondingly, it is also defined the total dimensionless spread parameter that characterizes the broadening of the transfer function for the *i*th monodisperse-particle outlet as:

$$\sigma_i \equiv \frac{\sigma_{\Gamma_i}}{\Delta\Psi_i^*} \,. \tag{2.46}$$

Note that $\Delta\Psi_i^*$ is the mean change in stream function for particles going from the aerosol inlet to the *i*th monodisperse-particle outlet, while σ_{Γ_i} is the standard deviation of the particle and fluid stream functions ($\Delta\Phi_i$ is fixed) in going this same distance. Thus, σ_i is a true relative standard deviation due to diffusion in both stream function and electrical mobility (Equation 2.25).

To evaluate $\sigma_{\Gamma_{i,j}}$ one needs to estimate the velocity υ of the particles within the DMA. The axial component of the particle velocity υ_z is determined by fluid convection, and thus the average axial fluid velocity in the *j*th segment is given by:

$$U_j = \frac{Q_{t_j}}{\pi\left(R_2^2 - R_1^2\right)} \,. \tag{2.47}$$

The magnitude of the radial component of the velocity υ_r of a particle having electrical mobility $Z_{p_i}^*$ estimated at the outer wall (i.e., $r = R_2$) is the same for all segments and is given by:

$$U_{E_i}^* \equiv -Z_{p_i}^* E_r\,(r = R_2) = \frac{\left(Q_{sh_i} + Q_{m_i}\right)}{4\pi L_i R_2} = \frac{Q_{t_i}}{2\pi(1+\beta_i)L_i R_2} \,. \tag{2.48}$$

For particles traveling on streamline Γ_i^*, the transit time through the classifier (i.e., the time in which a particle covers the distance from $R_2\ to\ R_1$) can be approximated by:

$$\tau_i = \frac{R_2}{2U_{E_i}^*} \,. \tag{2.49}$$

For convenience the following dimensionless variables are defined:

$$\tilde{r} \equiv \frac{r}{R_2} \,, \tag{2.50}$$

$$\tilde{\upsilon}_{i,j} \equiv \frac{\upsilon_{i,j}}{U_j} = \frac{\pi\left(R_2^2 - R_1^2\right)}{Q_{t_j}} \upsilon_{i,j} \,, \tag{2.51}$$

and

$\tilde{t}_i \equiv \frac{t}{\tau_i} = \frac{2U^*_{E_i}t}{R_2}$, so that

$$d\tilde{t}_i = \frac{2U^*_{E_i}dt}{R_2}\,. \tag{2.52}$$

It is further defined the dimensionless diffusion coefficient corresponding to the particles that exit through the *ith* outlet as:

$$\widetilde{D}_i \equiv \frac{D}{R_2U^*_{E_i}} = \frac{4\pi L_i D}{Q_{sh_i}+Q_{m_i}}\,. \tag{2.53}$$

The inverse of this parameter is analogous to the migration *Peclét* number as defined by Flagan (1999). Evaluating Equation 2.30 for particles having electrical mobility $Z^*_{p_i}$, one should substitute v_E with $U^*_{E_i}$ given by Equation 2.48 and use the corresponding particle diffusivity given by $D^*_i = \frac{Z^*_{p_i}\,kT}{q}$. The migration *Peclét* number associated with the *i*th exit is then:

$$Pe^*_{\mathrm{mig}_i} = \frac{(R_2-R_1)U^*_{E_i}}{D^*_i} = \frac{\left(Q_{sh_i}+Q_{m_i}\right)}{4\pi L_i D^*_i}\left(1-\frac{R_1}{R_2}\right) = \frac{\tilde{Z}_{p_i}}{\widetilde{D}_i}\left(1-\frac{R_1}{R_2}\right). \tag{2.54}$$

The non-dimensional form of Equation 2.43 now becomes:

$$\sigma^2_{i,j} = \left[\frac{2\pi(1+\beta_i)}{Q_{t_i}}\right]^2 R_2U^*_{E_i}\left[\frac{Q_{t_j}}{\pi\left(R_2^2-R_1^2\right)}\right]^2 R_2^2\left(\frac{R_2}{2U^*_{E_i}}\right)2\widetilde{D}_i\int_{\Gamma^*_{i,j}}\tilde{v}_{i,j}{}^2\tilde{r}^2d\tilde{t}_i\,.$$

With the help of the geometric parameter:

$$\gamma \equiv \left(\frac{R_1}{R_2}\right)^2, \tag{2.55}$$

the dimensionless diffusional broadening parameter can be written as:

$$\sigma^2_{i,j} = G_{i,j}\widetilde{D}_i \quad \text{for} \quad 1 \le i \le j \le n\,, \tag{2.56}$$

where

$$G_{i,j} \equiv 4\left(\frac{Q_{t_j}}{Q_{t_i}}\right)^2\left(\frac{1+\beta_i}{1-\gamma}\right)^2\int_{\Gamma^*_{i,j}}\tilde{v}_{i,j}{}^2\tilde{r}^2d\tilde{t}_i \tag{2.57}$$

is a unique geometric- and flow-condition-dependent parameter for each combination of aerosol exit *i* and segment *j*.

2.3.2.2 The Path of Integration for the Diffusional Broadening Parameter

In order to calculate the integral in the $G_{i,j}$ factor, it is necessary to determine the path of integration $\Gamma^*_{i,j}$ and the velocity along that path. To do that, one must make some simplifying approximations about the flow field in the MMO-DMA in order to obtain an analytical solution for the integral. Following Stolzenburg and McMurry (2008), it is assumed that the axial flow profile is static within each segment, either flat or fully-developed. Thus, all radial flows are confined to the boundaries between the segments at the midlines of the aerosol entrance and exit slits. At these boundaries, the axial flow is assumed to make an instantaneous transition from the upstream profile to the downstream profile. A non-diffusing particle following a fluid streamline at this transition will make an instantaneous radial jump inward as shown in Figure 2.2b which is assumed to have negligible contribution to the integral (cf. Appendix A-Part B).

The path of integration is simply the trajectory of a non-diffusing particle, having centroid electrical mobility $Z^*_{p_i}$, that begins on the inlet centroid streamline Ψ_a. The condition $\Delta\Gamma_i = \Delta\Psi + Z^*_{p_i}\Delta\Phi = 0$ fixes the ratio of flow crossed along the trajectory to the electric flux crossed, or simply the distance z, down the MMO-DMA column. This is exemplified by Equation 2.25 for the end point of the trajectory where the ratio $\left(Q_{sh_i} + Q_{m_i}\right)/2L_i$ is a constant, independent of position. Thus, if $Q_{i,a}$ is the flow bounded by Ψ_a and the value of the stream function at any position (r, z) along the trajectory, then:

$$Q_{i,a} = \frac{z}{L_i} \cdot \frac{\left(Q_{sh_i} + Q_{m_i}\right)}{2} \,. \tag{2.58}$$

Using the known axial flow profile and total flow at any axial distance z, $Q_{i,a}$ can be related to a radial position, thereby completely determining the trajectory. To this end, let Q_i be the flow between the trajectory at z and the outer wall at R_2. Then,

$$Q_i = Q_{i,a} + \frac{1}{2} Q_a = \frac{z}{\mathrm{L}_i} \cdot \frac{\left(Q_{sh_i} + Q_{m_i}\right)}{2} + \frac{1}{2} Q_a \,. \tag{2.59}$$

The total flow at z is just Q_{t_j} where $L_{j+1} < z < L_j$. The ratio Q_i/Q_{t_j} is then the flow fraction between the particle trajectory at (r, z) and the outer wall at R_2. This flow fraction is given by the integral (Stolzenburg, 1988; Stolzenburg and McMurry, 2008):

$$F_\gamma(\omega) \equiv (1 - \gamma)^{-1} \int_\omega^1 f_\gamma(\omega') d\omega' = Q_i/Q_t, \tag{2.60}$$

where $f_\gamma(\omega) \equiv \frac{u_z}{U}$ is the dimensionless axial velocity profile. Here,

$$\omega \equiv \left(\frac{r}{R_2}\right)^2 = \tilde{r}^2 \ \text{, for } \ \gamma \le \omega \le 1 \tag{2.61}$$

is a dimensionless radial position variable. The upstream and downstream end points (ω, z) of the trajectory through segment j are then given by $\left(\omega_{i,j,u}, L_{j+1}\right)$ and $\left(\omega_{i,j,d}, L_j\right)$, respectively, where,

$$F_\gamma\left(\omega_{i,j,u}\right) = Q_i\left(L_{j+1}\right)/Q_{t_j} = \frac{L_{j+1}}{\mathrm{L}_i} \cdot \frac{\left(Q_{sh_i} + Q_{m_i}\right)}{2Q_{t_j}} + \frac{Q_a}{2Q_{t_j}} \text{, and} \tag{2.62}$$

$$F_\gamma\left(\omega_{i,j,d}\right) = Q_i\left(L_j\right)/Q_{t_j} = \frac{L_j}{\mathrm{L}_i} \cdot \frac{\left(Q_{sh_i} + Q_{m_i}\right)}{2Q_{t_j}} + \frac{Q_a}{2Q_{t_j}} \,. \tag{2.63}$$

All that remains to complete the determination of the trajectory and path of integration is to define the dimensionless axial flow profile $f_\gamma(\omega)$.

For the case of plug flow (Stolzenburg, 1988), $f_\gamma(\omega) \equiv 1$ and the flow fraction is:

$$F_\gamma(\omega) = \frac{1-\omega}{1-\gamma}\,. \tag{2.64}$$

For the case of Poiseuille or fully-developed flow, the dimensionless velocity is (Bird et al., 2007):

$$f_\gamma(\omega) \equiv \mathrm{A}_\gamma[(1-\gamma)ln\omega - (1-\omega)ln\gamma], \tag{2.65}$$

where:

$$\mathrm{A}_\gamma \equiv \left[-\frac{1}{2}(1+\gamma)ln\gamma - (1-\gamma)\right]^{-1}\,. \tag{2.66}$$

In this case the flow fraction equals to (Stolzenburg, 1988):

$$F_\gamma(\omega) = -\mathrm{A}_\gamma\left[\frac{(1-\omega)^2}{2(1-\gamma)}ln\gamma + \omega ln\omega + (1-\omega)\right]. \tag{2.67}$$

2.3.2.3 Evaluation of the Diffusional Broadening Parameter

With the path of integration determined, the attention is now turned on the integrand of the diffusional broadening parameter. As already mentioned, the velocity $\boldsymbol{v}$ of the particles at any point within the DMA is given by Equation 2.15, i.e., $\boldsymbol{v} = \boldsymbol{u} + Z_p\boldsymbol{E}$. Consistent with the approximation of the flow field in the previous section, it is assumed that, within the segments, there is no radial component of the air velocity (this is a good assumption if one ignores the flow patterns in the vicinity of the aerosol inlet and exits). The radial particle velocity component is then,

$$v_{r_i} = v_r(Z_p = \mathrm{Z}^*_{p_i}) = \mathrm{Z}^*_{p_i} \cdot E_r\,(r) = -U^*_{E_i}\frac{R_2}{r}\,. \tag{2.68}$$

Assuming also that $E_z = 0$ everywhere within the DMA column (again, this is a valid assumption if one ignores the regions close to the aerosol inlet and exit slits) the axial component of particle velocity is:

$$v_{z_j} = u_z(r)\,. \tag{2.69}$$

The dimensionless particle velocity can then be expanded as:

$$\tilde{v}_{i,j}^2 = \frac{v_{z_j}^2 + v_{r_i}^2}{U_j^2} = \left(\frac{u_z(\omega)}{U_j}\right)^2 + \left(\frac{U_{E_i}^*}{U_j}\right)^2 \frac{1}{\omega} \,. \tag{2.70}$$

Considering now that:

$$v_{r_i} = \frac{dr}{dt} \Longrightarrow dr = v_{r_i} dt \,,$$

one obtains:

$$d\omega = \frac{2rdr}{{R_2}^2} = \frac{2rv_{r_i}dt}{{R_2}^2} = \frac{2rdt}{{R_2}^2}\left(-U_{E_i}^* \frac{R_2}{r}\right) = -\frac{2U_{E_i}^*}{R_2} = -d\tilde{t}_i \,. \tag{2.71}$$

Substituting Equations 2.69-2.71 into Equation 2.57 yields:

$$G_{i,j} = 4\left(\frac{Q_{t_j}}{Q_{t_i}}\right)^2 \left(\frac{1+\beta_i}{1-\gamma}\right)^2 \int_{\omega_{i,j,d}}^{\omega_{i,j,u}} \left[\left(\frac{u_z(\omega)}{U_j}\right)^2 + \left(\frac{U_{E_i}^*}{U_j}\right)^2 \frac{1}{\omega}\right] \omega d\omega, \tag{2.72a}$$

which can be rewritten as:

$$G_{i,j} = 4\left(\frac{Q_{t_j}}{Q_{t_i}}\right)^2 \left(\frac{1+\beta_i}{1-\gamma}\right)^2 \left[\int_{\omega_{i,j,d}}^{\omega_{i,j,u}} f_\gamma^2(\omega)\omega d\omega + \left(\frac{U_{E_i}^*}{U_j}\right)^2 \int_{\omega_{i,j,d}}^{\omega_{i,j,u}} d\omega\right]. \tag{2.72b}$$

From Equations 2.47, 2.48 and 2.55, it is derived:

$$\left(\frac{U_{E_i}^*}{U_j}\right)^2 = \left(\frac{Q_{t_i}}{2\pi(1+\beta_i)L_i R_2} \cdot \frac{\pi\left(R_2^2 - R_1^2\right)}{Q_{t_j}}\right)^2 = \left(\frac{Q_{t_i}}{Q_{t_j}} \cdot \frac{(1-\gamma)}{2(1+\beta_i)} \cdot \frac{R_2}{L_i}\right)^2 .$$

The $G_{i,j}$ factor can now be written as:

$$G_{i,j} = G_{i,j,axial} + G_{i,j,radial} \,, \tag{2.73}$$

where

$$G_{i,j,axial} \equiv 4\left(\frac{Q_{t_j}}{Q_{t_i}}\right)^2 \frac{(1+\beta_i)^2}{1-\gamma} \left[I_\gamma\left(\omega_{i,j,d}\right) - I_\gamma\left(\omega_{i,j,u}\right)\right] , \tag{2.74}$$

$$G_{i,j,radial} \equiv \left(\frac{R_2}{L_i}\right)^2 \left(\omega_{i,j,u} - \omega_{i,j,d}\right), \text{ and} \tag{2.75}$$

$$I_\gamma(\omega) \equiv \frac{1}{1-\gamma} \int_\omega^1 f_\gamma^2(\omega')\omega' d\omega' , \tag{2.76}$$

as defined by Stolzenburg (1988).

For plug flow Stolzenburg (1988) calculates:

$$I_\gamma(\omega) = \frac{(1-\omega^2)}{2(1-\gamma)}\,, \tag{2.77}$$

and for Poiseuille flow

$$I_\gamma(\omega) = A_\gamma^2(1-\gamma)^{-1}\left\{\begin{array}{c} -\frac{1}{2}\omega^2[(1-\gamma)ln\omega-(1-\omega)ln\gamma]^2 \\ +\left[\frac{1}{2}\omega^2(1-\gamma)+\frac{1}{3}\omega^3 ln\gamma\right] \\ \cdot[(1-\gamma)ln\omega-(1-\omega)ln\gamma] \\ +\frac{1}{4}(1-\omega^2)(1-\gamma)^2 \\ +\frac{5}{18}(1-\omega^3)(1-\gamma)ln\gamma \\ +\frac{1}{12}(1-\omega^4)ln^2\gamma \end{array}\right\}. \tag{2.78}$$

Finally, the dimensionless diffusional broadening parameter can be written in several different forms:

$$\sigma_i^2 = \sum_{j=n}^{i}\sigma_{i,j}^2 = \widetilde{D}_i\sum_{j=n}^{i}G_{i,j} = \widetilde{D}_i G_i = \tilde{Z}_{p_i}\widetilde{D}_i^* G_i = \tilde{Z}_{p_i}\sigma_i^{*2}\,, \tag{2.79}$$

where

$$G_i \equiv \sum_{j=n}^{i} G_{i,j}\,, \tag{2.80}$$

and $\widetilde{D}_i^*$ and σ_i^* are, respectively, $\widetilde{D}_i$ and σ_i evaluated for particles having electrical mobility $Z_{p_i}^*$. Note that the former depend only on instrument parameters while the latter depend on particle size as well.

2.3.2.4 Derivation of the Transfer Function for Diffusing Particles

The transfer function of the *i*th exit of the MMO-DMA for diffusing particles is given by Equation 2.13, which, using Equations 2.14 and 2.42, yields (cf. Appendix A-Part C):

$$\Omega_{d_i} = \frac{\sqrt{2}\sigma_{\Gamma_i}}{2(\Psi_2-\Psi_1)}\left\{\mathcal{E}\left(\frac{\Psi_{i+3}-\Psi_1+Z_p\Delta\Phi_i}{\sqrt{2}\sigma_{\Gamma_i}}\right)-\mathcal{E}\left(\frac{\Psi_{i+3}-\Psi_2+Z_p\Delta\Phi_i}{\sqrt{2}\sigma_{\Gamma_i}}\right)\right.$$
$$\left.-\mathcal{E}\left(\frac{\Psi_{i+2}-\Psi_1+Z_p\Delta\Phi_i}{\sqrt{2}\sigma_{\Gamma_i}}\right)+\mathcal{E}\left(\frac{\Psi_{i+2}-\Psi_2+Z_p\Delta\Phi_i}{\sqrt{2}\sigma_{\Gamma_i}}\right)\right\}. \tag{2.81}$$

Here $\mathcal{E}$ is the integral of the error function defined as:

$$\mathcal{E}(x) \equiv \int_0^x \text{erf}(u)\, du = x\, \text{erf}(x) + \frac{1}{\sqrt{\pi}} \exp(-x^2)\,, \qquad (2.82)$$

where the standard error function is given by:

$$\text{erf}\,(x) \equiv \frac{2}{\sqrt{\pi}} \int_0^x \exp(-u^2) du\,. \qquad (2.83)$$

Using the dimensionless variables defined by Equations 2.26-2.28 and 2.46, the transfer function of the i^{th} exit of the MMO-DMA for diffusing particles can be re-expressed as (cf. Appendix A-Part C):

$$\begin{aligned}\Omega_{d_i} = \frac{\sqrt{2}\sigma_i}{2\beta_i(1-\delta_i)} \Bigg\{ & \mathcal{E}\left(\frac{\tilde{Z}_{p_i} - (1+\beta_i)}{\sqrt{2}\sigma_i}\right) - \mathcal{E}\left(\frac{\tilde{Z}_{p_i} - (1+\beta_i\delta_i)}{\sqrt{2}\sigma_i}\right) \\ & - \mathcal{E}\left(\frac{\tilde{Z}_{p_i} - (1-\beta_i\delta_i)}{\sqrt{2}\sigma_i}\right) + \mathcal{E}\left(\frac{\tilde{Z}_{p_i} - (1-\beta_i)}{\sqrt{2}\sigma_i}\right) \Bigg\}\,.\end{aligned} \qquad (2.84)$$

Predictions using the diffusing transfer function given by Equation 2.84 are in good agreement with the measurements provided by Chen et al. (2007), for the specific design they proposed. The details of this comparison are presented in Giamarelou et al. (2013).

2.4. Resolution of the MMO-DMA

According to Zhang and Flagan (1996), the resolution of a DMA is the ratio of the mobility corresponding to the peak of the transfer function Z_p^* to the Full Width of the mobility transfer function at its Half Maximum (FWHM), $\mathcal{R} \equiv \frac{Z^*}{\Delta Z_{FWHM}}$. The limiting resolution for DMAs with a single monodisperse-particle outlet is that predicted using the non-diffusive transfer function to estimate ΔZ_{FWHM} (e.g., Knutson and Whitby, 1975). Because the larger particles are classified at higher voltages applied between the two electrodes, the limiting resolution (i.e., ignoring particle diffusivity) is obtained under these conditions and can be expressed as $\mathcal{R}_{nd} = \frac{1}{\beta(1+|\delta|)}$. For balanced flows (i.e., $\delta = 0$) the limiting resolution is reduced to $\mathcal{R}_{nd} = \frac{1}{\beta}$. By analogy, the resolution of the *ith* exit of the MMO-DMA can be calculated as:

$$\mathcal{R}_{nd_i} = \frac{1}{\beta_i(1+|\delta_i|)}\,, \tag{2.85}$$

and for balanced flows, i.e., when the sample flow rate of the i^{th} exit is equal to the aerosol flow rate $\delta_i = 0$ or ($Q_{s_i} = Q_a$), as:

$$\mathcal{R}_{nd_i} = \frac{1}{\beta_i} \equiv \mathcal{R}_{k_i}\,. \tag{2.86}$$

The resolution of each DMA channel can be evaluated by using numerical values of its transfer function. When particle diffusivity is taken into account, the spread of the transfer function, and thus the resolution of the DMA depends on the particle migration *Peclét* number through σ, and on the flow ratios β and δ. Flagan (1999) showed that for small particles the resolution is proportional to the square root of the applied voltage. Downard et al. (2011) extended this approach for the opposed migration aerosol classifiers (OMACs) and the inclined grid mobility analyzers (IGMAs), and showed that at low voltages both these instruments exhibit better resolution compared to that of the DMA. Using their approach it is derived here a general expression for estimating the resolution of the i^{th} exit of the MMO-DMA for given operating conditions.

Since the introduction of the closed loop sheath flow system (Kousaka et al., 1985) it is more common to operate the DMA with balanced flows, which for the case of the MMO-DMA means that $\delta_i = (Q_{s_i} - Q_a)/(Q_{s_i} + Q_a) = 0$. Operationally, the closed loop would work more conveniently with $\sum_{i=1}^{n} Q_{s_i} = Q_a$, but for comparison with previous works for the conventional DMA the case of $Q_{s_i} = Q_a$ will be considered here. In this case the dimensionless diffusional transfer function for the i^{th} outlet (i.e., Equation 2.84), can be written as:

$$\Omega_{d_i} = \frac{\sqrt{2}\sigma_i}{2\beta_i}\left\{\mathcal{E}\left(\frac{\tilde{Z}_{p_i}-(1-\beta_i)}{\sqrt{2}\sigma_i}\right) - 2\mathcal{E}\left(\frac{\tilde{Z}_{p_i}-1}{\sqrt{2}\sigma_i}\right) + \mathcal{E}\left(\frac{\tilde{Z}_{p_i}-(1+\beta_i)}{\sqrt{2}\sigma_i}\right)\right\}. \tag{2.87}$$

To simplify the calculations and without loss of generality the dimensionless mobility is defining as:

$$\zeta_i \equiv \mathcal{R}_{k_i}\left(\tilde{Z}_{p_i} - 1\right), \tag{2.88}$$

and the dimensionless variance:

$$\tilde{\sigma}_i^2 = \sigma_i^2 {\mathcal{R}_{k_i}}^2 . \tag{2.89}$$

After substituting Equations 2.88 and 2.89 into Equation 2.87 and rearranging, the dimensionless transfer function becomes:

$$\Omega_{d_i} = \frac{\sqrt{2}\tilde{\sigma}_i}{2}\left\{\mathcal{E}\left(\frac{\zeta_i+1}{\sqrt{2}\tilde{\sigma}_i}\right) - 2\mathcal{E}\left(\frac{\zeta_i}{\sqrt{2}\tilde{\sigma}_i}\right) + \mathcal{E}\left(\frac{\zeta_i-1}{\sqrt{2}\tilde{\sigma}_i}\right)\right\}. \tag{2.90}$$

For convenience it is further defined:

$$x_i \equiv \frac{\zeta_i}{\sqrt{2}\tilde{\sigma}_i}, \text{ and } \Delta x_i \equiv \frac{1}{\sqrt{2}\tilde{\sigma}_i}, \tag{2.91}$$

so that Equation 2.90 can be simplified to:

$$\frac{\Omega_{d_i}}{\Delta x_i} = \frac{1}{2}\left\{\frac{\mathcal{E}(x_i+\Delta x_i) - 2\mathcal{E}(x_i) + \mathcal{E}(x_i-\Delta x_i)}{(\Delta x_i)^2}\right\}. \tag{2.92}$$

The fraction within braces on the right side is a central difference approximation of the second derivative of the integrated error function $\mathcal{E}$, which is equal to $\frac{2}{\sqrt{\pi}} exp(-{x_i}^2)$.

Following Flagan (1999), one now considers the situation $\beta^2 \ll \sigma_i^2 \ll 1$. The first condition indicates that the width of the transfer function is dominated by the effect of diffusion over the base width determined by the flow ratio. The second condition indicates that the diffusion-broadened width is still small compared to the peak,

$\tilde{Z}^*_{p_i} = 1$, such that relative variation of $\tilde{Z}_{p_i}$ is small within the width, and $\sigma_i^2 = \tilde{Z}_{p_i} \cdot {\sigma_i^*}^2 \approx {\sigma_i^*}^2$ can be approximated as constant. This also means that the transfer function is still relatively symmetric about the peak. Both of these conditions are necessary and sufficient to accept the central difference approximation above as reasonably accurate.

Under these conditions, the behavior of the transfer function for diffusing particles can be estimated by:

$$\lim_{\Delta x_i \to 0} \frac{\Omega_{d_i}}{\Delta x_i} = \frac{1}{\sqrt{\pi}} \exp\left(-{x_i}^2\right) , \tag{2.93}$$

so that the transfer function of the *ith* exit can be expressed as:

$$\Omega_{d_i} = \frac{\Delta x_i}{\sqrt{\pi}} \exp\left(-{x_i}^2\right) . \tag{2.94}$$

Using Equations 2.91, 2.88, 2.89 and 2.86 and rearranging, it is obtained:

$$\Omega_{d_i} = \frac{1}{\sqrt{2\pi}\tilde{\sigma}_i} \exp\left(\frac{-{\zeta_i}^2}{2\tilde{\sigma}_i^2}\right) = \frac{\beta_i}{\sqrt{2\pi}\sigma_i} \exp\left(\frac{-\left(\tilde{Z}_{p_i}-1\right)^2}{2\sigma_i^2}\right) . \tag{2.95}$$

In a similar manner we obtain that for non-balanced flows:

$$\Omega_{d_i}(\delta_i \neq 0) = \frac{1+\delta_i}{\sqrt{2\pi}\tilde{\sigma}_i} \exp\left(\frac{-{\zeta_i}^2}{2\tilde{\sigma}_i^2}\right) = \frac{\beta_i(1+\delta_i)}{\sqrt{2\pi}\sigma_i} \exp\left(\frac{-\left(\tilde{Z}_{p_i}-1\right)^2}{2\sigma_i^2}\right) . \tag{2.96}$$

As shown in Equation 2.95, the transfer function of the *ith* exit of the MMO-DMA reduces to a Gaussian distribution with standard deviation σ_i. In this case the position of the peak corresponds to the centroid electrical mobility, i.e., $\tilde{Z}_{p_i} = 1$, and the FWHM is related to the standard deviation by $\mathrm{FWHM} = 2\sqrt{2\ln 2}\sigma_i$ (Taylor, 1997). Based on the definition of Zhang and Flagan (1996), i.e., $\mathcal{R} \equiv \frac{Z^*}{\Delta Z_{FWHM}}$, the resolution of the *ith* exit of the MMO-DMA, estimated by using the approximate diffusional transfer function (cf. Equation 2.95), can be expressed as:

$$\mathcal{R}_{diff_i} = \frac{1}{2\sqrt{2\ln 2}\sigma_i^*} = \frac{1}{2\sqrt{2\ln 2}}\left[\frac{Pe_{mig_i}^*}{G_i \cdot (1 - R_1/R_2)}\right]^{1/2} . \qquad (2.97)$$

To derive Equation 2.97 one has to use Equations 2.54 and 2.79. Note that Equation 2.57 differs from the expression given by Flagan (1999; Equation 2.57) in that he incorporates the extra factor of $(1 - R_1/R_2)$ into the definition of G_i. Beginning with Equation 2.54 and expressing the particle migration *Peclét* number as a function of the applied voltage between the two electrodes:

$$Pe_{mig_i}^* = \frac{(R_2 - R_1)\left(-Z_{p_i}^*\right)E_r(R_2)}{Z_{p_i}^* kT/q} = \frac{(R_2 - R_1)\cdot V}{(kT/q)[R_2 \ln(R_1/R_2)]} = \left(\frac{qV}{kT}\right) f \ , \qquad (2.98)$$

the diffusion-limited resolution becomes:

$$\mathcal{R}_{diff_i} = \frac{1}{2\sqrt{2\ln 2}}\left[\frac{qVf}{kTG_i \cdot (1 - R_1/R_2)}\right]^{1/2} = \frac{1}{2\sqrt{2\ln 2}}\left[\frac{qV}{kTG_i \cdot \ln(R_1/R_2)}\right]^{1/2} , \qquad (2.99)$$

where $f \equiv \frac{1 - R_1/R_2}{\ln(R_1/R_2)}$. It should be noted that $\mathcal{R}_{diff_i}$ depends on the geometry of the MMO-DMA and on the operating conditions. Under the assumption that the particles entering the DMA are singly charged, and that the operating temperature is ambient (i.e., $T = 298\text{K}$), $\frac{kT}{q} = \frac{kT}{e} = 0.0255\text{V}$ where e is the elementary charge. In a similar manner with the single monodisperse-particle outlet DMA (Flagan, 1999) the diffusion-limited resolution becomes:

$$\mathcal{R}_{diff_i} = 2.648\left[\frac{V}{G_i \cdot \ln(R_1/R_2)}\right]^{1/2} . \qquad (2.100)$$

The smallest particle sizes that can be accurately classified with DMAs are affected by particle diffusion. The extent to which particle diffusion can affect the performance of a DMA can be characterized by the diffusion-onset voltage V_{diff} which can be estimated by the intersection of $\mathcal{R}_{nd}$ and $\mathcal{R}_{diff}$ (Flagan, 1999). Below this voltage, the classification resolution of a DMA is significantly reduced by particle diffusivity (Seol et al., 2002). As a result, when equating Equation 2.86 with Equation

2.100 for balanced flows, the diffusion-onset voltage for the i^{th} exit of a cylindrical MMO-DMA becomes:

$$V_{diff_i} = 0.143\,\frac{G_i \cdot \ln(R_1/R_2)}{\beta_i^2}\,. \tag{2.101}$$

To obtain an expression that describes the variation of the resolution with voltage over the entire operating range it is needed to evaluate certain moments of the transfer function. For an ideal DMA, Stolzenburg (1988) calculated the variance of the non-diffusing transfer function as $S_{nd}^2\left[\tilde{Z}_p\right] = \frac{1}{6}\beta^2(1+\delta^2)$. For the case of the MMO-DMA the variance of the i^{th} exit is given by:

$$S_{nd_i}^2\left[\tilde{Z}_{p_i}\right] = \frac{1}{6}{\beta_i}^2\left(1+{\delta_i}^2\right)\,, \tag{2.102}$$

so that $\mathcal{R}_{nd_i}$ can be written as:

$$\mathcal{R}_{nd_i} = \frac{1}{\beta_i(1+|\delta_i|)} = \frac{\sqrt{1+\delta_i^2}}{\sqrt{6}S_{nd_i}(1+|\delta_i|)}\,. \tag{2.103}$$

When particle diffusivity becomes important Stolzenburg (1988) and Stolzenburg and McMurry (2008) showed that for the diffusing transfer function the corresponding moment for the conventional DMA becomes $S_d^2\left[\tilde{Z}_p\right] = \frac{1}{6}\beta^2(1+\delta^2) + \sigma^{*2}\left(1+2\sigma^{*2}\right)$, which for the case of the MMO-DMA can be written in the form:

$$S_{d_i}^2\left[\tilde{Z}_{p_i}\right] = \frac{1}{6}{\beta_i}^2\left(1+{\delta_i}^2\right) + \sigma_i^{*2}\left(1+2\sigma_i^{*2}\right)\,. \tag{2.104}$$

Following Flagan (1999), one replaces S_{nd_i} with S_{d_i} in Equation 2.103 and apply it over the entire range of σ_i , thus obtaining:

$$\mathcal{R}_{approx_i} = \frac{1}{\sqrt{6}S_{d_i}}\left(\frac{\sqrt{1+\delta_i^2}}{1+|\delta_i|}\right)\,. \tag{2.105}$$

Equally valid would be to replace σ_i^* with S_{d_i} in Equation 2.97 to give:

$$\mathcal{R}_{approx_i} = \frac{1}{2\sqrt{2\ln 2}S_{d_i}}\,. \tag{2.106}$$

The leading numerical factors of these two formulations differ only by 4%. But clearly, there is too much dependence on the flow asymmetry parameter δ_i in Equation 2.105 in the diffusion-limited regime. For $0 \leq \delta_i < 1$, the factor in the parentheses of Equation 2.105 can range from 1 up to $1/\sqrt{2}$, a 30% possible variation. This degree of variation with δ_i is not present in Equation 2.106 in the diffusion-limited regime where ${\sigma_i^*}^2 \gg \beta_i^2$. Similarly, Equation 2.106 is off by the same factor in the non-diffusing limit. Thus, neither approach yields a valid approximation for the resolution of the DMA over the entire range of σ_i when unbalanced flows are considered.

For the case of balanced flows, i.e., $\delta_i = 0$,

$$\mathcal{R}_{approx_i} = \left[{\beta_i}^2 + 6{\sigma_i^*}^2\left(1 + 2{\sigma_i^*}^2\right)\right]^{-1/2} \tag{2.107}$$

is a good approximation to within 4% in the diffusion-limited regime and is exact in the non-diffusing limit. Here,

$${\sigma_i^*}^2 = G_i\widetilde{D}_i^* = G_i \frac{4\pi L_i D_i^*}{Q_{sh_i}+Q_{m_i}} \cdot \frac{Z_{p_i}^* kT/q}{D_i^*} \cdot \frac{(Q_{sh_i}+Q_{m_i}) ln(R_1/R_2)}{4\pi L_i V Z_{p_i}^*} = \frac{G_i kT ln(R_1/R_2)}{qV} . \tag{2.108}$$

To maximize the resolution of the MMO-DMA, ${\sigma_i^*}^2$ should be minimized. For a given geometry, i.e., for fixed γ values, and flow rate ratios β_i and δ_i, ${\sigma_i^*}^2$ decreases continuously with increasing $Pe_{mig_i}^*$ or voltage, corresponding to a decreasing length or increasing sheath flow. For conventional DMAs, one seeks to minimize the effect of particle diffusivity by optimizing the distance between aerosol inlet and monodisperse-particle outlet (i.e., by setting the term $\frac{2LR_2\sqrt{I_\gamma}}{{R_2}^2-{R_1}^2}$ according to Rosell-Llompart et al., 1996, and de la Mora, 2010, or the term $\frac{2LR_2(1+\beta)}{{R_2}^2-{R_1}^2}$ according to Flagan, 1990, close to unity). For the MMO-DMA such an optimization is appropriate only for the n^{th} monodisperse particle outlet, for which one can use the approaches proposed for the conventional DMAs.

2.5 Conclusions

This chapter provides the derivation of an analytical expression for the transfer function of a cylindrical DMA with multiple monodisperse outlets (namely an MMO-DMA) using the same approach followed by Stolzenburg (1988). First, the transfer function for each monodisperse-particle outlet Ω_{nd_i}without taking into account particle diffusivity (cf. Equation 2.29) is derived, and then the analysis extended to the derivation of the transfer function Ω_{d_i} for diffusing particles (cf. Equation 2.84). The derived MMO-DMA transfer functions differ from the conventional DMA transfer function (Stolzenburg, 1988) in that every individual channel has an associated sheath flow rate Q_{sh_i} (cf. Equation 2.5) and excess flow rate Q_{m_i} (cf. Equation 2.6) as shown in Figure 2.1a.

By analogy to the conventional DMA, the limiting resolution of the i^{th} monodisperse-particle outlet of the MMO-DMA for non-diffusing particles can be determined by $\mathcal{R}_{nd_i} = \frac{1}{\beta_i(1+|\delta_i|)}$ and for balanced flows by $\mathcal{R}_{nd_i} = \frac{1}{\beta_i}$, where β_i and δ_i are non-dimensional flow parameters corresponding to each outlet (cf, Equations 2.27 and 2.28, respectively). In the diffusion-limited regime, assuming that the transfer function of the MMO-DMA is Gaussian the diffusion-limited resolution $\mathcal{R}_{diff_i}$ for each outlet (cf. Equations 2.97, 2.99 and 2.100) is derived, using the approach followed by Flagan (1999) and Downard et al. (2011). Combining the two limiting cases (i.e., for non-diffusing and for diffusing particles), I further derive an approximate resolution $\mathcal{R}_{approx_i}$ (Equations 2.107-2.108) for balanced flows only, which can be applied over the entire range of particle mobilities and diffusional broadening parameters.

2.6 Acknowledgements

I thank Loukas Vitiniotis, Dias Haralambopoulos, and Michiel Kreutzer for the constructive discussions on various parts of the paper. I also thanks Andy Downard for sharing his theoretical and experimental results.

Chapter 3

3. Comparison between the Theoretical and Experimental Performance of a Differential Mobility Analyzer with three Monodisperse-Particle Outlets

Note: This chapter appeared as reference: Giamarelou, M., Stolzenburg, M., Chen, D-R., Biskos, G., 2013. Comparison Between the Theoretical and Experimental Performance of a Differential Mobility Analyzer with Three Monodisperse-Particle Outlets, *Aerosol Sci. & Technol.*, 47: 406-416.

3.1 Abstract

Differential Mobility Analyzers (DMAs) with more than one monodisperse-particle outlet can offer a number of advantages compared to conventional single monodisperse-particle outlet designs. Chen et al. (2007) have designed and tested a DMA with three monodisperse-particle outlets (3-MO-DMA), whereas Giamarelou et al. (2012) have recently (cf. Chapter 2) provided the theoretical framework for determining the performance of such an analyzer. The objective of this chapter is to compare the theoretical with the experimental performance of this DMA. Resolutions determined by the theoretically predicted transfer functions for the three monodisperse-particle outlets are compared with measurements when the DMA was operated under different operating conditions. Predictions and measurements show good agreement when the DMA is operated at low sheath flow rates and for aerosol outlets relatively far from the aerosol inlet. At higher sheath flow rates and for aerosol outlets relatively near the inlet there is evidence that the discrepancy between theoretical predictions and measurements may disappear but the chances of flow disturbances in the classifier increase as well. The theory derived at the previous chapter (cf. Giamarelou et al., 2012) for Multiple Monodisperse-Outlet DMAs

(MMO-DMAs) is thus seen as successful in predicting the performance of this instrument, provided that disturbances in the flow field are avoided.

3.2 Introduction

The Differential Mobility Analyzer (DMA) is the most efficient tool for determining the size of aerosol particles in the sub-micrometer and nanometer range by directly measuring their electrical mobility (Flagan, 1998; McMurry, 2000; Biskos et al., 2008). When used as classifiers in electrical mobility spectrometers, DMAs are typically operated in either a scanning or a stepping mode in order to select particles over a wide range of the mobility spectrum. The required time for scanning or stepping of the operating conditions (typically the potential difference between the two electrodes) can range between 30 s to a few minutes depending on the desired resolution of the measurements and the particle detector employed (Wang et al., 2002). Using fast-response mixing-type Condensation Particle Counters (CPCs) (e.g., Okuyama et al., 1984; Kousaka et al., 1985) in electrical mobility spectrometers one can use scanning times down to a few seconds without sacrificing the resolution of the mobility distribution measurement (Wang et al., 2002). Such particle counters, however, are not yet widely available.

In order to reduce the response time and/or to increase the dynamic range of electrical mobility spectrometers, efforts have been made in developing mobility classifiers that can simultaneously classify particles in different channels. Instruments that fulfill these two objectives include the Tartu Spectrometer (Tammet et al., 1998; 2002), the Fast Mobility Particle Spectrometer (FMPS; Johnson et al., 2004) and the Differential Mobility Spectrometer (DMS; Biskos et al., 2005). Although these instruments have a short response time (i.e., of the order of a second) and a wide dynamic range (from a few nanometers up to a few microns), they suffer from (a) low resolution as a result of the finite width of the channels, and (b) low signal-to-noise ratio because detection is performed by electrometers. A solution around these two limitations is to use a Multiple Monodisperse-Outlet DMA (MMO-DMA), in combination with Condensation Particle Counters (CPCs). An MMO-DMA operated at fixed conditions can simultaneously select monodisperse particles of different sizes with a very high resolution, whereas the detection limit of CPCs can enable measuring aerosols of very low particle concentrations.

Chen et al. (2007) built and tested a DMA having three monodisperse-particle outlets, and recently Giamarelou et al. (2012) (cf. Chapter 2) have derived a generalized theoretical framework for describing the performance of any MMO-DMA. The performance of a DMA can be fully determined by its transfer function, i.e., the function that gives the probability of a particle of a given mobility that enters the classifier to exit through the monodisperse-particle outlet. From the theoretical point of view, the DMA transfer function for relatively large particles can be derived by considering their deterministic trajectories within the column (cf. Knutson and Whitby, 1975). For smaller particles, however, Brownian motion causes deviation from their deterministic paths, thereby resulting in a broadening of the transfer function (Kousaka et al., 1986; Stolzenburg, 1988; Flagan, 1999; Haywood et al., 1999; Salm, 2000; de la Mora, 2002). From the experimental point of view, the transfer function of the DMA can be determined using a tandem DMA system (Fissan et al., 1996; Birmilli et al., 1997; Martinsson et al., 2001). In this system, the first DMA is used to produce a flow of monodisperse particles, which is then passed through the second DMA whose transfer function needs to be evaluated. The use of two identical DMAs operated under the same flow conditions is preferred as it minimizes the error propagation of the retrieved transfer function (Mei et al., 2011).

In this chapter, the experimental measurements of the transfer function of the DMA with three monodisperse-particle outlets (referred to as the 3-MO-DMA from this point onwards) provided by Chen et al. (2007) are used to evaluate the performance of the theoretical MMO-DMA transfer function derived at the previous chapter (cf. Giamarelou et al., 2012). First, the predicted with the measured transfer functions for 20-nm particles when the DMA is operated under balanced and unbalanced flow conditions are compared. To evaluate how well the model captures the effect of particle diffusivity then it is compared the predicted with the measured resolution for each outlet when particles of different diameter are classified through the DMA.

3.3 Methodology

3.3.1. Experimental

Figure 3.1 shows a schematic diagram of the 3-MO-DMA that is used in the evaluation. Details of its design are provided by Li (2006) and Chen et al. (2007). In brief, it is a cylindrical DMA with two coaxial electrodes having radii of 2.54 and 3.49 cm, and monodisperse-particle outlets located 2.54, 7.62, and 15.24 cm from the polydisperse aerosol inlet. The polydisperse aerosol flow is introduced alongside the central high-voltage electrode, and the classified particles are repelled to the outer electrode where the three outlets are located. Although the current design was not optimized for high-resolution particle classification, the data provided by Chen et al. (2007) are the only available experimental results at present with which I can compare the predictions of the theoretical model.

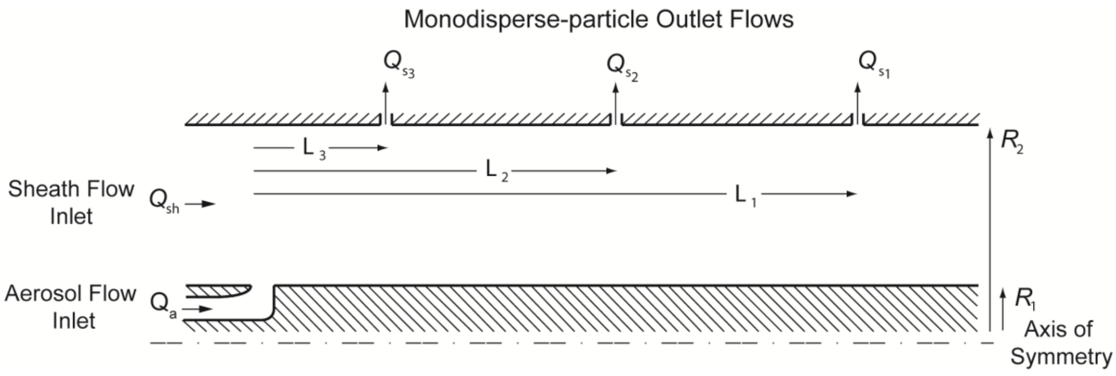

Figure 3.1: Schematic diagram of the DMA with three monodisperse-particle outlets (3-MO-DMA) located at distances $\boldsymbol{L_1}$ =15.24, $\boldsymbol{L_2}$ =7.62, and $\boldsymbol{L_3} =$ 2.54 cm downstream of the polydisperse aerosol inlet. The radii of the inner and the outer electrodes are $\boldsymbol{R_1}$ =1.27 cm and $\boldsymbol{R_2} =$ 1.75 cm.

The transfer function of the 3-MO-DMA has been determined experimentally using the Tandem DMA (TDMA) technique (cf. Li, 2006, for a detailed description of these measurements). In brief, a nano-DMA (TSI Model 3085) was used as the first DMA in the system. The operating flows and the applied potential difference between the electrodes of the nano-DMA were adjusted for each measurement in order to select particles having diameters from 6 to 45 nm (Li, 2006; Chen et al., 2007). Two operating modes of the 3-MO-DMA were used during the measurements: in the first mode the total polydisperse aerosol flow was equal to the sum of the three outlet streams (i.e., unbalanced flow conditions), whereas in the second mode the sampling flow rate at each outlet was equal to the polydisperse aerosol inlet flow rate (i.e., balanced flow conditions). The potential difference between the electrodes of the 3-MO-DMA, used as the second DMA in the TDMA setup, was varied in order to measure the number of particles collected through the different channels.

The transfer function of the multiple-outlet DMA was then determined using a piecewise-linear function deconvolution algorithm (Li, 2006; Li et al., 2006). This algorithm retrieves the DMA transfer function without pre-assuming its shape. The entire electrical mobility window of the true transfer function is divided into N subsections, and a linear function is assumed in each one of them. A conjugate gradient method is used to obtain the optimal values of the parameters defining the piece-wise linear function by fitting the predicted TDMA response to the experimental measurements. A least-square error criterion is used for the convergence of the iteration procedure (cf. Li, 2006; Li et al., 2006).

3.3.2. Theoretical

The theoretical framework for determining the transfer function of cylindrical DMAs with multiple monodisperse-particle outlets (MMO-DMAs) has been derived in the previous chapter. Assuming that the flow field is axisymmetric and steady and that the airflow is laminar and incompressible, the transfer function of the i^{th} outlet of the MMO-DMA for diffusing particles is given by (cf. Equation 2.84; Section 2.3):

$$\Omega_{d_i} = \frac{\sqrt{2}\sigma_i}{2\beta_i(1-\delta_i)}\left\{\mathcal{E}\left(\frac{\tilde{Z}_{p_i}-(1+\beta_i)}{\sqrt{2}\sigma_i}\right) - \mathcal{E}\left(\frac{\tilde{Z}_{p_i}-(1+\beta_i\delta_i)}{\sqrt{2}\sigma_i}\right) - \mathcal{E}\left(\frac{\tilde{Z}_{p_i}-(1-\beta_i\delta_i)}{\sqrt{2}\sigma_i}\right) + \mathcal{E}\left(\frac{\tilde{Z}_{p_i}-(1-\beta_i)}{\sqrt{2}\sigma_i}\right)\right\}, \tag{3.1}$$

where i = 1, 2 or 3 corresponds to one of the three outlets of the DMA used in this study (cf. Figure 3.1), and $\mathcal{E}$ denotes the integral of the error function. In Equation 3.1, σ_i is the dimensionless diffusional broadening parameter, β_i and δ_i are the dimensionless flow parameters, and $\tilde{Z}_{p_i}$ is the dimensionless particle electrical mobility, all corresponding to the i^{th} outlet.

One way to quantify the disparity between the theoretical and the measured transfer functions or resolutions is to introduce several adjustable parameters into Equation 3.1 in order to fit the model to the measurements. The parametric transfer function can be expressed as follows:

$$\Omega'_{d_i} = \eta_i \frac{\sqrt{2}\sigma'_i}{2\beta'_i(1-\delta'_i)}\left\{\mathcal{E}\left(\frac{\tilde{Z}_{p_i}-(1+\Delta\tilde{Z}'_i+\beta'_i)}{\sqrt{2}\sigma'_i}\right)-\mathcal{E}\left(\frac{\tilde{Z}_{p_i}-(1+\Delta\tilde{Z}'_i+\beta'_i\delta'_i)}{\sqrt{2}\sigma'_i}\right)\right. \\ \left.-\mathcal{E}\left(\frac{\tilde{Z}_{p_i}-(1+\Delta\tilde{Z}'_i-\beta'_i\delta'_i)}{\sqrt{2}\sigma'_i}\right)+\mathcal{E}\left(\frac{\tilde{Z}_{p_i}-(1+\Delta\tilde{Z}'_i-\beta'_i)}{\sqrt{2}\sigma'_i}\right)\right\}, \tag{3.2}$$

where ${\sigma'_i}^2 \equiv f_{G_i}\sigma_i^2 + \sigma_{mix_i}^2$. The adjustable parameters can be interpreted as follows:

- η_i is the ratio of the penetration efficiency through the DMA plumbing leg in the TDMA experimental setup, excluding the DMA classification section itself, over the penetration efficiency through the parallel plumbing leg that bypasses the DMA in order to allow for the measurement of the aerosol concentration upstream of the DMA (cf. Figure 2 of Chen et al., 2007). This parameter represents a simple vertical scaling of the transfer function and has no effect on the resolution. It is a necessary scaling factor in our analysis as the measured Ω'_{d_i} given by Chen et al. (2007) has not been corrected for particle losses beyond the DMA classification section.
- $\Delta\tilde{Z}'_i$ is the offset of the centroid of the measured transfer function from that of the theoretical one, caused by a possible offset of the analyzer voltage or a discrepancy in the average sheath flow, $(Q_{sh_i} + Q_{m_i})/2$. $\Delta\tilde{Z}'_i$ is typically small and has negligible effect on the resolution.
- β'_i and δ'_i represent corrections to the flow parameters due to errors in the measured flow rates. In the absence of any mixing of flows, δ'_i determines the height of the non-diffusing transfer function, whereas β'_i and δ'_i together determine its width at half the maximum. An increase in β'_i or $|\delta'_i|$ over its nominal value reduces the resolution.
- $\sigma_{mix_i}^2$ represents the additional spread of the measured transfer function relative to the predicted one, due to the existence of non-ideal mixing of flows

originating near the aerosol inlet or outlet slits. The manner of its incorporation into the equations above gives only a crude estimate of the effects of mixing on the transfer function and the resolution. Together with the adjusted flow parameters, $\sigma_{mix_i}^2$ determines $\mathcal{R}'_{nd_i} = \mathcal{R}'_{nd_i}\left(\beta'_i, \delta'_i, \sigma_{mix_i}^2\right)$, the fitted resolution in the non-diffusing limit. In the fitting process, the actual adjustable parameter used to determine β'_i is $f_{\mathcal{R}_{nd_i}}$, a multiplicative adjustment factor for $\mathcal{R}_{nd_i}$.

- f_{G_i} accounts for any error in the theoretical estimate of G_i (cf. Section 2.3.2) where $\sigma_{i,corrected}^2 = f_{G_i}\sigma_i^2 = f_{G_i}G_i\widetilde{D}_i = f_{G_i}\left(G_{i,axial} + G_{i,radial}\right)\widetilde{D}_i$. $G_{i,radial}$, in particular, is likely to be underestimated in the theory due to the neglect of radial flows near the aerosol entrance and exit slits. The neglected contribution to G_i can be substantial, particularly at the aerosol outlet where the particles follow a sharply converging flow into the narrow slit. Any error in the measured average sheath flow used in the calculation of $\widetilde{D}_i$ is also incorporated into f_{G_i}.
- ${\sigma'_i}^2$ is the total adjusted spread parameter which is calculated from f_{G_i} and $\sigma_{mix_i}^2$, as indicated above. When ${\sigma'_i}^2 > \sigma_i^2$, the peak of the transfer function is lowered and broadened. Both of these effects work to decrease the measured resolution relative to that predicted. Note that $\sigma_{mix_i}^2$, which is independent of particle size, has the same effect as σ_i^2 even in the non-diffusing limit, as noted above.

The parameters η_i, $\Delta\tilde{Z}'_i$, and $\sigma_{mix_i}^2$ or f_{G_i} are used to fit the model to the measured transfer function. The other two adjustable parameters, β'_i and δ'_i, remain fixed at their respective theoretical values. Besides the height η_i, the primary requirement to fit the model to the measured transfer function was found to be the spread ${\sigma_i'}^2$. For a single transfer function measured at a given set of conditions, it is virtually impossible to distinguish the effects of f_{G_i} and $\sigma^2_{mix_i}$. Thus, the predicted transfer function was fitted to the measured both ways. The variable parameters η_i, $\Delta\tilde{\mathrm{Z}}_{\mathrm{i}}'$, and $\sigma^2_{mix_i}$ or f_{G_i} allow for the (nearly) independent adjustment of the area, mean and standard deviation, respectively, of the model transfer function which can then be fit to the corresponding quantities of the measured transfer function. As $\eta_i < 1$ is an expected result, it is only the deviation $\Delta\tilde{Z}' \neq 0$ and $\sigma^2_{mix_i} > 0$ or $f_{G_i} \neq 1$ that are of interest as measures of the disparity between the measured transfer function and the original prediction (i.e., Equation 3.1).

The measured and predicted resolutions of the DMA can be numerically determined from the measured and predicted transfer functions, respectively, as the inverse of the Full Width at Half Maximum (FWHM) normalized by the centroid mobility. When fitting the model to the measured resolution it was found most convenient to use the adjustable parameters $f_{\mathcal{R}_{nd_i}}$, f_{G_i} and δ_i'. Parameter η_i has no effect on the resolution, and the effects of small variations in $\Delta\tilde{Z}'$ are virtually undetectable. For negligible variations in $\mathcal{R}_{nd_i}'$ (i.e., within the uncertainty of the flow rate measurements) about the predicted value of the resolution in the non-diffusing limit:

$$\mathcal{R}_{nd_i} = \frac{1}{\beta_i(1+|\delta_i|)} \ , \tag{3.3}$$

β_i' was adjusted while $\sigma^2_{\mathrm{mix_i}}$ was fixed at zero. For a significant reduction in the measured $\mathcal{R}_{nd_i}'$, $\sigma^2_{mix_i} > 0$ was varied and β_i' was held at its predicted value, β_i. For particle sizes between the non-diffusing and diffusing limits, δ_i' can be used to obtain a good fit to the measured resolution in the absence of mixing. This is explained in more detail below. The adjustable factor f_{G_i} multiplying G_i, a geometric- and flow-dependent parameter, govern the asymptotic behavior of the resolution in the diffusing limit:

$$\mathcal{R}_{diff_i} = \frac{1}{2\sqrt{2ln2}}\frac{1}{\sigma_i^*} = \frac{1}{2\sqrt{2ln2}}\left[\frac{qV}{kTG_i \cdot ln(R_1/R_2)}\right]^{\frac{1}{2}}, \tag{3.4}$$

where q is the charge of the particles, V the applied potential between the two DMA electrodes having radii R_1 and R_2, T the operating temperature, and k the Boltzmann constant. Detailed expressions of G_i, β_i and δ_i can be found in the Section 2.3. The optimal values of the adjustable parameters were obtained by a nonlinear least-square curve-fitting algorithm based on the interior-reflective Newton method (Coleman and Li, 1994; 1996).

3.4 Results

Figure 3.2 shows the comparison between predicted and measured transfer functions when the 3-MO-DMA is operated at different conditions. Measurements and predictions shown in Figure 3.2a correspond to the transfer function for the outlet furthest from the inlet (i.e., outlet #1 in Figure 3.1) when the flow rates through the DMA are $\mathrm{Q_{sh}} = 20\,\mathrm{lpm}$, $\mathrm{Q_a} = 2.4\,\mathrm{lpm}$ and $\mathrm{Q}_{s1} = \mathrm{Q}_{s2} = \mathrm{Q}_{s3} = 0.8\,\mathrm{lpm}$, and the potential difference between the two electrodes is set to select particles having mobility diameter of 20 nm. Although these operating conditions correspond to an unbalanced flow scheme (i.e., $\delta_i \neq 0$), they enable the use of a closed loop sheath flow system that gives a higher measurement precision. On the other hand, in the case of balanced flows (which can only be achieved with an open sheath-flow system), one can maximize the transfer function of each outlet by increasing the $\mathrm{Q_{si}}/\mathrm{Q_a}$ ratio.

Two model transfer functions are shown in Figure 3.2a. The first, “Predicted”, corresponds to calculations using Equation 3.1, and the second, “Fitted”, uses

Equation 3.2 after matching the area, mean and standard deviation to the respective values from the measurements. The values of the adjustable parameters in Equation 3.2 to achieve the fit are $\eta' = 0.808$, $\Delta\tilde{Z}' = 0.0038$, and $\sigma_{mix} = 0.0161$ or $f_G = 1.71$. The first value indicates that there is a 19% relative loss in the plumbing leading up to and following the DMA classification section compared to that in the DMA bypass line. The second value indicates a shift in the centroid of the transfer function of less than 0.4% which is well within the experimental uncertainty of the sheath and excess air flow rates. The third value (as σ_{mix} or f_G) represents a 14% increase in the spread of the transfer function as measured by its total variance. The FWHMs for the measured, predicted and fitted transfer functions are 0.121, 0.125 and 0.127, respectively. Overall, the predicted and the measured transfer functions are in good agreement in this case.

Figure 3.2b compares the predicted with the measured transfer function for sample outlet #3 (L_3 = 2.54 cm) of the DMA when the flow rates through the classifier are $Q_{sh} = 20$ lpm, $Q_a = 1.5$ lpm and $Q_{s1} = Q_{s2} = Q_{s3} = 1.5$ lpm, and the centroid particle diameter is 20 nm. In this case the operating conditions correspond to balanced flow conditions (i.e., $\delta_i = 0$), resulting in a shape of the transfer function that is closer to triangular.

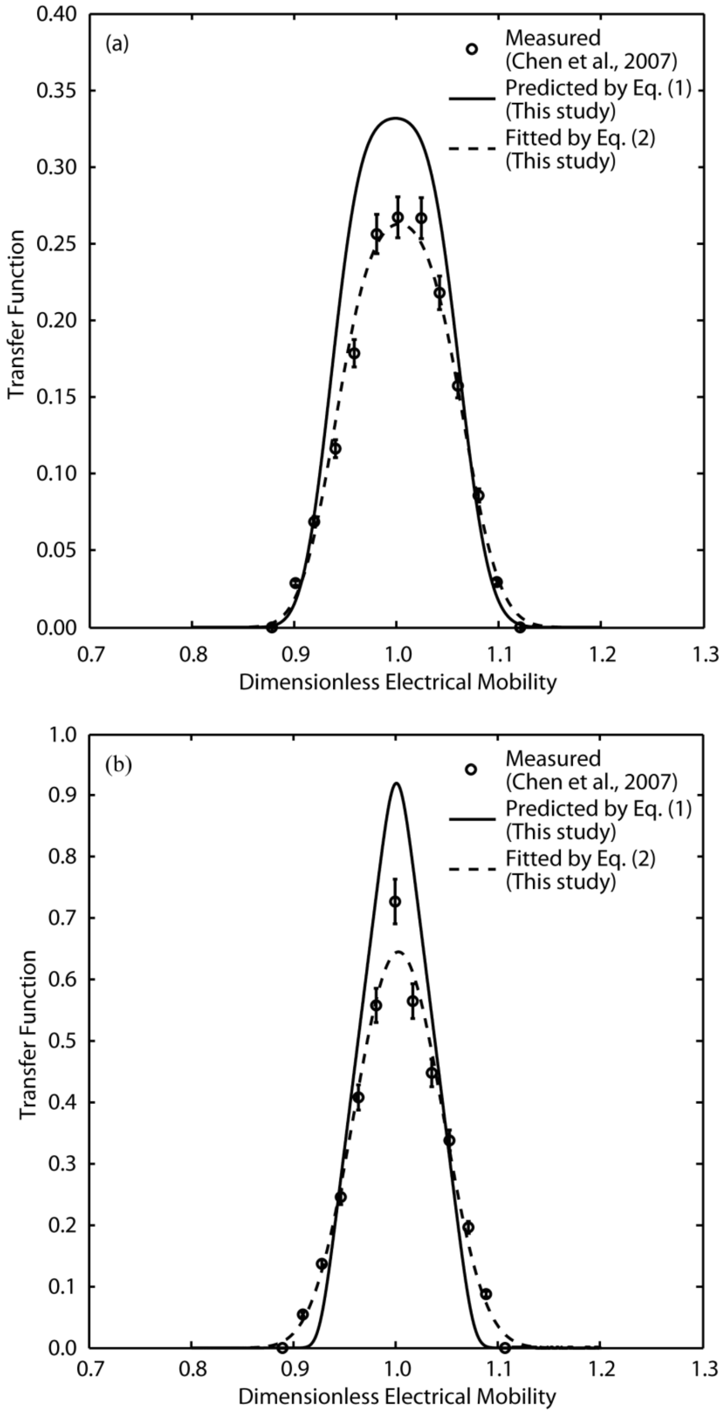

Figure 3.2: Comparison between predicted and measured transfer functions of the 3-MO-DMA for (a) the outlet furthest from the inlet (i.e., $L_1 = 15.24$ cm) when the flow rates through the column are $Q_{sh} = 20$ lpm, $Q_a =$ 2.4 lpm, $Q_{s1} = Q_{s2} = Q_{s3} = 0.8$ lpm, and the potential difference between the two electrodes is V = 196 V, and for (b) the outlet nearest to the inlet (i.e., $L_3 = 2.54$ cm) when the flow rates are $Q_{sh} = 20$ lpm, $Q_a = 1.5$ lpm, $Q_{s1} = Q_{s2} = Q_{s3} = 1.5$ lpm, and the potential difference between the two electrodes is V = 1260 V. In both cases the potential difference between the two DMA electrodes is set to select particles having mobility diameter of 20 nm.

The fitting process yielded values of the adjustable parameters as follows: $\eta' = 0.896$, $\Delta\tilde{Z}' = 0.0020$, and $\sigma_{mix} = 0.0253$ or $f_G = 12.1$. This last corresponds to a

64% increase in the total variance of the transfer function. The FWHMs for the measured, predicted and fitted transfer functions are 0.089, 0.081 and 0.100, respectively. Both measures of spread or width indicate that the measured transfer function is substantially broader than the predicted one.

Table 3.1: Values and 95% confidence limits of the fit parameters $\boldsymbol{\delta'}$, $\boldsymbol{f_{\mathcal{R}_{nd}}}$ and $\boldsymbol{f_G}$ used in Equation 3.2 to fit the modeled to the measured resolutions.

Resolution Fit Parameters

Outlet	δ'	$f_{\mathcal{R}_{nd}}$	f_G
Figure 3.3a			
#1	-0.46±0.38	1.004±0.014	0.97±0.17
#2	-0.42±0.18	1.003±0.006	1.25±0.15
#3	-0.68±1.65	1.010±0.014	2.78±1.25
Figure 3.3b			
#1	±0.15±1.08	1.000±0.221	1.11±2.70
#2	±0.12±0.18	0.994±0.064	2.23±0.44
#3	±0.15±0.10	0.995±0.026	5.33±0.63
Figure 3.4a			
#1	-0.04±0.35	1.033±0.233	1.35±0.64
#2	-0.07±0.11	1.003±0.030	1.03±0.60
#3	0.00±0.85	1.015±0.828	0.22±0.29

Next it is compared the predicted with the measured resolution of each of the monodisperse-particle outlets as a function of particle size. As described in Section 3.3, the resolution of each monodisperse-particle outlet of the DMA can be determined numerically as the inverse of the FWHM of the measured or predicted transfer functions, and analytically using Equations 3.3 and 3.4 for the non-diffusing and diffusing limiting cases, respectively. Figures 3.3-3.5 show measured (symbols), predicted (normal lines, Equation 3.1) and fitted model (bold lines, Equation 3.2) resolutions at various sets of DMA operating conditions. Shaded areas about the predicted lines correspond to a ±2% uncertainty in the measured flow rates. Fit parameters and their 95% confidence intervals are summarized in Table 3.1. The confidence intervals are unusually wide because of the small sample sizes for the measurements.

Figure 3.3 shows the comparison between predicted and measured resolutions as a function of particle size for all three outlets of the DMA when the sheath flow rate is set to 20 lpm. The data shown in Figure 3.3a correspond to unbalanced flow conditions whereas those in Figure 3.3b to balanced flows. In the case of the unbalanced flows (i.e., $Q_{sh} = 20\,\text{lpm}$, $Q_a = 2.4\,\text{lpm}$ and $Q_{s1} = Q_{s2} = Q_{s3} = 0.8\,\text{lpm}$), there is an excellent agreement between the experimental and the numerically-predicted resolution for sample outlets #1 and #2 for the whole particle size range tested (i.e., from 6 to 45 nm). For outlet #3 the agreement is within experimental uncertainty for particles having mobility diameter down to 10 nm, but for smaller particles the predicted resolution overestimates the measurements by up to 8.5% (e.g., for the 6-nm particles). Note that the point at 45 nm for outlet #3 is clearly outside reasonable limits of uncertainty in the non-diffusing resolution as determined by the measurements in the 10-30 nm range such that it has been designated as an outlier and excluded from analysis here. Considering a ±2% uncertainty in the flow rates (i.e., using a 2% increase or decrease of the sheath flow rate with simultaneous 2% decrease or increase of both the aerosol and the sample flow rates, respectively) gives a maximum uncertainty in the predicted resolution of ±4.2% for outlet #1, ±4.0% for outlet #2, and ±3.8% for outlet #3. The uncertainty increases for the outlets furthest from the inlet because more flows (i.e., those of the outlets that precede) indirectly define the total flow in the respective sections of the column. For outlet #1, the fitted model is nearly indistinguishable from the prediction. For the other two outlets, there is a clear difference between the fitted/measured resolutions and that of the predicted at and below 10 nm. For outlet #2, the predicted value of $f_G = 1.00$ is just beyond the confidence interval of the fitted value of $f_G = 1.25$, whereas for outlet

#3 the fitted value of f_G is significantly greater than one. The confidence intervals of the fitted values of δ' all include the nominal value of $\delta = -0.5$.

Figure 3.3b shows the comparison between measured and predicted resolution when the DMA is operated under balanced flows (i.e., $Q_{sh} = 20$ lpm, $Q_a = 2.4$ lpm and $Q_{s1} = Q_{s2} = Q_{s3} = 2.4$ lpm). Because the flow removed by each monodisperse-particle outlet relative to the total flow through the DMA is much higher compared to the case of the unbalanced flows (i.e., measurements and predictions shown in Figure 3.3a), the resolution here decreases noticeably as one moves from the nearest to the furthest outlet from the aerosol inlet. Agreement between numerically predicted and measured resolution is within experimental uncertainty for particles larger than ca. 10 nm for both sample outlets #2 and #3. For smaller particles the numerical predictions overestimate the measurements by as much as 22% (e.g., for the 6-nm particles classified through outlet #3). For sample outlet #1 the theoretically-predicted resolution is systematically less than the measured resolution for the entire size range. For all three outlets the fitted value of δ' is notably different from zero. Theoretically, the modeled resolution is independent of the sign of δ. Note that the confidence intervals for the fitted parameters for outlet #1 are especially large due to the reduced sample size for this data set. As in Figure 3.3a, the fitted values of f_G for outlets #2 and #3 are significantly greater than one. For the fits shown in both figures, the value of f_G increases the closer the outlet is to the inlet. The fitted values of $\mathcal{R}_{nd}$ are within 1% or less of the corresponding predicted values, well within the range defined by the uncertainty of the flows, also in both cases.

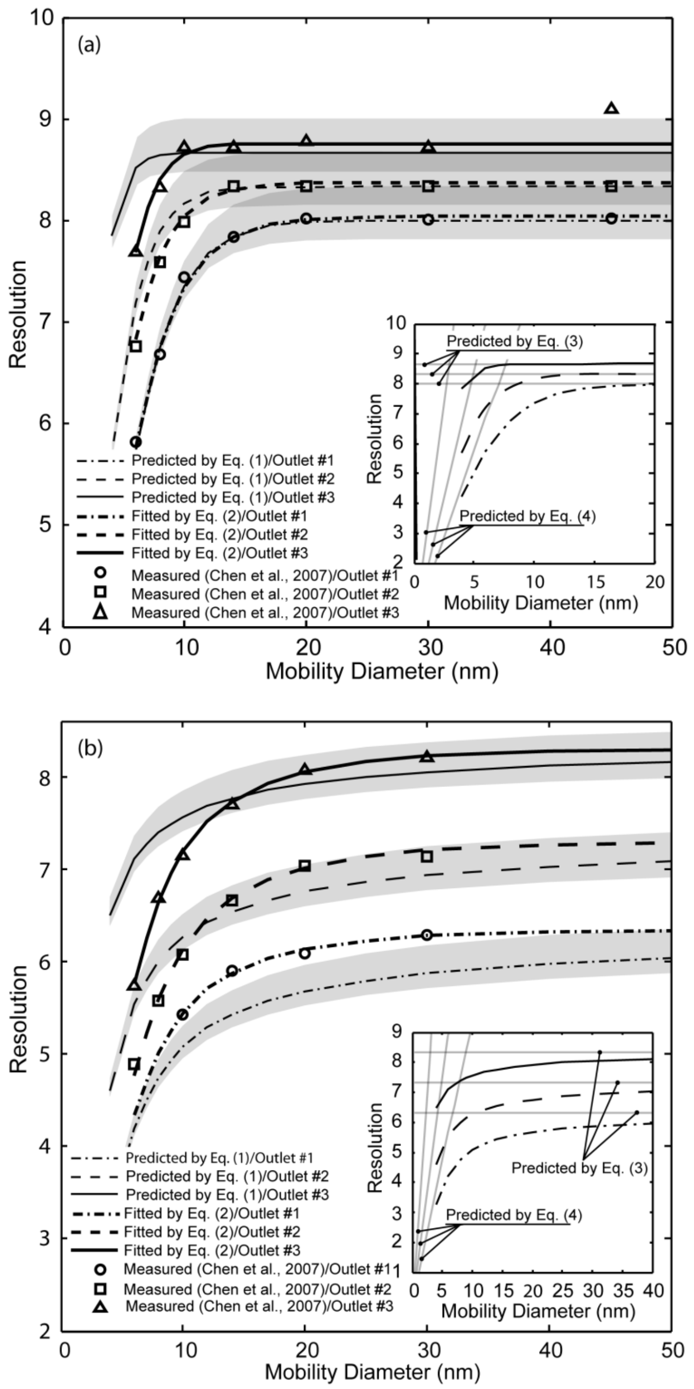

Figure 3.3: Comparison between predicted (curves) and measured (symbols) resolutions for outlets 1 (dashed-dot), 2 (dashed), and 3 (solid) of the 3-MO-DMA. The flow rates through the DMA are (a) $Q_{sh} = 20$ lpm, $Q_a = 2.4$ lpm, $Q_{s1} = Q_{s2} = Q_{s3} = 0.8$ lpm (i.e., unbalanced flows), and (b) $\mathrm{Q_{sh}} = 20$ lpm, $\mathrm{Q_a} = 2.4$ lpm, $Q_{s1} = Q_{s2} = Q_{s3} = 2.4$ lpm (i.e., balanced flows). Normal curves correspond to the numerical predictions when using the nominal flows, and the shaded area when assuming a ±2% variation, respectively. Bold curves correspond to the model (Equation 3.2) fitted to the measurements. Inset: Predictions using the numerical (black line, Equation 3.1), the non-diffusing limit (grey horizontal line, Equation 3.3), and the diffusing limit (grey sloped line, Equation 3.4) resolutions. (Eq. (1) is Eq. 3.1 and Eq. (2) is Eq. 3.2)

Figure 3.4 shows the comparison between predicted and measured resolutions for all three monodisperse-particle outlets of the DMA when the sheath flow rate is set to 36 lpm. Figures 3.4a and 3.4b show the predicted and the measured resolutions in the case of unbalanced and balanced flow conditions, respectively. When the DMA is operated under unbalanced flows (i.e., $Q_a = 4.5\ \text{lpm}$ and $Q_{s1} = Q_{s2} = Q_{s3} = 1.5\ \text{lpm}$), the experimental and the theoretically-predicted resolutions of all three outlets are in agreement, within experimental uncertainty, for particles having mobility diameters larger than ca. 14 nm. More specifically, for sample outlet #3 the measured resolution for almost the entire size range is between the two limiting predicted curves that correspond to a ±2% change in the flow rates. For sample outlets #2 and #1 that happens only for particles larger than ca. 14 nm, and for smaller particles the measured resolution drops faster than the predicted. The nominal value of δ for all three outlets is -0.5, but, surprisingly, the fitted values of δ for all three are essentially zero. Contrary to the plots in Figures 3.3a and 3.3b, the value of f_G decreases the closer the outlet is to the inlet. Some of the fits here also show greater deviations from the predicted values of $\mathcal{R}_{nd}$ than in Figure 3.3.

Figure 3.4b shows the comparison between predicted and measured resolutions for monodisperse-particle outlets #2 and #3 of the DMA (experimental data for outlet #1 are not available) when the sheath flow is set to 36 lpm, and the aerosol and sample flows are balanced (i.e., $Q_a = 1.5\ \text{lpm}$ and $Q_{s1} = Q_{s2} = Q_{s3} = 1.5\ \text{lpm}$). Under these operating conditions the experimental measurements deviate substantially from the numerically predicted resolutions. This deviation increases from 10.8 to 16.6% for outlet #3, and from 1.0 to 34.7% for outlet #2 when particle size increases from 6 to 45 nm. The reduction of the measured $\mathcal{R}_{nd}$ values from the theoretically predicted

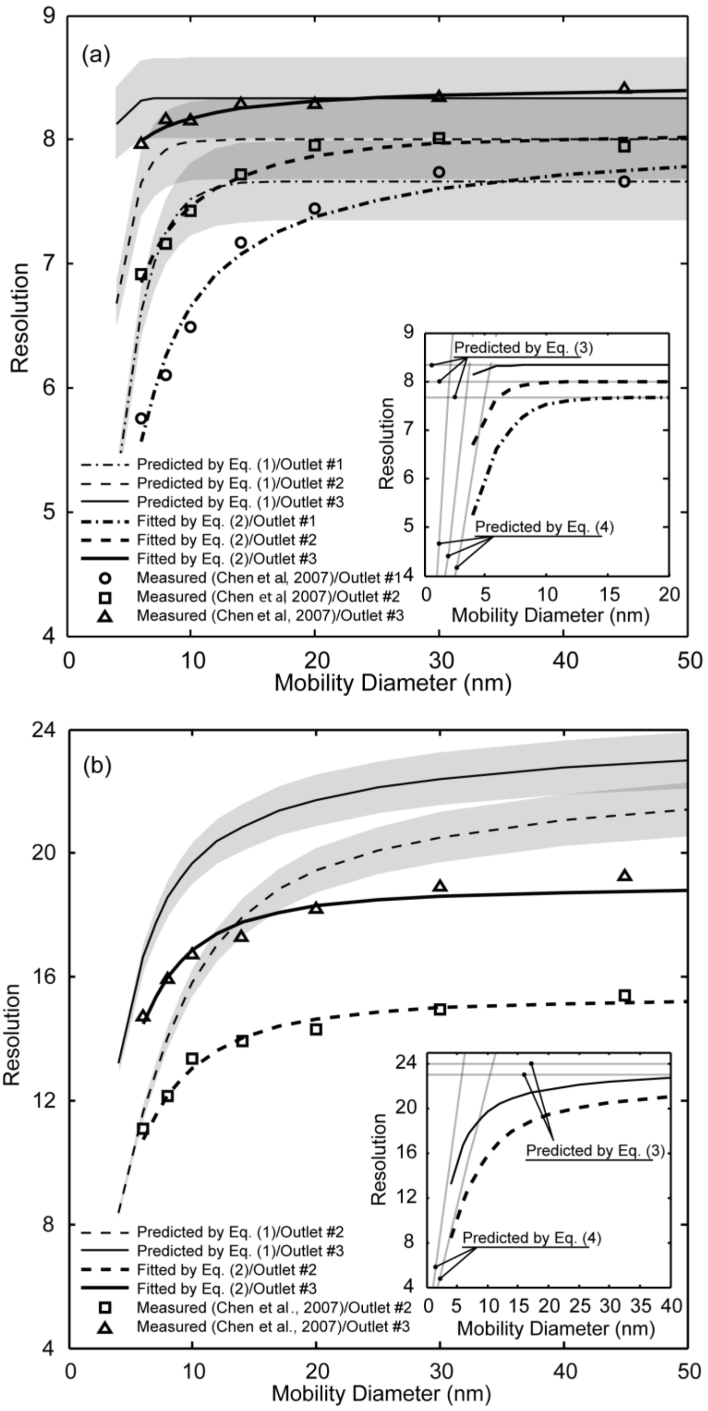

Figure 3.4: Comparison between predicted (curves) and measured (symbols) resolution for outlets 1 (dashed-dot), 2 (dashed), and 3 (solid) of the 3-MO-DMA. The flow rates through the DMA are (a) $Q_{sh} = 36$ lpm, $Q_a = 4.5$ lpm, $Q_{s1} = Q_{s2} = Q_{s3} = 1.5$ lpm (i.e., unbalanced flows), and (b) $Q_{sh} = 36$ lpm, $Q_a = 1.5$ lpm, $Q_{s1} = Q_{s2} = Q_{s3} = 1.5$ lpm (i.e., balanced flows). Normal curves correspond to the numerical predictions when using the nominal flows, and the shaded area when assuming a ±2% variation, respectively. Bold curves correspond to the model (Equation 3.2) fitted to the measurements. Inset: Predictions using the numerical (black line, Equation 3.1), the non-diffusing limit (grey horizontal line, Equation 3.3), and the diffusing limit (grey sloped line, Equation 3.4) resolutions. (Eq. (1) is Eq. 3.1 and Eq. (2) is Eq. 3.2).

ones is substantially beyond that which might be accounted for by uncertainties in flows. This can only be due to some sort of flow disturbance in the DMA. Though the model of Equation 3.2 using $\sigma_{mix_i}^2 > 0$ with $\beta_i' = \beta_i$ was used to fit the measurements, the uncertainty of the fitted parameters was so large as to render the fitted values meaningless.

Figure 3.5 compares the predicted and the measured resolution for sample outlets #1 and #2 when the DMA is operated at $Q_{sh} = 50$ lpm, $Q_a = 4.5$ lpm, and $Q_{s1} = Q_{s2} = Q_{s3} = 1.5$ lpm. The discrepancy between measured and numerically-predicted values is high, with the measured resolution being less than the predicted in all cases. The difference increases from 30.9 to 38.5% for outlet #1, and decreases from 21.8 to 1.8% for outlet #2 when particle size increases from 6 to 45 nm. For outlet #2, the gradual approach of the resolution to the non-diffusing limit as diameter increases cannot be fit with the model given in Equation 3.2 while the resolution for outlet #1 is clearly limited by flow mixing.

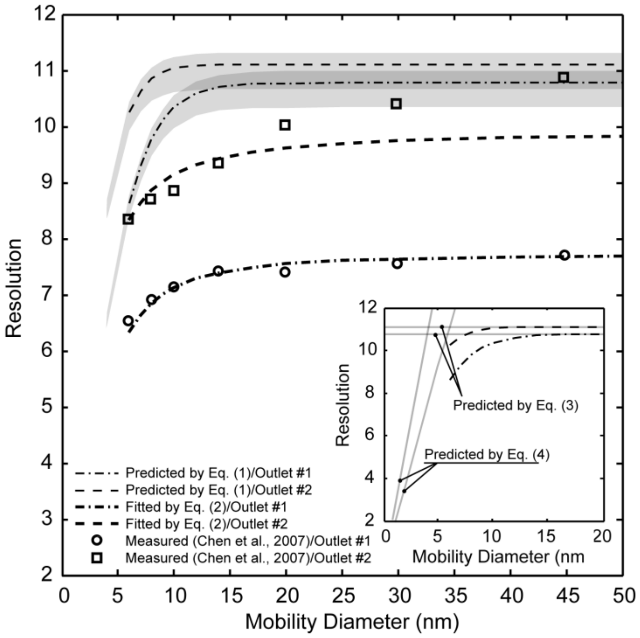

Figure 3.5: Comparison between predicted (curves) and measured (symbols) resolution for outlets 1 (dashed-dot), and 2 (dashed) of the 3-MO-DMA. The flow rates through the DMA are $\boldsymbol{Q_{sh} = 50\ \mathrm{lpm}}$, $\boldsymbol{Q_a = 4.5\ \mathrm{lpm}}$, $\boldsymbol{Q_{s1} = Q_{s2} = Q_{s3} = 1.5\ \mathrm{lpm}}$ (i.e., unbalanced flows). Normal curves correspond to the numerical predictions when using the nominal flows, and the shaded area when assuming a ±2% variation, respectively. Bold curves correspond to the model (Equation 3.2) fitted to the measurements. Inset: Predictions using the numerical (black line, Equation 3.1), the non-diffusing limit (grey horizontal line, Equation 3.3), and the diffusing limit (grey sloped line, Equation 3.4) resolutions. (Eq. (1) is Eq. 3.1 and Eq. (2) is Eq. 3.2).

3.5 Discussion

Consider, first, the transfer functions in Figure 3.2. Though the fit is quite good in Figure 3.2a ($\delta \neq 0$) with only a slight increase in spread, the fit in Figure 3.2b ($\delta = 0$) is only fair with a significant increase in spread and a distinct problem at the peak of the transfer function. As noted in both the predicted and modeled curves, any amount of diffusion should quickly round the apex of the familiar triangular non-diffusing transfer function. This is also true of any disturbance ($\sigma_{mix}^2 > 0$) in the flows of the DMA. It is therefore puzzling to see such a prominent peak on the measured transfer function. This could in part be an artifact of the fitted piecewise-linear spline which has a node right at the centroid. Such a spline will inherently have difficulty tracking any sharp bend in the transfer function. In such a situation, the spline nodes will tend to be on the outside of the bend as is the case here. The extension of the node above the anticipated rounded peak of the model, however, is greater than expected, even with the addition of a bit of measurement uncertainty. The slight flaring of the base of the measured transfer function from a strictly triangular shape would tend to confirm the effect of a small amount of diffusion not evident in the peak. An explanation for this seeming contradiction is not forthcoming.

The shape of the non-diffusing transfer function can have a marked effect on the resolution as a function of particle diameter. Consider the sharpness of the bend between the theoretically-predicted non-diffusing and diffusing limits of the resolution shown in Figures 3.3a and 3.3b. For $|\delta| = 0.5$ as in Figure 3.3a the bend is quite sharp while for $|\delta| = 0$ as in Figure 3.3b the bend is much gentler. This can be readily explained as follows. The effect of diffusion as diameter decreases can be thought of as running a Gaussian average of ever-increasing width over the span of the transfer function. Given the piece-wise linear nature of the theoretical transfer function, for an initially narrow averaging window, there is no effect on the bulk of the linear sections but the corners are rounded. This initial rounding is restricted to the regions immediately adjacent to the corners and does not reach to the center of the linear pieces of the transfer function. For a trapezoidal transfer function (i.e., $|\delta| > 0$), this means that neither the height nor the FWHM is affected for small amounts of diffusion. Thus, the resolution is maintained at the value of $\mathcal{R}_{nd}$ even with a significant degree of diffusion. Even when the averaging effect reaches the midpoints of the sides of the trapezoid, the effects from the upper and lower corners will actually cancel each other out. It is only when the averaging window gets wide enough, such that it reaches the midpoint of the top of the trapezoid, that the effects of the upper corners add together to lower the peak of the transfer function, thus increasing the FWHM value and lowering the resolution. For a triangular transfer function (i.e.,

$|\delta| = 0$), the peak of the transfer function begins to be rounded even with the smallest amount of diffusion, thereby decreasing the height of the transfer function and the resolution. As a result, the behavior of the mid-range of the resolution curve is quite sensitive to the value of $|\delta|$.

In Figure 3.3b, the fits of the model to the resolution data required consistent values of $|\delta'|$ notably greater than the nominal value $|\delta| = 0$. This can be explained by possible flow mismatches between the aerosol inlet and outlet. The control and measurement of the DMA outlet #3 flow may have lead to a mismatch between Q_a and Q_{s3}, that is much higher compared to those corresponding to the other two aerosol outlets as indicated by the sharper slope in the measurements. This potential mismatch in these flows may have lead to a value of δ different from zero. The seeming difference between the fitted values of $\delta' \cong -0.4$ (note that the higher value of δ' for outlet #3 has a much wider confidence interval) and a nominal value of $\delta = -0.5$ would tend to confirm this mismatch in flows. Since this offset in δ' from δ is in the positive direction, this suggests that the flow through the aerosol outlet was greater than that reported.

In Figure 3.3, both plots show the same increasing trend of the fitted values of f_G as the aerosol outlet gets nearer the aerosol inlet. This discrepancy between theory and measurements seems most likely to be due to a problem with the theory. One of the weaknesses of the theory is the estimate of G_{radial}, a geometric- and flow-dependent factor associated with the radial velocity of a particle in the DMA. The expression used in Section 2.3.2.3 (cf. Giamarelou et al., 2012) to calculate G_{radial} does not capture the effects of radial flows in the vicinity of the aerosol inlet and outlet slits, as concluded from sensitivity tests (not shown here). This was justified by a rough calculation of the effect while the particle passes through the region near an outlet slit while transiting to an outlet slit further downstream. Also in this calculation, $L_i \gg R_2 - R_1$ such that the contribution to G_{total} due to the axial component of particle velocity was far greater than that of the radial component. The component of G_{radial} that is neglected is probably due to the accelerating flow velocity in the converging flow as the particles approach the outlet slit that it will exit. The flow velocities in that region are generally much higher than those in the diverging flow from the aerosol inlet slit because the outlet slits are usually much narrower than the inlet slit. It is also very important to match the inlet aerosol flow velocity with the sheath flow to avoid flow disturbances. The higher the particle velocity the greater the contribution to the estimate of G, so the neglected contribution to G at the outlet slit should be greater than that at the inlet slit. A very crude estimate of the former contribution indicates that it can more than double the value of G_{radial}, but, even for $L_i \cong 5 \cdot (R_2 - R_1)$, corresponding to the aerosol outlet nearest to the inlet where the radial velocities relative to the axial velocities are the greatest, the relative contribution of G_{radial} to G_{total} is still quite small. Thus, it is difficult to see how this effect could account for fitted f_G values as high as 5.

In Figure 3.4a, the fits of the model to the measurements look good though not quite as good as those in Figure 3.3. For all the outlets, the fitted values of δ' are essentially zero as compared to their nominal value of -0.5. The offsets here are greater than those observed in Figure 3.3, but also positive. The fitted values for f_G nominally show the opposite trend with outlet distance from the inlet. However, the value $f_G = 1$ is within the confidence intervals for both outlets #1 and #2. For outlet #3, given the lack of data near the diffusing limit for the resolution, it is surprising that the confidence interval for f_G should be so small, even smaller than that of the other outlets. Potential problems associated with the fitting process do not necessarily contradict the possibility for $f_G = 1$ for all the outlets. This would be in contrast to the trend found in the fits of Figure 3.3, but it can be explained by the higher sheath flow which can increase G_{axial} relative to G_{radial} such that any error in the latter could become negligible relative to G_{total}. Finally, upon closer inspection, one can observe a high degree of correlation between the residuals of the measurements about the respective curves of the fitted models for outlets #1 and #2 in Figure 3.4a. This would suggest that these residuals are not due to random errors in the measurements but rather an inadequacy in the theory. There is nothing obvious in the model that could be modified to accommodate this phenomenon.

For Figures 3.4b and 3.5, there is strong evidence of problems from disturbances in the flow. Though Figures 3.4a and 3.4b both use a sheath flow of 36 lpm, the difference in the aerosol inlet flows may account for the presence of flow disturbances for the conditions in the measurements shown in Figure 3.4b while not for those in Figure 3.4a. Most DMAs are designed to minimize the chance of flow disturbances at the confluence of the aerosol inlet and sheath flows for a flow ratio of 1/10. This flow ratio is much closer to that corresponding to the conditions of the measurements shown in Figure 3.4a (0.125) than for those in Figure 3.4b (0.042). As a result, there may be flow disturbances at this confluence in the latter case while not in the former. For outlet #2 in Figure 3.5, the measurements show a clear trend to approach the theoretical resolution in the non-diffusing limit. This is very different from the observed behavior of the measurements at outlet #1, where the measured resolution appears to plateau in the non-diffusing limit at values well below of those of the predicted resolution. Although this difference is odd, it is possible that it is a consequence of some complexity of the flow mixing that the crude model used in Equation 3.2 cannot mimic.

3.6. Conclusions

The performance of the MMO-DMA transfer function model provided by in Chapter 2 (cf. Giamarelou et al., 2012) was shown to be in good agreement with measurements using the 3-MO-DMA designed and tested by Chen et al. (2007) when operated with low flow rates. The measured and calculated transfer functions were in good agreement when the sheath flow rate was 20 lpm. This was true both for balanced and unbalanced flow conditions, and assuming some measurement errors in the aerosol outlet flow associated with flow mismatches. This was the case only for the aerosol outlets furthest from the inlet. For outlets closer to the inlet, the predictions overestimate the measured resolutions, possibly due to an inadequacy of the theory. For higher sheath flows (i.e., 36 lpm and greater), the theoretical overestimation of the measured resolution for outlets closer to the inlet may essentially disappear but the chance of flow disturbances increases significantly, thereby reducing the resolution. At least for the 3-MO-DMA designed and tested by Chen et al. (2007), using low sheath flows to avoid flow disturbances are particularly important. As for the theory, it appears that additional work is needed to improve the accuracy for relatively short column lengths.

Chapter 4

4. Data Inversion of Tandem-DMA Aerosol Measurements: Inter-comparison of the TDMAfit and TDMAinv Data Inversion Algorithms

4.1 Abstract

Aerosol particles in the atmosphere are of significant importance because they can strongly affect human health and the climate of the Earth. The effects of the atmospheric aerosols depend on their concentration, size and chemical composition. The hygroscopic behavior of aerosol particles is a function of their size, composition and shape. Differential Mobility Analyzers (DMAs) are the most commonly used instruments measuring the size of aerosol particles. Tandem-DMA systems, i.e., two DMAs operated in series, are used for probing size-dependent properties of aerosol particles such as their hygroscopicity and volatility. To retrieve either size distributions when using a single DMA or the size-depended properties when using Tandem-DMA systems sophisticated inversion techniques are need. This chapter presents a short review of available inversion techniques, and compares the output of a slightly modified version of the TDMAfit inversion algorithm of Stolzenburg and McMurry (1988), with that of the TDMAinv inversion algorithm provide by Gysel et al. (2009). Both algorithms are based on the least-square fitting technique.

4.2 Introduction

4.2.1 Tandem-DMAs

The differential mobility analyzer (DMA) introduced by Hewitt (1957) has been used for measuring size of aerosol particles (e.g., Knutson, 1976; Hoppel, 1978; Alofs and Balakumar, 1982; ten Brink et al., 1983). When DMAs are combined with detectors (aerosol electrometers or CPCs), they can record the size distribution of the particles in a scanning or stepping mode. The DMA has been widely applied in a variety of aerosol measurement applications including the generation of monodisperse aerosol standards for instrument calibration (Liu and Pui, 1974; Hoppel, 1978; Knutson, 1976; Fissan et al., 1983; Scheibel and Porstendorfer, 1983; ten Brink et al., 1983; Kousaka et al., 1985).

TDMA measurements have been used for studying the hygroscopic properties of aerosols (Liu et al., 1978), heterogeneous reactions involving aerosol droplets (e.g., McMurry et al., 1983) and the evaporation rates of organic aerosols (Rader et al., 1987). Rader and McMurry (1986) demonstrated that the TDMA technique is extremely sensitive, as they measured diameter changes with a precision of ca. 0.3%, thus these systems can provide very precise measurements of the growth or shrinking of the particles. Also, TDMA systems have been used to measure the transfer functions of different DMAs. Moreover, Kousaka et al. (1985) confirmed that for ultrafine particles diffusion within the DMAs leads to major discrepancies between the TDMA measurements and theoretical predictions of size distributions based on the theory of Knutson and Whitby (1975).

A TDMA system typically consists of four components (cf. Figure 4.1):

a. a first DMA (DMA-1) for selecting particles within a very narrow range,

b. an aerosol conditioner,

c. a second DMA (DMA-2) for measuring DMA changes in the size of the monodisperse particles, and
d. a particle counter, e.g., condensation particle counter (CPC), aerosol electrometer (AE), optical particle counter (OPC).

Monodisperse aerosol particles generated by DMA-1 undergo a size change in the aerosol conditioner before entering DMA-2. Size changes occur, for example, as a result of particle condensation, evaporation of gaseous species onto/from the particles, which in many cases can be induced by heterogeneous chemical reactions allowed to occur in the conditioner. Consequently, DMA-2 is used to measure the resulted changes in particle size.

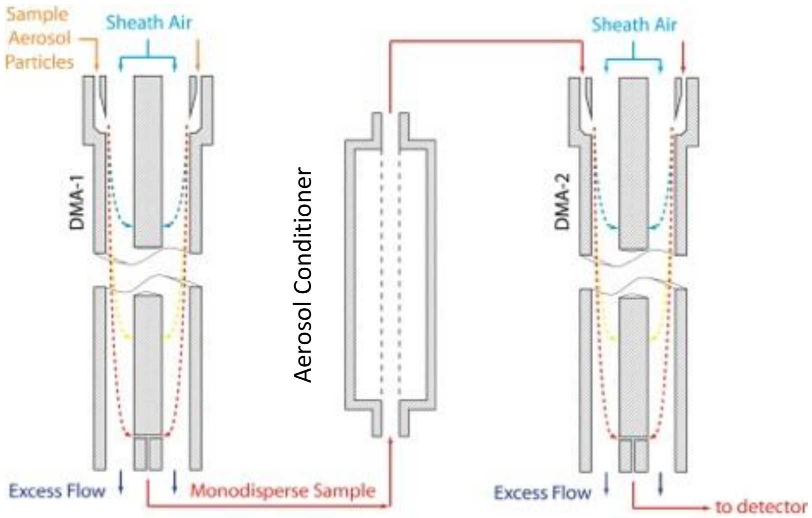

Figure 4. 1: Schematic diagram of a Tandem DMA.

4.2.2 Instrument Response

4.2.2.1 DMA Response

The concentration and the size distribution of the aerosol particles exiting the DMA depend on both operating characteristics of the DMA, and on characteristics of the aerosol sample. Since the pioneering work of Knutson (1976), the performance of the DMA can be fully characterized by its transfer function, i.e., the probability that an aerosol particle that enters at the inlet slit will exit via the sampling slit. For quite some time expression of the transfer function have been developed/used without considering diffusivity. Stolzenburg (1988) extended this analysis for the case of diffusing particles.

The size distribution of aerosol exiting the DMA depends both on the operating characteristics of the DMA and on the characteristics of the aerosol entering the DMA. Thus, the response of the DMA, i.e., the signal of the particle counter, depends on DMA's transfer function, on the size distribution of the classified aerosol, and on the efficiency of the counter. The derivation of the DMA response is described briefly.

The diameter and charge distribution of the classified aerosol is defined as (Stolzenburg 1988): $n(d_p, n_p)\mathrm{d}d_p \equiv$ number of particles per unit volume entering the classifier carrying n_p number of charges and diameter in the range d_p and $d_p + \mathrm{d}d_p$. For convenience, it can be reformed to mobility distribution as: $\hat{n}(Z_p)\mathrm{d}Z_p \equiv$ number of particles per unit volume entering the classifier with electrical mobility in the range Z_p and $Z_p + \mathrm{d}Z_p$.

In combination with the DMA transfer function, Ω, (e.g., Stolzenburg,1988; cf. Equation 2.69) the mobility distribution exiting a DMA is given by the relation:

$$\frac{Q_a}{Q_s}\Omega(\tilde{Z}_p)\,\hat{n}(Z_p)\mathrm{d}Z_p, \tag{4.1}$$

where $\tilde{Z}_p$ is the dimensionless electrical mobility (cf. Equations 2.25-2.26) and the flow ratio $\frac{Q_a}{Q_s}$ adjusts for the possibility of unequal aerosol flows. Moreover, $\hat{n}(\tilde{Z}_p)$ can be reduced to a size distribution function multiplied by various size dependent factors characterizing the aerosol system upstream of the classifier, e.g., fraction of charged particles, their transport efficiency, etc..

In most cases $\Omega(\tilde{Z}_p)$ is a much narrower function than $\frac{Q_a}{Q_s}\,\hat{n}(\tilde{Z}_p)$. As a result the behavior of the DMA output distribution is dominated by characteristics of the classifier transfer function. Thus, effects of the shape of the input distribution on the output distribution can be treated as perturbations of this basic behavior. For example, if one considers the base case of a flat input distribution, i.e., $\frac{Q_a}{Q_s}\,\hat{n}(\tilde{Z}_p) = \frac{Q_a}{Q_s}\,\hat{n}(\text{constant})$, then the output distribution, i.e., $\frac{Q_a}{Q_s}\Omega(\tilde{Z}_p)\,\hat{n}(Z_p)$ is a scaled form of the transfer function.

The response function (i.e., the function for predicting the measured signal from the instrument can be defined as:

$R(d_p, n_p)$ ≡ response of receiving particle counter per unit concentration of particles having charge n_p and diameter d_p.

What is typically measured by a system including a DMA and a particle counter (cf. Figure 4.2) is the integrated response given by (Stolzenburg 1988):

$$I(V) \equiv \sum_{n_p>0} \int_0^\infty R(d_p, n_p)\,\frac{Q_a}{Q_s}\Omega(\tilde{Z}_p, n_p, V)\,n(d_p, n_p)\mathrm{d}d_p\ . \tag{4.2}$$

Here, $I(V)$ denote the response of the sensor as a function of the rod voltage. When a CPC is used as a detector the response has units of cm^{-3}, while for a electrometer sensor gives a response in amperes. For CPC, the response induced by a single particle is independent of the number of charges it carries, while for the electrometer the response is weighted more heavily towards the multiply charged particles.

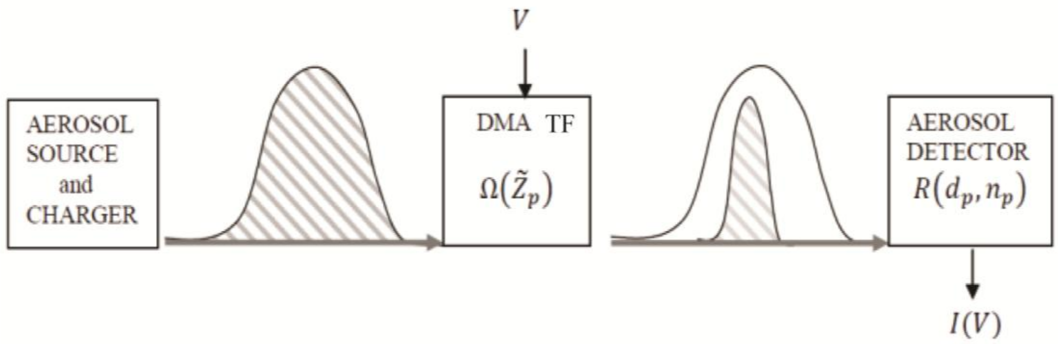

Figure 4.2: DMA Measurement System.

4.2.2.2 TDMA Response

Initially, a polydisperse aerosol is introduced in the first DMA (DMA-1) of the TDMA system (cf. Figures 4.1 and 4.3), which is characterized by its mobility distribution, $\hat{n}(Z_{p1})$. DMA-1 selects aerosol particles in a narrow quasi-monodisperse size interval, about the centroid mobility Z_{p1}^* according to the transfer function $\Omega_1(Z_{p1}, V_1)$. The size-selected particles are subsequently conditioned in an aerosol conditioner (e.g., in a humidifier or heated tube), before entering the second DMA (DMA-2). The new size distribution of the conditioned particles is determined by DMA-2 and a particle counter.

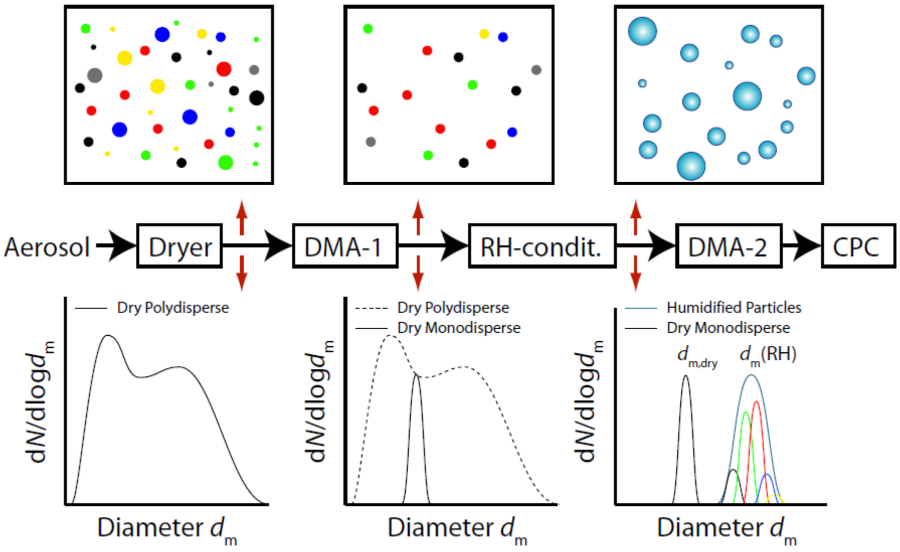

Figure 4.3: Tandem Differential Mobility Analyzer (TDMA) operation (Adapted with modifications from Gysel (2003)).

Consequently, the signal produced by the TDMA system is the integrated responses of the aerosol detector as a function of operating conditions (i.e., principally the voltage as long as the flows are fixed), i.e.,

$$I(V_1, V_2) \equiv \int_0^\infty R(Z_{p2}) \frac{Q_{a2}}{Q_{s2}} \Omega_2(Z_{p2}, V_2) P(Z_{p1}) \frac{Q_{a1}}{Q_{s1}} \Omega_1(Z_{p1}, V_1) \hat{n}(Z_{p1}) dZ_{p1}. \quad (4.3)$$

Here, $Z_{p2} = f_c(Z_{p1})$, is the transformed particle mobility at DMA-2, $R(Z_{p2})$ is the particle counter response function, $\Omega_2(Z_{p2}, V_2)$ is the DMA-2 transfer function and $P(Z_{p1})$ is the penetration efficiency of the aerosol conditioner.

4.2.3 Application of Data Inversion Techniques in Aerosol Metrology

Physical theories allow us to make predictions so that with a complete description of a physical system to be able to predict the observations. Predicting the result of measurements is called the modeling, or the forward problem. The inverse problem is finding an unknown property of an object from actual observations (measurements) of this object (Ramm, 2005; Tarantola, 2005).

For aerosol size spectrometers, their response, i.e., the measured size distribution, depends on the real size distribution and on the instrument kernel function (cf. Equation 4.3). The data inversion problem then is to determine which particle size distribution can cause a given measured response in an instrument the linear response curve of which is known. In general, a finite number of instrument responses can be obtained, so that the problem can be declared as (Crump and Seinfeld, 1981): find the size distribution f such that:

$$L_i f = y_i, \quad i = 1,2, \dots, n, \quad (4.4)$$

where f is the unknown size distribution, y_i the i^{th} datum, and L_i the i^{th} instrument response linear functional. The problem defined by Equation 4.4 is well posed if it is uniquely solvable for every y and the solution f varies continuously with the data y.

A well-posed problem is characterized by the following three conditions (Crump and Seinfeld, 1981):

a) For every y there is a solution f.

b) The solution f is unique.

c) The solution f is stable.

If one of the conditions fail then the problem is called ill-posed.

In the case of aerosol size distribution measurements with a mobility analyzer the general inversion problem (Equation 4.4) can be written as:

$$y_i = \int_a^b K_i(x) f(x) dx + \varepsilon_i, \quad i = 1,2,\ldots,N \tag{4.5}$$

where y_i are the discrete measurements points, $f(x)$ the unknown size distribution function, x is a size parameter, K_i is the kernel function of the ith instrument channel (i.e., the instrument response), a and b are the size limits within which the size distribution is measured, and ε_i is the instrument error in that channel.

A problem to be taken into account in determining the size distribution measurements is that in most applications in aerosol science, the system of equations in Equation 4.5 is underdetermined with the number of measurements being less than the number of unknowns. This means that, even in the absence of measurement error, there is no unique solution, or in other words, many solutions satisfy the same set of measurements. In order to select one among a multitude of solutions, additional information has to be used. This is done in the form of *a priori* constraints on the solution. To some extent, these constraints are arbitrarily imposed, and hence care should be taken to ensure that the constraints are physically justifiable.

A selection of techniques that seek solution to the ill-posed problem of retrieving the size distribution measurements in different ways and with different levels of success have been proposed. These techniques methods include:

(a) linear approaches
    i) least-squares solutions,
    ii) regularization,
    iii) decomposition techniques
(b) non-linear approaches
    i) gradient search methods,
    ii) extreme value estimation,
    iii) Bayesian methods.

Each of these techniques has certain deficiencies, and indeed, it is doubtful that any method can fulfill the ideal of perfect reconstruction of a size distribution from a limited set of data. A list of inversion methods used in aerosol size measurements is shown in Table 4.1. These methods can in principle be used to invert the signals from any kind of spectrometers (e.g., electrical mobility, light scattering, cascade filter samples, etc.).

Knutson (1976) published the first method for inverting the data from counters coupled with a DMA (and a bipolar charger) to obtain aerosol size spectra. The Knutson method required various approximations and assumptions, which were not numerically justified. However, the Knutson inversion technique is extremely simple, in that it yields a system of linear equations that may be solved recursively.

The second inversion algorithm developed for the Electrical Mobility Analyzer (EMA) was provided by Hoppel (1978) (EMA is a Mobility Analyzer operated at a step mode, while its successor Scanning Mobility Particle Sizer (SMPS) is operated in a scan-mode). This algorithm consists of a successive approximations, of the size distributions, with the first obtained by neglecting the multiply charged particles. The first approximation is then used to estimate the number of multiply charged particles, and thus obtain a second approximation. The process is repeated until it converges. Hoppel (1978) provided only a few numerical examples of the accuracy of his technique.

A third inversion technique was proposed by Haaf (1980). It employs a trial and error procedure in which the response of EMS (and other familiar spectrometers) is calculated for an assumed size distribution, and compared to the actual measured response. The assumed size distribution is then adjusted until the difference between the actual response and the computed response is minimum. The inversion method proposed by Haaf is much more complicated than those of Knutson and Hoppel. Twomey (1975) applied a similar iterative procedure to invert filter transmission measurements to aerosol size distributions.

Crump and Seinfeld (1981) used the GCV method for aerosol inversion problems. Later, Yee (1989) used Tikhonov regularization to reconstruct size distributions from noisy diffusion battery measurements. Ramachandran and Kandlikar (1996) used the Zeroth-order regularization approach for handling Personal Cascade Impactor data. Also, Lloyd et al. (1997) used the L-curve method for analyzing diffusion battery data.

Table 4.1: Inversion Techniques for determining aerosol particle size spectra.

Inversion Technique	References	Constraints /a priori Information	Comments
I. Linear methods			
1. Least-squares		None	Very unstable in presence of measurement error
2. Constrained least-squares	Phillips (1962)	Second difference	Solution could take on negative values
	Twomey (1963) Twomey (1977a) Rizzi et al. (1982)	first difference or deviation from trial solution is minimized	
3. Tikhonov regularisation	Tikhonov and Arsenin (1977) Hansen (1992) Hansen and O'Leary (1993)		
a.	Crump and Seinfeld (1981)	Norm of second derivative minimized	
b.	Yee (1989)	Shannon - Jaynes entropy maximized	Intrinsically positive solution
c.	Lesnic et al. (1995)	Norm of first derivative minimized; positivity of solution	
d. Selection of λ	Wahba (1977) Golub et al. (1979) Crump and Seinfeld (1982)	Minimize the generalized cross validation (GCV) function	GCV function can have a flat minimum and can be difficult to locate
e.	Ramachandran et al. (1996)	Discrepancy principle	Computationally simple, but can oversmooth solution
f.	Hansen (1992) Hansen and O'Leary (1993) Lloyd et al. (1997)	L-curve method	Reliable but computationally intensive

Table 4.1: (continued)

Inversion Technique	References	Constraints /a priori Information	Comments
4. Synthesis of basis functions			
a. Eigenvalue decomposition	Twomey (1963) Twomey (1975) Capps et al. (1982)	Disregard of replace problematic eigenvalues using filters	Measurements chosen to remove singularity
b.	Curry (1989)	Smoothness constraint	
c. Second derivative expressed as sum of orthogonal functions	Ramachandran and Leith (1992)	Norm of second derivative minimized	
			Intrinsically positive solution
II. Non-linear methods			
1. Chahine method	Chahine (1968) Grassl (1971) Santer and Herman (1983) Ferri et al. (1989)	Initial guess solution is positive	Final solution always positive. High - frequency oscillations or choppiness in solution
2. a. Twomey's method	Twomey (1975) Hitzenberger and Rizzi (1986)	Initial guess solution is positive	
b.	Markowski (1987) Roth and Filippov (1996)	Initial guess solution is positive. Smoothness constraint	
c.	Winklmayr et al. (1990)	Use smoothed kernel fuctions	
III. Extreme value estimation	Paatero (1991)		

4.2.4 Inversion of Tandem DMA Measurements

The measurement signal of a TDMA, i.e., the measurement distribution function (MDF), is the particle concentration at the outlet of DMA-2 which depends on the size distribution of the polydisperse aerosol, its charging state, the transfer function of DMA-1, the conversion function of the aerosol conditioner, and the transfer function of DMA-2. As the MDF is only a skewed and smoothed integral transform of the particle's actual growth/shrinkage factor probability density function (G/SF-PDF), an inversion algorithm has to be applied to the MDF of TDMA measurements to retrieve the G/SF-PDF.

TDMA data analysis seeks to: (a) determine the mean size-change of the sample, (b) provide the number fractions of particles in different G/SF ranges and (c) retrieve the correct shape of the G/SF-PDF in detail. The simplest method is to use the MDF without any data inversion to determine the standard deviation and the modal diameter of the G/SF-PDF, (e.g., Liu et al., 1978; Weingartner et al., 2002). However, this method does not accomplish any of the goals determined above, except for samples exhibiting unimodal growth with narrow G/SF-PDF, where the MDF can be used to determine the mean G/SF. Another method is to invert for the smearing and skewing effect of the second DMA only, in order to recover the recorded particle size distribution after the particle conditioning (e.g., Cocker et al., 2001; Stratmann et al., 1997; Voutilainen et al., 2000). This approach fulfils all set goals because the particle size distribution after treatment resembles the G/SF-PDF except for some smoothing caused by the finite width of the size range of the particles selected with the first DMA. Finally, a third group of methods seeks to recover the actual G/SF-PDF by inversion of the MDF using a complete TDMA forward function (e.g., Cubison et al., 2005; Stolzenburg and McMurry, 1988). This last group of methods fulfills all the goals set for the TDMA analysis, within the limitations set by the measurement uncertainties and inversion algorithm itself.

The TDMAfit (Stolzenburg and McMurry, 1988) is the most widely used inversion algorithm. It uses multiple Gaussian distributions to fit the G/SF-PDF, whereas the mean G/SF, standard deviation and number fraction in each Gaussian mode are varied until the observed MDF is reproduced by the retrieved G/SF distribution. However, when fitting multiple modes with largely overlapping modes or shoulders the successful convergence may depend on the initial guess and may not be robust. This results to difficulties when analyzing automatically large data sets. Gysel et al. (2009) developed an alternative TDMA data inversion approach, which has successfully been tested and applied to large HTDMA data sets from laboratory and field studies (e.g., Allan et al., 2008; Gysel et al., 2007; Meyer et al., 2009; Sjogren et al., 2008). The algorithm is considered robust and applicable for automated data inversion.

4.3 Methodology

4.3.1 TDMAfit Algorithm

The typical TDMA data used as input to the TDMAfit algorithm consist of at least 5 pairs of values (N_2, V_2), where N_2 is the concentration downstream the DMA-2 and V_2 is the corresponding applied voltage at the DMA-2. V_2 values are selected suitably so that to reveal the distribution shape. If the distribution is bimodal then at least 10-12 points are needed. These data points produce a bell-shaped curve, with the maximum N_2 corresponding to a voltage related to the mean particle size entering DMA-2 (i.e., the voltage that corresponds to classifying the centroid diameter at DMA-2) (Rader and McMurry, 1986; Stolzenburg and McMurry, 1988; Stolzenburg, 1988). For the case of a bimodal distribution the suggested procedure initially fits the two peaks separately by trial and error, and these estimations are then used as initial guesses for the two-peak TDMA fit (Stolzenburg and McMurry, 1988).

The TDMAfit algorithm uses a least square fitting procedure to fit theoretical TDMA transfer functions to $N_2(V_2)$. The algorithm employed is adapted from the FORTAN program CURFIT in Bevington (1969), which is based on the gradient-expansion algorithm of Marquardt (1963). This algorithm combines the methods of gradient search and linearization of the fitting function. Three fitting parameters are used, namely, $f_N =$ the fraction of particles leaving DMA-1 that are detected in a given DMA-2 peak, $f_V =$ the mobility growth factor for a given DMA-2 peak and $f_\beta =$ the correction factor for the width of $N_2(V_2)$. The parameter f_β is unity if there is no spreading due to diffusion, inhomogeneities in aerosol chemical composition, or improper DMA performance (Stolzenburg and McMurry, 1988).

Here, a modified version of the TDMAfit algorithm of Stolzenburg and McMurry (1988) is presented (cf. Figure 4.4). The program is written at C and uses the least square fitting algorithm used to minimize chi-square adapted from the C program MPFIT (Markwardt, 2010), which uses the Levenberg-Marquardt technique (Marquardt, 1963) to solve the least-squares problem. The program takes as input the TDMA data produced with the second DMA operated at scanning mode. One assumption made to the algorithm is that if the total number concentration of the monodisperse aerosol distribution exiting DMA-1 is unknown (e.g., lack of a CPC downstream of DMA-1) it is approximated by the relation:

$$N_1 = N_2 \cdot \frac{Q_{excess\,(DMA-2)}}{Q_{aerosol\,(DMA-2)}}. \tag{4.6}$$

The modified algorithm uses as initial guess the data point with the maximum concentration without the users interference. A significant difference with the original TDMAfit algorithm is that for the case of bimodal distributions initially the first peak is fitted and then the algorithm uses, automatically, as initial guess for the second peak the next maxima. The input data set for the TDMAfit algorithm include: (a) the size distribution measurements, (b) the DMAs geometries and operation parameters, and (c) the execution parameters, e.g., if the data will be fitted with single-peak, two-peak or even three-peak Gaussian functions, if the zero concentration data points will be used or ignored, and, even interfere to automatically clean the noise of the samples by setting the concentration to zero, outside of a specific range of diameters. The preparation of the input data set manually is a difficult and time-consuming task, thus the input data set is prepared by a Python program (van Rossum and Drake, 2001). The TDMAfit output is processed with the use of two separate Python programs, one for the one-peak fit and one for the two-peak fit, respectively. The resolved data is then analyzed with a MatLab program to obtain the best result for each sample and moreover the corresponding graphs, if needed.

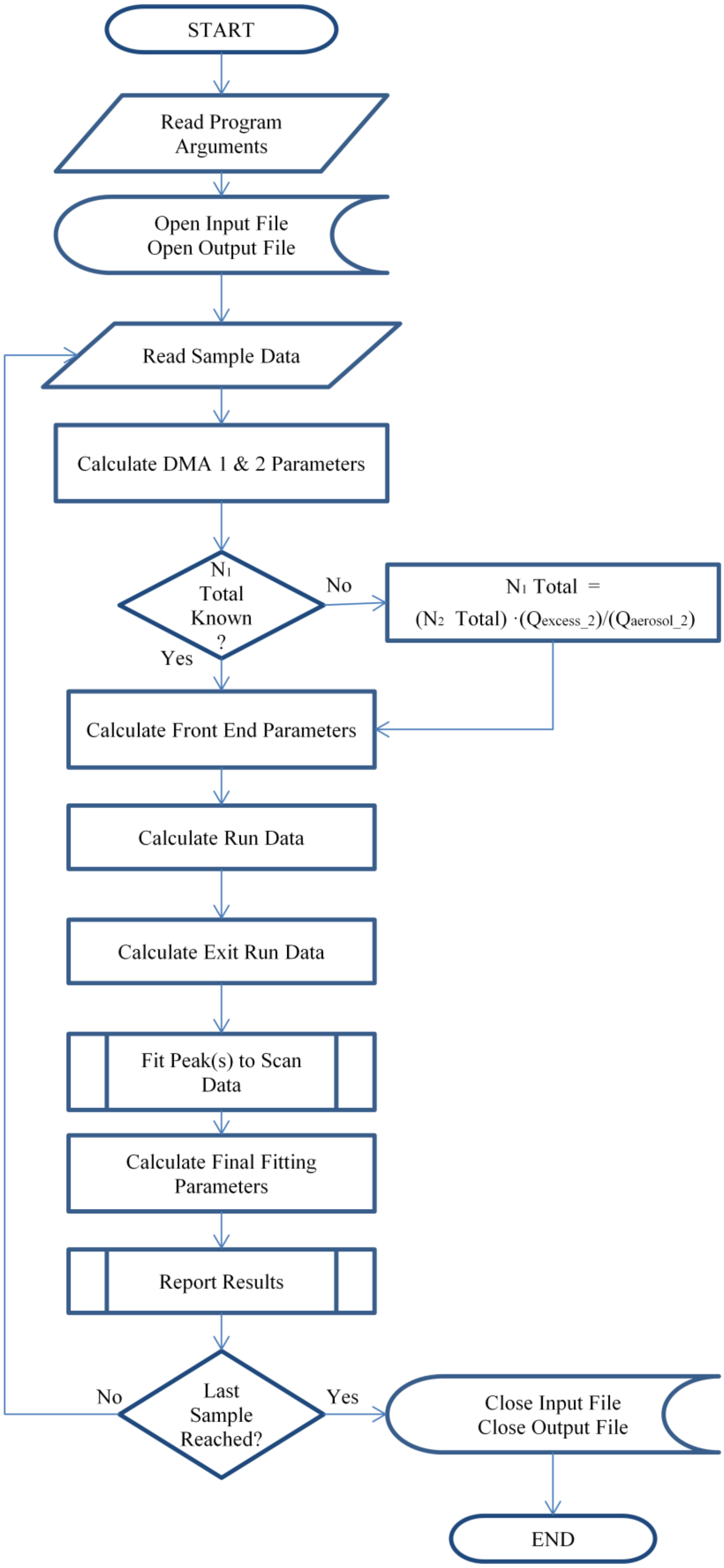

Figure 4.4: Flow diagram of the modified TDMAfit algorithm.

In order to test the program, I have used raw TDMA data from a field campaign in an urban environment (Athens, Greece) containing many samples with bimodal growth factor distributions. A selection of different cases from this campaign has been made, as a base to establish the selection criteria for the best TDMAfit result. As will be discussed later, for samples exhibiting unimodal growth factor distributions (i.e., single-peak distributions measured by DMA-2) with no noise and good count statistics, there is no need for such decision. Initially, I have analyzed the data to establish decision criteria that can determine whether the measured distributions are best fitted by either a unimodal or a bimodal distribution. This decision is based on the Root Mean Square (RMS) value of the fit. Once the decision for the best fit is made, the corresponding growth factor value or values is reported. The analysis is semi-automatic, with the user interfering with the program only to adjust the maximum meaningful growth factor value (i.e., based on literature data for the chemistry of the aerosol at similar conditions/environments) and/or the RMS acceptable range. The later depends on the amount of noise in the data, which depends on whether the TDMA data is initially treated or not before analyzed with the TDMAfit algorithm. It should be noted that mathematically the best fit corresponds to RMS ~ 1, whereas based on the data analysis presented below, a good fit may correspond to RMS values between 0.75 and 1.5.

Aerosol size distribution measurements obtained from a DMA-CPC or a TDMA system account for an amount of noise resulted from: (a) the CPC accuracy and/or (b) new particle formation in the DMA column due to sparking (especially when the humidity in the DMA-2 is above 80%). The process of sparking is initiated by gas breakdown when high voltage is applied in the DMA column. This is followed by evaporation of the electrode material in the vicinity of the spark, which is then cooled to form particles.

Samples with either a small or a significant amount of noise at the raw counts (and the corresponding dN/dlogdp data; i.e., counts that do not correspond to the real aerosol distribution) at the upper limit of the classified diameter range resulting from sparking have been fitted without initially clearing the noise from the data. In most cases this has been succeeded by using a two peak fit to the data, thus the algorithm is forced to fit the real distribution peak and not the spark, and a representative growth factor value is reported. The same approach has been used for the fitting of samples with noise at the lower detection limit of the size spectra, which is usually attributed to CPC count errors.

Figure 4.5 shows characteristic examples of noisy samples fitted with the TDMAfit algorithm, using the 1-peak and 2-peak process. These examples are representative as the size distribution data are affected by either noise, spark, or both. Figures 4.5a and 4.5b show the 1-peak and the 2-peak fit of sample 1, respectively which has poor count statistics (total raw counts <100) and particles produced by sparking, (note that none of the spark data points is higher than the actual distribution peak). This results to a good fit, as the initial guess used from the TDMAfit, i.e., the maximum concentration data point, matches with the actual peak diameter. The 1-peak fit gives growth factor value 1.80, and RMS = 1.86. When, a 2-peak distribution is fitted to the measurements (cf. Figure 4.5b) the RMS = 1.47, and the reported growth factor values is 1.80 and 0.76, with the latter to correspond to noise (cf. Table 4.2).

Figures 4.5c and 4.5d show a case of the bimodal distribution sample 2 with a great amount of noise at the end of the scanning range, only due to sparking (i.e., there is no noise near the actual size distribution). As shown at Table 4.2, the 1-peak fit gives growth factor value 1.63, and RMS = 3.00, while the 2-peak fit gives growth factor values 1.64 and 1.18, with RMS=2.80. The 1-peak fit process, fits the distribution with the maximum concentration peak, while the 2-peak fit process gives the same growth factor value, and fits well and the smaller peak. The calculated curve in both cases fit well the measured data, while ignoring the noise at the end of the scanning range (cf. Figures 4.5c and d). As will be mentioned later (cf. discussion of Figure 4.6), this sample, though measurements and TDMAfit retrieved data match, it will be flagged out of the analysis based on the criteria for a 'good TDMAfit result'. Thus, it becomes clear that without pre-treatment of the data, i.e., flagging out data points that correspond to noise, the RMS gets values significant higher than unity, indicating a bad fit.

Figures 4.5e and 4.5f show a case of noisy size distribution sample, with the noise data points contributing to a signal indicating particle concentrations similar or higher to the measured peak. For the case of the 1-peak fit process (cf. Figure 4.5e) the noise is fitted as the distribution peak, and the reported growth factor value is too high (>>2.2). When the sample is processed with the 2-peak fit (cf. Figure 4.5f) the actual distribution peak is also retrieved. For this case the decision taking criteria as presented at Figure 4.6, ignores the artifacts introduced by the noise.

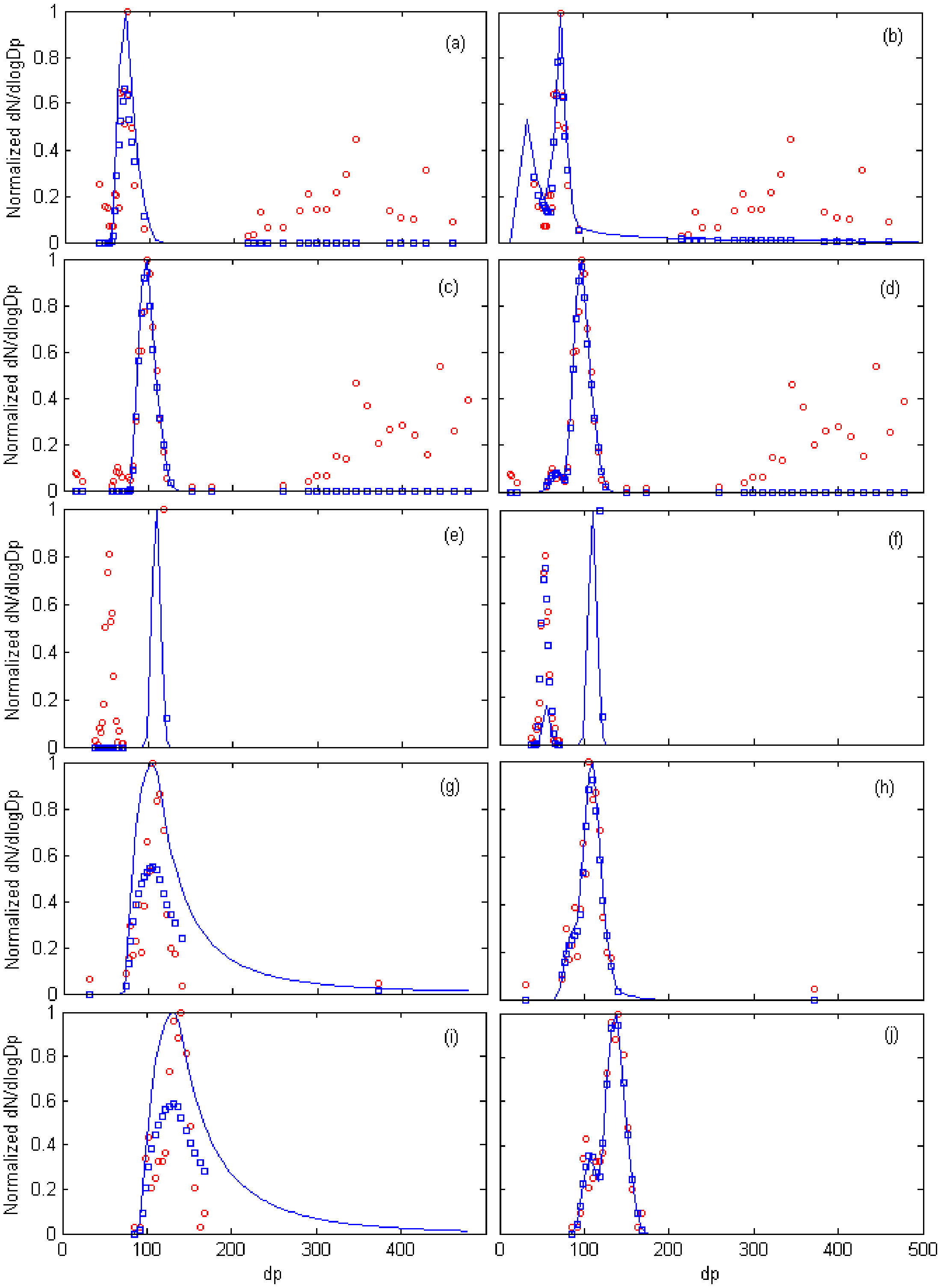

Figure 4.5: TDMA samples fitted with the TDMAfit algorithm. 1-peak fit process: (a) sample 1; (c) sample 2; (e) sample 3; (g) sample 4; (i) sample 5. 2-peak fit process: (b) sample 1; (d) sample 2; (f) sample 3; (h) sample 4; (j) sample 5.

Figures 4.5g - 4.5j show the measured and the fitted data for samples 4 and 5. Both samples have poor count statistics. The 1-peak fit gives a good agreement between measured and fitted data, especially regarding the peak diameter value. Though, for both samples the 1-peak fit RMS values are > 1.5. When the samples are fitted with the 2-peak fit algorithm a better agreement between measurements and predictions is obtain, while the RMS values are slightly below 1.0. The distributions are in both cases bimodal with sample 4, to present a "shoulder" with growth factor 1.16, before the clear peak with growth factor value 1.37. Sample 5, on the other hand, is a clear bimodal distribution with growth factor values 1.37 and 1.08, for the highest and the lowest peak, respectively.

Table 4.2 shows the total raw counts of each fitted sample, as well as the TDMAfit algorithm results. Samples 1, 4 and 5 are considered to be with poor count statistics, i.e., total raw counts < 100, fitted by the TDMAfit algorithm either with 1-peak fit or with 2-peak fit process. In all samples the RMS values for the 1-peak fit are significantly higher than one, which indicates a good fit. The RMS values for the 2-peak fit are closer to unity.

Table 4.1: TDMAfit algorithm results for 1-peak and 2-peak fit.

		1-Peak Fit		2-Peak Fit		
Sample	Raw Counts	Growth Factor (g)	RMS	Growth Factor (g_1)	Growth Factor (g_2)	RMS
1	78	1.80	1.86	1.80	0.76	1.47
2	250	1.63	3.00	1.64	1.18	2.80
3	137	2.73	4.73	2.74	1.33	1.33
4	86	1.37	1.63	1.37	1.16	0.83
5	104	1.36	1.99	1.37	1.08	0.98

Based on observations from the entire data set, characteristic examples of which were presented above, Figure 4.6 shows the criteria required to simplify the analysis of the

TDMAfit results. It should be mentioned that for testing the program's creditability and accuracy, as well its performance with noisy or with poor count statistics data, raw data from an urban environment have been used. These data were selected as they are considered to be the most difficult cases for analysis compared to data, e.g., from remote areas, where the particles are better mixed.

The criteria analysis for the best fit is based initially on the RMS values of the 1-peak and 2-peak fit processes. When the RMS values are out of the acceptable range the results for that fit are flagged out. For the case that the RMS value for both 1-peak and 2-peak fit is in the acceptable range, the selection criteria is then focused on the comparison of the growth factor values resulting from the two fit approaches. In brief, the basic steps are presented (cf. Figure 4.6 for detailed analysis). Initially, the two growth factor values reported from the 2-peak fit are processed. If their difference is in a range specified by the user (for this campaign it is considered that peaks with growth factors values deferring less than 0.1 are actually 1-peak) the average of the two growth factors is used instead for the rest of the analysis. At the next step the average value is compared with the growth factor reported by the 1-peak fit. Again, if the two values, i.e., the average and the 1-peak growth factor, have differences less than a threshold (which is empirically defined, based on the expected standard deviation of the Gaussian distribution describing the measurements) the value reported from the 1-peak fit is kept as the correct value, considering that the sample is a unimodal distribution. If, on the other hand, the growth factor values reported from the 2-peak fit are clearly distinguished (distance greater than the threshold value) both values are kept, assuming a bimodal distribution. The final step, is checking whether the growth factor values are in a physically meaningful growth factor range, which also is determined from the user, given the conditions of the sampling area. This last

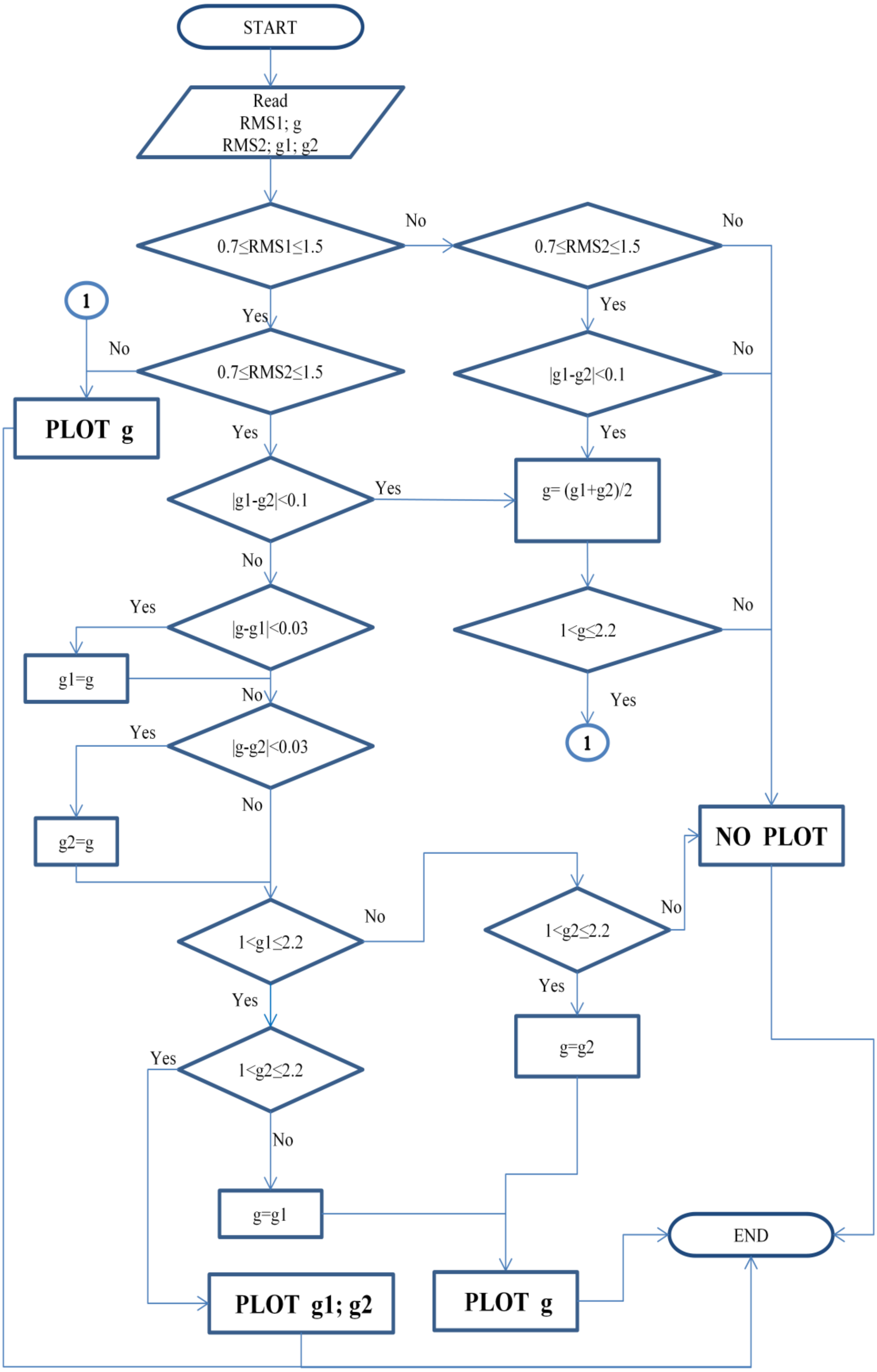

Figure 4.6: Flow diagram with the criteria for the selection of the unimodal or bimodal distribution growth factor values as calculated by TDMAfit algorithm. The values are for the case of the urban field campaign at Athens, and must be adjust to the conditions of the campaign analyzed.

check, allows to flag out peaks that are actually either sparks or noise. For data that are initially treated, i.e., sparks and noise have been cleaned, or are from either laboratory studies or from remote areas, thus correspond to unimodal distributions, the analysis can be simplified, as the 2-peak fit process can be ignored.

4.3.2 TDMAinv Algorithm

The TDMAinv (Gysel et al., 2009) inversion approach uses a piecewise linear function to represent the inverted growth factor probability density function (GF-PDF). It transforms the input, i.e., the mobility distribution to a growth factor distribution. TDMAinv uses the same principle as the TDMAfit, i.e., the goal is to find the inverted GF-PDF that minimizes the chi-square residual obtained between the measurement distribution function (MDF) and the reconstituted MDF (R-MDF). The latter is calculated from the inverted GF-PDF through the TDMA's forward function. The innovation of the TDMAinv algorithm, and its basic difference from TDMAfit, is the description of the inverted GF-PDF as a piecewise linear function rather than a Gaussian function (cf. Gysel et al., 2009; Figure 4). The TDMAinv algorithm, which is implemented in Wave Metrics' IGOR Pro Software, also uses the Levenberg-Marquardt minimization method to reduce chi-square.

TDMAfit uses the DMA transfer functions, to calculate the instrument response kernel (Stolzenburg and McMurry, 1988). On the other hand, TDMAinv calibrates the kernel based on the MDFs of the samples. For the calibration of the kernel samples with sufficiently low RH, i.e., the GF ~ 1.0, and with sufficiently high number of counts are taken into account. Gysel et al. (2009) report that a similar MDF can result from either a narrow unimodal or a bimodal GF-PDF with separated modes. The TDMAinv user determines the DMA broadening factor according to the kernel calibration results. Empirically, a DMA broadening factor of unity should be used when both DMAs are operated with flow rate ratios of 1/10 (as in the present study). Another, important inversion parameter for the TDMAinv is the retrieval bin width, which is associated with the kernel width. The usual bin width resolutions is between 0.05 and 0.10. Either too small or too high bin resolution can result to improper fit convergence, i.e., bad inversion. In such a case, the retrieval of the MDF should be repeated with a different bin width, and even with shifted bin positions (cf. TDMAinv Toolkit Manual, Gysel, 2009; pp. 40-41). In this study, a bin width value of 0.1 has been used.

The normalized chi-square value is used for the diagnosis of a good fit. A value in the order of unity indicates a good fit, whereas higher values indicate either a bad representation of the MDF by the inverted GF-PDF or underestimated measurement uncertainties (Gysel et al., 2009). The TDMAinv code reports for each sample the growth factor value corresponding to the MDF. If the sample exhibits a bimodal MDF the reported growth factor value is the average of the growth factor of the two modes. At the latter case, the growth factor at each mode is estimated, by integrating the inverted growth factor probability density function (GF-PDF) in a mode of growth factors (cf. Equation C.9 in Gysel et al., 2009).

Figure 4.7 shows the TMDA measurements (samples 1-5, also shown in Figure 4.6 and Table 4.2, but fitted with the TDMAfit algorithm) fitted by the TDMAinv. For all cases the retrieved MDFs agree well with the measurements, while the GF-PDF fits well both the unimodal (cf. Figure 4.7a-c) and the bimodal (cf. Figure 4.7d-e) samples. The reported GF values for samples 1-3 match with those reported from the TDMAfit 1-peak, while for samples 4 and 5, a separate integration for each mode results to the same growth factor values as those reported by TDMAfit 2-peak fit. The integration GF range for the bimodal distributions has been properly selected for each sample.

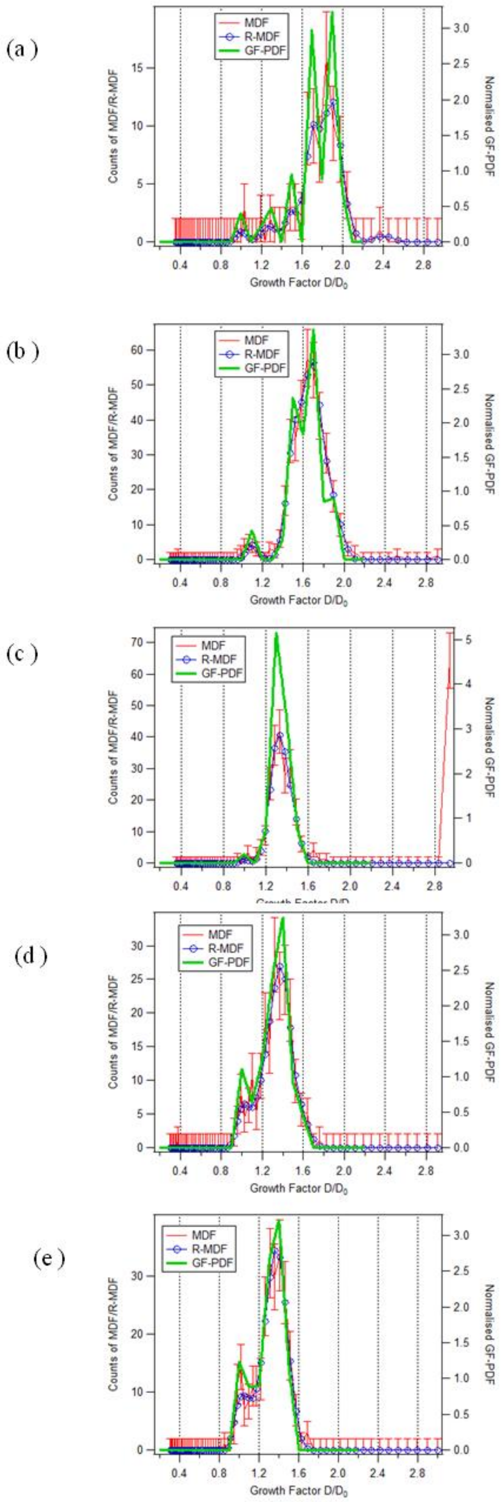

Figure 4.7: TDMA samples (as in Figure 4.5) fitted with the TDMAinv algorithm. (a) sample 1; (b) sample 2; (c) sample 3; (d) sample 4; (e) sample 5. Red line: Measurements (MDF); Blue line with circle: Calculated measurements (R-MDF; Retrieval back through forward); Green line: inverted GF-PDF (Retrieved growth distribution).

4.4 Results and Discussion

Urban field campaign measurements have been used (cf. Section 4.3) to test the modified TDMAfit code and to establish criteria that will be used to analyze the results. In this section an inter-comparison of the TDMAfit and TDMAinv algorithms is presented. The two algorithms have been used to analyze TDMA hygroscopicity measurements with pure KBr particles performed in the laboratory and at field campaigns of various environments, i.e., urban, sub-urban and remote areas.

Figure 4.8 shows TDMA measurements in an urban environment. The samples were processed with TDMAfit algorithm without initial treatment, i.e. without cleaning the noise. The TDMAinv algorithm was also used with the same untreated data. However, as the data inversion by TDMAinv algorithm is performed between specific GF values, that results to elimination of noise, at least at a significant level (cf. Figures 4.6a and c vs. 4.7a and b).

When the samples exhibit unimodal distributions the growth factor of the mode is reported for both the TDMAfit and the TDMAinv. For samples with bimodal distributions (distinct modes) the growth factor of the mode with the highest concentration and the average of the two modes growth factor value for the TDMAfit and the TDMAinv are reported, respectively. Figure 4.8a shows the evolution of growth factor estimations obtained from TDMAfit 1-peak fit and TDMAinv, for an urban environment field campaign (Athens campaign). The TDMA "untreated" input data were analyzed at the total size range by the TDMAfit, while the analysis with the TDMAinv was conducted in the growth factor range 0.7-2.5. Being so, for the TDMAinv analysis too high GF values (e.g., > 3) were not obtained, as the noise observed at the end of the scan was flagged out. A good agreement between the two algorithm results is observed, with ca. 6% of the samples having > 5% difference (cf. Figure 4.8b).

Figures 4.8c-f show the same TDMA measurements, though with a more sophisticated analysis, i.e., they have been fitted with both the 1-peak and the 2-peak distribution using the TDMAfit algorithm, and the corresponding results were then processed on the basis of the criteria analysis presented in section 4.3.1. For the TDMAinv algorithm an step extra of estimating the growth factor of each mode of the bimodal samples, with integration of the retrieved GF-PDF at selected GF ranges, has been added in the analysis. Based on the initial analysis of the TDMAfit results, as well as, by visually checking the bimodal distributions, two GF ranges for the TDMAinv mode integration have been used, i.e., 0.95-1.25 and 1.25-2.2. Initially, a third mode between 1.25 and 1.65 was used, but as the agreement between the two algorithms was not significantly improved (ca., ~3% of the bimodal distribution samples) only the first two modes were used. To the best of my knowledge, the TDMAinv algorithm does not support integration of the retrieved GF-PDF at different GF range for each sample of a data set (i.e., a set of samples with the same dry). As a result, the analysis of the bimodal distribution samples is done for all the samples of a data set at a predefined GF range for each mode. To determine the growth factor at a different mode range, one must repeat the process and select different GF range suitable for each sample. This process is time consuming, as for a set of ~ 950 samples, classified at five different subsets, i.e., five different dry diameters, the time needed to process integration for each mode for all the measurements is ~ 5 min (I note that less than 5 min is the time need for the whole (1-peak and 2-peak process) TDMAfit analysis).

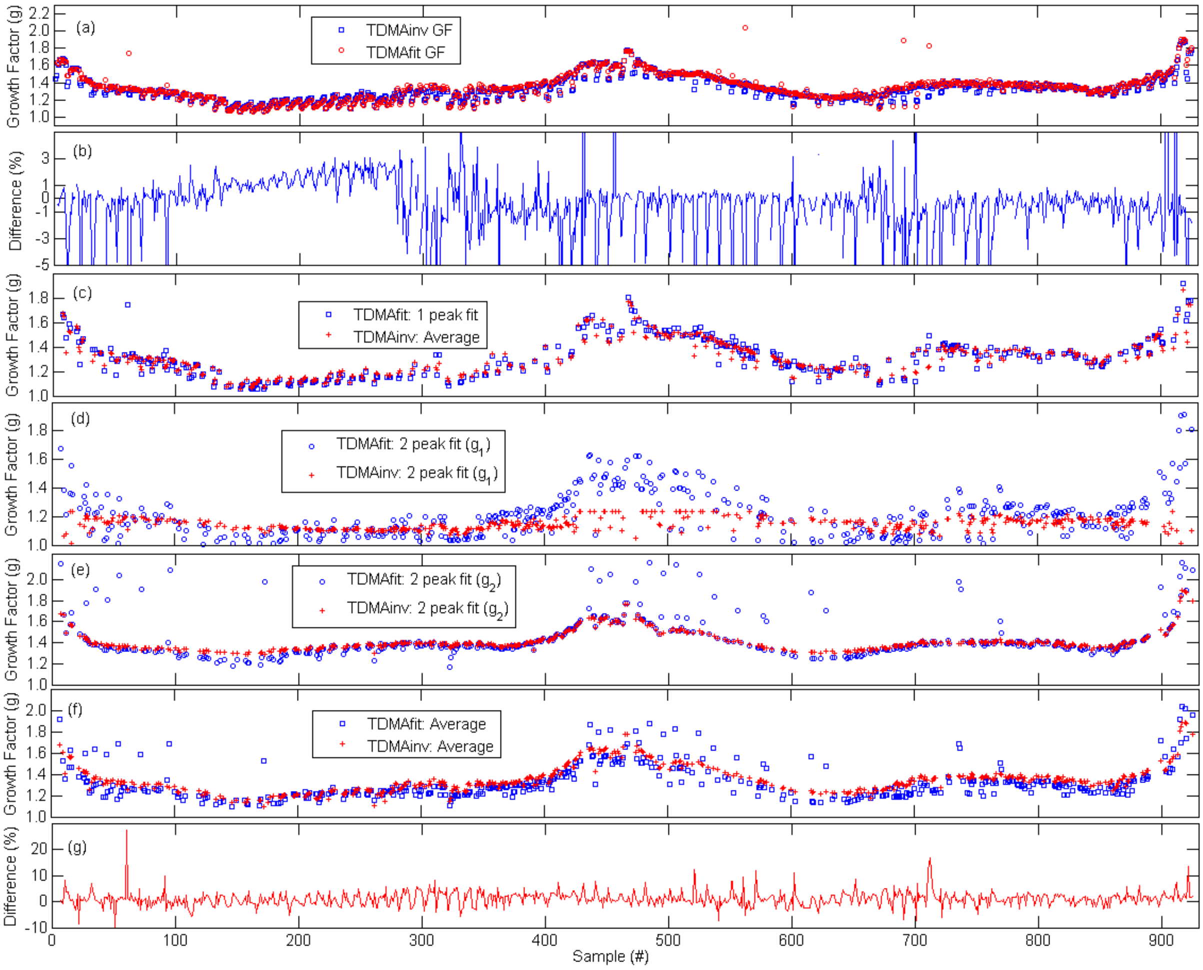

Figure 4.8: TDMA urban measurements (Athens campaign**)** analyzed by TDMAfit and TDMAinv: (a) Comparison of the growth factor values from TDMAinv (average) and TDMAfit (1-peak fit); (b) Growth factor reported at (a) difference (%). Based on the criteria analysis for the TDAMfit (cf. Figure 4.6): (c) Unimodal distribution samples GF values; (d) Bimodal distribution samples 1st mode GF; (e) Bimodal distribution samples 2nd mode GF; (f) Bimodal distribution samples average GF; (g) Growth factor difference (%) for the unimodal values subplot (c) and the average value subplot (f). The growth factor values for the bimodal distributions corresponding to the TDMainv program are calculated at the modes 0.95-1.25 and 1.25-2.2.

Figure 4.8c shows the growth factor values for unimodal samples reported by the two programs which are in good agreement. The growth factor value of the first mode of the bimodal samples, (cf. Figure 4.8d) does not agree well for the two programs. This can be attributed to the definition of the first mode GF ranges used at the TDMAinv program. As the upper limit of the integration range was set at 1.25, which is lower than the observed growth factor value for ca. 40% of the bimodal samples, which was up to ~1.60. On the other hand, the growth factor value for the second mode (i.e., the higher GF value) is in good agreement (cf. Figure 4.8e) as this mode's GF was always

> 1.25, i.e., the lower limit for the integration mode range used at the TDMAinv program. Despite this apparent disagreement to the first mode growth factor value of the bimodal distributions, if one compares the average growth factor value calculated for each bimodal sample (cf. Figure 4.8f), it can be concluded that there is a good agreement between the estimated growth factors by the two programs. The difference of the estimated growth factor values is in the range of ±10% (cf. Figure 4.8g). If the samples with poor count statistics are removed from the data set the difference of the estimated growth factor is ca. ±3%.

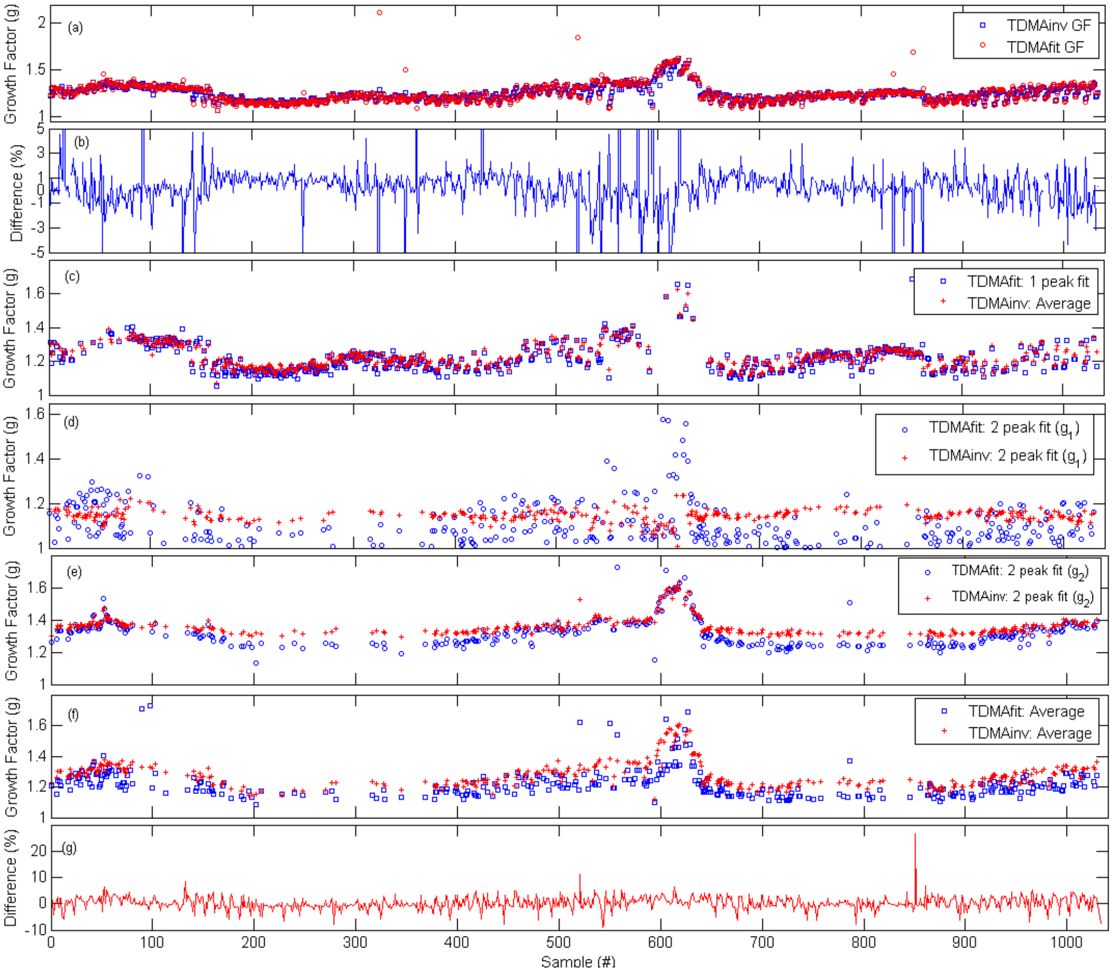

Figure 4.9: TDMA sub-urban measurements (Patra campaign**)** analyzed by TDMAfit and TDMAinv: (a) Comparison of the growth factor values from TDMAinv (average) and TDMAfit (1-peak fit); (b) Growth factor reported at (a) difference (%). Based on the criteria analysis for the TDAMfit (cf. Figure 4.6): (c) Unimodal distribution samples GF values; (d) Bimodal distribution samples 1st mode GF; (e) Bimodal distribution samples 2nd mode GF; (f) Bimodal distribution samples average GF; (g) Growth factor difference (%) for the unimodal values subplot (c) and the average value subplot (f). The growth factor values for the bimodal distributions corresponding to the TDMainv program are calculated at the modes 0.95-1.25 and 1.25-2.2.

Figure 4.9 shows TDMA measurements in a sub-urban environment, which include a significant amount of bimodal distributions. The data from this campaign are less noisy compared to those of the urban environment campaign (cf. Figure 4.8). Figure 6.9a shows the comparison of the growth factor values as reported by TDMAinv (average value) and TDMAfit (1-peak fit). The agreement between values obtained by the two program is good with 6% of the samples to have differences greater than 5% (cf. Figure 4.8b). Figures 6.8c-g show the data analysis of the same data set using the criteria described above (cf. Figure 4.6) with the necessary adjustments (e.g., maximum growth factor value 1.80). Figure 4.9c shows the estimated growth factors of the unimodal distributions, which agree well. While, Figure 4.9d shows the first mode growth factor are estimated by the two programs (cf. the discussion for Figure 4.8d), an apparent disagreement is observed. Figure 4.9e, shows the estimated growth factor values for the second mode of the bimodal distributions, which agree well. As shown in Figure 4.9f, this campaign has a significant amount of bimodal distributions, which are well captured by both algorithms, and the agreement between the results is better than that for the urban campaign. Most of the results have differences in the range ±5% (cf. Figure 4.9g).

The analysis of unimodal distribution samples, with uniform chemical composition, as those obtained at remote environment field campaigns (e.g., Limnos field campaign) proceeds with less difficulties, as there is no need for the bimodal distribution analysis. As one can see in Figure 4.10a, the initial analysis of the untreated TDMA data are well fitted by both programs, with the in-between agreement to be in the range ±2% (cf. Figure 4.10b).

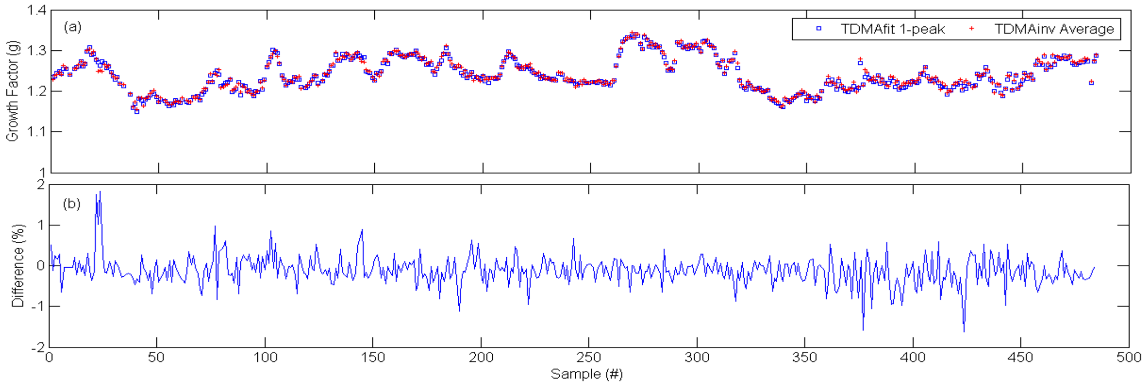

Figure 4.10: TDMA remote environment measurements (Limnos campaign**)** analyzed by TDMAfit and TDMAinv: (a) Comparison of the growth factor values from TDMAinv (average) and TDMAfit (1-peak fit); (b) Growth factor reported at (a) difference (%).

When the two algorithms are used to analyze TDMA measurements obtained by deliquescence-mode experiments with pure salt aerosol particle (e.g. KBr), as shown in Figure 4.11a, the agreement is perfect for the unimodal samples without noise (the difference is less than 0.5%; cf. Figure 4.11b). The growth factor value of the three samples that mismatch (cf. Figure 4.11a-b) is due to noise input at the measured distribution, which is fitted as a second mode by the TDMAinv program. Thus, the average value of the actual mode and noise reported by TDMAinv is slightly higher than that reported by the 1-peak fit process by the TDMAfit. Figure 4.11c shows a correction to those samples, by estimating the growth factor using the mode integration growth factor value, which results to an overall better agreement (cf. Figure 4.11d).

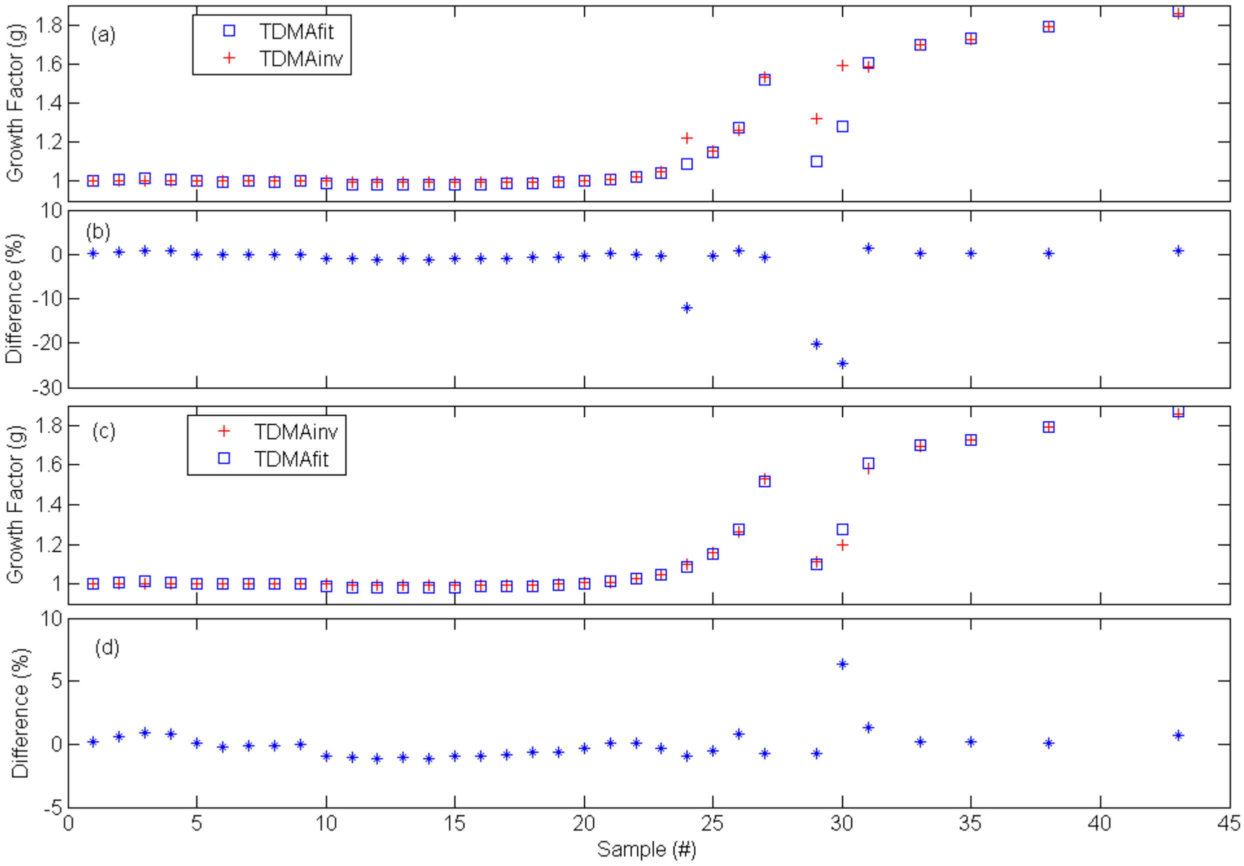

Figure 4.11: Pure salt aerosol particles (KBr, 60 nm deliquescence) TDMA measurements. (a) Comparison of the growth factor values from TDMAinv (average) and TDMAfit (1-peak fit); (b) Growth factor reported at (a) difference (%). (c) Same as (a) with correction to the TDMAinv data, i.e., the mode growth factor values was used instant of the average value estimated to samples with noise, in the range of the analysis; (d) difference (%).

Based on the analysis of the TDMA measurements presented above (cf. Figures 4.8-4.11) it can be concluded that:

- After an initial analysis, the user should go through the extreme RMS value cases and check graphically the data.
- Samples with poor statistics are better fitted by TDMAinv. That could be due to the initial guess, which is influenced from noise, or due to the weighting of the data point at the fitting procedure which is based on the counts of the data in TDMAfit.
- Samples with noise (at the begin or the end of the scanned distribution) are fitted well with the TDMAfit but due to the noise the RMS value is >> 1, thus based on the rejection criteria a good fit sample with significant amount of

noise might be flagged out (RMS>1.5). The flagged-out samples must be checked manually to clear out the noise and re-process.

- Samples with noise can be processed by TDMAinv easier, as the user can conveniently determine the GF range for the analysis and eliminate data points that do not belong to the actual size distribution, i.e., there is no need to clear them manually.
- When comparing the initial results of the two algorithms, i.e., the 1-peak fit growth factor value by TDMAfit and the average growth factor value by TDMAinv it is observed:
  - samples with growth factor difference ca. 2% are unimodal samples with low amount of noise,
  - samples with difference growth factor between 2 and 5% are either bimodal distributions, and the growth factor value given by TDMAfit corresponds to the mode with the highest concentration, while TDMAinv gives the average of the two modes growth factor, or they are unimodal distributions with significant amount of noise,
  - samples with growth factor difference >5% correspond to distributions with great amount of noise, which should be either flagged out or cleaned from noise and re-processed.
- The numerical limitations used at the TDMAfit results as criteria for the categorization of a distribution as unimodal or bimodal (cf. Figure 4.6, and the discussion for it), should be tested and adjusted for the various field campaigns conditions. For example, the majority of the measurements obtained in remote area field campaign (cf. Figure 4.10), are unimodal distributions. TDMAfit 1-peak fit growth factor value and TDMAinv average growth factor agree well.

When the categorization criteria were used, with minor adjustments for the maximum growth factor value and without adjusting the rest of the criteria, a significant amount of samples were mistakenly categorized as bimodal distributions, as noise or sparks were fitted as a second mode.

- Samples with noise, at the first and/or last bins of the scan range, if not initially treated, are fitted with RMS values between 0.75 and 1.5 (or 0.85 to 1.60) depending on the amount of noise. Although the peak diameter is fitted with a good accuracy, and thus the growth factor is well estimated, the criteria used to categorize the samples as unimodal or bimodal distributions, at ca. 30% of the cases for the remote area campaign, i.e., Limnos campaign, failed to distinguish whether the distribution is indeed unimodal better fitted with the 2-peak fit, or a bimodal.

After the initial analysis the user should check the extreme RMS value samples graphically and decide if the data should be treated for noise, or a sample with poor count statistics should be flagged-out. For field campaigns with a large number of samples (as those analyzed in this chapter) the time needed for visually checking the samples one-by-one corresponds to a couple of days (one needs about 20 hours to check and take notes for ~ 12.000 figures showing the measured, the fitted data and the calculated curves based on the fitted parameters, without including the time needed to create, even automatically, those figures). The usage of the criteria for the decision taking analysis, i.e., whether the distribution is unimodal or bimodal, limits the number of the cases to be visually checked to less than half (i.e., to samples with extreme high RMS value, which is < 5% of the total samples, with the time needed to be reduced to less than 2 hours).

4.5 Conclusions

The TDMAfit and TDMAinv data inversion algorithms are widely used to analyze TDMA measurements from laboratory and field studies. One significant difference between the two algorithms is that the TDMAfit takes into account the operating conditions of the two DMAs by estimating their transfer functions, while TDMAinv fits a kernel function using a parameter that considers only the broadening of the transfer function based the sheath to aerosol flow ratio. Another significant difference of the two algorithms is the analysis process, itself: the TDMAfit algorithm requires no user intervention, apart from providing the initial data. For a typical measuring suite of ~ 1000 samples, processing is completed in under 5 min using a midrange personal computer. On the other hand, the TDMAinv requires users intervention in the various steps of the process and decisions to be taken for the various parameter values. The time needed for TDMAinv to analyze the same measuring suite at the same personal computer is approximately an hour or even more. When processing samples of multiple initial dry diameters the required processing time is more. For example, when process 40 samples corresponding to the same initial dry diameter the time needed to run the TDMAinv steps was ca. 10 min, using the same personal computer. In general, reported growth factor values from the two algorithms are in good agreement. When the measured distributions are unimodal and the data are not noisy, the estimated growth factor values reported by the two algorithms agree within less than ±2%. For noisy unimodal measurements, the agreement of the reported growth factor values is related to the level of the noise as well as the pre-treatment of the measurements before the analysis. Finally, when the analyzed measurements are bimodal distributions, the TDMAfit algorithm reports the growth factors for both modes, while the TDMAinv reports initially the average of the two modes values, which results to disagreement between the calculated values. If the data are further processed with the TDMAinv, i.e., estimate the growth factor of each mode with integration of the GF-PDF at a GF range, the estimated growth factor values for the bimodal distributions also agree well.

Chapter 5

5. Hygroscopic Properties of Potassium-Halide Nanoparticles

5.1 Abstract

The hygroscopic properties of KBr, KCl, and KI nanoparticles having diameters from 8 to 60 nm were measured using a tandem Differential Mobility Analyzer. In all cases, the deliquescence and efflorescence relative humidity values increased with decreasing particle diameter. Apparent non-prompt phase transitions observed for particles smaller than 10 nm can be explained by either surface adsorption of water prior to deliquescence, or crystallization from aqueous solutions to form non-uniformly-shaped particles following efflorescence. The associated growth factors also decreased with decreasing particle diameter, in agreement with predictions of the Köhler theory. The theoretically predicted growth curves agree with the measurements when a size-depended shape factor for the dry particles is included in the analyses. The shape factors required ranged from unity (indicating spherical particles) for KCl and KBr, to values as high as 1.38 for KI. These results expand the existing knowledge with respect to the hygroscopic behavior of inorganic salts of atmospheric relevance.

5.2 Introduction

Inorganic salt particles can exist in either the solid or the aqueous-solution state depending on whether they are exposed to low or high relative humidity (RH) conditions (Tang and Munkelwitz, 1984;1994; Martin, 2000; Wise et al., 2005). The points in RH space where the transition from solids to aqueous solutions (i.e., the deliquescence RH; DRH) or vice versa (i.e., the efflorescence RH; ERH) take place can differ substantially, leading to a hysteresis effect (Martin, 2000; Topping, 2008; Biskos et al., 2006a; Mifflin et al., 2009). At RH values between DRH and ERH, the particles can be in either the solid or aqueous-solution state depending on their RH history (Wexler and Seinfeld, 1991). In the aqueous-solution state the water content of the particles depends on RH.

To understand the hygroscopic behavior of internally mixed aerosols one needs to fully understand the properties of the pure particles. Since the pioneering work of Hilding Köhler (1936), a number of studies have investigated the hygroscopic behavior of pure inorganic aerosol particles having diameters greater than 100 nm using electrodynamic balances (Cohen et al., 1987a; 1987b; Tang and Munkelwitz, 1993; Zhang and Chan, 2002) and mobility analysis (Tang, 1996; Tang et al., 1977; 1997). Particles in the nanosize regime (i.e., particles having diameters < 100 nm) can exhibit altered physical properties compared to larger particles and bulk materials (Anastasio and Martin, 2001). The hygroscopic properties of common atmospheric nanoparticles (i.e., NaCl and $(NH_4)_2SO_4$) having diameters smaller than 50 nm have systematically been studied by Hameri et al. (2000; 2001) and later by Biskos et al. (2006a; 2006b; 2006c). For example, the DRH of sub-50-nm NaCl particles was shown to increase with decreasing particle size as a result of the higher contribution of surface energy to total free energy of the gas-particle system as compared to the larger particles (Biskos et al., 2006a). In addition, the water uptake of the aqueous-solution droplets is reduced as particle size decreases below 50 nm due to the Kelvin effect (Kohler, 1936; Seinfeld and Pandis, 2006; Pruppacher and Klett, 1997).

Efflorescence of pure ionic droplets is the result of homogeneous nucleation which in contrast to deliquescence is a kinetic process (Seinfeld and Pandis, 2006). The nucleation rate is inversely proportional to the concentration of ions in the droplet and thus on its volume (or size). As a result of the Kelvin effect, for sub-50 nm particles, the ERH (i.e., the RH at which the nucleation initiates) increases as the particle diameter decreases (Martin, 2000; Gao et al., 2006; 2007; Hameri et al., 2000).

Particles that occur in the atmospheric environment typically are internal mixtures of a number of compounds. Sea salt particles for example consist of $\mathrm{Na^+}$, $\mathrm{Mg^{2+}}$, $\mathrm{K^+}$, $\mathrm{Cl^-}$, $\mathrm{SO_4^{2-}}$, $\mathrm{Br^-}$ and $\mathrm{I^-}$ (Seinfeld and Pandis, 2006). Kelly and Wexler (2006) have shown that hydrates and potassium salts components of a sea-salt system have an important influence on the water uptake of the sea-salt particles. Despite their small presence on atmospheric particles, bromide and iodide ions show a tendency to segregate to the salt surface in the presence of water, thus are expected to be of high importance (Minambres et al., 2011).

Pure letovicite particles, as well as mixtures of letovicite and ammonium bisulfate, of diameters ranging from 15 to 60 nm have also been studied by Mifflin et al. (2009). To the best of my knowledge measurements of the hygroscopic behavior of potassium salt nanoparticles are not yet available.

This chapter, provides new measurements of the DRH, ERH, and hygroscopic growth of potassium-halide particles (namely, KBr, KCl, KI) having diameters from 8 to 60 nm. Crystallization of some materials to form non-spherical particles is inferred, and shape factors for the solid particles are estimated. The findings expand the existing knowledge on the hygroscopic behavior of inorganic salt nanoparticles, thereby helping us understand their role in the atmosphere.

5.3 Experimental

5.3.1 Generation of Aerosol Particles

The vaporization-condensation technique was used to generate the salt nanoparticles characterized in this study. The advantage of this technique is that it generates particles of very high purity (Scheibel and Porstendorfer, 1983; Biskos et al., 2006a; 2006c), in part because no solvent is required. To synthesize the particles, high-purity (>99.5%) granular salts were placed within a quartz tube inserted in a Thermolyne (Model 21100) tube furnace. Ultrapure N_2 was flowed continuously through the tube, which was maintained at high temperatures. Salt vapors produced by the high temperatures were carried by the N_2 flow downstream the furnace where they were cooled down to room temperature thereby forming nanoparticles by nucleation. Adjusting the temperature of the furnace from 500 to 700 °C, polydisperse aerosol particle populations were produced of mean diameters that varied from 10 to ~ 45 nm.

Particles produced by vaporization-condensation are typically highly agglomerated (Flagan and Lunden, 1995). A pre-conditioning stage was therefore used to restructure the agglomerates to compact particles before measuring their hygroscopic behavior (Biskos et al., 2006a; 2006b; Hameri et al., 2001; Flagan and Lunden, 1995; Kramer et al., 2000). To do so, the dry aerosol (i.e., having RH < 5%) exiting the tube furnace was passed through a Nafion conditioner submerged in water (NCW; Perma Pure Model MD-110) to increase the RH of the aerosol flow above 95%. Subsequently, the RH of the resulting aerosol was decreased to values below 5% by passing it through a Nafion conditioner operated with an RH-adjustable air sheath flow (NCA). The history of the conditioned polydisperse particles was therefore 5% → 95% → 5%.

5.3.2 Measurements of Particle Hygroscopicity

A tandem nano-differential mobility analyzer (TnDMA; Rader and McMurry, 1986) system was used to investigate the hygroscopic properties of the potassium-halide aerosol particles. Details of the apparatus are provided in Biskos et al. (2006a; 2006c). In brief, the pre-conditioned particles generated by the vaporization-condensation method were passed through a ^{210}Po bipolar charger and a first differential mobility analyzer (DMA-1; TSI 3085). DMA-1, was used to select monodisperse particles which were then exposed to one of two RH profiles, depending on whether deliquescence- or efflorescence-mode experiments were conducted. For the deliquescence-mode experiments, the RH of the aerosol flowing downstream of DMA-1 was stepwise increased using an NCA at X% RH before entering a second DMA (DMA-2). The RH history of the monodisperse sample in these experiments was therefore 5% → X%. For the efflorescence-mode experiments an NCW and an NCA were used in series. The NCW was used to increase the RH of the monodisperse sample downstream of DMA-1 to values > 95%, whereas the NCA that followed decreased the RH of the sample in a stepwise manner. The RH history of the monodisperse sample downstream of DMA-1 in this case was 5% → 95% → X%. The mobility distribution of the particles exiting the humidification system was measured by DMA-2 and an ultrafine CPC. The sheath and the aerosol flow in both DMAs were 3 and 0.3 lpm, respectively. In order to ensure that the size of the particles does not change between the RH conditioner and DMA-2, the values of RH_a and RH_s in DMA-2 were continuously measured during the experiments (cf. Biskos et al., 2006b) and kept < 3%, in accordance with Hameri et al. (2000; 2001) experiments.

5.3.3 Data Analysis

A modified version of the TDMAfit (Stolzenburg and McMurry, 1988) algorithm as described in Chapter 4 was used to determine the hygroscopic growth factors of the particles from the hygroscopic TnDMA measurements. The algorithm compensates for differences in the conditions within the experimental setup. More specifically, it corrects the measurements for discrepancies in the measured electrical mobility of the particles by the two DMAs resulting from differences in temperature and pressure. The algorithm uses the least squares method of Levenberg Marquardt (Marquardt, 1963; Markwardt, 2010) to fit Gaussian-shaped transfer functions to the measured response of the system. The fitted parameters are (1) the particle penetration through the system, (2) the growth factor of the particles due to their water uptake, and (3) the flow conditions in the two DMAs. To locate the peak positions and the associated particle-number concentrations that give the best fit to the measurements, the algorithm employs a search routine with a number of convergence criteria and constraints. The best solution is reached when a chi-squared function of the fit residual changes by less than 0.1% and each of the fitted parameters deviates by less than 10% of its respective estimated uncertainty (Stolzenburg and McMurry, 1988).

5.4 Theory

The mobility diameter growth factor g measured by the hygroscopic TnDMA is defined as (Biskos et al., 2006c):

$$g(RH) = \frac{d_p(RH)}{d_{p,dry}}, \tag{5.1}$$

where $d_{p,dry}$ and $d_p(RH)$ are the mobility diameters of the particle at the dry state (i.e., selected by DMA-1 at < 5% RH) and at increased RH, respectively.

The measured growth factors are compared with predictions that consider the Kelvin effect and the possible change in particle shape from non-spherical (dry solid particles) to spherical (aqueous-solution droplets). The predicted growth factor can be expressed as follows:

$$g(RH) = \left(\frac{100\rho_s}{w_t\rho_{aq}(w_t)}\right)^{1/3} \chi \frac{C_c(\lambda, d_{ve,dry})}{C_c(\lambda, d_{p,dry})}, \qquad (5.2)$$

where d_{ve} is the volume equivalent diameter, ρ_s and χ are the density and the dynamic shape correction factor of the dry particles, while w_t and $\rho_{aq}(w_t)$ are the water content (weight percent) and the density of the aqueous-solution droplets. The dynamic shape factor, χ, is defined as the ratio of the drag force experienced by the non-spherical particle to the drag force of a sphere having the same volume and velocity as the non-spherical particle (Hinds, 1999). The particle water content is related to RH through the water activity a_w. For particles having diameters > 100 nm, $RH = 100\ a_w$. Particles in the nanosize regime are affected by the curvature and thus by the surface tension of the droplets. The dependence of the water activity to RH of the particles in this case is given by:

$$RH = 100\ a_w\, exp\left(\frac{4M_w\sigma_{aq}(w_t)}{RT\rho_w d_{ve}(RH)}\right), \qquad (5.3)$$

where ρ_w is the density of the water, M_w is the molar mass of water, R is the universal gas constant, and T is the temperature. σ_{aq} is the surface tension of the aqueous droplet given by:

$$\sigma_{aq} = (a + bm) \times\ 10^{-3}. \qquad (5.4)$$

Here m is molality, whereas the values for parameters a and b are given in Table 5.1. The water content w_t is related to the water activity of the system as follows:

$$a_w = C_i + \sum C_i w_t^i. \qquad (5.5)$$

The polynomial constants of Equation 5.5 for all salts investigated in this study are also provided in Table 5.1. The density of the aqueous-solution droplets required in Equation 5.2 can be predicted by the polynomial:

$$\rho_{aq} = A_0 + \sum A_i w_t^i, \tag{5.6}$$

where $\mathrm{A_0}$ and $\mathrm{A_i}$ are constants (cf. Table 5.1 and references therein). Finally, C_c in Equation 5.2 is the Cunningham slip correction factor given by:

$$C_c(\lambda, d) = 1 + \frac{\lambda}{d}\left[2.34 + 1.05\, exp\left(-0.39\frac{d}{\lambda}\right)\right], \tag{5.7}$$

where λ is the mean free path of the carrier gas and d the diameter of the particles ($d_{ve,dry}$ and $d_{p,dry}$). Using Equations 5.2-5.7 one can predict the hygroscopic growth of the particles and compare them with the measurements (Equation 5.1).

Table 5.1: Density of the dry particles $\boldsymbol{\rho_s}\ (\boldsymbol{Kg\,m^{-3}})$, density of droplet $\boldsymbol{\rho_{aq}}\ (\boldsymbol{Kg\,m^{-3}})$, water activity $\boldsymbol{a_w}$ and surface tension $\boldsymbol{\sigma_{aq}}\ (\boldsymbol{N\,m^{-1}})$.

Salt	Density of the dry particles $\rho_s\ (Kg\,m^{-3})$	Density of droplet $\rho_{aq}\ (Kg\,m^{-3})$ [a]	Water activity a_w [b]	Surface Tension $\sigma_{aq}\ (N\,m^{-1})$
KBr	2750 [c]	$A_0 = 1000$ $A_1 = 6.7054$ $A_2 = 0.0597$ $A_3 = -1.0559 \text{ x } 10^{-4}$ $A_4 = 2.7455 \text{ x } 10^{-6}$	$C_0 = 0.9999$ $C_1 = -0.0027$ $C_2 = -2.2336 \text{ x } 10^{-5}$ $C_3 = -4.6610 \text{ x } 10^{-7}$ $C_4 = -5.3239 \text{ x } 10^{-9}$	$a = 68.573$ $b = 3.7522$ [d]
KCl	1987 [e]	$A_0 = 995$ $A_1 = 7.5$ $A_2 = -8.0 \text{ x } 10^{-2}$ $A_3 = 2.667 \text{x } 10^{-3}$	$C_0 = 0.9999$ $C_1 = -0.0043$ $C_2 = -2.5015 \text{ x } 10^{-5}$ $C_3 = -1.5253 \text{ x } 10^{-6}$ $C_4 = 4.2756 \text{ x } 10^{-9}$	$a = 104$ $b = 11.714$ [d]
KI	3130 [c]	$A_0 = 1001.1$ $A_1 = 6.5929$ $A_2 = 0.0898$ $A_3 = -8.0703 \text{x } 10^{-4}$ $A_4 = 1.438 \text{ x } 10^{-5}$	$C_0 = 0.9999$ $C_1 = -0.0020$ $C_2 = -1.5577 \text{x } 10^{-5}$ $C_3 = -4.1034 \text{ x } 10^{-7}$ $C_4 = -2.5447 \text{x } 10^{-9}$	$a = 72.792$ $b = 1.1074$ [f]

(a) Forsythe (2003) ; (b) Robinson and Stokes (2002); (c) Perry and Green (1997); (d) Shah et al. (2013); (e) Hutchison (1944); (f) Ali et al. (2009).

5.5 Results and Discussion

When RH = DRH in the deliquescence-mode experiments, the dry inorganic salt particles spontaneously take up water to form aqueous-solution droplets and thus promptly increase their diameter. Earlier studies with NaCl and ammonium sulfate nanoparticles report a slight increase in size at RH values significantly less than the DRH (Flagan and Lunden, 1995; Hameri et al., 2000; Kelly and Wexler, 2006). This behavior can be attributed to either imperfect crystal growth or to adsorption of water. Moreover, an increased salt concentration near the surface of the particle may occur as a result of evaporation, followed by crystallization of the surface and formation of a solid shale around the droplet. This in turn affects the density of the smaller particles relatively more than that of larger particles (Hameri et al., 2001), with the density of the smaller particle to increase more compared to that of the larger ones. Hameri et al. (2000) suggested that this apparent gradual hygroscopic behavior can be attributed to the operating conditions of the TDMA; mainly to differences between the aerosol flow (RH_a) and the sheath (RH_s) in DMA-2. They have demonstrated that when the aerosol flow RH was kept 4-5% lower than the sheath flow of DMA-2 the measured size is accurate.

Figures 5.1-5.3 show the measured and the predicted hygroscopic growth curves for all the salt nanoparticles studied in this work, whereas Table 5.2 summarizes their DRH and ERH values. Growth factors at RH = 75±2%, measured in the efflorescence-mode experiments, are also shown in Table 5.2. In all the measurements, the uncertainties in the sheath and aerosol flows (calibrated within ±1%), the voltage of the central rod (measured within ±0.1%) and in the geometric dimension of the DMA resulted in a propagated uncertainty of less than ±2.5% in the diameter of the particles selected by DMA-1 and measured by DMA-2 (Biskos et al.,

Table 5.2: Deliquescence and Efflorescence Relative Humidity values and growth factors at 75% RH.

	KBr					KCl					KI				
	DRH range	DRH mean	ERH	ERH mean	g(75%)	DRH range	DRH mean	ERH range	ERH mean	g(75%)	DRH range	DRH mean	ERH range	ERH mean	g(75%)
60 nm	72.4-78.1	75.3	54.7-56.2	55.5	1.57	-	-	-	-	-	53.6-64.3	59.0	40.6-49.9	45.3	1.53
40 nm	77.5-81.1	79.3	57.9-60.0	59.0	1.56	80.8-82.9	81.9	56.2-60.7	58.5	1.44	-		-		-
30 nm	79.7-80.9	80.3	57.8-61.2	59.5	1.52	-	-	-	-	-	54.6-64.4	59.5	41.9-55.6	48.7	1.46
20 nm	80.7-81.7	81.2	58.0-62.1	60.1	1.54	79.6-85.5	82.6	51.1-72.2	61.7	1.33	57.1-63.9	60.5	43.1-57.1	50.1	1.45
15 nm	-		62.6-65.0	63.8	1.36	79.7-91.2	85.5	60.8-74.6	67.7	1.25	58.4-64.9	61.7	48.6-63.7	56.1	1.4
10 nm	87.1-88.7	87.9	63.4-65.3	64.3	1.43	80.9-91.1	86	70.1-82.1	76.1	1.21	-	-	-		-
8 nm	88.9-90.5	89.7	-		-	82.3-86.6	86.6	-	-	-	84.7-89.3	87.0	-	-	-
Bulk	79.9-82.0 [a]	81.0	52.0 [b]			85±1% [c] 84.3 [d]		56±1% [c] 53 [d]							

(a) Martin (2000); Cohen et al. (1987a); (b) Martin (2000); Cohen et al. (1987b); (c) Cohen et al. (1987a); Freney et al. (2009); (d) Tang (1980).

Table 5.3: Shape factor values used at theoretical model, Equation 5.1.

	60 nm	40 nm	30 nm	20 nm	15 nm	10 nm	8 nm
KBr	0.96	-	0.98	-	-	1.00	1.06
KCl	-	1.00 (1.14)	-	1.00 (1.12)	1.05 (1.12)	-	0.92
KI	0.95	-	-	0.95	1.00 (0.95)	-	1.38

2006b). The RH sensors were regularly calibrated during the experiments, resulting in an uncertainty of the measured DRH and ERH values of ±2%.

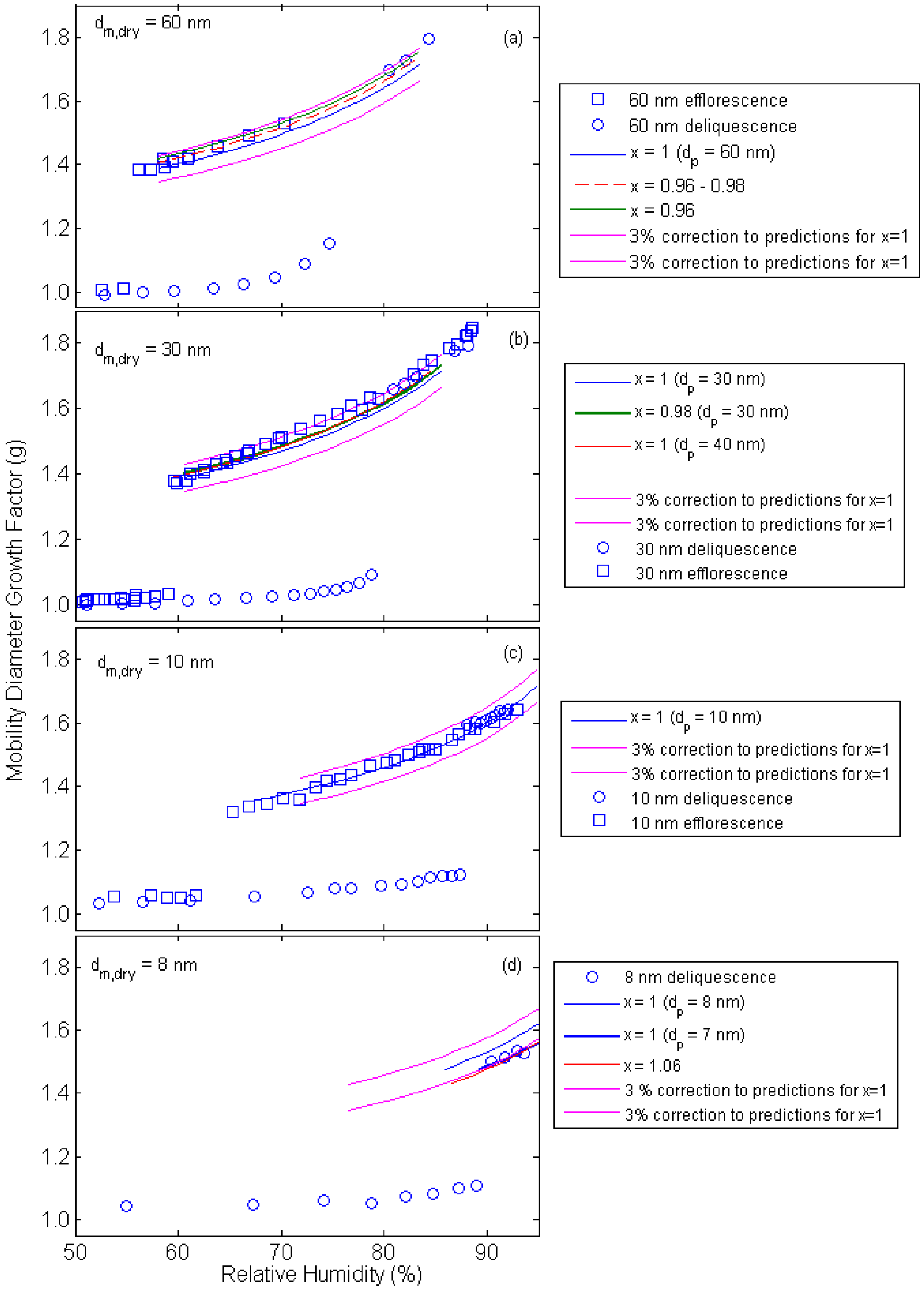

Figure 5.1: Mobility-diameter growth factors of KBr nanoparticles. Experimental growth factors are shown by the data points: circles correspond to measurements recorded during deliquescence-mode experiments, and squares during efflorescence-mode experiments. In both cases the particles were generated by the vaporization-condensation technique. Lines show the growth factors of the theoretical model with Kelvin effect and shape correction factor. Models are evaluated for $\mathbf{10 < w_t < 80}$ %.

Figure 5.1 shows the measured and predicted hygroscopic growth factors of KBr nanoparticles during deliquescence- and efflorescence-mode experiments. Deliquescence of the largest particles ($d_{p,dry}$ = 60 nm) occurs between 72.4 and 78.1%, whereas efflorescence between 54.7 and 56.2% (cf. Table 5.2). The DRH and ERH are then estimated as the mean values of these ranges, i.e., 75.3% and 55.5%, respectively, which are within ±3% agreement with observations made for large particles and bulk materials reported in the literature (Martin, 2000; Cohen et al., 1987a; 1987b). Both the DRH and the ERH mean values increase monotonically (from 75.3 to 89.7% and from 55.5% to 64.3%, respectively) as particle diameter decreases (cf. Figure 5.1 and Table 5.2). Best fits of the DRH and ERH as a function of dry particle diameter for the range 8 to 60 nm are $\mathrm{DRH}\left(d_p\right) = 55.9 d_p^{-0.3098} + 60.2$ and $\mathrm{ERH}\left(d_p\right) = -3.7 d_p^{0.3735} + 73.5$.

The particle size distributions measured by DMA-2 when the RH was around the DRH and ERH can exhibit either two distinct peaks, corresponding to the solid and the aqueous particles, or a broadened peak which includes particle populations in the two different states (cf. Figure B.1-B.5). For the 60-nm KBr particles (cf. Figure B.1) in the deliquescence-mode experiments for instance, the recorded mobility distributions are identical (i.e., they have the same mean and standard deviation) when the particles are exposed to RH conditions ranging from ca. 8 to 70%. When the RH increases further, the distributions are slightly shifted to larger sizes and become broader. During the efflorescence-mode experiments, on the other hand, the mobility distribution scans for the 60-nm KBr particles are bimodal when the RH is between 56 and 58%, i.e., near the ERH (cf. Figure B.1). For RH values higher than the ERH, the mobility distributions of the monodisperse particles are unimodal, albeit broadened. These observations can be attributed to either inhomogeneity along the experimental setup or stochastic nucleation and crystallization of individual aerosol particles in the apparatus

(Martin, 2000). The inhomogeneity along the experimental setup can be caused by small differences in the temperature (ca. ±0.5℃ during all measurements), and consequently the RH within the Nafion tube humidity exchanger and DMA-2 (Biskos et al., 2006b), which can cause particles to experience slightly different RH values compared to the ERH.

Russell and Ming (2002) have suggested that observed growth factors between 1 and $g(\mathrm{DRH})$ (e.g., for AS see Hameri et al. (2000)) can be attributed to insufficient humidification time during the measurements. Tang et al. (1986) report that in electrodynamic balance experiments with 15 and 20 μm KCl droplets a few minutes residence time was required to ensure water-vapor equilibrium, which theoretically is established within a fraction of a second. The residence time in our experiments was sufficient to ensure water-vapor equilibrium. Similar behavior was observed for all particle sizes investigated in our study, with bimodal distributions being more often observed as the particle diameter decreased, especially for the efflorescence-mode measurements (cf. Figures B.2-B.5).

Differences between theoretical predictions and experimental observations can also be attributed to changes of the shape of the particles from one state to the other. To investigate whether this is a possible explanation, Figure 5.1 also shows predictions of the model described by Equations 5.2-5.7 assuming a shape factor correction for the dry particles. Table 5.3 presents the shape factor values used in the theoretical model that give the best agreement between measurements and predictions. Assuming a size-dependent shape factor that varies from 0.96 to 1.06 as particle diameter decreases from 60 to 8 nm in the calculations (cf., Table 3, Figure 5.1) improves the agreement between predictions and measurements to ±1%. Although this improvement indicates that the solid particles may be slightly non-spherical, differences of this order can also be attributed to the accuracy of the measurements and uncertainty in the parameters of the theoretical model (Hameri et al., 2000; 2001) (e.g., density, surface tension).

As a result of the Kelvin effect, the growth factors at any given RH decrease with decreasing particle size. The hygroscopic growth factor of KBr nanoparticles at 75% RH decreases from 1.57 to 1.43 as particle diameter reduces from 60 to 10 nm. When particles are exposed to the low relative humidities (e.g., below ca. 50%) particles should stay crystalline, i.e., growth factor of unity. Nonetheless, it has been observed a slight increase of the growth factor well before the DRH point even for particles with diameter ≤ 10 nm (as also observed by Hameri et al., 2000). The small particle growth observed at RH values just below the DRH is the result of water adsorption prior to deliquescence. For a small number of measurements at low RH values (< 30%) where the difference between the RH of the aerosol and sheath flow was >2% growth factors ~0.98 were observed, which have been corrected to 1.

Figure 5.2 shows the measured and predicted hygroscopic growth curves for KCl particles derived from deliquescence- and efflorescence-mode measurements. The DRH mean values increased from 81.9 to 86.6% as particle size decreased from 40 to 8 nm (cf. Table 5.2). For the larger particles (d_p >10 nm, cf. Figures B.7-B.10) a gradual increase in the growth factors prior to deliquescence is observed, while the corresponding size distributions are either wide or bimodal. For the 40-nm particles for RH < DRH point it is observed that the water uptake results to a growth factor of ca. 1.2. The recorded size distributions by DMA-2 during the deliquescence-mode experiments (cf. Figure B.6) are initially shifted to ca. 45 nm (RH ~ 80%), becoming bimodal with a smaller peak at ca. 50 nm and a second peak at ca. 60 nm (RH ~ 82%). The mean ERH values increase from 58.5 to 76.1% when the particle size decreases from 40 to 10 nm (cf. Table 5.2). Compared to the efflorescence-mode experiments where a continuously gradual increase of the growth factor is observed, a more clear phase transition is observed in the deliquescence-mode measurements although some intermediate points are recorded prior to deliquescence. The continuous increase of particle growth in the efflorescence-mode experiments corresponds to measurements where the size distribution becomes broader. In these cases, two populations co-exist in those samples: a population of solid particles and a population of aqueous droplets. The available TDMA data inversion algorithms (i.e., TDMAfit and TDMAinv, cf. Chapter 4) cannot estimate growth factors corresponding to two modes when they are not distinguished, i.e., when they are measured as a wide unimodal distribution. As already mentioned this hygroscopic behavior can be related to experimental artifacts such as differences at RH_s and RH_a higher than ±2%, the resolving power of the two DMAs for the operating conditions employed. Best fits of the DRH and ERH as a function of dry particle diameter for the range 8 to 40 nm are $\mathrm{DRH}\left(d_p\right) = 25.2d_p^{-0.2789} + 72.7$ and $\mathrm{ERH}\left(d_p\right) = 728.0d_p^{-1.551} + 55.8$, respectively.

The hygroscopic growth of the KCl particles at RH ca. 75% decreased from 1.47 to 1.21 as particle size decreases from 40 to 8 nm (cf. Table 5.2). An offset between growth factors measured during deliquescence- and efflorescence-mode experiments is observed for all the KCl measurements. Considering that the measurements where performed in different days, these differences are within the experimental uncertainty of the TDMA system. For all particle sizes examined is observed a slight disagreement between the experimental measurements and the theoretical predictions, however most of the estimations fall in the range of the ± 3% uncertainty range of the Köhler curves (cf. Figure 5.2). To improve the agreement in the slopes of the measurements and the predictions in Figure 5.2, additional theoretical curves are presented. These theoretical curves correspond to the Köhler theory without shape factor correction, and are estimated for particle diameter $d_p = d_{p,dry} \pm$ 3 nm, and only for the 40-nm particles it was used a diameter with greater deviation, i.e., $d_p =$

28 nm, to match measurements and predictions (cf. Figure 5.7a). These discrepancies can be attributed to small differences in the operating conditions or uncertainties in the model parameters (i.e., surface tension, density, etc.). For particle sizes ≥ 15 nm in the deliquescence-mode experiments, a better agreement between predicted and measured growth factors is achieved when a shape factor value equal to one, i.e., corresponding to spherical particles, is employed. Based on the shifted dry diameter values used before to fit efflorescence-mode measurements and theoretical predictions one concludes that a shape factor correction should be used in the theoretical model. In this case, the shape factors range from 1.08 up to 1.14 as the particle sizes increased (cf. Table 5.3).

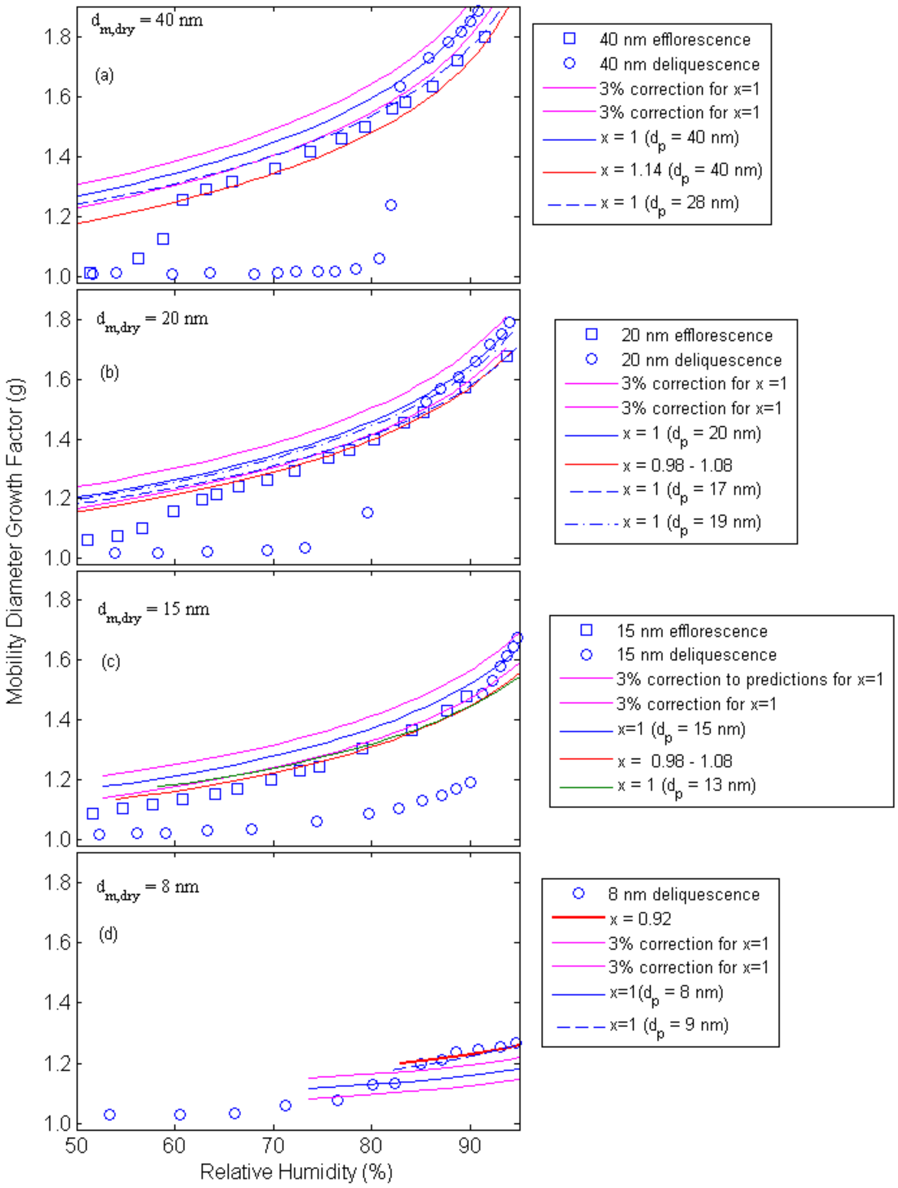

Figure 5.2: As in Figure 5.1, but for KCl nanoparticles. Models are evaluated for $\mathbf{10 < w_t < 75}$ %.

During the deliquescence-mode experiment for the 8-nm KCl particles one observes a gradual increase of the growth factor without a clear phase transition from dry particle to droplet. The mobility distributions measured in this experiment were significantly wider for RH values > 55% (cf. Figure B.9). For RH_s > 80% the distributions reveal a second, which is not distinguishable due to poor count statistics. The shape factor used to fit the data in this case is 0.92, however if it is assumed an error of ~ 12% in the determination of the dry diameter the experimental data match with the theoretical predictions without using a shape factor correction (cf. Figure 5.2d).

The measured and predicted hygroscopic growth curves for KI nanoparticles are shown in Figure 5.3. As the particle size decreases from 60 to 8 nm, the mean DRH increases from 59.0 to 87.0% (cf. Table 5.2). In a similar manner, the ERH mean values increase from 45.3 to 56.1% as particle diameter decreases from 60 to 10 nm. During deliquescence-mode experiments the size distributions obtained are unimodal and broader near the DRH point, except for the case of the 15-nm particles, where prior the deliquescence bimodal distributions have be observed (cf. Figure B.10). The slight increase of diameter prior the deliquescence ($g < 1.1$) can be related to water adsorption. For the 8-nm KCl particles a gradual increase of the growth factor is reported, while the size distribution remain unimodal with insignificant change in their standard deviation. This is related to significant amount of water on the surface of the particles at intermediate RH values from 10 to 50%. During the efflorescence-mode experiments, the observed size distributions remain unimodal although they become significantly wider for particles larger than 20 nm exposed at RH values near the ERH. Best fits of the DRH and ERH as a function of dry particle diameter for the range 8 to 60 nm are $\mathrm{DRH}(d_p) = 6.5 \times 10^{-4} d_p^{-3.735} + 59.2$ and $\mathrm{ERH}(d_p) = 3277.0 d_p^{-2.115} + 45.3$, respectively.

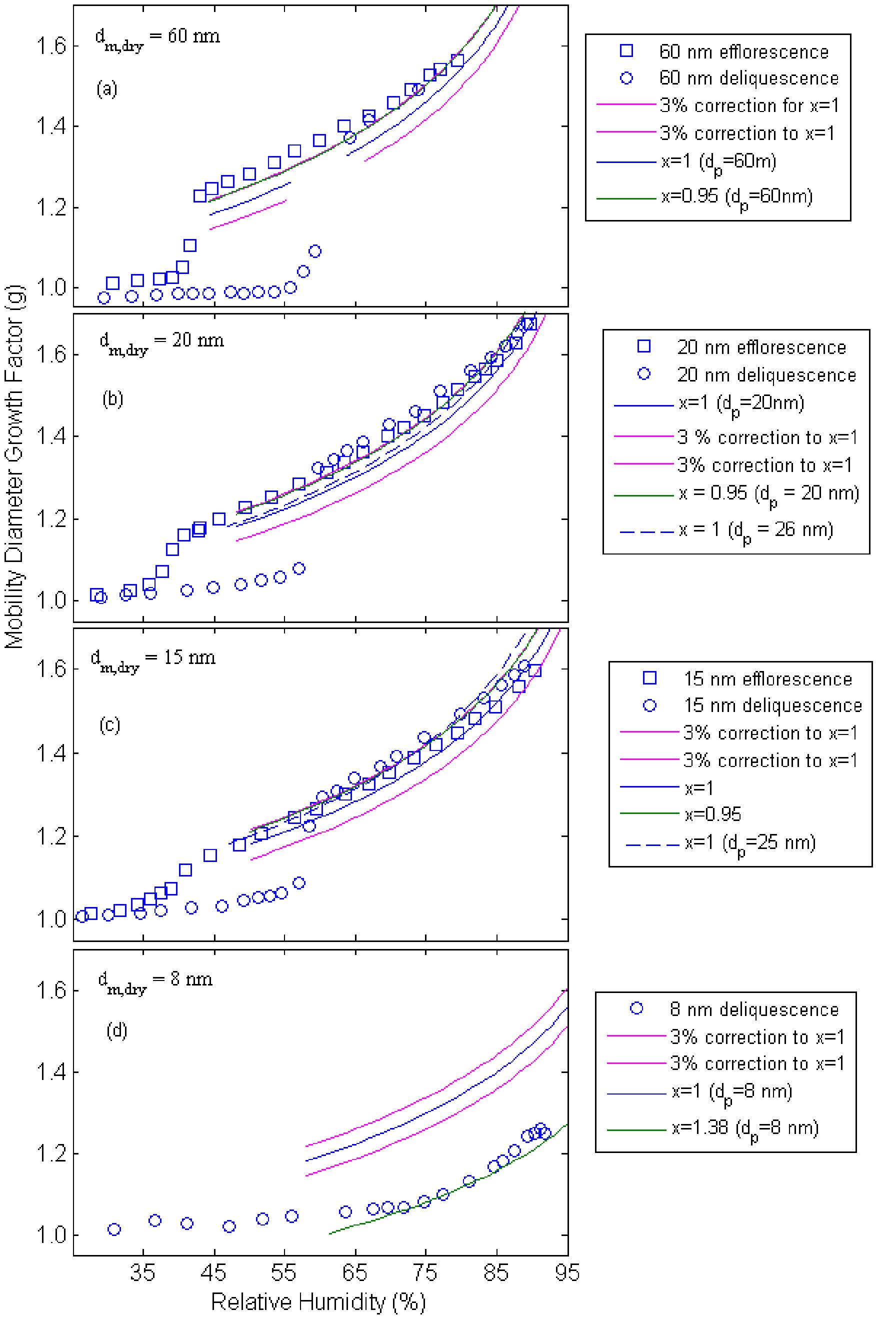

Figure 5.3: As in Figure 5.1, but for KI nanoparticles. Models are evaluated for $\mathbf{10 < w_t < 80}$ %.

The growth factor at 75% RH decrease from 1.53 to 1.30 when the particle mobility diameter decreases from 60 to 10 nm. Experimental data and theoretical predictions for the > 8-nm particles agree within ±3% with theoretical predictions. The experimental data fit well with the predictions including the Kelvin effect and a size dependent shape correction factor of 0.95. The theoretical hygroscopic curve predicted for $d_{p,dry}$ = 15 nm with a shape factor of

0.95, agrees with the that predicted for $d_{p,dry} = 25$ nm, with shape factor correction of 1.0 (cf. Figure 5.3c). Lau et al. (2013) have found shape factor, χ, for spheres and cubes, to be 0.98 and 1.03, respectively. As such a difference at the selected dry diameter is out of the resolution of the DMA, one concludes that KI particles shape deviates from that of the sphere. For the 8-nm particle deliquescence-mode measurements deviate significantly from the theoretical predictions, and the ±3% correction resulting from the uncertainties at the parameter values. In this case, a shape correction factor equal to 1.38 needs to be used to the theoretical model so as predictions to match measurements. Such a shape factor corresponds to either cuboid or cylinder shapes (Lau et al., 2013).

5.6 Conclusions

Measurements of the hygroscopic behavior of halide salt nanoparticles, namely, KBr, KCl and KI are reported in this paper. All salts studied exhibit behavior similar to that observed previously for NaCl (Biskos et al., 2006c): the deliquescence and the efflorescence RH values increase while the associated growth factors decrease as the particle size decreases below 50 nm. In both, KBr and KCl, it is observed gradual water uptake, resulting to intermediate growth factors, before deliquescence takes place, similar finding is reported for NaCl and NaBr particles (Biskos et al., 2006a; Minambres et al., 2011). Water uptake of the larger KCl particles at RH ca. 83% are in agreement with the observations for bulk particles provided by Freney et al. (2009). KI particles steadily increased their water amount up to RH~50%. This work and earlier works by Hameri et al. (2001), Biskos et al. (2006a), Park et al. (2009) and Mifflin et al. (2009) reveal that nanosize effect can attribute to an increase of the DRH above that of the bulk particles. The deliquescence hygroscopic curves show that water absorption on the particles prior to deliquescence results to the growth of the particles. Thus, both solid and aqueous solution particles may coexist for RH < DRH. The observations of significant water adsorption prior to deliquescence tend to support the model of Russell and Ming (2002) what assumes coated-surface particles.

The growth factors progressively decreased for smaller dry particle diameters. To fit the hygroscopic growth curves model that takes into account the Kelvin effect and an accessional shape-factor correction was used. With the exception of the 8-nm KI particles, experimental hygroscopic curves and theoretical model predictions without shape-factor correction agree within ±3%. A tunable size-dependent shape factor is used to better fit theoretical predictions to the measurements, with its values to be close to unity, indicating that the shape of the dry particles was spherical or nearly spherical (Stolzenburg and McMurry, 1988).

Chapter 6

6. The Origin of Nucleation Mode Atmospheric Particles in the High Arctic

Note: Giamarelou, M., Eleftheriadis, K., Nyeki S., Tunved, P., Torseth, K., Biskos, G., 2014. The Origin of Nucleation Mode Atmospheric Particles in the High Arctic. Submitted.

6.1 Abstract

Long-term observations show that nanoparticle formation, i.e., nucleation events are common in the summer-time high Arctic (Tunved et al., 2013; Karl et al., 2012), and are linked to local photochemical activity. However, theories disagree on the chemical precursors of resulting nanoparticles and on the species involved in their subsequent growth, thereby making it difficult to predict their impact on climate. Inorganic compounds can be produced by oxidation of sulfur dioxide emitted mostly from lower latitudes (Kulmala et al., 2004; Sipilä et al., 2010) or marine organosulfur species (Chang et al., 2011), whereas organic compounds can be produced from marine condensable species (Karl et al., 2012) or microgel fragments (Leck and Bigg, 2010). To identify which species are involved in nanoparticle growth in the high Arctic and thus better characterize their composition, this chapter reports measurements of their size distribution and for the first time the volatility of monodisperse particles having diameters ≤ 40 nm. The volatility measurements suggest that organic compounds are not present on nanoparticles to any large extent. Along with gas concentration and meteorological data, our observations provide strong evidence that a predominant fraction of the 12-nm particle population is ammoniated sulfates. These findings provide an important insight into nucleation mode atmospheric particles observed in

remote regions, which can be implemented in climate models to quantify their direct and indirect effects on the planetary radiative budget.

6.2 Introduction

Quantifying the contribution of natural and anthropogenic particles on regional and global climate requires information of their size and chemical composition. Although nucleation events have been observed in many locations around the globe (Kulmala et al., 2004), the mechanisms leading to new particle formation (NPF) are only beginning to be fully understood (Kulmala et al., 2013). Sulfuric acid, formed by the oxidation of sulfur dioxide (originating either from anthropogenic emissions or oxidation of marine dimethyl sulfide) in the presence of water vapor, is involved in the nucleation and growth of atmospheric particles (Sipilä et al., 2010). Because sulfuric acid cannot alone account for observed growth rates in most remote environments (Kulmala et al., 2013), other components such as ammonia (Korhonen et al., 1999), marine iodine compounds (O'Dowd et al., 2002), amines (Paasonen et al., 2012), and condensable organic species (Riipinen et al., 2012) are also considered to variously participate.

Earlier studies, based on chemical composition (Heintzenberg and Leck, 1994) and particle size distribution (Covert and Heintzenberg, 1993; Wiedensohler et al., 1996; Nyeki et al., 2005) measurements, have suggested that nucleation events in the high Arctic are mainly caused by photochemical activity involving the gas-phase formation of sulfuric acid. All chemical composition measurements to date, however, have used filter and impactor samples collected over hours to days. As a result, their association with nanoparticle formation and growth events has not been possible. Microscopy studies involving single-particle analysis have also suggested that sulfates and nitrates are present in the particle phase (Geng et al., 2010). Direct evidence linking these observations to nucleation events, however, is also lacking as investigated particles had diameters $d > 100$ nm.

Measuring the chemical composition of nanoparticles at a high temporal resolution in background/remote regions is a challenge even for state-of-the-art aerosol mass spectrometers due to their low mass concentrations and small sizes. Alternatively, a way of indirectly probing nanoparticle chemical composition is by measuring their integral properties (e.g., volatility and/or hygroscopicity; Frey et al., 2008) which offer relatively strong constraints on their composition. Previous volatility studies in the high Arctic concerned either large monodisperse particles ($d \sim 200$ nm; Covert and Heintzenberg, 1993) that are only tenuously associated with recent nucleation events, or polydisperse particles (Nyeki et al., 2005; Eleftheriadis et al., 2004) which cannot be used to indirectly determine their size-resolved composition. In this study, atmospheric aerosols observed in the summertime high Arctic are characterized based on: 1) the particle size distribution, and 2) the volatility of monodisperse particles.

6.3 Experimental Setup and Procedure

Atmospheric aerosol particles were sampled through an all-weather roof-top inlet on Zeppelin station. By using a high flow-rate of 35 lpm, from which instruments sub-sampled, losses in the main inlet were minimized. Components of the main and sub-sampling tubes were stainless-steel, and resulted in a sample temperature ~ 21°C (< 20% RH) before reaching the instruments. An ultrafine Condensation Particle Counter (CPC), a Differential Mobility Particle Sizer (DMPS) and a Volatility Tandem

Differential Mobility Analyzer (VTDMA) were used to measure the total number concentration, the number size distribution, and the volatility of atmospheric particles, respectively. The CPC (TSI Model 3025) had a theoretical cutoff detection limit at d = 3 nm, and was operated with a 1.5 lpm flow-rate. The DMPS consisted of a medium-sized Hauke-type Differential Mobility Analyzer (DMA) and another CPC (TSI Model 3760). A neutralizer was used to establish an equilibrium charge distribution on the particles before they entered the DMA where they were classified according to their electrical mobility. The aerosol and sheath flow-rates through the DMA were adjusted to 1.5 and 10 lpm, respectively, during the campaign. With these settings, the system was capable of measuring the particle size distribution in the d = 10 – 635 nm range every 20 minutes. Particle number concentrations in the d = 3 – 10 nm range ($N_{3\text{-}10}$) were obtained by subtracting DMPS from CPC data.

The VTDMA consisted of a ^{85}Kr aerosol neutralizer, two custom-made DMAs, a temperature-controlled thermodenuder placed between both DMAs, and a CPC (TSI 3025) downstream of the second DMA. The sampled polydisperse particles were passed through the ^{85}Kr aerosol neutralizer and the first DMA in which the applied voltage between both electrodes was adjusted to select monodisperse particles with d = 12, 40, 150 and 200 nm. Particles then passed through an improved low-flow thermodenuder (Fierz et al., 2007), and were exposed to temperatures T_D of 30, 120 and 230 °C in the heating section (10 cm), followed by gradual cooling in the absorption section (20 cm), before their size distribution from d = 7 to 280 nm was measured with the second DMA and CPC. The aerosol residence time in the thermodenuder and absorption section was 1.0 s. This improved design allowed more flexibility in setting the temperature profile along the thermodenuder, and allowed retention of gas-phase volatile species in the absorption section without re-condensation. Both DMAs employed a closed-loop recirculation system for the sheath flow, which was adjusted to 5.5 lpm, while the aerosol flow-rate was 1.5 lpm through the VTDMA. Each VTDMA measurement cycle at a specific thermodenuder temperature and monodisperse particle size took 15 minutes in order to ensure adequate counting statistics.

Depending on their composition, monodisperse particles will behave differently in a thermodenuder. For instance, sulfuric acid particles will dissociate completely at $T_D \geq$ 120 °C, and ammoniated sulfates at $T_D \geq 230$ °C. Refractory particles such as NaCl or BC will not change in size nor will their concentration decrease when exposed to these temperatures. To fully characterise the performance of the VTDMA at different T_D, the system was checked with various laboratory-generated particles before field deployment. Firstly, particle losses in the VTDMA were determined to be < 15% for d = 10 nm, and < 5% for Aitken/Accumulation mode particles at all T_D using monodisperse NaCl particles. All data was corrected for these losses. Secondly, the efficiency of the system to completely dissociate ammonium sulfate particles at T_D = 230 °C (1.5 lpm aerosol flow-rate, 1.0 s residence time) was confirmed as in other studies (Villani et al., 2007). Polydisperse ammonium sulfate particles were generated by atomizing a 1% aqueous solution in an atomizer particle generator (TOPAS Model ATM220), and dried to < 20% RH in a diffusion drier. The behaviour of ammonium sulfate particles was then characterised in the VTDMA, by conducting a temperature scan up to 250 °C at 10 °C steps. A reduction in N was not observed at T_D = 30 or 120 °C. However, N began to reduce at ~ 200 °C, and had reduced by 95 – 98 % at 230 °C. This offers a relatively strong constraint on the presence of ammoniated sulfates in atmospheric particles.

BC concentration was measured using an Aethalometer (Magee Scientific Model AE-31) with a 30-minute time resolution. Daily SO_2 and NH_3 gas concentrations were determined using a triple filter pack followed by ion chromatography analysis (Engvall et al., 2008). UV and global radiation measurements were conducted with a Total Ultraviolet Radiometer (Eppley Laboratory, Inc.), and a Pyranometer (Kipp and Zonen Model CMP22), respectively.

6.4 Results and Discussion

The characterization of the atmospheric aerosols observed in the summertime high Arctic is made using high temporal resolution measurements of: 1) the particle size distribution by a Differential Mobility Particles Sizer (DMPS), and 2) the volatility of monodisperse particles by a Volatility Tandem Differential Mobility Analyzer (VTDMA) system. Measurements took place at the Zeppelin atmospheric research station (78.90ºN, 11.88ºE; 474 m asl) near Ny-Ålesund, Svalbard, from 15 June to 6 July 2008 (Day of Year; DOY 167 - 187). Identification of five extended nucleation events was based on the following particle number concentration (N) criteria: 1) $N_{3-10} > N_{10-635}$ (diameter range given in subscript; cf. Section 6.3), and 2) $N_{10-635} > 100\ cm^{-3}$. Shaded areas in Figures 6.1 and 6.5 indicate these events. A sixth event was also identified when VTDMA but not size distribution measurements were available. Nucleation events in Figure 6.1a are reflected in elevated values of N_{3-10} and N_{10-30}, with averages ~ 600 and 4100 cm^{-3}, respectively, as opposed to ~ 150 and 1300 cm^{-3} during all other periods. Despite the continuous daylight during the campaign, new particles in the range $d = 3 – 10$ nm (Figure 6.1b) were first observed around midday by the instruments when UV radiation exhibited maximum values > 25 $W.m^{-2}$ (Figure 6.1c).

Daily precursor gas measurements of SO_2 and NH_3 (Figure 6.1d) gave average concentrations ~ 0.03 μg.S.m^{-3} and 0.18 μg.N.m^{-3}, which are comparable to long-term averages of ~ 0.07 μg.S.m^{-3} (Engvall et al., 2008) and 0.17 μg.N.m^{-3}, respectively. To identify nucleation events attributable to local anthropogenic pollution, Figure 6.1d also shows the aerosol black carbon (BC) concentration whose average value of ~ 10 ng.m^{-3} is typical of summer periods (5 – 15 ng.m^{-3}) from long-term measurements (Eleftheriadis et al., 2009). Two local ship pollution episodes occurred on DOY 178 and 181, as indicated by the sharp spikes in BC concentration. Interestingly, nucleation events were not observed during these episodes or thereafter, indicating that emitted gases did not directly result in NPF. Evidence for long-range pollution was obtained from 5-day back-trajectory analysis (Figure 6.2). Air masses arriving at Zeppelin station during events originated from the high Arctic (latitudes > 70 °N), and had been confined to a layer < 1000 m asl along their paths. In addition, air masses spent > 95% time over sea pack-ice or snow/ice-covered land, suggesting that they were representative of background Arctic conditions. However, evidence of a long-range pollution episode on DOY 173 – 175 is visible as a weak peak in BC concentration. Although the 5-day back-trajectory indicated an origin from northern Greenland, VTDMA results discussed further below (Figure 6.5), suggest that the nucleation event on DOY 173 occurred in an air mass influenced by long-range transported anthropogenic pollution. Based on these observations, four nucleation events (light shaded periods, Figure 6.1d) were deemed to have occurred in background Arctic air masses while two (dark shaded) were deemed to have an anthropogenic influence. The four events can be described as "regional" where nucleation and growth occur fairly uniformly over several hours to days throughout the air mass (Kulmala et al., 2004). Growth rates of recently nucleated particles determined from Figure 6.1a during these events gave average values ≤ 1.0 nm.h^{-1} for the range d = 10 – 20 nm. Similarly low values for the same range have been previously observed in sub-Arctic and Antarctic regions (Kulmala et al., 2004; Yli-Juuti et al., 2011). Current models (Yli-Juuti et al., 2013) and observations (Yli-Juuti et al., 2011) suggest that sulfuric acid together with organic acids and amines can contribute to the growth of nanoparticles with d = 3 – 20 nm, yielding growth rates up to 3.0 nm.h^{-1}. In the absence of the organic species, however, the predicted growth rates are comparable to our observations, indicating that sulfuric acid is the most dominant precursor for nanoparticle growth in the region.

The above evidence was further investigated by analyzing whether the sulfuric acid concentration ([H_2SO_4]) was able to explain the increase in $N_{3\text{-}10}$ during NPF. Although [H_2SO_4] was not measured, a recent empirical proxy model (Mikkonen et al., 2011) was used instead (cf. Appendix C). Predicted daily-average [H_2SO_4] values were between ~0.005×10^6 and 0.039×10^6 molecules.cm^{-3} during the campaign, which are similar to the lowest values measured in the Finnish sub-Arctic (Mikkonen et al., 2011). Regression analysis showed that the highest correlation between [H_2SO_4] and $N_{3\text{-}10}$ occurs when a 6-h lag is applied to the calculated proxy (Figure 6.3). This period can be attributed to the average time required for fresh clusters to grow above the CPC detection limit (d >3 nm). Figure 6.4 shows the correlation (R^2 = 0.72) between $N_{3\text{-}10}$ and daily averages of 6-h-lagged [H_2SO_4] data. A power-law fit giving an exponent of ~ 1.1 agrees well with values derived from observations at a sub-Arctic site (Rippinen et al., 2007) where sulfuric acid particle formation of $N_{3\text{-}6}$ was attributed to either cluster activation (exponent = 1) or kinetic nucleation (exponent = 2). The above observations imply that sulfuric acid participated in nanoparticle formation and growth, which it is explored further by providing robust evidence from volatility measurements.

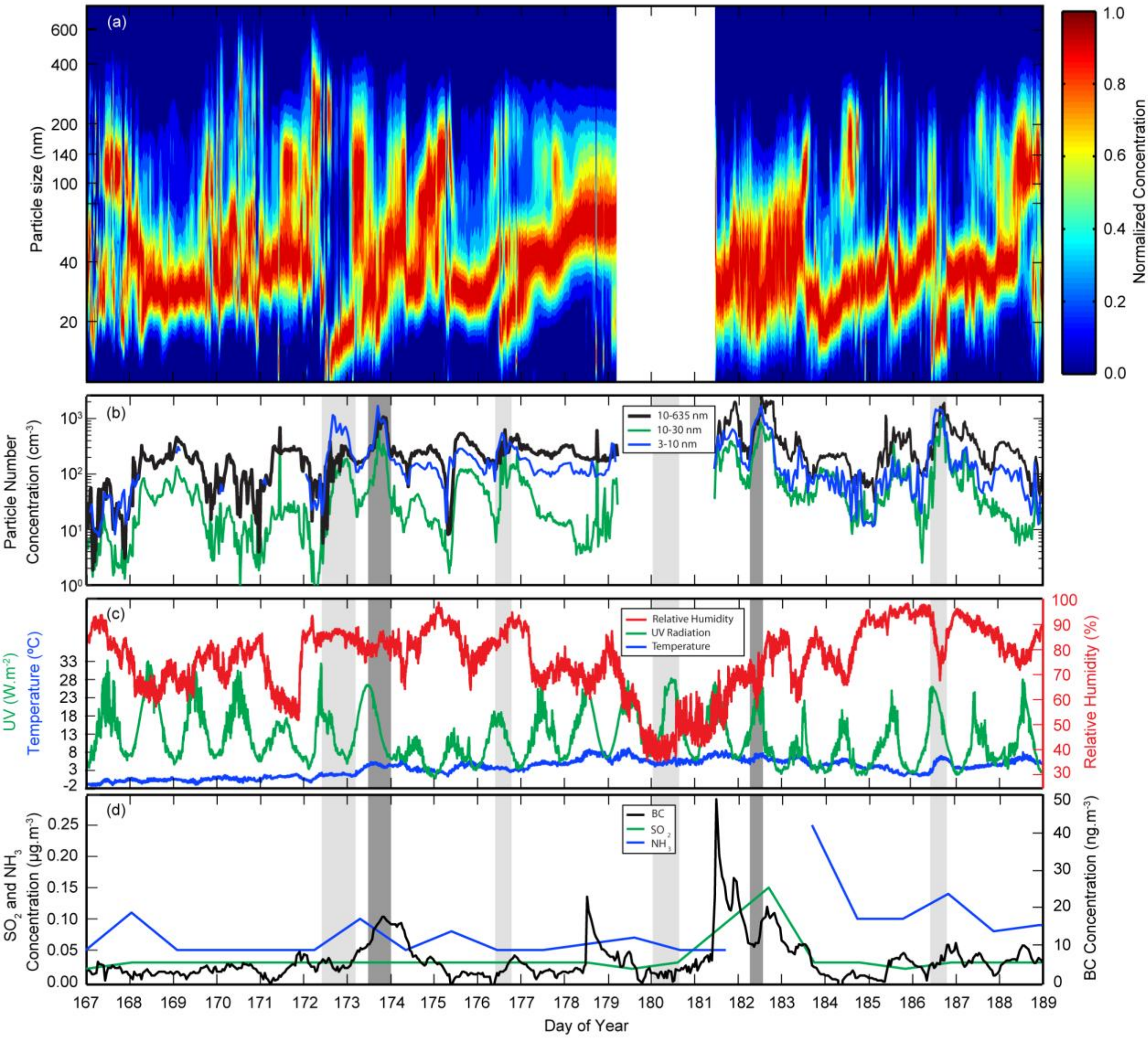

Figure 6.1: Evolution of particle size distributions, meteorological parameters, and concentrations of gaseous species measured at Ny-Ålesund from 15 June (DOY 167) to 7 July (DOY 189) 2008. (a) Normalized particle number size distributions. (b) Hourly average particle number concentration for the size ranges: d = 10 – 635 nm (black line), d = 10 – 30 nm (green line), and d = 3 – 10 nm (blue line). (c) Hourly average ambient temperature (blue line), UV radiation (green line), and relative humidity RH (red line). (d) Concentrations of BC, SO2 and NH3 (black, red and blue lines, respectively). Nucleation events occurring on 20 – 21, 21, 24, 30 June (DOY 172 – 173, 173, 176, 182) and 4 July (DOY 186), are indicated by the light shaded (background Arctic air masses) and dark shaded (anthropogenically-influenced) periods which had an average duration of 13.4 and 10.4 hours, respectively. Identification of the event on 28 June (DOY 180) was based on VTDMA results (cf. Figure 6.3). The UV radiation exhibited a diurnal pattern with maximum values on event days that varied from 18 to 32 W.m-2. The ambient temperature varied from 0 to 7°C during nucleation events, and from -2 to 8°C during the campaign. RH generally varied from 60 to 90% during nucleation events except for a brief decrease to ~ 40% on DOY 180. Meteorological conditions throughout the rest of the campaign were characteristic of the summer period. All events occurred under clear skies or moderate/low (< 25%) cloud coverage as indicated by short-wave ($\lambda = 0.3 – 2.8$ µm) downward radiation (not shown).

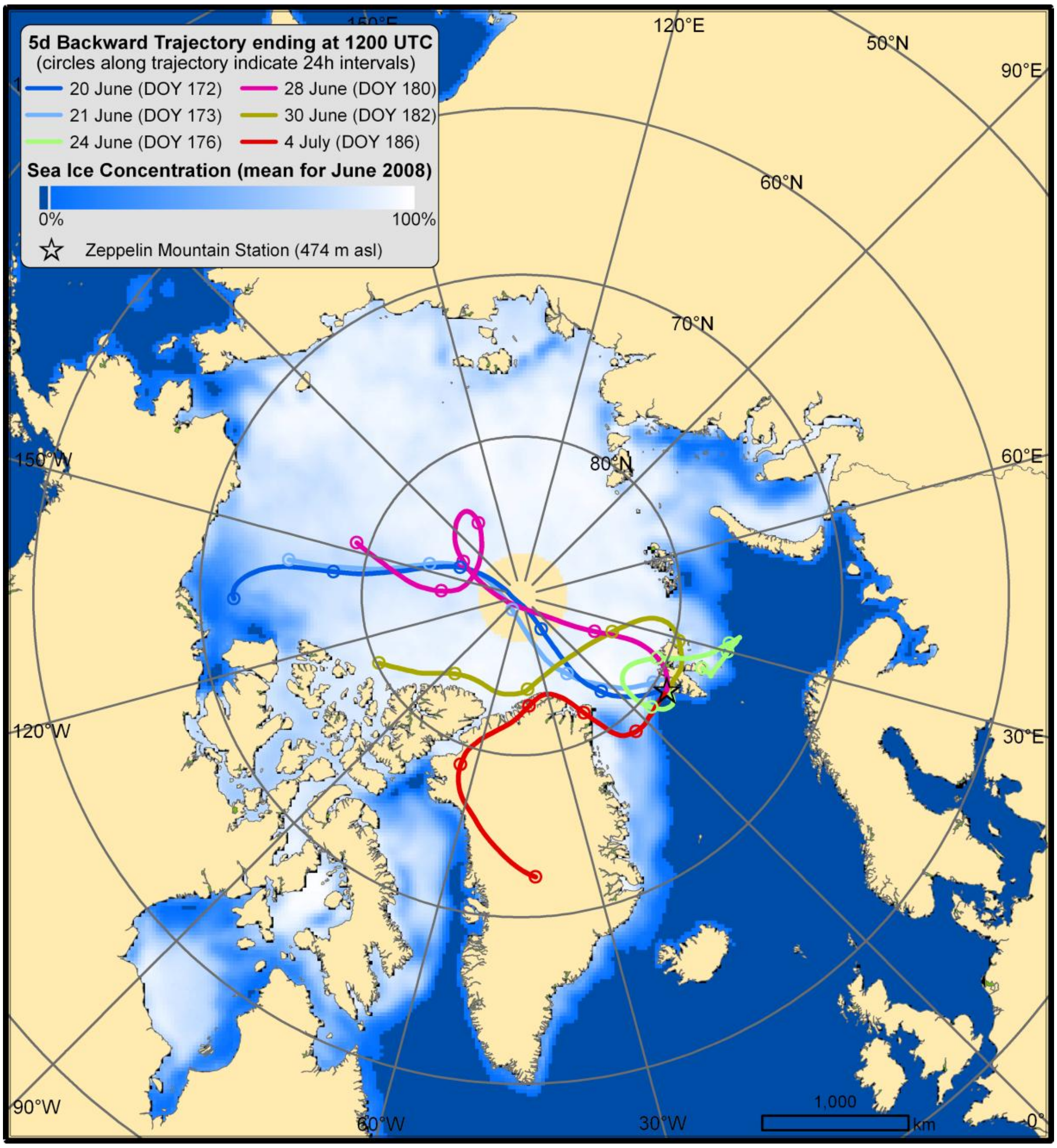

Figure 6.2: Air mass back-trajectories (5-days) arriving at the Zeppelin atmospheric research station (78.90ºN, 11.88ºE; 474 m asl) near Ny-Ålesund, Svalbard at 12:00 UTC on days when nucleation events were observed. The trajectories were determined by the NOAA HYSPLIT model (NOAA, 2014). The sea ice concentration corresponds to the average June 2008 coverage (NSIDC, 2014).

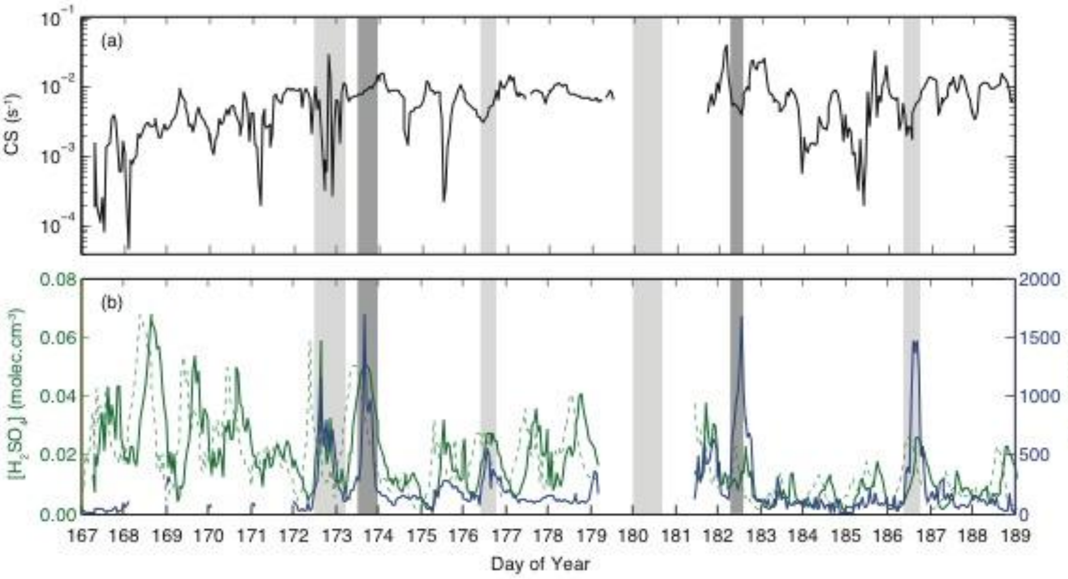

Figure 6.3: Evolution of the hourly-averaged condensation sink (a), the H_2SO_4 proxy concentration (green lines) and nanoparticle concentration (blue line) in the d = 3 – 10 nm range (b). Solid and dashed green lines correspond to hourly H_2SO_4 concentrations when shifted and not shifted by 6 h, respectively.

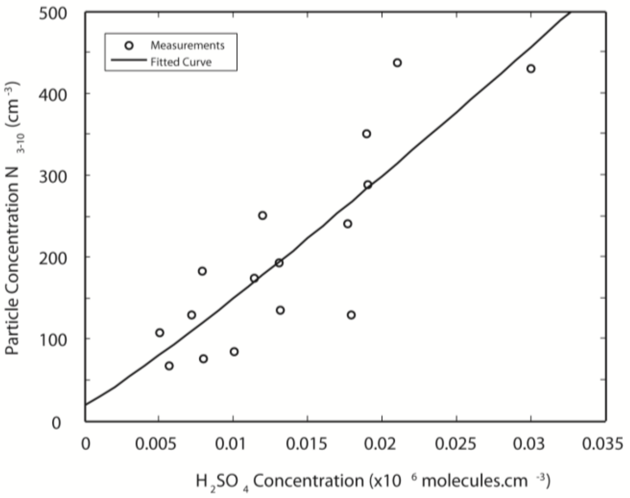

Figure 6.4: Correlation between particle number concentration and the [H_2SO_4] proxy. Nanoparticle concentrations are for the d = 3 – 10 nm range, while a 6-h lag has been applied to [H_2SO_4] data.

Figure 6.5 illustrates VTDMA measurements of monodisperse particles (*d* = 12, 40, 200 nm) at thermodenuder temperatures T_D = 30, 120, 230 °C. It should be noted that monodisperse particles either retained their sizes or shrank considerably, below the VTDMA detection limit (i.e., *d* ~ 7 nm), after passing through the thermodenuder. Particle volatility was therefore determined by comparing their number concentration before and after heat treatment. Figure 6.5a-c shows that non-events were characterized by low *N* that consisted mainly of refractory components, in some cases up to 100%. Sea-salt and BC are the likeliest candidates for particles of this size. In contrast, nucleation events exhibited elevated concentrations, especially for 12-nm particles. When the particles were treated in the thermodenuder, N_{12} decreased by 75 – 95% (average ~ 85%) at T_D = 230°C but remained unchanged at 120 °C. This strongly suggests that the majority of particles are solely composed of ammoniated sulfates with only a ≲15% number fraction composed of refractory components. This behavior contrasts that observed during the anthropogenically-influenced event on DOY 173 when N_{12} decreased by <20% at T_D = 230°C. The corresponding refractory number fraction of > 60% is consistent with slightly enhanced BC concentrations during this event. Only one observation of a reduction (~ 10%) in N_{12} was made at T_D = 120 °C on DOY 172, implying the presence of sulfuric acid particles.

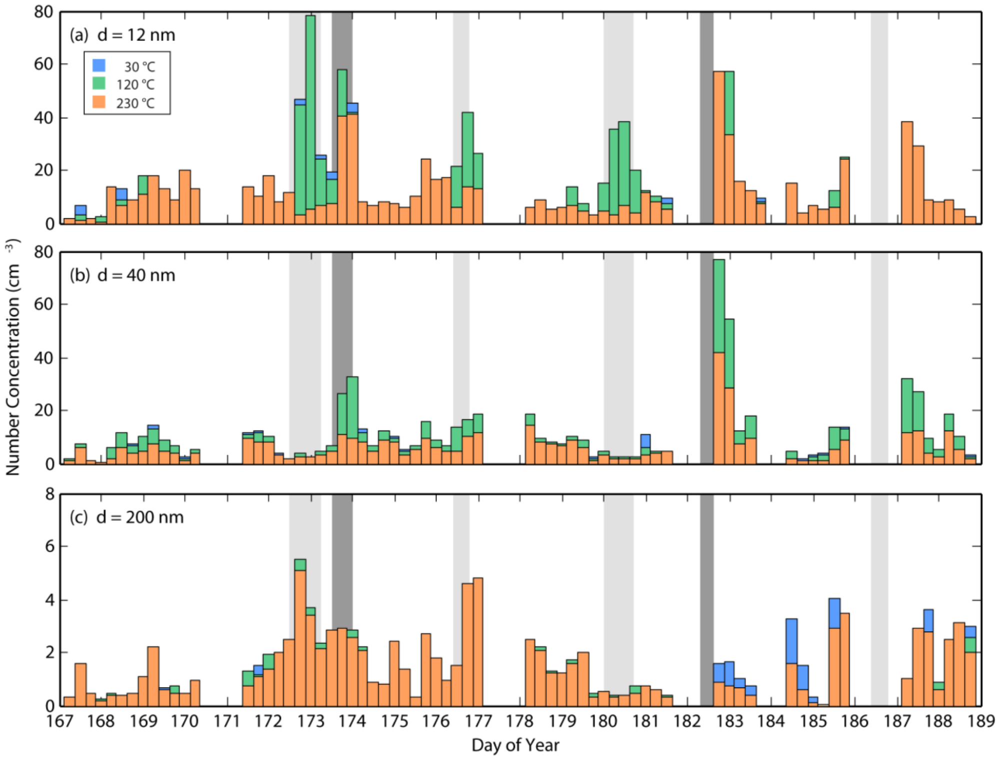

Figure 6.5: Monodisperse particle number concentrations measured by the VTDMA after thermodenuder processing. Stacked bars correspond to 30 °C (blue), 120 °C (green), and 230 °C (orange) thermodenuder temperatures for (a) d = 12 nm particles (b) 40 nm, and (c) 200 nm. Bar widths represent 6-h average values.

For the larger particles investigated (Figure 6.5b-c), it is observed that N_{40} decreased by < 50%, N_{150} by < 20% (not shown in Figure 6.5) and N_{200} by < 15% at T_D = 230 °C during nucleation events, while no change occurred at T_D = 120 °C. This behavior again indicates the presence of ammoniated sulfates, with an evident decreasing trend in their number fraction as particle size increases. The corresponding increase in the number fraction of refractory particles with size suggests that BC and/or sea-salt (Tunved et al., 2006) particles were progressively observed.

An alternative explanation of these VTDMA results in terms of organic species rather than ammoniated sulfates is also possible. Organic atmospheric particles typically consist of a complex rather than a simple mixture of organic species (Riipinen et al., 2012; Tunved et al., 2006; Zhang et al., 2012). Such particles exhibit a smooth rather than a "step-wise" temperature-dependence in thermodenuders which has been attributed to the presence of multiple organic species each with different volatility characteristics (Häkkinen et al., 2012). Such behavior contrasts the observations during nucleation events when N_{12} decreased by 75 – 95% at T_D = 230 °C. An unambiguous interpretation in terms of ammoniated sulfates cannot be made, as a single organic species with similar volatility characteristics may have been present, however, such a scenario is unlikely in atmospheric particles.

These observations do not exclude the possibility that nanoparticles may have a non-volatile core smaller than that measured by the VTDMA. For instance, if 12-nm particles were an internal mixture of ammoniated sulfates and a refractory component then an estimated shrinkage > 80% by volume at T_D = 230 °C would be required to reveal a non-volatile core below the VTDMA detection limit at d ~ 7 nm. Clusters and nanoparticles that can serve as seeds for growth during nucleation events are significantly smaller than this limit, making these measurements incapable of probing the early stages of new particle formation.

6.5 Conclusions

In summary, the measurements reported here strongly support the hypothesis that the growth of 12-nm nanoparticles in the summertime high Arctic is driven by mechanisms involving sulfuric acid and ammonia. These particles can account for ~ 85% of the population during nucleation events. The remainder is attributed to refractory particles, probably consisting of BC and/or sea-salt which play a negligible role during the events, but can account for up to 100% of the population during non-event days. The observations further suggest that the majority of the sub-40 nm particle population during nucleation events does not exist in the form of sulfuric acid but rather as partly or fully neutralized ammoniated sulfates. The fraction of these particles decreases to < 15% as particle diameter increases to 200 nm. Considering the observed spatial and temporal extent of nucleation events in the summertime high Arctic (Tunved et al., 2013; Karl et al., 2012; Kulmala et al., 2004), these observations suggest that ammoniated sulfate nanoparticles may be more ubiquitous in this region than previously thought. These findings provide an important insight into nucleation mode atmospheric particles observed in remote regions, which can be implemented in climate models to quantify their direct and indirect effects on the planetary radiative budget.

Chapter 7

7. Summary and Conclusions

This study focused on the derivation of a theoretical framework on the operation of a multiple monodisperse outlet DMA (MMO-DMA). Its performance was compared with experimental measurements using the 3-MO-DMA designed and tested by Chen et al. (2007). Two widely used algorithms for inverting TDMA measurements, namely, TDMAfit (Stolzenburg and McMurry, 1988) and TDMAinv (Gysel et al., 2009), have been compared. Finally, TDMA measurements were used to determine the hygroscopicity and the volatility of laboratory-generated and ambient nanoparticles, respectively.

Chapter 2 provides an analytical expression for the transfer function of a cylindrical MMO-DMA using the same approach followed by Stolzenburg (1988). Initially, the derivation of the transfer function for each monodisperse-particle outlet Ω_{nd_i} which does not take into account particle diffusivity (cf. Equation 2.29), is described, and then the analysis is extended to derive the transfer function Ω_{d_i} for diffusing particles (cf. Equation 2.84). The derived MMO-DMA transfer functions differ from the conventional DMA transfer function (Stolzenburg, 1988) in that every individual channel has an associated sheath flow rate Q_{sh_i} (cf. Equation 2.5) and excess flow rate Q_{m_i} (cf. Equation 2.6) as shown in Figure 2.1a. By analogy to the conventional DMA, the limiting resolution of the i^{th} monodisperse-particle outlet of the MMO-DMA for non-diffusing particles can be determined by $\mathcal{R}_{nd_i} = \frac{1}{\beta_i(1+|\delta_i|)}$, where β_i and δ_i are non-dimensional flow parameters corresponding to each outlet (cf. Equations 2.27). In the diffusion-limited regime, assuming that the transfer function of the MMO-DMA is Gaussian, the diffusion-limited resolution $\mathcal{R}_{diff_i}$ for each outlet is derived (cf.

Equations 2.97, 2.99 and 2.100), using the approach followed by Flagan (1999) and Downard et al. (2011). Combining the two limiting cases (i.e., for non-diffusing and for diffusing particles), an approximate resolution $\mathcal{R}_{approx_i}$ (cf. Equations 2.107-2.108) is further derived for balanced flows only, which can be applied over the entire range of particle mobilities and diffusional broadening parameters.

Chapter 3 compares the previously derived transfer function of the MMO-DMA with measurements using the 3-MO-DMA designed and tested by Chen et al. (2007). The performance of the model MMO-DMA transfer function was shown to be in good agreement with the experimental measurements when operated with low flow rates. This was true both for balanced and unbalanced flow conditions, while assuming some measurement errors in the aerosol outlet flow associated with flow mismatches. This was the case only for the aerosol outlets furthest from the inlet. For outlets closer to the inlet, the predictions overestimate the measured resolutions, possibly due to an inadequacy of the theory. For higher sheath flows the theoretical overestimation of the measured resolution for outlets closer to the inlet may essentially disappear but the chance of flow disturbances increases significantly, thereby reducing the resolution. Finally, it appears that additional work is needed to improve the accuracy for relatively short column lengths.

Chapter 4 describes inversion algorithms for size distribution and hygroscopicity/volatility measurements involving differential mobility analyzers, and compares the performance of two widely used inversion codes for TDMA measurements, namely, TDMAfit and TDMAinv. The two algorithms have been tested for both laboratory and field measurements at remote and urban environments. Good agreement was obtained for the retrieved hygroscopic growth factors given by the two algorithms with an average difference of ± 2%. It is demonstrated that when calculating the growth factor of bimodal size distributions the modified TDMAfit algorithm more practically reports the growth of each mode automatically, while TDMAinv initially reports the average growth of the two modes. Further, processing is needed to estimate the growth factor of each mode by integrating the growth factor distribution over the growth factor range of this mode. Both lognormal distribution functions and linear piece-wise distribution functions, as used by TDMAfit and TDMAinv algorithms, were found to be suitable for describing the hygroscopic behavior of aerosols in laboratory studies as well as in various field environments, from urban polluted air to less polluted sub-urban and even to clean air remote environments. Further, research is required to determine which criteria and parameters are most relevant for the determination of the actual hygroscopic growth factor.

Chapter 5 presents measurements of the hygroscopicity of potassium-halide particles (namely, KBr, KCl, and KI), with diameters ranging from 8 to 60 nm using an H-TDMA system. Inorganic particles are mostly hygroscopic and exhibit the properties of deliquescence and efflorescence, i.e., the transition from solids to aqueous solutions and vice versa, when the relative humidity in the surrounding atmosphere reaches a certain level. All salts studied exhibit behavior similar to that observed previously for NaCl, i.e., the deliquescence and the efflorescence RH values increase while the associated growth factors decrease as the particle size decreases below 50 nm. Growth factor at RH = 75% was between 1.57-1.43, 1.44-1.24 and 1.53-1.40, for KBr, KCl and KI, respectively, when size decreased from 60 to 8 nm. In both KBr and KCl gradual water uptake is observed resulting to intermediate growth factors, before deliquescence takes place. KI particles steadily increased their water amount up to RH ~ 50%. Hygroscopic growth curves were fitted by theoretical predictions including both the Kelvin effect and an accessional shape-factor correction. The shape factor values used were close to unity, indicating that the shape of the dry particles was spherical or nearly spherical. Here DRH and ERH are expressed as functions of the particle diameter for convenience of being readily adopted in modeling computations.

TDMAs provide indirect information about the chemical composition of aerosols, which is particularly important when the concentration or size of particles is too small for chemical analysis. Chapter 6 studies the properties of atmospheric particles in the high-Arctic during nucleation events using size distribution combined with volatility measurements performed with a VTDMA. Volatility data obtained by the VTDMA measurements (i.e., aerosol refractory components) are used to characterize the source of precursor gases and the mechanisms involved in new particle formation. The measurements reported here strongly support the hypothesis that the growth of 12-nm nanoparticles in the summertime high Arctic is driven by mechanisms involving sulfuric acid and ammonia. These particles can account for ~ 85% of the population during nucleation events. The remainder is attributed to refractory particles, probably consisting of BC and/or sea-salt which play a negligible role during the events, but can account for up to 100% of the population during non-event days. The observations further suggest that the majority of the sub-40 nm particle population during nucleation events does not exist in the form of sulfuric acid but rather as partly or fully neutralized ammoniated sulfates. The fraction of these particles decreases to <15% as particle diameter increases to 200 nm. These observations suggest that ammoniated sulfate nanoparticles may be more ubiquitous in this region than previously thought. These findings provide an important insight into nucleation mode atmospheric particles observed in remote regions, which can be implemented in climate models to quantify their direct and indirect effects on the planetary radiative budget.

The analysis of current DMA instrumentation clearly illustrates the importance of the development of DMA designs that permit faster and more complicated measurements, both at single DMA and TDMA systems. The new theoretical framework for the operation of a MMO-DMA will play an important role in the development of new instrumentation and its application in TDMA systems. Moreover, the analysis of hygroscopicity/volatility measurements illustrate the importance of TDMA inversion techniques, which should be carefully tested under various conditions. In conclusion, the hygroscopicity and volatility observations, the theoretical framework for the MMO-DMA operation and the TDMA data analysis tools developed in this thesis will improve the aerosol measurement techniques, and hence our understanding of the aerosol properties and the aerosol-cloud-climate interaction.

7. Περίληψη και Συμπεράσματα

Η μελέτη αυτή επικεντρώνεται στην ανάπτυξη ενός θεωρητικού πλαισίου για την λειτουργία DMA με πολλαπλές εξόδους μονο-μεγεθών σωματιδίων (MMO-DMA). Η απόδοσή του συγκρίθηκε με πειραματικά δεδομένα από ένα 3-MO-DMA (DMA με 3 εξόδους) που σχεδιάστηκε και δοκιμάστηκε από τους Chen et al. (2007). Δύο ευρέως χρησιμοποιούμενοι αλγόριθμοι αντιστροφής TDMA μετρήσεων, οι TDMAfit (Stolzenburg and McMurry, 1988) και TDMAinv (Gysel et al., 2009) συγκρίθηκαν. Τέλος, TDMA μετρήσεις χρησιμοποιήθηκαν για τον προσδιορισμό της υγροσκοπικότητας και της πτητικότητας εργαστηριακά-κατασκευασμένων και ατμοσφαιρικών σωματιδίων, αντίστοιχα.

Το Κεφάλαιο 2 παρέχει την αναλυτική έκφραση της συνάρτησης μεταφορά που διέπει τη λειτουργία ενός κυλινδρικού MMO-DMA χρησιμοποιώντας την ίδια προσέγγιση όπως ο Stolzenburg (1988). Αρχικά, περιγράφεται η δημιουργία της συνάρτησης μεταφοράς για κάθε έξοδο μονο-μεγεθών σωματιδίων Ω_{nd_i} η οποία δεν λαμβάνει υπόψη τη διάχυση των σωματιδίων (βλ. Εξίσωση 2.29), ενώ έπειτα η ανάλυση επεκτείνεται στην δημιουργία της συνάρτησης μεταφοράς Ω_{d_i} για τα διαχεόμενα σωματίδια (βλ. Εξίσωση 2.84). Η παραχθείσα συνάρτηση μεταφοράς διαφέρει από αυτή του συμβατικού DMA (Stolzenburg, 1988) στο ότι κάθε ξεχωριστό κανάλι έχει την αντίστοιχη ροή καθαρού αέρα (sheath flow) Q_{sh_i} (βλ. Εξίσωση 2.5) και ροή εναπομένοντα αέρα (excess flow) Q_{m_i} (βλ. Εξίσωση 2.6) όπως φαίνεται στο Σχήμα 2.1α. Κατά αναλογία με το συμβατικό DMA, η οριακή διακριτική ικανότητα (limiting resolution) της $i^{στης}$ εξόδου μονο-μεγεθών σωματιδίων του MMO-DMA για τα μη-διαχεόμενα σωματίδια μπορεί να καθοριστεί από τη σχέση $\mathcal{R}_{nd_i} = \frac{1}{\beta_i(1+|\delta_i|)}$, όπου β_i και δ_i είναι αδιάστατες παράμετροι ροής που αντιστοιχούν σε κάθε έξοδο (βλ. Εξίσωση 2.27). Στην περιοχή που καθορίζεται από τη διάχυση, υποθέτοντας ότι η συνάρτηση μεταφοράς είναι κανονική κατανομή (Gaussian), η περιοριζόμενη από τη διάχυση διακριτική ικανότητα $\mathcal{R}_{diff_i}$ για κάθε έξοδο υπολογίζεται (βλ. Εξίσωσεις 2.97, 2.99 και 2.100) χρησιμοποιώντας την προσέγγιση των Flagan (1999) και Downard et al. (2011). Επιπλέον, συνδυάζοντας τις δύο οριακές περιπτώσεις (δηλαδή για τα μη-διαχεόμενα και για τα διαχεόμενα σωματίδια), μια προσεγγιστική διακριτική ικανότητα $\mathcal{R}_{approx_i}$ (βλ. Εξισώσεις 2.107 και 2.108) υπολογίζεται για την περίπτωση των ισορροπημένων ροών μόνο, η οποία μπορεί να εφαρμοστεί για όλο το εύρος των κινητικοτήτων των σωματιδίων και των παραμέτρων διακύμανσης της διάχυσης.

Το Κεφάλαιο 3 συγκρίνει τη συνάρτηση μεταφοράς για ένα MMO-DMA όπως προσδιορίσθηκε στο προηγούμενο κεφάλαιο με μετρήσεις που πραγματοποιήθηκαν χρησιμοποιώντας ένα 3-MO-DMA σχεδιασμένο και δοκιμασμένο από τους Chen et al. (2007). Η απόδοση της θεωρητικής συνάρτησης μεταφοράς του MMO-DMA είναι σε καλή συμφωνία με τις πειραματικές μετρήσεις όταν το όργανο λειτούργησε με χαμηλές ροές αέρα. Αυτό ισχύει τόσο στην περίπτωση λειτουργίας με τη χρήση ισορροπημένων όσο και μη-ισορροπημένων ροών, υποθέτοντας κάποιο λάθος στη ροή εξόδου των σωματιδίων συσχετιζόμενη με ασυμφωνία των ροών. Αυτό ίσχυε μόνο για τις εξόδους σωματιδίων μακρύτερα από την είσοδο. Για τις εξόδους πλησιέστερα στην είσοδο, οι προβλέπεις υπερεκτιμούν τις μετρούμενες διακριτικές ικανότητες, πιθανότερα λόγω κάποιας ανεπάρκειας της θεωρίας. Για υψηλότερες ροές καθαρού αέρα η θεωρητική υπερεκτίμηση της μετρούμενης διακριτικής ικανότητας για τις εξόδους πλησιέστερα στην είσοδο μπορεί ουσιαστικά να εξαφανίζεται, ωστόσο καθώς η πιθανότητα για τυρβώδη ροή αυξάνεται σημαντικά η διακριτική ικανότητα μειώνεται. Τέλος, προκύπτει ότι επιπλέον δουλεία χρειάζεται για τη βελτίωση της ακρίβειας κολώνων DMA με αναλογικά μικρό μήκος.

Το Κεφάλαιο 4 περιγράφει κώδικες αντιστροφής για κατανομές μεγέθους και μετρήσεις υγροσκοπικότητας/πτητικότητας που πραγματοποιούνται με αναλυτές διαφορικής κινητικότητας, και συγκρίνει την απόδοση δύο ευρέως διαδεδομένων αλγορίθμων αντιστροφής TDMA μετρήσεων, των TDMAfit και TDMAinv. Οι δύο αλγόριθμοί ελέγχθηκαν τόσο με εργαστηριακές μετρήσεις όσο και με μετρήσεις σε απομονωμένα και αστικά περιβάλλοντα. Καλή συμφωνία επιτεύχθηκε στις τιμές των συντελεστών υγροσκοπικής αύξησης όπως αυτές προέκυψαν από τους δύο αλγόριθμούς με τη μέση διαφορά να είναι στο ± 2%. Αποδείχθηκε ότι όταν υπολογίζεται ο συντελεστής αύξησης για κατανομές με δύο μέγιστα ο τροποποιημένος αλγόριθμος TDMAfit πιο πρακτικά δίνει αυτόματα τον συντελεστή αύξησης της κάθε κορυφής της κατανομής, ενώ το TDMAinv αρχικά δίνει τον μέσο όρο των συντελεστών αύξησης των δύο κορυφών. Έτσι, επιπρόσθετη επεξεργασία είναι απαραίτητη για τον υπολογισμό του συντελεστή αύξησης της κάθε κορυφής με την ολοκλήρωση της κατανομής των συντελεστών αύξησης, σε εύρος κατάλληλο για κάθε κορυφή. Τόσο κανονικές λογαριθμικές (lognormal) κατανομές όσο και διαδοχικές γραμμικές (linear piece-wise) κατανομές, βρέθηκε ότι είναι κατάλληλες για την περιγραφή της υγροσκοπικής συμπεριφοράς των αεροζόλ τόσο σε εργαστηριακές μελέτες όσο και σε μελέτες πεδίου, σε διάφορα περιβάλλοντα, από μολυσμένο αστικό αέρα, σε λιγότερο μολυσμένο ημι-αστικό μέχρι σε καθαρό αέρα σε απομονωμένες περιοχές. Επιπρόσθετη μελέτη πρέπει να διεξαχθεί για τον καθορισμό των κριτηρίων και των παραμέτρων που θα είναι οι πλέον κατάλληλοι για τον προσδιορισμό του πραγματικού συντελεστή υγροσκοπικής αύξησης.

Το Κεφάλαιο 5 παρουσιάζει μετρήσεις υγροσκοπικότητας σωματιδίων αλογόνων του καλίου (ονομαστικά, KBr, KCl, KI), με διαμέτρους από 8 έως 60 nm με τη χρήση ενός συστήματος H-TDMA. Τα ανόργανα σωματίδια είναι κυρίως υγροσκοπικά και παρουσιάζουν τις ιδιότητες της υγροποίησης και της στερεοποίησης, δηλαδή την μετάβαση από στερεά σε υδατικά διαλύματα και το αντίστροφο, όταν η σχετική υγρασία στην περιβάλλουσα ατμόσφαιρα φτάνει σε ένα συγκεκριμένο επίπεδο. Όλα τα άλατα που μελετήθηκαν παρουσιάζουν συμπεριφορά όμοια με αυτή που παρατηρήθηκε προηγούμενα για το NaCl, δηλαδή οι τιμές της σχετικής υγρασίας υγροποίησης και στερεοποίησης αυξάνονται, ενώ ο αντίστοιχος συντελεστής αύξησης μειώνεται καθώς το μέγεθος του σωματιδίου μειώνεται κάτω από τα 50 nm. Ο συντελεστής αύξησης σε σχετική υγρασία 75% κυμάνθηκε μεταξύ 1.57-1.43, 1.44-1.24 και 1.53-1.40, για το KBr, KCl και KI, αντίστοιχα, όταν το μέγεθος του σωματιδίου μειώθηκε από τα 60 στα 8 nm. Τόσο το KBr όσο και το KCl προσροφούν σταδιακά νερό καταλήγοντας σε ενδιάμεσους συντελεστές αύξησης πριν την υγροποίηση. Το KI σταθερά αυξάνει το ποσό του νερού που περιέχει μέχρι περίπου σχετική υγρασία ίση με 50%. Οι καμπύλες υγροσκοπικότητας προσομοιώνονται με θεωρητικές προβλέψεις που περιλαμβάνουν τόσο το φαινόμενο Kelvin όσο και έναν επιπρόσθετο συντελεστή διάθρωσης σχήματος. Οι τιμές που χρησιμοποιήθηκαν στον συντελεστή διόρθωσης σχήματος είναι κοντά στη μονάδα, υποδηλώνοντας ότι το σχήμα των ξηρών σωματιδίων είναι σφαιρικό ή σχεδόν σφαιρικό. Οι τιμές DRH και ERH εκφράζονται ως συνάρτηση της διαμέτρου των σωματιδίων για την ευκολότερη χρήση τους σε υπολογιστικά μοντέλα.

Τα TDMAs παρέχουν έμμεση πληροφορία για τη χημική σύσταση των αεροζόλ, η οποία είναι ιδιαιτέρως σημαντική όταν η συγκέντρωση ή το μέγεθος των σωματιδίων είναι πολύ μικρό για χημική ανάλυση. Το Κεφάλαιο 6 μελετά τις ιδιότητες των ατμοσφαιρικών σωματιδίων στην περιοχή πάνω από τον Αρκτικό Κύκλο κατά τη διάρκεια περιπτώσεων παραγωγής νέων σωματιδίων χρησιμοποιώντας την κατανομή μεγέθους σε συνδυασμό με μετρήσεις πτητικότητας που διεξήχθηκαν με ένα VTDMA σύστημα. Δεδομένα πτητικότητας που προήλθαν από το VTDMA (όπως ο προσδιορισμός των δύστηκτων συστατικών των σωματιδίων (refractory components)) χρησιμοποιούνται για τον χαρακτηρισμό της πηγής, των πρόδρομων αερίων και των μηχανισμών που εμπλέκονται στο σχηματισμό των νέων σωματιδίων. Οι μετρήσεις που αναφέρονται εδώ υποστηρίζουν ισχυρά την υπόθεση ότι η αύξηση του μεγέθους των 12-nm νανο-σωματιδίων κατά τη θερινή περίοδο στην περιοχή πάνω από τον Αρκτικό Κύκλο καθοδηγείται από μηχανισμούς στους οποίους εμπλέκονται το θειικό οξύ και η αμμωνία. Αυτά τα σωματίδια μπορούν να αποτελέσουν περίπου μέχρι και το 85 % του συνολικού πληθυσμού κατά την διάρκεια συμβάντων σχηματισμού νέων σωματιδίων. Το υπολειπόμενο μέρος του πληθυσμού αποδίδεται σε δύστηκτα σωματίδια, πιθανώς αποτελούμενα από αιθάλη (BC) και/ή θαλάσσια άλατα τα οποία έχουν ένα αμελητέο ρόλο κατά τη διάρκεια των περιστατικών δημιουργίας νέων σωματιδίων, αλλά μπορεί να αποτελέσουν μέχρι και το 100% του πληθυσμού κατά τις υπόλοιπες περιόδους. Οι παρατηρήσεις επιπλέον προτείνουν ότι η πλειονότητα του πληθυσμού των κάτω των 40-nm σωματιδίων κατά τη διάρκεια των περιστατικών δημιουργίας νέων σωματιδίων δεν απαντάται με τη μορφή θειικού οξέος αλλά μάλλον ως μερικώς ή πλήρως εξουδετερωμένα άλατα του θειικού αμμωνίου. Το ποσοστό αυτών των σωματιδίων μπορεί να μειωθεί και κάτω του 15% όταν η διάμετρος των σωματιδίων αυξάνεται στα 200 nm. Αυτές οι παρατηρήσεις υποδηλώνουν ότι τα νανο-σωματίδια αλάτων του θειικού αμμωνίου μπορεί να είναι ευρύτερα διαδεδομένα στην περιοχή από ότι θεωρείτο μέχρι τώρα. Αυτά τα ευρήματα παρέχουν μια σημαντική βαθύτερη γνώση για τα ατμοσφαιρικά σωματίδια στην κλάση των πυρήνων συμπύκνωσης (nucleation mode) που παρατηρούνται σε απομακρυσμένες περιοχές, η οποία μπορεί να εφαρμοστεί σε μοντέλα για την ποσοτικοποίηση των έμμεσων και άμεσων επιπτώσεων ισοζύγιο ενέργειας του πλανήτη.

Η ανάλυση των υφιστάμενων οργάνων DMA δείχνει εμφανώς τη σπουδαιότητα της ανάπτυξης οργάνων DMA που θα επιτρέπουν ταχύτερες και πιο πολύπλοκές μετρήσεις, τόσο σε απλά DMA όσο και σε TDMA συστήματα. Το νέο θεωρητικό πλαίσιο για την λειτουργία του MMO-DMA θα έχει ένα σημαντικό ρόλο στην ανάπτυξη των νέων οργάνων και των εφαρμογών τους σε TDMA συστήματα. Επιπρόσθετα, η ανάλυση μετρήσεων υγροσκοπικότητας/πτητικότητας αναδεικνύει την σπουδαιότητα των τεχνικών αντιστροφής TDMA μετρήσεων, οι οποίες θα πρέπει να έχουν προσεχτικά δοκιμαστεί κάτω από ποικίλες συνθήκες. Συμπερασματικά, οι παρατηρήσεις υγροσκοπικότητας και πτητικότητας των αιωρούμενων σωματιδίων, το θεωρητικό πλαίσιο για τη λειτουργία των MMO-DMA και τα εργαλεία για την ανάλυση TDMA δεδομένων που αναπτύχθηκαν σε αυτή τη διατριβή θα βελτιώσουν τις τεχνικές μέτρησης αιωρούμενων σωματιδίων, και επομένως τη γνώση για τις ιδιότητες τους και την αλληλεπίδραση αιωρούμενων σωματιδίων - νεφών - κλίματος.

Bibliography

Ackerman, S. A., Stephens, G. L., 1987. The Absorption of Solar Radiation by Cloud Droplets: An Application of Anomalous Diffraction Theory. *J. Atmos. Sci.*, 44: 1574-1588.

Anastastio, C., Martin, S. T., 2001. Atmospheric Nanoparticles, in *Nanoparticles and the Environment.* Eds.: Banfield, J.F., Navrotsky, A., Mineralogical Society of America, 44: 293–349, Washington, D.C.

Ali, K., Shah, A. A., Bilal, S., Shah, A. A., 2009. Surface tensions and thermodynamic parameters of surface formation of aqueous salt solutions: III. Aqueous solution of KCl, KBr and KI. *Colloids and Surfaces A: Physicochem Eng. Aspects*, 337: 194–199.

Allan, J. D. et al., 2008. Clouds and aerosols in Puerto Rico – a new evaluation. *Atmos Chem Phys*, 8: 1293–1309.

Alofs, D. J., Balakumar, P., 1982. Inversion to obtain aerosol size distributions from measurements with a differential mobility analyzer. *J. Aerosol Sci.*, 13: 513–527.

Bevington, P. R., 1969. *Data Reduction and Error Analysis for the Physical Sciences*. McGraw-Hill.

Bird, R.B., Stewart, W.E., Lightfoot, E.N., 2007. *Transport Phenomena*. Second Edition, John Wiley & Sons, Inc., New York.

Birmilli, W., Stratmann, F., Wiedensohler, A., Covert, D., Russell, L.M., Berg, O., 1997. Determination of Differential Mobility Analyzer Transfer Functions Using Identical Instruments in Series. *Aerosol Sci. & Technol.*, 27: 215-223.

Biskos, G., Reavell, K., Collings, N., 2005. Description and Theoretical Analysis of a Differential Mobility Spectrometer. *Aerosol Sci. & Technol.*, 39: 527-541.

Biskos, G., Malinowski, A., Russel, L. M., Buseck, P. R., Martin, S. T., 2006a. Nanosize Effect on the Deliquescence and the Efflorescence of Sodium Chloride Particles. *Aerosol Sci. Technol.*, 40: 97–106.

Biskos, G., Paulsen, D., Russel, L. M., Buseck, P. R., Martin, S. T., 2006b. Prompt deliquescence and efflorescence of aerosol nanoparticles. *Atmos. Chem. Phys.*, 6: 4633 - 4642.

Biskos, G., Russel, L. M., Buseck, P. R., Martin, S. T., 2006c. Nanosize effect on the hygroscopic growth factor of aerosol particles. *Geophys. Res. Lett.*, 33: L07801.

Biskos, G., Vons, V., Yurteri C.U, Schmidt-Ott, A., 2008. Generation and Sizing of Particles for Aerosol-based Nanotechnology. *KONA Powder & Particle*, 26: 13-35.

Brunelli, N. A., Flagan, R. C., Giapis, K. P., 2009. Radial differential mobility analyzer for one nanometer particle classification. *Aerosol Sci. & Technol.*, 43: 53–39.

Capps, C. D., Henning, R. L., Hess, G. M., 1982. Analytic inversion of remote-sensing data. *Appl. Opt.*, 21: 3581–3587.

Chahine, M. T., 1968. Determination of the Temperature Profile in an Atmosphere from its Outgoing Radiance. *J. Opt. Soc. Am.*, 58: 1634–1637.

Charlson, R.J., Schwartz, S.E., Hales, J.M., Cess, R.D., Coakley, J.A., Jr., Hansen, J.E., Hofmann, D.J., 1992. Climate Forcing by Anthropogenic Aerosols. *Science*, 255: 423-430.

Chang, R.Y.-W. et al., 2011. Relating atmospheric and oceanic DMS levels to particle nucleation events in the Canadian Arctic. *J. Geophys. Res.*, 116: D00S03.

Chen, D.R., Li, W., Cheng, M.D., 2007. Development of a Multiple-Stage Differential Mobility Analyzer (MDMA). *Aerosol Sci. & Technol.*, 41: 217-230.

Cocker, D. R., Whitlock, N. E., Flagan, R. C., Seinfeld, J. H., 2001. Hygroscopic Properties of Pasadena, California Aerosol. *Aerosol Sci. Technol.,* 35: 637–647.

Cohen, M. D., Flagan, R. C., Seinfeld, J. H., 1987a. Studies of Concentrated Electrolyte Solutions Using the Electrodynamic Balance. 1. Water Activities for Single-Electrolyte Solutions. *J. Phys. Chem.*, 91: 4563–4574.

Cohen, M. D., Flagan, R. C., Seinfeld, J. H., 1987b. Studies of Concentrated Electrolyte Solutions Using the Electrodynamic Balance. 3. Solute Nucleation. *J. Phys. Chem.*, 91: 4583–4590.

Coleman, T.F. , Li, Y.,1994. On the Convergence of Reflective Newton Methods for Large-Scale Nonlinear Minimization Subject to Bounds. *Math Program*, 67: 189-224.

Coleman, T.F., Li, Y., 1996. An Interior, Trust Region Approach for Nonlinear Minimization Subject to Bounds. *SIAM J. Optimiz.*, 6: 418-445.

Covert, D., Heintzenberg, J., 1993. Size distributions and chemical properties of aerosol at Ny Ålesund, Svalbard. *Atmospheric Environ. Part -Gen. Top.*, 27: 2989–2997.

Crump, J. G., Seinfeld, J. H., 1981. A New Algorithm for Inversion of Aerosol Size Distribution Data. *Aerosol Sci. & Technol*., 1: 15 - 34.

Cubison, M. J., Coe, H., Gysel, M. 2005. A modified hygroscopic tandem DMA and a data retrieval method based on optimal estimation. *J. Aerosol Sci.*, 36: 846–865.

Curry, B. P., 1989. Constrained eigenfunction method for the inversion of remote sensing data: application to particle size determination from light scattering measurements. *Appl. Opt.*, 28: 1345–1355.

de la Mora, F., 2002. Diffusion broadening on converging differential mobility analyzers. *J. Aerosol Sci.*, 33: 411-437.

de la Mora, F., 2010. Personal communication.

Dockery, D. W., Pope, C. A., Xu, X., Spengler, J. D., Ware, J. H., Fay, M. E., Ferris, B. G., Speizer, F. E., 1993. An association between air pollution and mortality in size U.S. cities. *J. Med.*, 329: 1753-1759.

Donaldson, K., Li, X. Y., MacNee, W., 1998. Ultrafine (nanometer) particle mediated lung injury. *J. Aerosol Sci.*, 29: 553-560.

Downard, A.J., Dama, J.F., Flagan, R.C., 2011. An Asymptotic Analysis of Differential Electrical Mobility Classifiers. *Aerosol Sci. & Technol*., 45: 717 – 729.

Eleftheriadis, K., Nyeki, S., Psomiadou, C., Colbeck, I., 2004. Background aerosol properties in the European Arctic. *Water Air Soil Pollut. Focus*, 4: 23–30.

Eleftheriadis, K., Vratolis S., Nyeki S., 2009. Aerosol black carbon in the European Arctic: Measurements at Zeppelin station, Ny-Ålesund, Svalbard from 1998–2007. *Geophys. Res. Lett.*, 36, L02809.

Endo, Y., Fukushima, N., Tashiro, S., Kousaka, Y., 1997. Performance of a Scanning Differential Mobility Analyzer. *Aerosol Sci. & Technol*., 26: 43-50.

Engvall, A.C. et al., 2008. Changes in aerosol properties during spring-summer period in the Arctic troposphere. *Atmos. Chem. Phys.*, 8: 445–462.

Ferri, F., Giglio, M., Perini, U., 1989. Inversion of light scattering data from fractals by the Chahine iterative algorithm. *Appl. Opt.*, 28: 3074–3082.

Fierz, M., Vernooij, M. G. C., Burtscher, H., 2007. An improved low-flow thermodenuder. *J. Aerosol Sci.*, 38: 1163–1168.

Fierz-Schmidhauser, R., Zieger, P., Wehrle, G., Jefferson, A., Ogren, J.A., Baltensperger, U., Weingarther, E., 2010. Measurement of Relative Humidity Dependent Light Scattering of Aerosol, *Atmos. Meas. Tech.*, 3: 39-50.

Fissan, H. J., Helsper, C., Thielen, H. J., 1983. Determination of particle size distributions by means of an electrostatic classifier. *J. Aerosol Sci.*, 14: 354–357.

Fissan, H., Hummes, D., Stratmann, F., Buscher, P., Neumann, S., Pui, D.Y.H., Chen, D., 1996. Experimental Comparison of Four Differential Mobility Analyzers for Nanometer Aerosol Measurements. *Aerosol Sci. & Technol*., 24: 1 – 13.

Forsythe, W. E., 2003. *Smithsonian Physical Tables*. Knovel.

Flagan, R.C., 1998. History of Electrical Aerosol Measurements. *Aerosol Sci. & Technol*., 28: 301-380.

Flagan, R.C., 1999. On Differential Mobility Analyzer Resolution. *Aerosol Sci. & Technol.*, 30: 566-570.

Flagan, R. C., Lunden, M. M., 1995. Particle structure control in nanoparticle synthesis from vapor phase. *Mat. Sci. Eng.*, A204: 113–124.

Freney, E., Martin, S., Buseck, P., 2009. Deliquescence and Efflorescence of Potassium Salts Relevant to Biomass-Burning Aerosol Particles. *Aerosol Sci. Technol.*, 43: 799–807.

Frey, A. et al., 2008. Application of the volatility-TDMA technique to determine the number size distribution and mass concentration of less volatile particles. *Aerosol Sci. Technol*., 42: 817–828.

Gao, Y., Chen, S.-B., Yu, L., 2006. Efflorescence Relative Humidity for Ammonium Sulfate Particles. *J. Phys. Chem. A*, 110: 7602–7608.

Gao, Y., Chen, S.-B., Yu, L., 2007. Efflorescence relative humidity of airborne sodium chloride particles: A theoretical investigation. *Atmos. Environ.*, 41: 2019–2023.

Geng, H. et al., 2010. Single-Particle Characterization of summertime Arctic aerosols collected at Ny-Ålesund, Svalbard. *Environ. Sci. Technol.*, 44: 2348–2353.

Giamarelou, M., Stolzenburg, M., Biskos, G., 2012. The Multiple Monodisperse Outlet Differential Mobility Analyzer: Derivation of its Transfer Function and Resolution. *Aerosol Sci. & Technol.*, 46: 951–965.

Giamarelou, M., Stolzenburg, M., Chen, D-R., Biskos, G., 2013. Comparison Between the Theoretical and Experimental Performance of a Differential Mobility Analyzer with Three Monodisperse-Particle Outlets. *Aerosol Sci. & Technol.*, 47: 406-416.

Golub, G. H., Heath, M., Wahba, G., 1979. Generalized Cross-Validation as a Method for Choosing a Good Ridge Parameter. *Technometrics,* 21: 215–223.

Grassl, H., 1971. Determination of Aerosol Size Distributions from Spectral Attenuation Measurements. *Appl. Opt.*, 10: 2534–2538.

Gysel, M., 2003. Hygroscopic properties of aerosols. Investigations of particles from jet engines and the remote troposphere. PhD Thesis. ETH, Swiss Federal Institute of Technology Zurich.

Gysel, M. et al., 2007. Closure study between chemical composition and hygroscopic growth of aerosol particles during TORCH2. *Atmos Chem Phys*, 7: 6131–6144.

Gysel, M., McFiggans, G. B., Coe, H., 2009. Inversion of tandem differential mobility analyser (TDMA) measurements. *J. Aerosol Sci.,* 40: 134–151.

Gysel, M., 2009, Brief Manual for TDMAinv Toolkit, PSI, Laboratory of Atmospheric Chemistry.

Haaf, W., 1980. Accurate Measurements of Aerosol Size Distribution – II. Construction of a New Plate Condenser Electric Mobility Analyzer and First Results. *J. Aerosol Sci.*, 11: 201-212.

Hagwood, C., Sivathanu, Y., Mulholland, G., 1999. The DMA Transfer Function with Brownian Motion a Trajectory/Monte-Carlo Approach. *Aerosol Sci. & Technol*., 30: 40-61.

Häkkinen, S.A.K. et al., 2012. Long-term volatility measurements of submicron atmospheric aerosol in Hyytiälä, Finland. *Atmos. Chem. Phys.*, 12: 10771-10786.

Hameri, K., Vakeva, M., Hansson, H.-C., Laaksonen, A., 2000. Hygroscopic Growth of Ultrafine Ammonium Suplhate Aerosol Measured Using an Ultrafine Tandem Differential Mobility Analyzer. *J. Geophys. Res.* 105: 22231–22242.

Hameri, K., Laaksonen, A., Vakeva, M., Suni, T., 2001. Hygroscopic Growth of Ultrafine Sodium Chloride Particles. *J. Geophys. Res.,* 106: 20749–20757.

Hansen, P. C., 1992. Analysis of discrete ill-posed problems by means of the L-curve. *SIAM Rev,* 34: 561–580.

Hansen, P. C., O’Leary, D. P., 1993. The use of the L-curve in the regularization of discrete ill-posed problems. *SIAM J Sci. Comput.*, 14: 1487–1503.

Haywood, J.M., Francis, P.N., Glew, M.D., Taylor, J.P., 2001. Optical Properties and Direct Radiative Effect of Saharan Dust: A Case Study of Two Saharan Dust Outbreaks Using Aircraft Data. *J. Geophys. Res.*, 106: 18417-18430.

Heintzenberg, J., Leck, C., 1994. Seasonal variation of the atmospheric aerosol near the top of the marine boundary layer over Spitsbergen related to the Arctic sulfur cycle. *Tellus Ser. B-Chem. Phys. Meteorol.*, 46: 52–67.

Hewitt, G. W., 1957. The charging of small particles for electrostatic precipitation. *Am. Inst. Electr. Eng. Part Commun. Electron. Trans. Of*, 76: 300–306.

Hinds, W.C., 1999. *Aerosol Technology: Properties, Behavior, and Measurement of Airborne Particles.*, John Wiley & Sons, Inc., New York.

Hitzenberger, R., Rizzi, R., 1986. Retrieved and measured aerosol mass size distributions: a comparison. *Appl. Opt.*, 25: 546-553.

Hoppel, W.A., 1978. Determination of the Aerosol Size Distribution from the Mobility Distribution of the Charged Fraction of Aerosols. *J. Aerosol Sci.*, 9: 41-54.

Hutchison, D.A., 1944. Density of Potassium Chloride. *Physical Review,* 66: 144–148.

IPCC, Solomon, S., Qin, D., Manning, M., Marquis, M., Averyt, K., Tignor, M. M. B., Miller, H. L. J., and Chen, Z. (eds.), 2007. *Climate Change 2007 – The Physical Science Basis. Contribution of Working Group I to the Fourth Assessment Report of the Intergovernmental Panel on Climate Change,* Cambridge University Press, Cambridge, 153–154 and 171–172.

Johnson, T., Caldow, R., Pöcher, A., Mirme, A. et al., 2004. A New Electrical Mobility Particle Sizer Spectrometer for Engine Exhaust Particle Measurements. *SAE Technical Paper* 2004-01-1341doi:10.4271/2004-01-1341.

Karl, M., Leck, C., Gross, A., Pirjola, L., 2012. A study of new particle formation in the marine boundary layer over the central Arctic Ocean using a flexible multicomponent aerosol dynamic model. *Tellus Ser. B-Chem. Phys. Meteorol.*, 64, 17158.

Kelly, J. T., Wexler, A. S., 2006. Water uptake by aerosol: Water activity in supersaturated potassium solutions and deliquescence as a function of temperature. *Atmos. Environ.*, 40: 4450–4468.

Knutson, E.O., Whitby, K.T., 1975. Aerosol Classification by Electric Mobility: Apparatus, Theory, and Applications. *J. Aerosol Sci.*, 6: 443-451.

Knutson, E. O., 1976. Extended Electric Mobility Method for Measuring Aerosol Particle Size and Concentration. In *Fine Particles*, Ed., Liu, B.Y.H., 739–762.

Köhler, H., 1936. The Nucleus in and the Growth of Hygroscopic Droplets. *Trans. Faraday Soc.*, 32: 1152–1161.

Kousaka, Y., Okuyama, K., Adachi, M., 1985. Determination of Particle Distribution of Ultra-Fine Aerosols using Differential Mobility Analyzer, *Aerosol Sci. & Technol.*, 4:209-225.

Kousaka, Y., Okuyama, K., Adachi, M., Mimura, T., 1986. Effect of Brownian Diffusion on Electrical Classification of Ultrafine Aerosol Particles in Differential Mobility Analyzer, *J. Chem. Eng. Japan*, 19: 401-407.

Kramer, L., Poschl, U., Niessner, R., 2000. Microstructural rearrangement of sodium chloride condensation aerosol particles on interaction with water vapor. *J. Aerosol Sci.*, 31: 673–685.

Kuang, Z.M., Yung, Y.L., 2000. Refrectivity Variations off the Peru Coast: Evidence for Indirect Effect of Anthropogenic Sulfate Aerosols on Clouds. *Geophys. REs. Lett.*, 27: 2501-2504.

Kulmala, M. et al., 2004. Formation and growth rates of ultrafine atmospheric particles: a review of observations. *J. Aerosol Sci.*, 35: 143–176.

Kulmala, M. et al., 2013. Direct observations of atmospheric aerosol nucleation. *Science*, 339: 943–946.

Korhonen, P. et al., 1999. Ternary nucleation of H2SO4, NH3, and H2O in the atmosphere. *J. Geophys. Res.*, 104: 26349–26353.

Lau, R., Chuah, H.K.L., 2013. Dynamic Shape Factor for particles of Various Shapes in the Intermediate Settling Regime. *Advanced Powder Technology*, 24: 306-310.

Leck, C., Bigg, E. K., 2010. New particle formation of marine biological origin. *Aerosol Sci. Technol*., 44: 570–577.

Lesnic, D., Elliott, L., Ingham, D. B., 1995. An inversion method for the determination of the particle size distribution from diffusion battery measurements. *J. Aerosol Sci.*, 26: 797–812.

Li, W., 2006. Operation of differential mobility analyzers (DMAs). PhD Thesis, Washington University, St. Louis.

Li, W., Li. ,L., Chen, D-R., 2006. Technical Note: A New Deconvolution Scheme for the Retrieval of the True DMA Transfer Function from the Tandem DMA Data. *Aerosol Sci. & Technol.*, 40: 1052-1057.

Liu, B.Y.H., Pui, D.Y.H., 1974. A Submicron Aerosol Standard and the Primary, Absolute Calibration of the Condensation Nuclei Counter. *J. Colloid & Interface Sci.*, 47: 155-171.

Liu, B. Y. H., Pui, D. Y. H., Whitby, K. T., Kittelson, D. B., Kousaka, Y., McKenzie, R. L., 1978. Aerosol Mobility Chromatograph - New Detector for Sulfuric-Acid Aerosols. *Atmos. Environ.*, 12: 99–104.

Lloyd, J. J., Taylor, C. J., Lawson, R. S., Shields, R. A., 1997. The use of the L-curve method in the inversion of diffusion battery data. *J. Aerosol Sci.*, 28: 1251–1264.

Loeb, N.G., Kato, S., 2002. Top-of-atmosphere Direct Radiative Effect of Aerosols over the Tropical Oceans from the Clouds and the earth's Radiant Energy System (CERES) Satelline Instrument. *J. Clim.*, 15: 1474-1484.

Martinsson, B.G., Karlsson, M.N.A., Frank, G., 2001. Methodology to Estimate the Transfer Function of Individual Differential Mobility Analyzers. *Aerosol Sci. & Technol.*, 35: 815-823.

Martin, S. T., 2000. Phase Transitions of Aqueous Atmospheric Particles. *Chem. Rev.*, 100: 3403–3453.

Marquardt, D. W., 1963. An Algorithm for Least-Squares Estimation of Nonlinear Parameters. *SIAM*, 11: 431–441.

Markowski, G. R., 1987. Improving Twomey’s Algorithm for Inversion of Aerosol Measurement Data. *Aerosol Sci. Technol.*, 7: 127–141.

Markwardt, C., 2010, MPFIT: A MINPACK-1 Least Squares Fitting Library in C. <http://www.physics.wisc.edu/~craigm/idl/cmpfit.html> (2014/05/25)

Maturilli, M. et al., 2012. Continuous meteorological observations at station Ny-Ålesund (2008-07). Alfred Wegener Institute for Polar and Marine Research - Research Unit Potsdam, doi:10.1594/PANGAEA.775676, In Supplement to: Maturilli, Marion; Herber, Andreas; Kϕnig-Langlo, Gert (2013): Climatology and Time Series of Surface Meteorology in Ny-Ålesund, Svalbard. *Earth System Science Data*, 5(1): 155-163, doi:10.5194/essd-5-155-2013.

McFiggans, G., Artaxo, P., Baltensperger, U., Coe, H., Facchini, M. C., Feingold, G., Fuzzi, S., Gysel, M., Laaksonen, A., Lohmann, U., Mentel, T. F., Murphy, D. M., O'Dowd, C. D., Snider, J. R., Weingartner, E., 2006. The Effect of Physical and Chemical Aerosol Properties on Warm Cloud Droplet Activation. *Atmos. Chem. Phys.,* 6: 2593–2649.

McMurry, P. H., Takano, H., Anderson, G. R., 1983. Study of the ammonia (gas)-sulfuric acid (aerosol) reaction rate. *Environ. Sci. Technol.*, 17: 347–352.

McMurry, P.H., 2000. A Review of Atmospheric Aerosol Measurements. *Atmos. Environ.,* 34: 1959-1999.

Mei, F., Huijing, F., Chen, D.-R., 2011. A Cost-effective Differential Mobility Analyzer (cDMA) for Multiple DMA Column Applications. *J. Aerosol Sci.*, 42: 462-473.

Meyer, N. K. et al., 2009. Analysis of the hygroscopic and volatile properties of ammonium sulphate seeded and unseeded SOA particles. *Atmos Chem Phys*, 9: 721–732.

Mikkonen, S. et al., 2011. A statistical proxy for sulphuric acid concentration. *Atmos. Chem. Phys.*, 11: 11319-11334.

Mifflin, A. L., Smith, M. L., Martin, S. T., 2009. Morphology Hypothesized to Influence Aerosol Particle Deliquescence. *Phys. Chem. Chem. Phys.*, 11: 10095–10107.

Minambres, L., Mendez, E., Sanchez, M. N., Castano, F., Basterretxea, F. J., 2011. Water uptake properties of internally mixed sodium halide and succinic acid particles. *Atmos. Environ.*, 45: 5896–5902.

NOAA, 2014. *HYSPLIT - Hybrid Single Particle Lagrangian Integrated Trajectory Model*. Available at http://www.arl.noaa.gov/ (9/2/2014).

NSIDC, 2014. *National Snow & Ice Data Center*. Available at http://nsidc.org/ (9/2/2014).

Nyeki, S. et al., 2005. Overview of aerosol microphysics at Arctic sunrise: Measurements during the NICE renoxification study. *Tellus Ser. B-Chem. Phys. Meteorol.*, 57: 40–50.

O’Dowd, C. D. et al., 2002. Marine aerosol formation from biogenic iodine emissions. *Nature*, 417: 632–636.

Okuyama, K., Kousaka, Y., Motouchi, T., 1984. Condensation Growth of Ultrafine Aerosol-Particles in a New Particle-Size Magnifier. *Aerosol Sci. & Technol.*, 3: 353-366.

Paatero, P., 1991. Extreme value estimation, a method for regularizing ill-posed inversion problems, in *Ill-posed Problems in Nature Sciences: Proceedings of the International Conference*, Ed., A. Tikhonov, 118-133.

Paasonen, P. et al., 2012. On the formation of sulphuric acid – amine clusters in varying atmospheric conditions and its influence on atmospheric new particle formation. *Atmos. Chem. Phys.*, 12: 9113–9133.

Park, K., Kim, J.-S., Miller, A. A., 2009. Study on effects of size and structure on hygroscopicity of nanoparticles using a tandem differential mobility analyzer and TEM. *J. Nanoparticle Res.*, 11: 175–183.

Perry, H. R., Green, W. D., 1997. *Perry's Chemical Engineers' Handbook*. McGraw-Hill.

Phillips, D. L. A, 1962. Technique for the Numerical Solution of Certain Integral Equations of the First Kind. *J ACM*, 9: 84–97.

Pourpix, M., Daval, J., 1990. Electrostatic Precipitation of Aerosol on Wafers, a New Mobility Spectrometer. In S. Masuda and K. Takahashi (eds.), *Aerosols: Science, Industry, Health and Environment* (Proceedings of the Third Int. Aerosol Conference, 24-27 Sept, 1990, Kyoto, Japan), Vol. II, Pergamon Press, Oxford, UK.

Pourprix, M.,1994. Sélecteur de particules chargées, a haute sensibilité, Brevet francais No. 94 06273, 24 Mal.

Pruppacher, H. R., Klett, J. D., 1997. *Microphysics of Clouds and Precipitation*. Kluwer.

Rader, D. J., McMurry, P. H., 1986. Application of the Tandem Differential Mobility Analyzer to Studies of Droplet Growth or Evaporation. *J. Aerosol Sci.*, 17: 771–787.

Rader, D. J., McMurry, P. H., Smith, S., 1987. Evaporation Rates of Monodisperse Organic Aerosols in the 0.02- to 0.2-μm-Diameter Range. *Aerosol Sci. Technol.,* 6: 247–260.

Ramachandran, G., Kandlikar, M., 1996. Bayesian analysis for inversion of aerosol size distribution data. *J. Aerosol Sci*., 27: 1099–1112.

Ramachandran, G., Leith, D., 1992. Extraction of Aerosol-Size Distributions from Multispectral Light Extinction Data. *Aerosol Sci. Technol.*, 17: 303–325.

Ramm, A. G., 2005. *Inverse problems: Mathematical and Analytical Techniques with Applications to Engineering*. Springer.

Robinson, R. A., Stokes, R. H., 2002. *Electrolyte Solutions*. Dover Publications Inc.

Roth, P., Filippov, A. V., 1996. In situ ultrafine particle sizing by a combination of pulsed laser heatup and particle thermal emission. *J. Aerosol Sci.,* 27: 95–104.

Riley, K.F., Hobson, M.P., Bence, S.J., 2009. *Mathematical Methods for Physics and Engineering*. Cambridge University Press, Cambridge.

Riipinen, I. et al., 2012. The contribution of organics to atmospheric nanoparticle growth. *Nature Geosci.,* 5: 453–458.

Rizzi, R., Guzzi, R., Legnani, R., 1982. Aerosol size spectra from spectral extinction data: the use of a linear inversion method. *Applied Optics*, 21:1578-1587.

Rosell-Llompart, J., Loscertales, I. G., Bingham, D., de la Mora, J.F., 1996. Sizing Nanoparticles and Ions with a Short Differential Mobility Analyzer. *J. Aerosol Sci.*, 27: 695-719.

Russell, L. M., Ming, Y., 2002. Deliquescence of small particles. *J. Chem. Phys.*, 116: 311–321.

Salm, J., 2000. Diffusion Distortions in a Differential Mobility Analyzer: The Shape of Apparent Mobility Spectrum. *Aerosol Sci. & Technol.,* 32: 602-612.

Santer, R., Herman, M., 1983. Particle size distributions from forward scattered light using the Chahine inversion scheme. *Appl. Opt.*, 22: 2294–2301.

Santos, J.P., Hontañón, E., Ramiro, E., Alonso, M., 2009. Performance Evaluation of a High-resolution Parallel-plate Differential Mobility Analyzer. *Atmos. Chem. Phys., 9*: 2419–2429.

Scheibel, H. G., Porstendorfer, J., 1983. Generation of Monodisperse Ag- and NaC1-Aerosols With Particle Diamemers Between 2 and 300 nm. *J. Aerosol Sci.*, 14: 113–126.

Schwartz, S.E., 1996. The Whitehouse Effect - Shortwave Radiative Forcing of Climate by Anthropogenic Aerosols: An Overview. *J. Aerosol Sci.,* 27: 359-382.

Seol, K. S., Yabumoto, J., Takeuchi, K., 2002. A Differential Mobility Analyzer with Adjustable Column Length for Wide Particle-Size-Range Measurements. *J. Aerosol Sci.,* 33: 1481–1492.

Seinfeld, J. H., Pandis, S. N., 2006. *Atmospheric Chemistry and Physics: From Air Pollution to Climate Change*. Wiley, New-Jersey.

Shah, A. A., Ali, K., Bilal, S., 2013. Surface tension, surface excess concentration, enthalpy and entropy of surface formation of aqueous salt solutions. *Colloids and Surfaces A: Physicochem Eng. Aspects*, 414: 183–190.

Sipilä, M. et al., 2010. The role of sulfuric acid in atmospheric nucleation. *Science*, 327: 1243–1246.

Sjogren, S. et al., 2008. Hygroscopicity of the submicrometer aerosol at the high-alpine site Jungfraujoch, 3580 m a.s.l., Switzerland. *Atmos Chem Phys*, 8: 5715–5729.

Stolzenburg, M., 1988. *An Ultrafine Aerosol Size Distribution Measuring System*, PhD Thesis, University of Minnesota, St. Paul, MN.

Stolzenburg, M. R., McMurry, P. H., 1988. *TDMAFIT Users Manual.* University of Minnesota, Department of Mechanical Engineering. Particle Technology Laboratory.

Stolzenburg, M., McMurry, P., 2008. Equations Governing Single and Tandem DMA Configurations and a New Lognormal Approximation to the Transfer Function. *Aerosol Sci. & Technol.*, 42: 421-432.

Stratmann, F., Kauffeldt, Th., Hummes, D., Fissan, H., 1997. Differential Electrical Mobility Analysis: A Theoretical Study. *J. Aerosol Sci. & Technol*., 26: 368-383.

Swietlicki, E., Hansson, H. C., Hameri, K., Svenningsson, B., Massling, A., McFiggans, G., McMurry, P. H., Petaja, T., Tunved, P., Gysel, M., Topping, D., Weingartner, E., Baltensperger, U., Rissler, J., Wiedensohler, A., Kulmala, M., 2008. Hygroscopic Properties of Submicrometer Atmospheric Aerosol Particles

Measured with H-TDMA Instruments in Various Environments - A Review. *Tellus B*, 60: 432–469.

Takeuchi, K., Yabumoto, J., Okada, Y., Kawai, T., Montajir, R. M., Goto, Y., 2005. A New Dual-Type DMA for Measuring Nanoparticles Emitted from Combustion Engines. *J. Nanoparticle Res.*, 7: 287–293.

Tammet, H., 1970. The Aspiration Method for the Determination of Atmospheric Ion Spectra (Vol. II). Jerusalem: Israel program for scientific translations.

Tammet, H., Mirme, A., Tamm, E., 1998. Electrical Aerosol Spectrometer of Tartu University. *J. Aerosol Sci.*, 29: S427-S428.

Tammet, H., Mirme, A., Tamm, E., 2002. Electrical Aerosol Spectrometer of Tartu University. *Atm. Res.*, 62*:* 315-324.

Tang, I. N., Munkelwitz, H. R., 1977. Aerosol Growth Studies - III Ammonium Bisulfate Aerosols In a Moist Atmosphere. *J. Aerosol Sci.*, 8: 321–330.

Tang, I. N., 1980. Deliquescence Properties and Particle Size Change of Hygroscopic Aerosols, in *Generation of Aerosols*, edited by Willeke K., Chapter 7. Butterworth, Stonham, Mass.

Tang, I. N., Munkelwitz, H. R., 1984. An investigation of solute nucleation in levitated solution droplets. *J. Colloid Interf. Sci.*, 98: 430–438.

Tang, I. N., Munkelwitz, H. R., Wang, N., 1986. Water Activity Measurements with Single Suspended Droplets: The NaCl-H2O and KCl-H2O Systems. *J. Colloid Interf. Sci.*, 114: 409–415.

Tang, I. N., Munkelwitz, H. R., 1993. Composition and Temperature Dependence of the Deliquescence Properties of Hygroscopic Aerosols. *Atmos. Environ.*, 27A: 467–473.

Tang, I. N., Munkelwitz, H. R., 1994. Aerosol Phase Transformation and Growth in the Atmosphere. *J. Appl. Meteorol.*, 33: 791–796.

Tang, I. N., 1996. Chemical and Size Effects of Hygroscopic Aerosols on Light Scattering Coefficients. *J. Geophys. Res.*, 101: 19245–19250.

Tang, I. N., Tridico, A. C., Fung, K. H., 1997. Thermodynamic and Optical Properties of Sea Salt Aerosols. *J. Geophys. Res.*, 102: 23269–23275.

Tarantola, A., 2005. *Inverse problem theory and methods for model parameter estimation*. SIAM. Philadelphia.

Taylor, J.R., 1997. *An Introduction to Error Analysis. The Study of Uncertainties in Physical Measurements*. Second Edition, University Science Books, Sausalito. CA.

ten Brink, H. M., Plomp, A., Spoelstra, H.,van de Vate, J. F., 1983. A high-resolution electrical mobility aerosol spectrometer (MAS). *J. Aerosol Sci.*, 14: 589–597.

Tikhonov, A. N., Arsenin, V. Y. 1977. *Solutions of Ill-posed Problems*. Winston & Sons.

Topping, D., 2008. Thermodynamics of Aqueous Systems. In *Environmental Chemistry of Aerosols*, Ed. Colbeck, I., 141–191, Blackwell Publishing Ltd.

Tunved, P. et al., 2006. High natural aerosol loading over boreal forests. *Science*, 312: 261-263.

Tunved, P., Ström, J., Krejci, R., 2013. Arctic aerosol life cycle: linking aerosol size distributions observed between 2000 and 2010 with air mass transport and precipitation at Zeppelin station, Ny-Ålesund, Svalbard. *Atmos. Chem. Phys.*, 13: 3643–3660.

Twomey, S., 1963. On the Numerical Solution of Fredholm Integral Equations of the First Kind by the Inversion of the Linear System Produced by Quadrature. *J ACM*, 10: 97–101.

Twomey, S., 1974. Pollution and the Planetary Albedo. *Atmos. Environ.*, 8: 1251-1256.

Twomey, S., 1975. Comparison of constrained linear inversion and an iterative nonlinear algorithm applied to the indirect estimation of particle size distributions. *J. Comput. Phys.*, 18: 188–200.

Twomey, S., 1977a. *Introduction to the Mathematics of Inversion in Remote Sensing and Indirect Measurements*. Elsevier.

Twomey, S., 1977b. Influence of pollution on shortwave albedo of clouds. *J. Atmos. Sci.*, 34: 1149–1152.

Wahba, G., 1977. Practical Approximate Solutions to Linear Operator Equations When the Data are Noisy. *SIAM J. Numer. Anal.*, 14: 651–667.

Wang, S.C., Flagan, R.C., 1990. Scanning Electrical Mobility Spectrometer. *Aerosol Sci. & Technol.,*13: 230-240.

Wang, J., McNeill, F.V., Collins, D.R., Flagan, R.C., 2002. Fast Mixing Condensation Nucleus Counter: Application to Rapid Scanning Differential Mobility Analyzer Measurements. *Aerosol Sci. & Technol*., 36: 678-689.

Weingartner, E., Gysel, M., Baltensperger, U., 2002. Hygroscopicity of Aerosol Particles at Low Temperatures. 1. New Low-Temperature H-TDMA Instrument: Setup and First Applications. *Environ. Sci. Technol.*, 36: 55–62.

Wexler, A. S., Seinfeld, J. H., 1991. Second-Generation Inorganic Aerosol Model. *Atmos. Environ.*, 25A: 2731–2748.

Wiedensohler, A. et al., 1996. Occurrence of an ultrafine particle mode less than 20 nm in diameter in the marine boundary layer during Arctic summer and autumn. *Tellus Ser. B-Chem. Phys. Meteorol.*, 48: 213–222.

Winklmayr, W., Wang, H.-C., John, W., 1990. Adaptation of the Twomey Algorithm to the Inversion of Cascade Impactor Data. *Aerosol Sci. Technol.*, 13: 322–331.

Wise, M. E., Surratt, J. D., Curtis, B., Shilling, J. E., Tolbert, M. A., 2003. Hygroscopic growth of ammonium sulfate/dicarboxylic acids. *J. Geophys. Res.*, 108: 4638–4645.

Wise, M. E., Biskos, G., Martin, S. T., Russel, L. M., Buseck, P. R., 2005. Phase Transitions of Single Salt Particles Studied Using a Transmission Electron Microscope with an Environmental Cell. *Aerosol Sci. Technol.*, 39: 849–856.

Van Rossum, G., Drake, F. L., 2001. *Python Reference Manual, PythonLabs, Virginia, USA, 2001. Available at http://www.python.org*.

Villani, P., Picard, D., Marchand, N., Laj, P., 2007. Design and validation of a 6-volatility tandem differential mobility analyzer (VTDMA). *Aerosol Sci. Tech*., 41: 898-906.

Voutilainen, A., Kolehmainen, V., Kaipio, J. P., 2000. *Statistical Inversion of Aerosol Size Measurement Data*.

Yee, E., 1989. On the interpretation of diffusion battery data. *J. Aerosol Sci.*, 20: 797–811.

Yli-Juuti, T. et al., 2011. Growth rates of nucleation mode particles in Hyytiala during 2003-2009: variation with particle size, season, data analysis method and ambient conditions. *Atmos. Chem. Phys.*, 11: 12865–12886.

Yli-Juuti, T. et al., 2013. Model for acid-base chemistry in nanoparticle growth (MABNAG). *Atmos. Chem. Phys.*, 13: 12507-12524.

Zhang, S., Akutsu, Y., Russell, L.M. , Flagan, R. C., Seinfeld, J. H., 1995. Radial Differential Mobility Analyzer. *Aerosol Sci. & Technol.*, 23: 357- 372.

Zhang, S.H., Flagan, R.C., 1996. Resolution of the Radial Differential Mobility Analyzer for Ultrafine Particles. *J. Aerosol Sci*., 27: 1179-1200.

Zhang, Y.-H., Chan, C. K., 2002. Understanding the Hygroscopic Properties of Supersaturated Droplets of Metal and Ammonium Sulfate Solutions Using Raman Spectroscopy. *J. Phys. Chem. A*, 106: 285–292.

Zhang, R., Khalizov, A., Wang, L., Hu, M., Xu, W., 2012. Nucleation and growth of nanoparticles in the atmosphere. *Chem. Rev.*, 112: 1957–2011.

Appendix A

Part A

From the definition of Dirac's delta function

$$2\int_0^x \delta_D(u)du = \begin{Bmatrix} +1, x > 0 \\ 0,\ x = 0 \\ -1, x < 0 \end{Bmatrix} \equiv H(x)\ , \qquad \text{(A-A.1)}$$

where $H(x)$ is a modification of the Heaviside step function so that

$$\int_0^x H(u)du = \begin{Bmatrix} +x,\ x \geq 0 \\ -x,\ x \leq 0 \end{Bmatrix} \equiv |x|\ . \qquad \text{(A-A.2)}$$

Upon substitution of Equations 2.14 and 2.20 into Equation 2.13, one gets

$$\Omega_{nd_i} = \int_{\Psi_1}^{\Psi_2} \left[\int_{\Psi_{i+2}}^{\Psi_{i+3}} \delta_D\left(\Psi_{out_i} - \Psi_{in} + Z_p \Delta\Phi_i\right) d\Psi_{out_i}\right] \frac{1}{(\Psi_2 - \Psi_1)} d\Psi_{in}\ . \qquad \text{(A-A.3)}$$

Substituting in $u_i \equiv \Psi_{out_i} - \Psi_{in} + Z_p \Delta\Phi_i$ and using Equation A-A.1, Equation A-A.3 yields

$$\begin{aligned} \Omega_{nd_i} = \frac{1}{2(\Psi_2 - \Psi_1)} \int_{\Psi_1}^{\Psi_2} \big[& H\left(\Psi_{i+3} - \Psi_{in} + Z_p \Delta\Phi_i\right) \\ & - H\left(\Psi_{i+2} - \Psi_{in} + Z_p \Delta\Phi_i\right)\big]\ d\Psi_{in} \end{aligned}\ . \qquad \text{(A-A.4)}$$

If one further substitutes $y_{i3} \equiv \Psi_{i+3} - \Psi_{in} + Z_p \Delta\Phi_i$, and $y_{i2} \equiv \Psi_{i+2} - \Psi_{in} + Z_p \Delta\Phi_i$ and use Equation A-A.2, the non-diffusing transfer function for the *i*th exit of the MMO-DMA becomes

$$\begin{aligned} \Omega_{nd_i} = \frac{1}{2(\Psi_2 - \Psi_1)} \big\{ & \left|\Psi_{i+3} - \Psi_1 + Z_p \Delta\Phi_i\right| - \left|\Psi_{i+3} - \Psi_2 + Z_p \Delta\Phi_i\right| \\ & - \left|\Psi_{i+2} - \Psi_1 + Z_p \Delta\Phi_i\right| + \left|\Psi_{i+2} - \Psi_2 + Z_p \Delta\Phi_i\right| \big\} \end{aligned}\ . \qquad \text{(A-A.5)}$$

To transform Equation A-A.5 to dimensionless form I begin by multiplying and dividing by $\Delta\Psi_i^*$ and using Equations 2.25 and 2.26 to get

$$\begin{aligned} \Omega_{nd_i} = \frac{\Delta\Psi_i^*}{2(\Psi_2 - \Psi_1)} \Bigg\{ & \left|\frac{\Psi_{i+3} - \Psi_1}{\Delta\Psi_i^*} - \tilde{Z}_{p_i}\right| - \left|\frac{\Psi_{i+3} - \Psi_2}{\Delta\Psi_i^*} - \tilde{Z}_{p_i}\right| \\ & - \left|\frac{\Psi_{i+2} - \Psi_1}{\Delta\Psi_i^*} - \tilde{Z}_{p_i}\right| + \left|\frac{\Psi_{i+2} - \Psi_2}{\Delta\Psi_i^*} - \tilde{Z}_{p_i}\right| \Bigg\} \end{aligned}\ . \qquad \text{(A-A.6)}$$

Using Equations 2.3, 2.24 and 2.27-2.28 one obtains:

$$\frac{2(\Psi_2-\Psi_1)}{\Delta\Psi_i^*}=\frac{2Q_a}{(Q_{sh_i}+Q_{m_i})/2}=2\beta_i(1-\delta_i)\ . \tag{A-A.7}$$

Also using Equations 2.3-2.6, 2.24 and the definitions in Equations 2.27-2.28, is calculated:

$$\frac{\Psi_{i+3}-\Psi_1}{\Delta\Psi_i^*}=\frac{\frac{1}{2}(Q_{sh_i}+Q_a)+\frac{1}{2}(Q_{m_i}+Q_{s_i})}{\frac{1}{2}(Q_{sh_i}+Q_{m_i})}=1+\frac{Q_a+Q_{s_i}}{Q_{sh_i}+Q_{m_i}}=1+\beta_i\ . \tag{A-A.8}$$

Similarly,

$$\frac{\Psi_{i+3}-\Psi_2}{\Delta\Psi_i^*}=1+\beta_i\delta_i\ , \tag{A-A.9}$$

$$\frac{\Psi_{i+2}-\Psi_1}{\Delta\Psi_i^*}=1-\beta_i\delta_i\ , \tag{A-A.10}$$

$$\frac{\Psi_{i+2}-\Psi_2}{\Delta\Psi_i^*}=1-\beta_i\ . \tag{A-A.11}$$

Substituting Equations A-A.7 - A-A.11 into A-A.6 and noting that $|-x|=|x|$, the dimensionless non-diffusing transfer function for the i^{th} exit of the MMO-DMA is obtained:

$$\begin{aligned}\Omega_{nd_i}=\frac{1}{2\beta_i(1-\delta_i)}\Big\{&\left|\tilde{Z}_{p_i}-(1+\beta_i)\right|-\left|\tilde{Z}_{p_i}-(1+\beta_i\delta_i)\right|\\&-\left|\tilde{Z}_{p_i}-(1-\beta_i\delta_i)\right|+\left|\tilde{Z}_{p_i}-(1-\beta_i)\right|\Big\}\end{aligned}\ . \tag{A-A.12}$$

Part B

In order to derive an analytical expression for the diffusing transfer function of the MMO-DMA, it is assumed a flow field with instantaneous changes in the axial velocity profile that causes discreet jumps in the particle trajectory. This is convenient for calculational purposes, but it does not capture the real radial flows near the aerosol entrance and exit slits. Our goal is to provide a rough estimate of the error incurred in the calculation of the integral represented by G_i as the result of ignoring the contribution of these radial flows to the total particle velocity.

Consider now an axial range about the j^{th} aerosol exit given by $-\Delta z \leq z - L_j \leq +\Delta z$. Within that range the contribution to G_i can be calculated as

$$\Delta G_i = \frac{2}{L_i}\left(\frac{4\pi}{Q_{sh_i}+Q_{m_i}}\right)\int_{L_j-\Delta z}^{L_j+\Delta z}(v_z^2 + v_r^2)r^2\frac{1}{v_z}dz, \tag{A-B.1}$$

where the integral has been left in dimensional form for convenience. This is calculated twice: once using the step jump in total flow from Q_{t_j} to $Q_{t_{j-1}}$ at $z = L_j$, and then using a linearly decreasing ramp in Q_t from Q_{t_j} at $z = L_j - \Delta z$ to $Q_{t_{j-1}}$ at $z = L_j + \Delta z$. In both cases, the axial flow profile will be considered to be fully-developed at all values of z. The first calculation ΔG_{step} corresponds to the model used in section 2.3.2.3 while the second ΔG_{ramp} uses a crude radial flow model sufficient for the purpose of this estimate and for particles relatively far from the exit slit, i.e., for particles headed for the i^{th} aerosol exit when $i < j$. The difference in these two values will be compared to G_i to give an estimate of the relative error in the latter and σ_i^2 due to use of the step in the flow profile.

Though ΔG_{step} can be calculated analytically, ΔG_{ramp} cannot; and both will be evaluated using simple numerical integration for the purpose of this estimate. As z is the variable of integration, it is necessary to relate v_r , v_z , and r or ω to z . The total flow for the two cases can be written as

$$Q_{t_{\text{step}}} = \begin{cases} Q_{t_j} & , \quad z < L_j \\ Q_{t_{j-1}} & , \quad z > L_j \end{cases} \text{, and} \tag{A-B.2}$$

$$Q_{t_{\text{ramp}}} = \frac{Q_{t_j}+Q_{t_{j-1}}}{2} - \frac{z-L_j}{\Delta z}\cdot\frac{Q_{s_j}}{2}\,. \tag{A-B.3}$$

The remainder of the derivation is essentially the same for both cases. The flow between the non-diffusing particle trajectory at z and the outer wall at R_2 can be rewritten from Equation 2.59 as

$$Q_i = Q_{i,j} + \frac{z-L_j}{L_i} \cdot \frac{Q_{sh_i}+Q_{m_i}}{2} \tag{A-B.4}$$

where $Q_{i,j} \equiv Q_i\big(z = L_j\big)$ as evaluated from Equation 2.59. The dimensionless radial position ω can be determined from the flow fraction function as given in Equations 2.66 and 2.67:

$$F_\gamma(\omega) = Q_i/Q_t \ . \tag{A-B.5}$$

The dimensional radial position is simply given by $r = R_2\sqrt{\omega}$. The average axial flow velocity is

$$U = \frac{Q_t}{\pi R_2^2(1-\gamma)} \ , \tag{A-B.6}$$

and the axial component of particle velocity is

$$v_z = U f_\gamma(\omega) \ , \tag{A-B.7}$$

where $f_\gamma(\omega)$ is given by Equation 2.65. v_r can be found by taking the derivative with respect to time for each side of Equation A-B.5. From the definition of $F_\gamma(\omega)$ in Equation 60

$$\frac{d}{dt}F_\gamma(\omega) = \frac{-1}{1-\gamma} f_\gamma(\omega)\frac{d\omega}{dt} = \frac{-1}{1-\gamma}\frac{v_z}{U}\frac{2r}{R_2^2}\frac{dr}{dt} = -\frac{2\pi v_z r}{Q_t} v_r \ . \tag{A-B.8}$$

The rate of change of Q_i is

$$\frac{dQ_i}{dt} = \frac{Q_{sh_i}+Q_{m_i}}{2L_i} \cdot v_z \ , \tag{A-B.9}$$

and the rate of change of Q_t is

$$\frac{dQ_{t_{\text{ramp}}}}{dt} = -\frac{Q_{s_j}}{2\Delta z} \cdot v_z \ , \quad \frac{dQ_{t_{\text{step}}}}{dt} = 0 \ . \tag{A-B.10}$$

Differentiating the right side of Equation A-B.5 gives:

$$\frac{d}{dt}F_\gamma(\omega) = \frac{1}{Q_t}\frac{dQ_i}{dt} - \frac{Q_i}{Q_t^2}\frac{dQ_t}{dt} = \frac{Q_{sh_i}+Q_{m_i}}{2L_iQ_t} \cdot v_z + \left[\frac{Q_{s_j}Q_i}{2\Delta z Q_t^2} \cdot v_z\right]_{\text{ramp}} \ . \tag{A-B.11}$$

Equating Equations A-B.8 and A-B.11 and rearranging gives:

$$v_r = \left[-\frac{Q_{sh_i}+Q_{m_i}}{4\pi L_i r}\right]_{\substack{\text{electrophoretic}\\ \text{migration}}} + \left[-\frac{Q_{s_j}}{4\pi\,\Delta z\, r}\left(\frac{Q_i}{Q_t}\right)\right]_{\text{advection}} \tag{A-B.12}$$

where the second term on the right side is only for the calculation of ΔG_{ramp} .

Thus, starting from z within the range $L_j - \Delta z \leq z \leq L_j + \Delta z$, one can calculate all the necessary variables ($\text{i.e.}, v_r$, v_z and r) to evaluate the integral in Equation A-B.1 numerically, and from that, ΔG_{step} and ΔG_{ramp}. G_i can be calculated as indicated in the section 2.3.2.3. If ΔG_{ramp} is taken as a reasonable approximation to the true value of ΔG_i as calculated from Equation A-B.1 using the true flow field, then $\left(\Delta G_{\text{step}} - \Delta G_{\text{ramp}}\right)/\Delta G_i$ can be interpreted as the relative error in the calculated value of G_i due to the neglect of the radial flow velocity component near the j^{th} aerosol exit where $j > i$. All that is left is to determine a value for Δz .

Firstly, a value of Δz is chosen that gives a rough match of radial flow velocities to axial flow velocities. Again, this is at some radial distance from the actual exit slit before the flow has converged significantly to pass through the relatively narrow slit. An example calculation has been done for the 3-monodisperse-particle-outlet DMA with $Q_{sh} = 20\,\text{lpm}$, $Q_a = 2\,\text{lpm}$ and $Q_{s_j} = 1.5\,\text{lpm}$, $j = 1, 2, 3$ designed and tested by Chen *et al.* (2007). For $i = 1$, the farthest outlet, and $j = 2$, the middle segment, the relative error in G_i is about -0.034%. As Δz decreases, the radial flow velocity increases and the error gets larger. For Δz equal to one fifth its original value, the error rises to -0.156% and, for five times the original value of Δz, the error is -0.010%. Thus, though there is much uncertainty in the most appropriate value for Δz, the relative error in the calculated values of G_i and σ_i^2 due to neglecting the radial flow near an exit slit that is passed is quite small, much less than 1% in this case.

At the very narrow exit slit for a particular particle trajectory (and to some extent at the entrance slit as well), the particle must pass through a region of much stronger radial flow, possibly resulting in a significantly greater error in the calculated G_i. A crude model of the converging flow here would be highly uncertain. Estimates of the errors incurred at the aerosol exit and entrance slits can be best addressed using a CFD model.

Part C

The final derivation of the transfer function for diffusing particles is analogous to that for non-diffusing particles in Part A. The single and double integrals of the base exponential function of f_{trans_i} (Equation 2.42) are obtained first:

$$\mathrm{erf}(x) \equiv \frac{2}{\sqrt{\pi}}\int_0^x \exp(-u^2)\ du \text{ , and} \tag{A-C.1}$$

$$\mathcal{E}(x) \equiv \int_0^x \mathrm{erf}(u)\, du = x \cdot \mathrm{erf}(x) + \frac{1}{\sqrt{\pi}}\exp(-x^2) \tag{A-C.2}$$

where $\mathrm{erf}(x)$ is the standard error function. The transfer function for diffusing particles is given by Equation 2.13, which using Equations 2.14 and 2.42 for f_{in} and f_{trans_i} , respectively, can be rearranged to

$$\Omega_{d_i} = \frac{1}{\Psi_2-\Psi_1}\int_{\Psi_1}^{\Psi_2}\left[\int_{\Psi_{i+2}}^{\Psi_{i+3}}\frac{1}{\sqrt{2\pi}\sigma_{\Gamma_i}}\exp\left[-\frac{1}{2}\left(\frac{\Psi_{out_i}-\Psi_{in}+Z_p\Delta\Phi_i}{\sigma_{\Gamma_i}}\right)^2\right]d\Psi_{out_i}\right]d\Psi_{in}\ . \tag{A-C.3}$$

One can now set:

$$u_i \equiv \frac{\Psi_{out_i}-\Psi_{in}+Z_p\Delta\Phi_i}{\sqrt{2}\sigma_{\Gamma_i}} \Longrightarrow du_i = \frac{d\Psi_{out_i}}{\sqrt{2}\sigma_{\Gamma_i}}\ ,$$

so that Equation A-C.3 yields

$$\Omega_{d_i} = \frac{1}{\Psi_2-\Psi_1}\int_{\Psi_1}^{\Psi_2}\left[\int_{y_{i2}}^{y_{i3}}\frac{1}{\sqrt{\pi}}\exp(-u_i^2)du_i\right]d\Psi_{in}\ ,$$

where $y_{i3} \equiv \frac{\Psi_{i+3}-\Psi_{in}+Z_p\Delta\Phi_i}{\sqrt{2}\sigma_{\Gamma_i}}$ and $y_{i2} \equiv \frac{\Psi_{i+2}-\Psi_{in}+Z_p\Delta\Phi_i}{\sqrt{2}\sigma_{\Gamma_i}}$. Using Equation A-C.1, it is obtained:

$$\Omega_{d_i} = \frac{1}{2(\Psi_2-\Psi_1)}\int_{\Psi_1}^{\Psi_2}\left[\mathrm{erf}\left(\frac{\Psi_{i+3}-\Psi_{in}+Z_p\Delta\Phi_i}{\sqrt{2}\sigma_{\Gamma_i}}\right) - \mathrm{erf}\left(\frac{\Psi_{i+2}-\Psi_{in}+Z_p\Delta\Phi_i}{\sqrt{2}\sigma_{\Gamma_i}}\right)\right]d\Psi_{in}\ , \tag{A-C.4}$$

analogous to Equation A-A.4 for non-diffusing particles. Noting that $dy_{i3} = -\frac{d\Psi_{in}}{\sqrt{2}\sigma_{\Gamma_i}}$ and $dy_{i2} = -\frac{d\Psi_{in}}{\sqrt{2}\sigma_{\Gamma_i}}$, Equation A-C.4 can be rewritten as

$$\Omega_{d_i} = \frac{-\sqrt{2}\sigma_{\Gamma_i}}{2(\Psi_2-\Psi_1)}\left[\int_{y_{i3}(\Psi_{in}=\Psi_1)}^{y_{i3}(\Psi_{in}=\Psi_2)} \mathrm{erf}(y_{i3})\, dy_{i3} - \int_{y_{i2}(\Psi_{in}=\Psi_1)}^{y_{i2}(\Psi_{in}=\Psi_2)} \mathrm{erf}(y_{i2})\, dy_{i2}\right].$$

Then using Equation A-C.2, the diffusing transfer function for the *i^th^* exit of the MMO-DMA becomes

$$\begin{aligned}\Omega_{d_i} = \frac{\sqrt{2}\sigma_{\Gamma_i}}{2(\Psi_2-\Psi_1)}\Bigg\{&\mathcal{E}\left(\frac{\Psi_{i+3}-\Psi_1+Z_p\Delta\Phi_i}{\sqrt{2}\sigma_{\Gamma_i}}\right) - \mathcal{E}\left(\frac{\Psi_{i+3}-\Psi_2+Z_p\Delta\Phi_i}{\sqrt{2}\sigma_{\Gamma_i}}\right)\\ &-\mathcal{E}\left(\frac{\Psi_{i+2}-\Psi_1+Z_p\Delta\Phi_i}{\sqrt{2}\sigma_{\Gamma_i}}\right) + \mathcal{E}\left(\frac{\Psi_{i+2}-\Psi_2+Z_p\Delta\Phi_i}{\sqrt{2}\sigma_{\Gamma_i}}\right)\Bigg\}.\end{aligned} \tag{A-C.5}$$

To transform this to dimensionless form, one begins by multiplying and dividing by $\Delta\Psi_i^*$ the prefactor on the right side of Equation A-C.5 as well as the argument of each $\mathcal{E}$ function. Using the definition in Equation 2.46 and following the examples of Equations A-A.6 - A-A.11, one calculates:

$$\frac{\sigma_{\Gamma_i}}{(\Psi_2-\Psi_1)} = \frac{\sigma_{\Gamma_i}}{\Delta\Psi_i^*}\cdot\frac{\Delta\Psi_i^*}{(\Psi_2-\Psi_1)} = \frac{\sigma_i}{\beta_i(1-\delta_i)}, \tag{A-C.6}$$

$$\frac{\Psi_{i+3}-\Psi_1+Z_p\Delta\Phi_i}{\sqrt{2}\sigma_{\Gamma_i}} = \frac{(1+\beta_i)-\tilde{Z}_{p_i}}{\sqrt{2}\sigma_i}, \tag{A-C.7}$$

$$\frac{\Psi_{i+3}-\Psi_2+Z_p\Delta\Phi_i}{\sqrt{2}\sigma_{\Gamma_i}} = \frac{(1+\beta_i\delta_i)-\tilde{Z}_{p_i}}{\sqrt{2}\sigma_i}, \tag{A-C.8}$$

$$\frac{\Psi_{i+2}-\Psi_1+Z_p\Delta\Phi_i}{\sqrt{2}\sigma_{\Gamma_i}} = \frac{(1-\beta_i\delta_i)-\tilde{Z}_{p_i}}{\sqrt{2}\sigma_i}, \text{ and} \tag{A-C.9}$$

$$\frac{\Psi_{i+2}-\Psi_2+Z_p\Delta\Phi_i}{\sqrt{2}\sigma_{\Gamma_i}} = \frac{(1-\beta_i)-\tilde{Z}_{p_i}}{\sqrt{2}\sigma_i}. \tag{A-C.10}$$

Substituting Equations A-C.7 - A-C.10 into A-C.5 and noting that $\mathcal{E}(-x) = \mathcal{E}(x)$, it gives the dimensionless diffusing transfer function for the *i^th^* exit of the MMO-DMA

$$\begin{aligned}\Omega_{d_i} = \frac{\sqrt{2}\sigma_i}{2\beta_i(1-\delta_i)}\Bigg\{&\mathcal{E}\left(\frac{\tilde{Z}_{p_i}-(1+\beta_i)}{\sqrt{2}\sigma_i}\right) - \mathcal{E}\left(\frac{\tilde{Z}_{p_i}-(1+\beta_i\delta_i)}{\sqrt{2}\sigma_i}\right)\\ &-\mathcal{E}\left(\frac{\tilde{Z}_{p_i}-(1-\beta_i\delta_i)}{\sqrt{2}\sigma_i}\right) + \mathcal{E}\left(\frac{\tilde{Z}_{p_i}-(1-\beta_i)}{\sqrt{2}\sigma_i}\right)\Bigg\}.\end{aligned} \tag{A-C.11}$$

Appendix B

The Figures B.1-B.10 show size distribution of potassium-halide particles for deliquescence- and efflorescence-mode experiments.

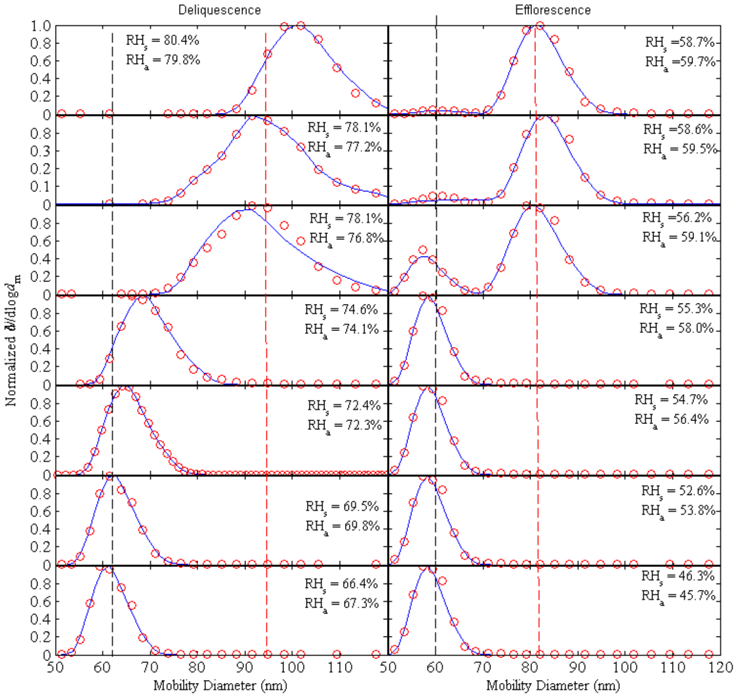

Figure B.1: KBr 60 nm deliquescence- and efflorescence- mode experiments. Size distributions measured and fitted with the TDMAfit algorithm.

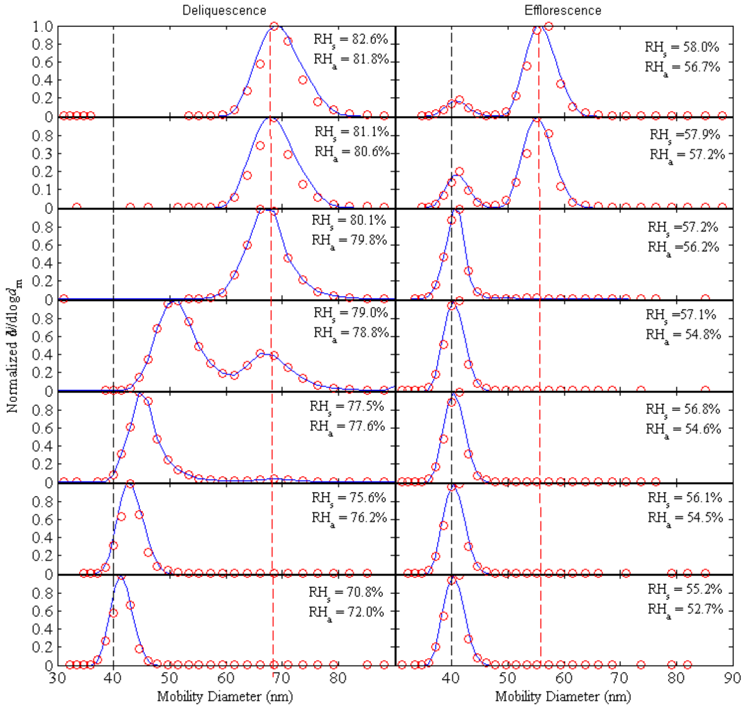

Figure B.2: KBr 40 nm deliquescence- and efflorescence- mode experiments. Size distributions measured and fitted with the TDMAfit algorithm.

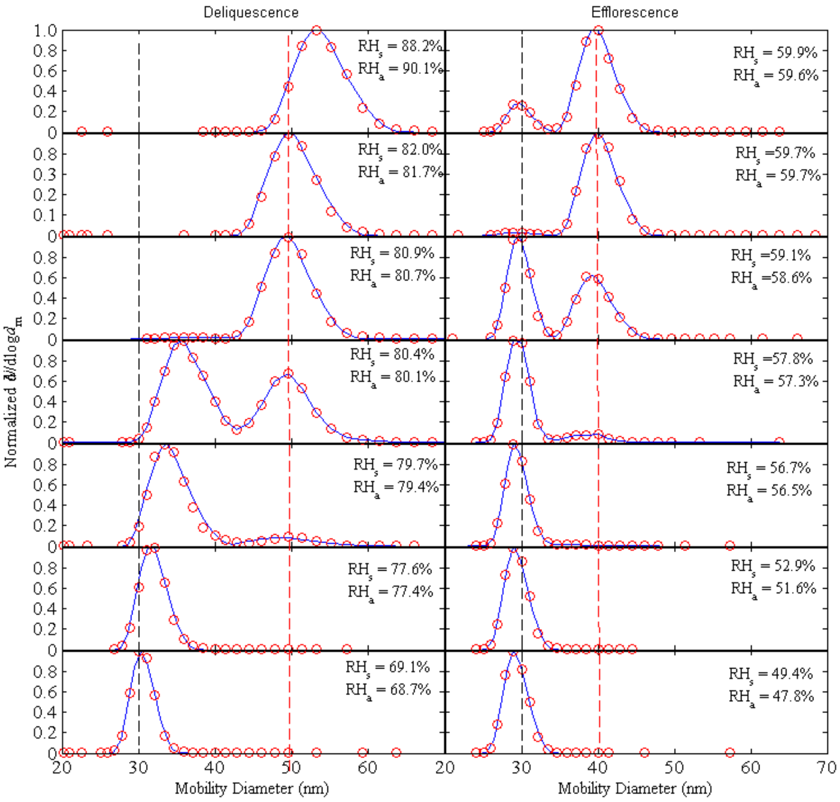

Figure B.3: KBr 30 nm deliquescence- and efflorescence- mode experiments. Size distributions measured and fitted with the TDMAfit algorithm.

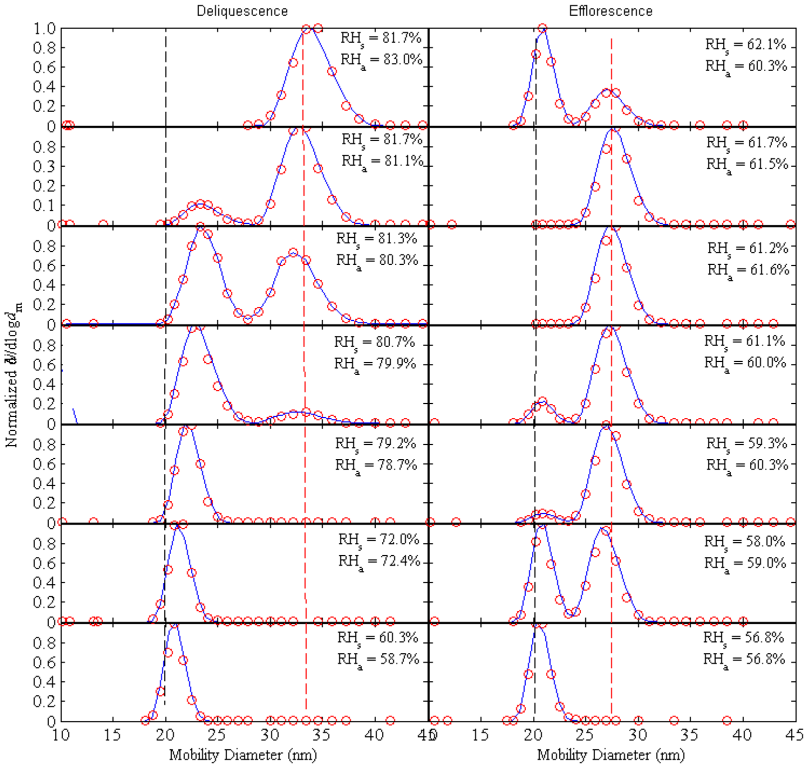

Figure B.4: KBr 20 nm deliquescence- and efflorescence- mode experiments. Size distributions measured and fitted with the TDMAfit algorithm.

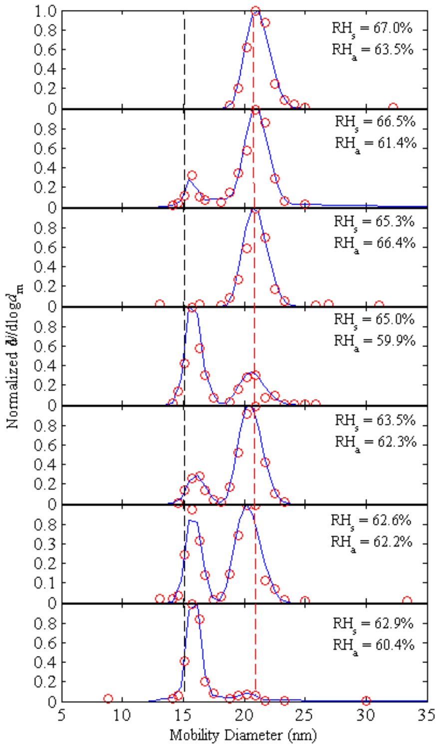

Figure B.5: KBr 15 nm efflorescence- mode experiments. Size distributions measured and fitted with the TDMAfit algorithm.

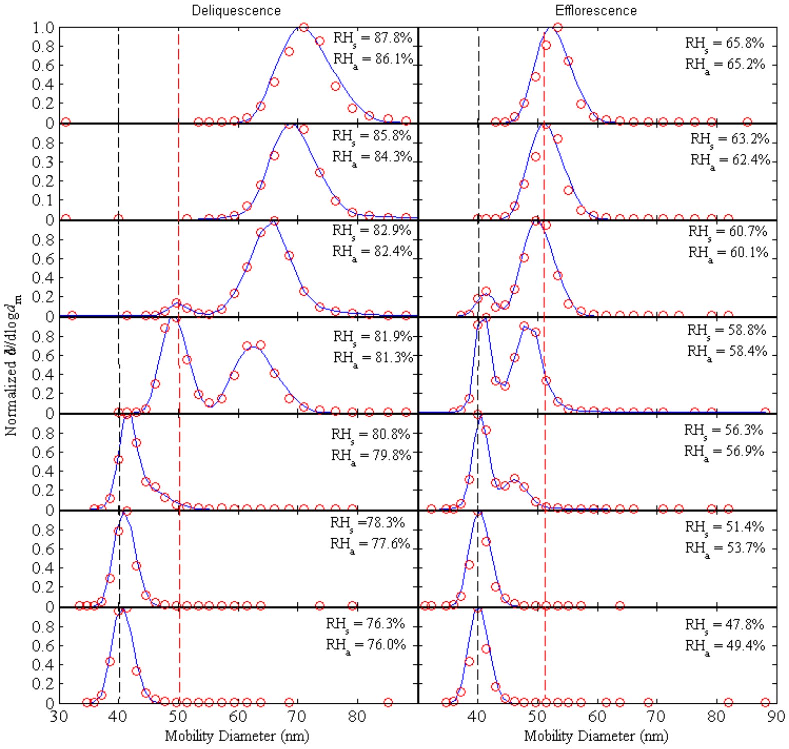

Figure B.6: KCl 40 nm deliquescence- and efflorescence- mode experiments. Size distributions measured and fitted with the TDMAfit algorithm.

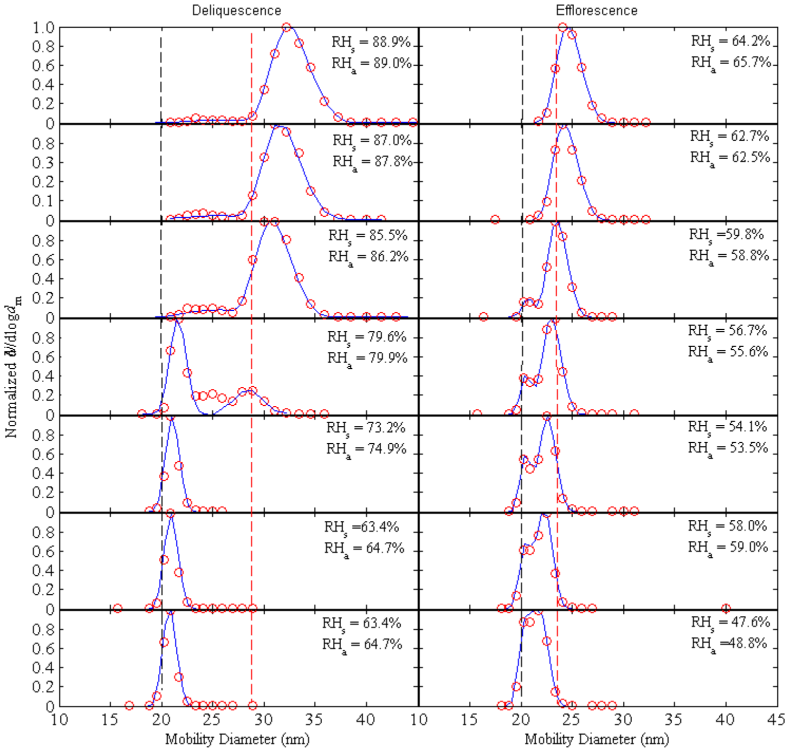

Figure B.7: KCl 20 nm deliquescence- and efflorescence- mode experiments. Size distributions measured and fitted with the TDMAfit algorithm.

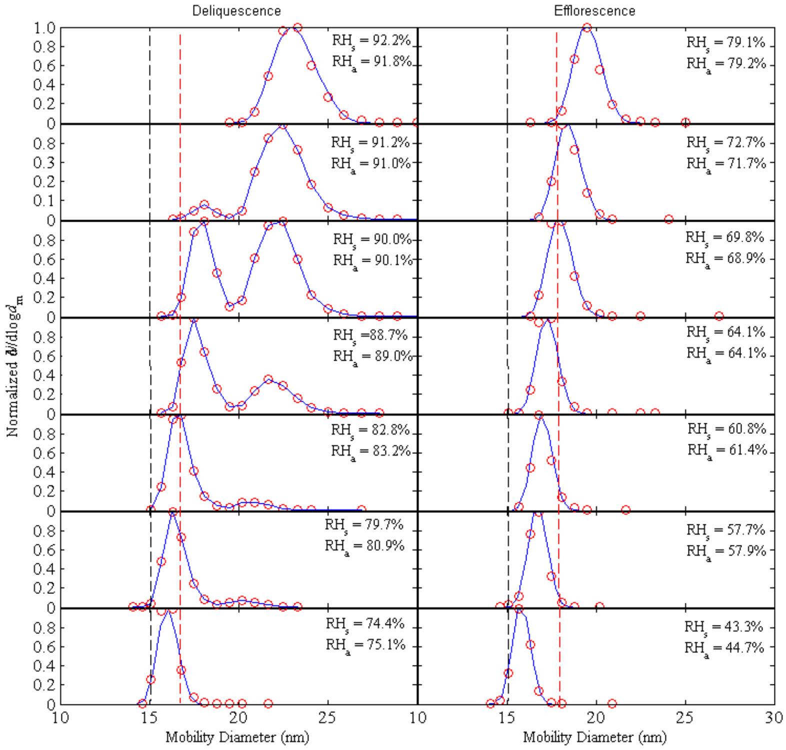

Figure B.8: KCl 15 nm deliquescence- and efflorescence- mode experiments. Size distributions measured and fitted with the TDMAfit algorithm.

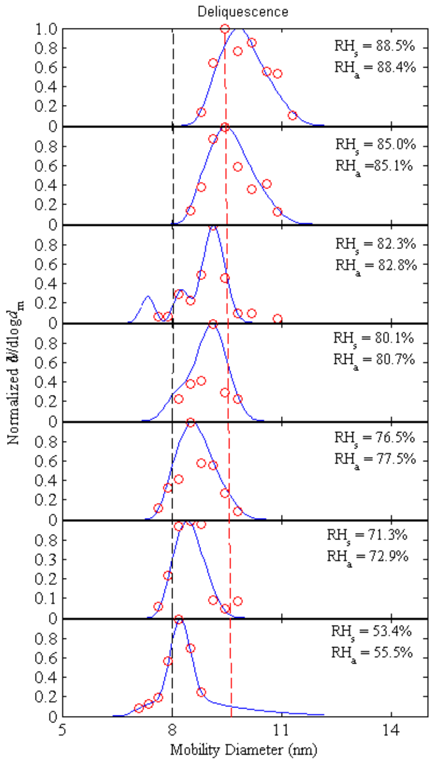

Figure B.9: KCl 8 nm deliquescence- mode experiments. Size distributions measured and fitted with the TDMAfit algorithm.

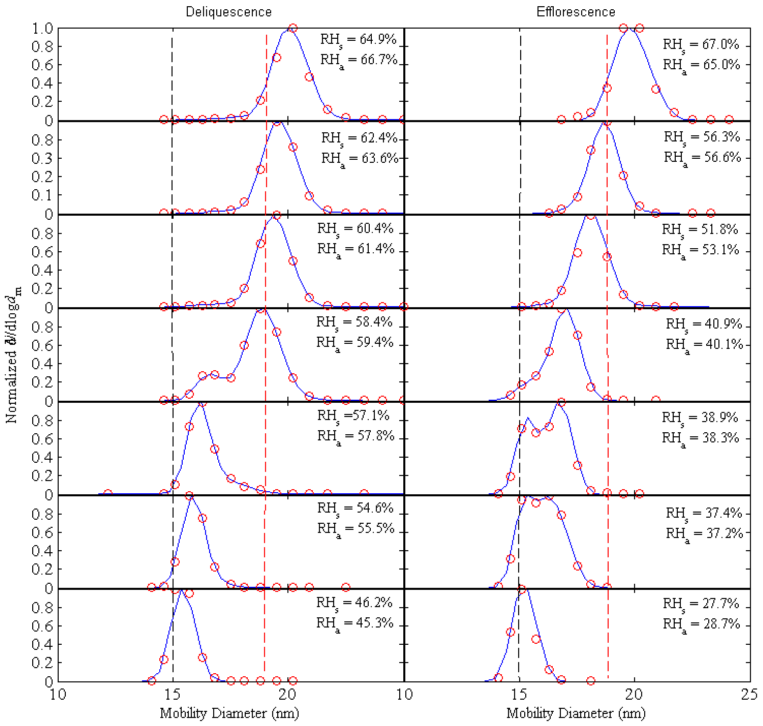

Figure B.10: KI 15 nm deliquescence- and efflorescence mode experiments. Size distributions measured and fitted with the TDMAfit algorithm.

Appendix C

Calculation of the H_2SO_4 proxy

The H_2SO_4 proxy concentration (molecules.cm^{-3}) has been estimated by (Mikkonen et al., 2011):

$$[\mathrm{H_2SO_4}] = 8.21 \times 10^{-3} \cdot k \cdot R \cdot [\mathrm{SO_2}]^{0.62} \cdot (CS \cdot RH)^{-0.13}, \qquad \text{(C.1)}$$

where R is the global radiation (W.m^{-2}) and RH is the relative humidity (%), whereas k (cm^3.molec$^-$1.s^{-1}) and CS (s^{-1}) are a temperature-dependent reaction rate constant and the condensational sink, respectively, given by:

$$k = \frac{A \cdot k_3}{(A + k_3)} exp\left[k_5 \left(1 + log_{10}\left(\frac{A}{k_3}\right)^2\right)^{-1}\right], \qquad \text{(C.2)}$$

$$CS = 2\pi D \int_0^\infty d\beta_m(d)N(d)dd = 2\pi D \sum_i d_i \beta_i N_i. \qquad \text{(C.3)}$$

Here, $\mathrm{A} = \mathrm{k_1[M](300/T)^{k_2}}$, T(K) is the temperature, $[\mathrm{M}] = 0.101 \times (1.381 \times 10^{-23}\mathrm{T})^{-1}$ is the air density (molecules^{-1}.cm^{-3}), $\mathrm{k_1} = 4 \times 10^{-31}$, $\mathrm{k_2} = 3.3$, $\mathrm{k_3} = 2 \times 10^{-12}$ and $\mathrm{k_5} = -0.8$. The data for the [H_2SO_4] proxy calculations were provided by Maturilli et al. (2012).